Zeitschrift: IABSE publications = Mémoires AIPC = IVBH Abhandlungen
Band: 34 (1974)

Teilband: IABSE Publications = Mémoires AIPC = IVBH Abhandlungen

Nutzungsbedingungen
Die ETH-Bibliothek ist die Anbieterin der digitalisierten Zeitschriften auf E-Periodica. Sie besitzt keine Urheberrechte an den Zeitschriften und ist nicht verantwortlich für deren Inhalte. Die Rechte liegen in der Regel bei den Herausgebern beziehungsweise den externen Rechteinhabern. Das Veröffentlichen von Bildern in Print- und Online-Publikationen sowie auf Social Media-Kanälen oder Webseiten ist nur mit vorheriger Genehmigung der Rechteinhaber erlaubt. Mehr erfahren

Conditions d'utilisation
L'ETH Library est le fournisseur des revues numérisées. Elle ne détient aucun droit d'auteur sur les revues et n'est pas responsable de leur contenu. En règle générale, les droits sont détenus par les éditeurs ou les détenteurs de droits externes. La reproduction d'images dans des publications imprimées ou en ligne ainsi que sur des canaux de médias sociaux ou des sites web n'est autorisée qu'avec l'accord préalable des détenteurs des droits. En savoir plus

Terms of use
The ETH Library is the provider of the digitised journals. It does not own any copyrights to the journals and is not responsible for their content. The rights usually lie with the publishers or the external rights holders. Publishing images in print and online publications, as well as on social media channels or websites, is only permitted with the prior consent of the rights holders. Find out more

Download PDF: 04.04.2026

ETH-Bibliothek Zürich, E-Periodica, https://www.e-periodica.ch

ASSOCIATION INTERNATIONALE DES PONTS ET CHARPENTES
INTERNATIONALE VEREINIGUNG FÜR BRÜCKENBAU UND HOCHBAU
INTERNATIONAL ASSOCIATION FOR BRIDGE AND STRUCTURAL ENGINEERING

MÉMOIRES
ABHANDLUNGEN
PUBLICATIONS

34-I

1974

PUBLIÉS PAR LE SECRÉTARIAT GÉNÉRAL À ZURICH
HERAUSGEGEBEN VOM GENERALSEKRETARIAT IN ZÜRICH
PUBLISHED BY THE GENERAL SECRETARIAT IN ZURICH

Editeur - Verleger - Publisher

Association Internationale des Ponts et Charpentes
Ecole Polytechnique Fédérale de Zurich

Internationale Vereinigung für Brückenbau und Hochbau
Eidgenössische Technische Hochschule Zürich

International Association for Bridge and Structural Engineering
Swiss Federal Institute of Technology, Zurich

En commission pour la vente en librairie
Kommissionsverlag für den Buchhandel - Copies for sale at

Verlag Leemann Zürich

Printed in Switzerland

Préface

La nécessité de publier rapidement les contributions scientifiques de nos membres nous empêche de publier des volumes de Mémoires liés à un thème donné. C'est d'ailleurs le rôle des publications relatives à un symposium ou à un congrès. Le présent volume contient douze apports à des préoccupations actuelles des spécialistes des ponts et charpentes. Ces exposés sont d'un très haut intérêt et s'inscrivent bien dans la tradition de nos Mémoires.

Je saisis cependant l'occasion de cette préface pour susciter la réflexion sur un nouveau style possible de nos publications. La mission de l'AIPC est de faire avancer la science et la technique des structures. Elle doit le faire dans un esprit large, considérant tous les matériaux, établissant des comparaisons sur les plans théoriques, conceptuels, d'exécution et économiques. Il serait donc heureux, dans tous les cas où la chose est possible, que l'auteur situe sa contribution par rapport aux autres théories ou systèmes et qu'il indique les répercussions possibles sur les plans de l'exécution et du coût.

Je remercie les auteurs et souhaite, pour l'avenir, une participation de collègues de langue française et allemande.

Zurich, avril 1974.

Le Président de l'AIPC:

Prof. MAURICE COSANDEY
Président de l'Ecole Polytechnique Fédérale de Lausanne

Les Secrétaires Généraux:

Dr. sc. techn. HANS VON GUNTEN
Professeur à l'Ecole Polytechnique Fédérale de Zurich

Dr. sc. techn. PIERRE DUBAS
Professeur à l'Ecole Polytechnique Fédérale de Zurich

JÖRG SCHNEIDER
Professeur à l'Ecole Polytechnique Fédérale de Zurich

Vorwort

Der Zwang, in rascher Folge die wissenschaftlichen Arbeiten unserer Mitglieder zu veröffentlichen, erlaubt es nicht, einzelne Bände unserer «Abhandlungen» einem in sich geschlossenen Themenkreis zu widmen. Im übrigen ist dies Aufgabe der anlässlich von Symposien und Kongressen herausgegebenen Veröffentlichungen. Der vorliegende Band enthält zwölf äusserst wertvolle Beiträge von Fachleuten aus dem Brückenbau und Hochbau und führt damit die bewährte Tradition unserer «Abhandlungen» fort.

Dieses Vorwort gibt mir jedoch Anlass zu gewissen Überlegungen über einen neuen Charakter unserer Veröffentlichungen: Die Aufgabe der IVBH besteht darin, Wissenschaft und Bautechnik zu fördern. Sie soll dies in einem weiten Gesichtskreis tun und dabei alle Baustoffe berücksichtigen sowie gleichmässig Theorie, Entwurf, Ausführung und Wirtschaftlichkeit behandeln. Es wäre deshalb wünschenswert, dass jeder Autor seinen Beitrag soweit möglich unter vergleichender Beachtung anderer Theorien bzw. Systeme bearbeitet und dabei auch die möglichen Rückwirkungen auf Ausführung und Kosten einbeziehen würde.

Ich danke den Verfassern und hoffe, in Zukunft auch die Kollegen französischer und deutscher Zunge hier vertreten zu sehen.

Zürich, April 1974.

Der Präsident der IVBH:

Prof. Maurice Cosandey
Präsident der Eidgenössischen Technischen Hochschule Lausanne

Die Generalsekretäre:

Dr. sc. techn. Hans von Gunten
Professor an der Eidgenössischen Technischen Hochschule Zürich

Dr. sc. techn. Pierre Dubas
Professor an der Eidgenössischen Technischen Hochschule Zürich

Jörg Schneider
Professor an der Eidgenössischen Technischen Hochschule Zürich

Preface

The requirement of early publication of our members' scientific contributions prevents us from compiling volumes of "Publications" on a given theme. This is essentially the role of publications relating to symposia or congresses. The present volume contains twelve contributions concerning current preoccupations of building and structural engineers. These papers are of considerable interest and correspond to the customary standard of our "Publications".

Nevertheless, I am taking the opportunity, in writing this preface, to invite some thoughts on a new style that could be introduced in our publications. The aim of the IABSE is to further the knowledge and technology of structures. This must be done in the broadest possible sens, taking into account all materials, establishing comparisons as to theory, concept, execution and economy. It would therefore seem to be advantageous for each author to situate, whenever possible, his contribution in relation to other theories or systems, and to indicate possible repercussions in execution and costs.

I thank the authors for their contribution and look forward to receiving some items also from our French and German speaking colleagues.

Zurich, April 1974.

The President of IABSE:

Prof. MAURICE COSANDEY
President of the Swiss Federal Institute of Technology, Lausanne

The General Secretaries:

Dr. sc. techn. HANS VON GUNTEN
Professor at the Swiss Federal Institute of Technology, Zurich

Dr. sc. techn. PIERRE DUBAS
Professor at the Swiss Federal Institute of Technology, Zurich

JÖRG SCHNEIDER
Professor at the Swiss Federal Institute of Technology, Zurich

Leere Seite
Blank page
Page vide

Table des matières - Inhaltsverzeichnis - Table of Contents

K. Aas-Jakobsen, M. Grenacher ..... English 1

Calcul des cadres en béton armé selon la théorie du 2e ordre
Berechnung von Stahlbetonrahmen nach der Theorie 2. Ordnung
Analysis of Slender Reinforced Concrete Frames

W. Bogucki, A. Niedzielski ..... English 19

La limite de fatigue d'acier et de soudages bout à bout dans des conditions déterminées de service
Die Dauerfestigkeit von Stahl und Stumpfschweissungen unter festbegrenzten Betriebsbedingungen
The Fatigue Strength of Steel and Butt Welds in Definite Working Conditions

A. Ghali, G. S. Tadros ..... English 25

Analyse par bandes finies de plaques continues
Über die Finite-Streifen-Berechnung von Platten
On Finite Strip Analysis of Continuous Plates

M. M. Ghamian, S. Krishnasamy, A. N. Sherbourne ..... English 35

Structures en acier soumises à des déflexions cycliques inégales
Stahlkonstruktionen unter zyklischer nicht konstanter Deformation
Steel Structures under Cyclic Unequal Deflections

S. K. Ghosh, M. Z. Cohn ..... English 71

Analyse de sections en béton armé soumises à un effort normal avec flexion au moyen d'un calculateur électronique
Computer-Berechnung von Stahlbetonquerschnitten unter kombinierter Biegung und Druck
Computer Analysis of Reinforced Concrete Sections under Combined Bending and Compression

J. Glück, M. Gellert ..... English 95

Généralisation de la méthode des bandes finies pour les continus solides
Verallgemeinerung der Finite-Streifen-Methode für Festkörperkontinua
Generalization of the Finite Strip Method for Solid Continua

D. A. Nethercot ..... English 107

Flambement de poutrelles soudées
Kippen geschweisster Balken und Träger
Buckling of Welded Beams and Girders

W. Oberndorfer ..... Deutsch 123

La construction du toit en porte-à-faux du stade de Lehen à Salzbourg, Autriche
Die Kragschalenkonstruktion des Stadions Lehen in Salzburg
The Cantilever Roof Construction of the Lehen Stadium at Salzburg, Austria

A. Sabzevari, E. Hjorth-Hansen ..... English 129

De l'augmentation de la stabilité aérodynamique de sections en double Té et en U
Über die Verbesserung der aerodynamischen Stabilität von H-förmigen und Kanalquerschnitten
On Improving the Aerodynamic Stability of H and Channel Sections

A. Selberg ..... English 145

De la capacité de cisaillement des âmes de poutres
Über die Schubkapazität von Trägerstegen
On the Shear Capacity of Girder Webs

A. N. Sherbourne, S. Krishnasamy ..... English 157

Poutres en acier doux: comportement et ruine sous l'influence de charges cycliques alternatives
Flussstahl-Balken: Verhalten und Versagen unter zyklischer Wechselbelastung
Mild Steel Beams: Behaviour and Failure under Cyclic Alternating Loads

R. F. Warner, J. H. Lambert ..... English 181

Relations entre moment, flexion et temps sur les poutres en béton armé
Beziehung zwischen Moment, Biegung und Zeit an Stahlbetonteilen
Moment-Curvature-Time Relations for Reinforced Concrete Beams

Analysis of Slender Reinforced Concrete Frames

Calcul des cadres en béton armé selon la théorie du 2e ordre

Berechnung von Stahlbetonrahmen nach der Theorie 2. Ordnung

K. AAS-JAKOBSEN
Dr. sc. techn., formerly, research associate

M. GRENACHER
Research associate

Institute of Structural Engineering, Swiss Federal Institute of Technology (ETH), Zurich (Switzerland)

1. Introduction

This paper outlines a method to determine the maximum load carrying capacity of a plane frame with given cross sections and reinforcements.

The present paper based on an investigation described in [1] differs from other investigations [2], [3], [4], [5], [6], [7], [8] in three respects:

— The frame can have an arbitrary geometry.

— An arbitrary load history can be followed.

— A displacement controlled procedure is used which allows the determination of unstable configurations of the frame.

The two main difficulties in the analysis of slender reinforced concrete frames are due to

— the influence of the displacements on the equilibrium of the frame, producing a "geometrical" non-linearity;

— the non-linear stress-strain-time relations for the materials causing a "material" non-linearity.

The two non-linearities are treated separately as shown schematically in Fig. 1. The geometrical non-linearity is considered in a second order elastic analysis. Given are loads P, bending rigidities EI and axial rigidities EA for all elements of the frame. The moment M, the axial force N and the corresponding strain distribution for all sections are determined. The strain

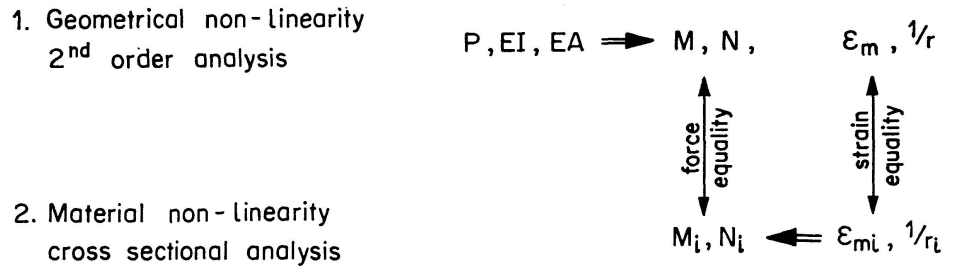

Fig. 1. Schematic illustration of the analysis.

distribution is given by two parameters. Herein, the middle strain ϵ_m in the reference axis of the members and the curvature $1/r$ are used.

The material non-linearity is taken into account in the cross sectional analysis. Given are cross section, reinforcement, stress-strain-time relation for the materials and a strain distribution (ϵ_{mi}, $1/r_i$). The subscript "i" is used for reference to the cross sectional analysis. The moment M_i and axial force N_i are determined.

The elastic and the cross sectional analysis are coupled together by the requirement of equality of the determined forces in the elastic and the cross sectional analysis. Similarly, equality of the strains determined in the elastic analysis and of the strains assumed in the cross sectional analysis must be satisfied.

The critical load of the structure corresponds to the peak on a load-deflection curve separating the stable from the unstable equilibrium configuration. In this range a deformation controlled procedure must be used to assure convergence. Hence, the deformation at some point of the structure is increased by steps to obtain the load-displacement response.

2. Second Order Elastic Analysis

The elastic frame analysis is performed by means of the finite element method. A frame may be visualized as an assemblage of elements interconnected at their ends which are referred to as nodal points or nodes. If the force-displacement relations for each element are known, the equilibrium configuration of the complete structure can be expressed in terms of the nodal

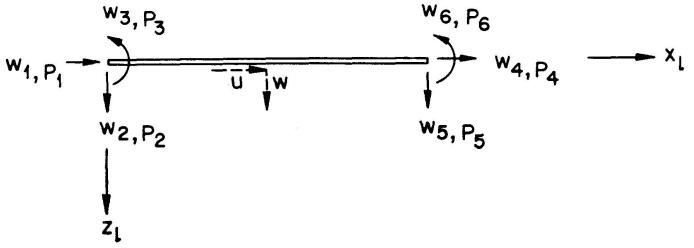

Fig. 2. Element in local coordinates.

displacements. The force-displacement relationship for the element shown in Fig. 2 can be written as

$$[K]\{w\} = \{P\}, \tag{1}$$

in which $\{w\}$ is the displacement vector of the element and $\{P\}$ the corresponding force vector:

$$\{w\} = \begin{Bmatrix} w_1 \\ w_2 \\ w_3 \\ w_4 \\ w_5 \\ w_6 \end{Bmatrix}, \qquad \{P\} = \begin{Bmatrix} P_1 \\ P_2 \\ P_3 \\ P_4 \\ P_5 \\ P_6 \end{Bmatrix}.$$

Applying standard finite element techniques, the stiffness matrix $[K]$ can be written as

$$[K] = [K_1] + [K_2],$$

where $[K_1]$ is the first order stiffness matrix,
$[K_2]$ is the non-linear geometrical stiffness matrix,
$[K_1]$ and $[K_2]$ are given in Fig. 3.

If the element is inclined at an angle θ with the x-axis, as shown in Fig. 4, the given stiffness matrix above relates to the local coordinates $x_l - z_l$. The

$$[K_1] = \begin{bmatrix} \frac{EA}{l} & & & -\frac{EA}{l} & & \\ & \frac{12EI}{l^3} & \frac{6EI}{l^2} & & -\frac{12EI}{l^3} & \frac{6EI}{l^2} \\ & & \frac{4EI}{l} & & -\frac{6EI}{l^2} & \frac{2EI}{l} \\ & \text{symmetric} & & \frac{EA}{l} & & \\ & & & & \frac{12EI}{l^3} & -\frac{6EI}{l^2} \\ & & & & & \frac{4EI}{l} \end{bmatrix} \qquad [K_2] = N \begin{bmatrix} & & & & & \\ & \frac{6}{5l} & \frac{1}{10} & & -\frac{6}{5l} & \frac{1}{10} \\ & & \frac{2l}{15} & & -\frac{1}{10} & -\frac{l}{30} \\ & \text{symmetric} & & & & \\ & & & & \frac{6}{5l} & -\frac{1}{10} \\ & & & & & \frac{2l}{15} \end{bmatrix}$$

Fig. 3. Local element stiffness matrix $[K]=[K_1]+[K_2]$.

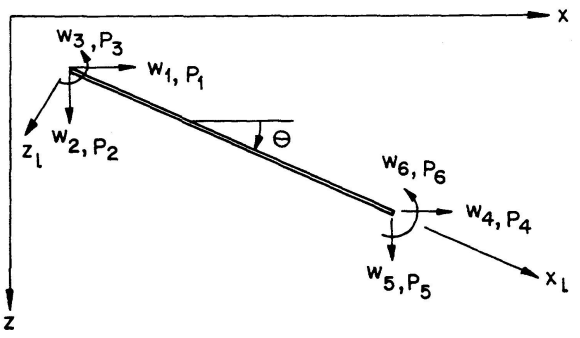

Fig. 4. Global forces and displacements.

global stiffness matrix $[K]$ in the x-z coordinate system is then given by

$$[K] = [R]^T [K_l] [R].$$

$[K_l]$ is the local stiffness matrix given in Fig. 3.

$[R]$ is the transformation matrix relating local displacements $\{w_l\}$ and global displacements $\{w\}$, or local loads $\{P_l\}$ and global loads $\{P\}$ as follows:

$$\{w_l\} = [R]\{w\}, \tag{2}$$
$$\{P_l\} = [R]\{P\},$$
$$[R] \quad \text{is given in Fig. 5.}$$

The global element stiffness matrix $[K] = [K_1] + [K_2]$ is given in Fig. 6.

$[R] =$

C	S				
-S	C				
		1			
			C	S	
			-S	C	
					1

$\{w_l\} = [R]\{w\}$

$\{P_l\} = [R]\{P\}$

$S = \sin\Theta$

$C = \cos\Theta$

Fig. 5. Transformation matrix $[R]$.

$[K_1] =$

$\frac{EA}{l} C^2 + \frac{12EI}{l^3} S^2$	$\left(\frac{EA}{l} - 12\frac{EI}{l^3}\right) SC$	$-\frac{6EI}{l^2} S$	$-k_{11}$	$-k_{12}$	k_{13}
	$\frac{EA}{l} S^2 + \frac{12EI}{l^3} C^2$	$\frac{6EI}{l^2} C$	$-k_{12}$	$-k_{22}$	k_{23}
		$4\frac{EI}{l}$	$-k_{13}$	$-k_{23}$	$\frac{2EI}{l}$
	symmetric		k_{11}	k_{12}	$-k_{13}$
				k_{22}	$-k_{23}$
					k_{33}

$[K_2] = N$

$\frac{6}{5 \cdot l} S^2$	$-\frac{6}{5l} SC$	$-\frac{1}{10} S$	$-k_{11}$	$-k_{12}$	k_{13}
	$\frac{6}{5l} C^2$	$\frac{1}{10} C$	$-k_{12}$	$-k_{22}$	k_{23}
		$\frac{2l}{15}$	$-k_{13}$	$-k_{23}$	$-\frac{l}{30}$
	symmetric		k_{11}	k_{12}	$-k_{13}$
				k_{22}	$-k_{23}$
					k_{33}

$S = \sin\Theta \quad C = \cos\Theta$

Fig. 6. Global element stiffness matrix $[K] = [K_1] + [K_2]$.

Similar to the force-displacement relationship for the element the force-displacement relationship for the complete structure, or the complete system of elements, can be written as

$$[K]\{w\} = \{P\}, \tag{3}$$

in which $\{w\}$ now contains all nodal displacements and $\{P\}$ all nodal loads.

The system stiffness matrix for the complete structure is obtained by superposition of the individual element stiffness matrices.

When the system stiffness matrix $[K]$ and the load matrix $\{P\}$ have been established, the system of equations is adjusted according to the given boundary conditions. If some displacement, for instance w_j, is identical to zero, this can be taken into account in a simple manner by replacing the diagonal stiffness coefficient K_{jj} by a large number, say 10^{50}.

The solution of the linear system of equations, Eq. (3) is most efficiently carried out taking into account the symmetry and the banded structure of the system stiffness matrix.

It should be noted that the axial force N must be known in order to evaluate the element matrix $[K_2]$ in Fig. 6. The axial force is usually not known in advance, and an iterative procedure must be used. In the first cycle N is chosen equal to zero and the first order forces are calculated. In the second cycle the axial forces found in the first cycle are used.

Usually the axial forces are practically not influenced by the second order effects, such that two cycles are generally sufficient.

When the displacements have been determined, the element forces are found by substituting $\{w\}$ back into Eq. (1). It should be noted that $[K]$ in Eq. (1) is the local element stiffness matrix given in Fig. 3. The global displacements are transformed into local displacements according to Eq. (2).

3. Cross Sectional Analysis

In the cross sectional analysis each section is divided into narrow strips which are assumed to behave as concentrically loaded fibers.

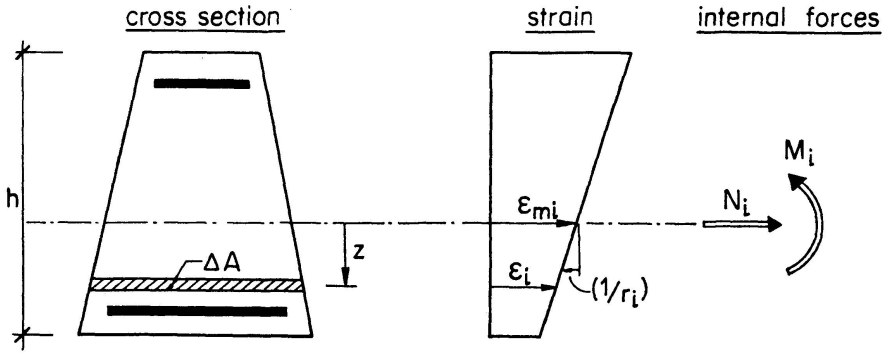

Fig. 7. Cross section, strain distribution and forces.

The resultant forces M_i and N_i are given by (Fig. 7)

$$\begin{aligned} M_i &= \sum \sigma z \Delta A, \\ N_i &= \sum \sigma \Delta A. \end{aligned} \tag{4}$$

The strain ϵ, positive when in tension, is assumed to be linearly distributed over the section. Then

$$\epsilon_i = \epsilon_{mi} - \left(\frac{1}{r_i}\right) z, \tag{5}$$

where ϵ_{mi} is the axial strain in the reference axis,
$\left(\frac{1}{r_i}\right)$ is the curvature,
z is the distance from the axis.

The assumed stress-strain relationship for a virgin concrete specimen (previously not loaded) under instantaneous loading up to failure is shown in Fig. 8. For instantaneous unloading or reloading a linear relation between stress and strain is assumed both for steel and concrete:

$$\sigma = E(\epsilon_i - \epsilon_c - \epsilon_p), \tag{6}$$

where σ is the stress in the considered strip,
E is the "elastic" modulus for the material,
ϵ_i is the total strain,
ϵ_c is the "plastic" strain in the strip from the previous load history,
ϵ_p is the initial strain in the strip, for instance due to prestressing.

The "plastic" strain ϵ_c is due to yielding, creep and shrinkage. At a given time, the magnitude of the plastic strain can be determined from Eq. (6):

$$\epsilon_c = \epsilon - \sigma/E - \epsilon_p. \tag{7}$$

Steel is assumed to be elasto-plastic as shown in Fig. 8. Thus, the stress given by Eq. (6) is limited by the yield stress f_s.

The concrete stress determined from Eq. (6) is assumed to be limited by the stress-strain relationship for a virgin concrete under instantaneous loading. Hence, the stress-strain relationship for a virgin specimen is the envelope curve for the concrete stress-strain relations. The concrete is assumed to have no tensile strength. Concrete shows a time-dependent increase of the plastic strain ϵ_{cc} due to shrinkage and creep.

At a constant sustained stress the plastic strain due to creep is assumed to be given by

$$\epsilon_{cc} = \epsilon_0 \varphi, \tag{8}$$

$$\varphi = \varphi_\infty \frac{t}{T+t}, \tag{9}$$

where φ_∞ is the limiting creep factor,
T is the elapsed time until half the limiting creep is reached,
ϵ_0 is the short-time strain given by:

$$\epsilon_0 = -0.002\left(1 - \sqrt{1 + \frac{\sigma_c}{f_c}}\right). \tag{10}$$

The hyperbolic expression in Eq. (9) has been used in a number of investigations and seems to be in reasonable agreement with experimental data.

Creep under variable stresses is calculated by dividing the stress history

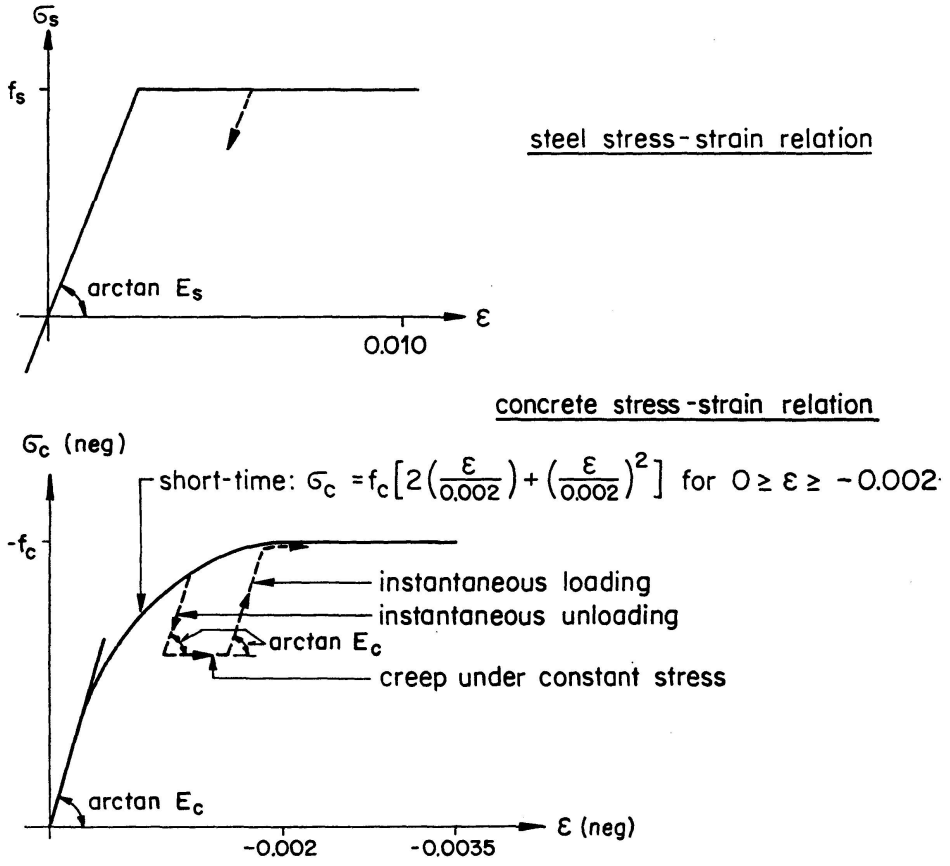

Fig. 8. Stress-strain relations.

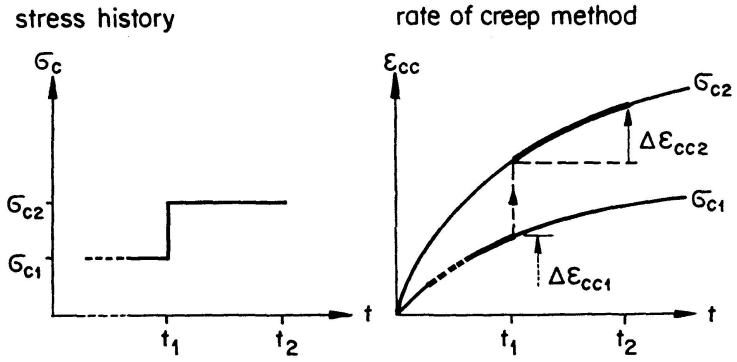

Fig. 9. Creep under variable stresses.

into time intervals and assuming a constant stress within each interval as indicated in Fig. 9. The "rate of creep" method is applied. It is assumed that the creep under variable stresses can be obtained from creep curves for constant stresses. Such curves, for two stress levels σ_{c1} and σ_{c2}, are indicated with solid lines in Fig. 9. In the time interval $\Delta t = t_2 - t_1$ the increase of strain under the stress σ_{c2} is given by

$$\Delta \epsilon_{cc} = \epsilon_0 \varphi_\infty \frac{t_1 + \Delta t}{T + t_1 + \Delta t} - \frac{t_1}{T + t_1}, \tag{11}$$

where

$$\epsilon_0 = -0.002 \left(1 - \sqrt{1 + \frac{\sigma_{c2}}{f_c}}\right).$$

The procedure for determining the stress σ_{c2} at the end of the time interval $t + \Delta t$ is outlined in Fig. 10. Given are the total strain ϵ at the time $t + \Delta t$, the prior plastic strain ϵ_{cc}, the initial strain ϵ_p and the stress σ_{c1} at the time t. As an approximative solution the stress σ_{c1} is used to determine the increase of creep strain $\Delta \epsilon_{cc}$ from Eq. (11). In the case of shrinkage, the corresponding shrinkage strain is added to $\Delta \epsilon_{cc}$. The stress σ_{c2} is determined from Eq. (6). If σ_{c2} exceeds the short-time stress corresponding to the total strain ϵ, the latter stress is chosen. The plastic strain ϵ_{cc} at the time $t + \Delta t$ is given by Eq. (7).

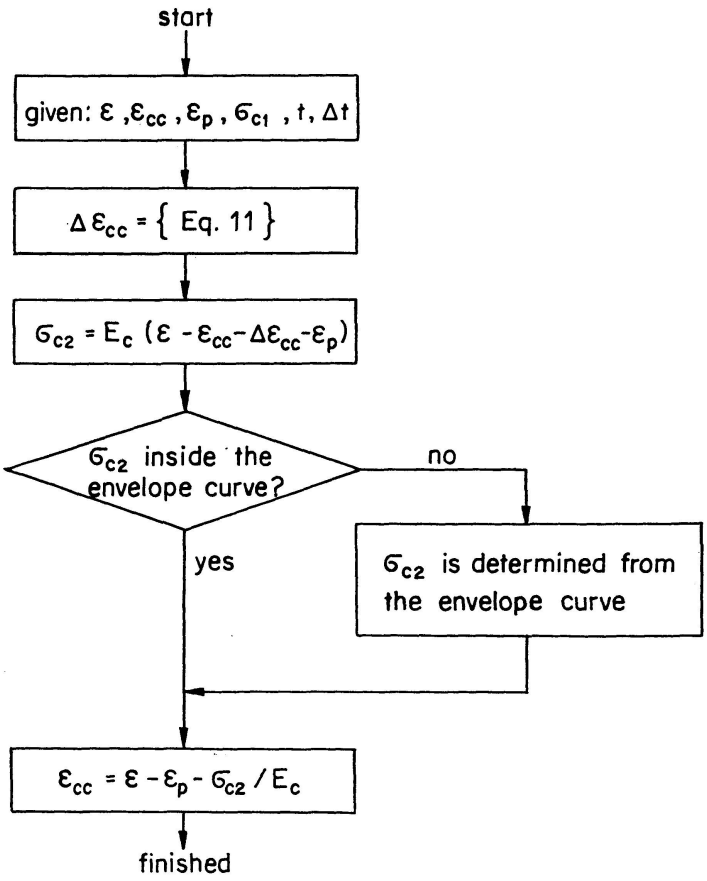

Fig. 10. Determination of stress and "plastic" strain.

4. Computation Procedure

The load carrying capacity of a frame with given cross sections and reinforcements is calculated in successive steps up to the maximum capacity.

Fig. 11 shows the flow-chart used for determining a point on the load-displacement curve. The procedure starts with assumed rigidities for all elements. In a second order elastic analysis, the elastic forces M and N, and the strain distribution expressed by middle strain ϵ_m and curvature $(1/r)$ are determined for all elements. The internal forces M_i and N_i are determined in

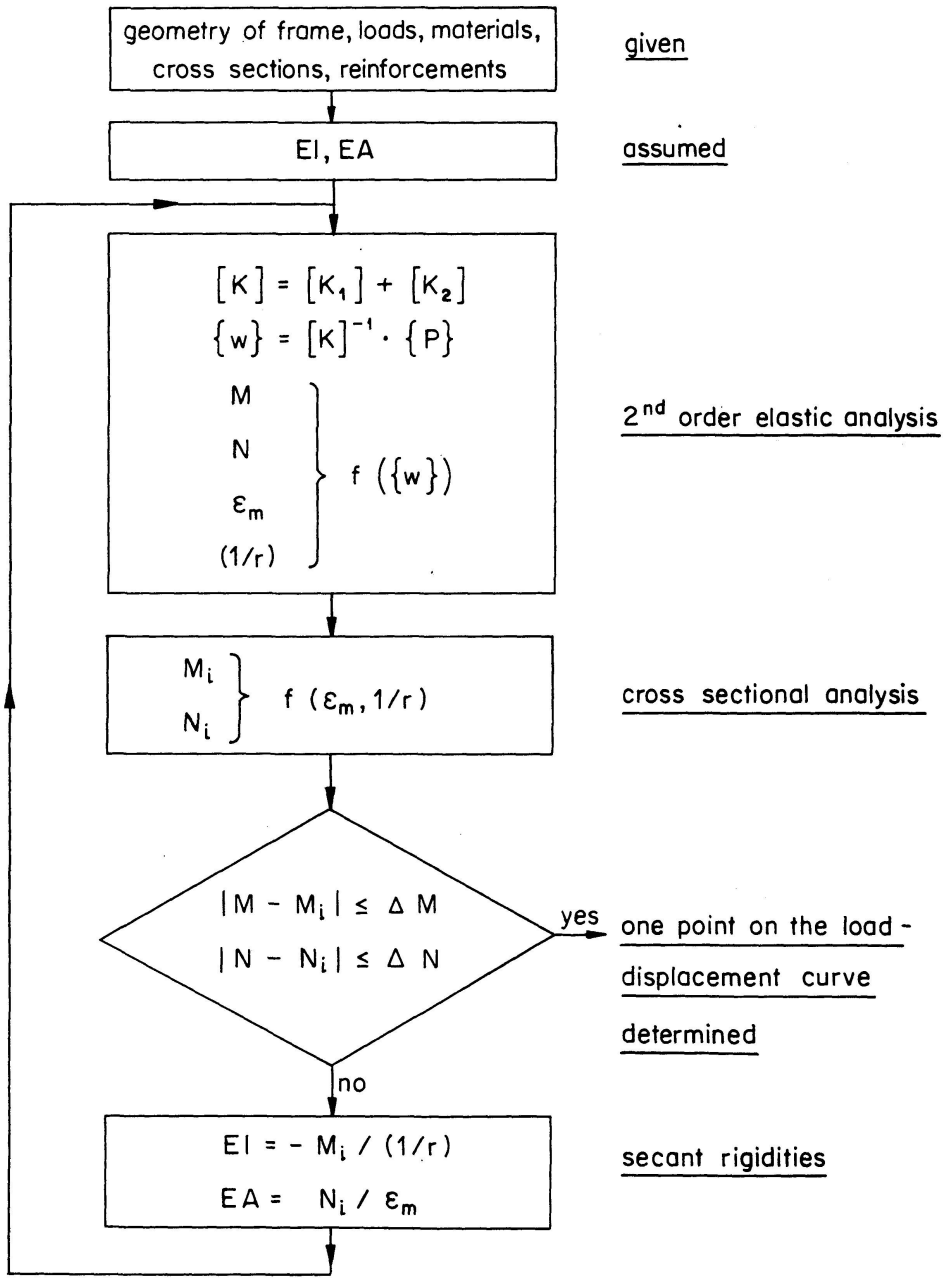

Fig. 11. Flow-chart for frame analysis.

a cross sectional analysis based on the strain distribution found in the elastic analysis. Thus strain equality is automatically satisfied. Force equality then becomes the iteration criterion of the procedure *). If equality is not satisfied, improved secant rigidities are determined from the internal forces, and the procedure is repeated.

The maximum load capacity of slender reinforced concrete frames is associated with instability as indicated in Fig. 12. In a load controlled procedure where the external load is increased in steps poor convergence develops near the maximum load. The unloading part of the curve cannot be calculated. In a displacement controlled procedure, where a characteristic displacement is increased step by step and the corresponding load is calculated, no problems of convergence are encountered.

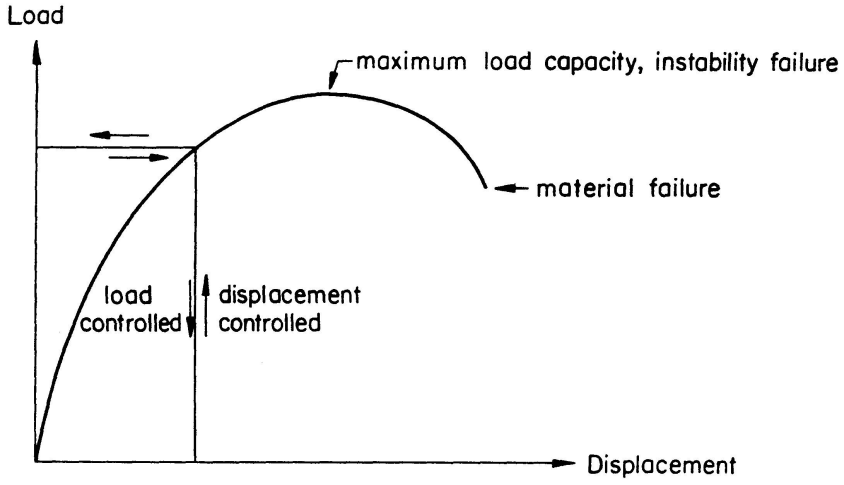

Fig. 12. Load-displacement curve for a slender reinforced concrete frame.

In the present study, external loads on a frame are divided into constant and proportional loads (Fig. 13). The latter are proportional to a load factor λ. A displacement controlled procedure will be used. The displacement w is increased in steps until the maximum value of λ has been found.

For each value of the specified displacement w, the corresponding load factor λ is found iteratively as outlined in the following. First rigidities are assumed for all elements. Then, the load factor λ is increased in steps until calculated and specified displacement coincide. New rigidities can now be determined in the cross sectional analysis. The procedure is repeated until assumed and calculated rigidities agree. The outlined procedure was slightly modified in the above mentioned program in order to speed up the convergence (see Fig. 13). Generally, a non-linear relation exists between the load

*) A slightly different procedure was used in the computer program [1] in order to ensure convergence. In the cross sectional analysis the middle strain ϵ_{mi} was determined iteratively to satisfy the axial force equilibrium. The curvature was kept constant. Moment and middle strain equalities become the iteration criterion in this case.

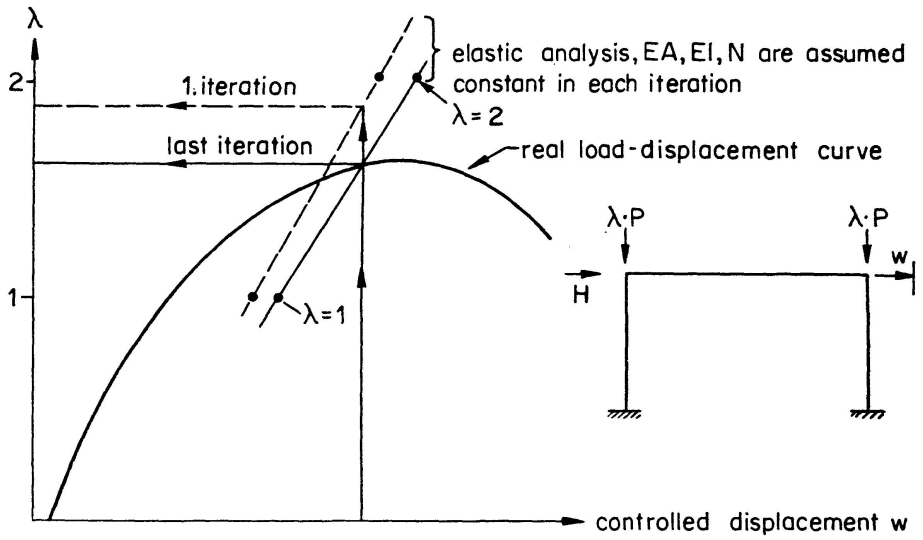

Fig. 13. Displacement controlled determination of a point on the real load-displacement curve.

factor and the displacements even if the rigidities are kept constant. The reason is that the geometrical stiffness matrix $[K_2]$ (Fig. 3) depends on the axial forces N which, in turn, depend on the load factor λ. However, if the axial forces introduced into the geometrical stiffness matrix are assumed independent of λ, a linear relation between λ and the displacement results. Hence, it is sufficient to consider two loading cases, for instance λ equal to 1 and λ equal to 2. The load factor corresponding to the specified displacement w is found by linear interpolation as indicated in Fig. 13. For this new load factor new rigidities and axial forces to be introduced in $[K_2]$ are determined. The procedure is repeated until the calculated rigidities and axial forces agree with the assumed ones.

Under sustained loads, specified by the long-time load factor λ_s and duration t, the displacement w can be calculated as follows:

The displacement w is increased in steps as before. For each step of w, the

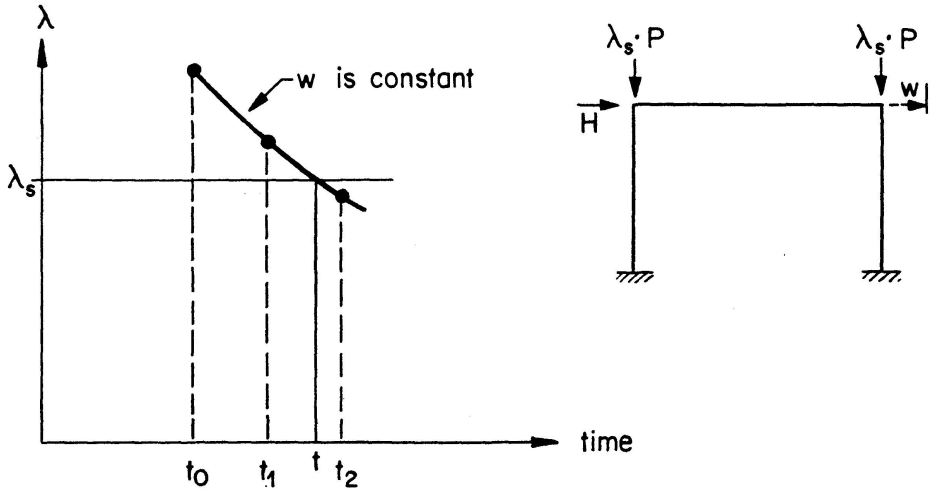

Fig. 14. Displacement controlled procedure under sustained loads.

time is increased in increments. (Fig. 14 corresponds to one value of w; the starting time is t_0.) For each increment of time the corresponding load factor λ is determined as before considering the creep of concrete. When the calculated load factor λ is equal to the given load factor λ_s, the time to reach the chosen displacement has been found. If the calculated λ at the starting time t_0 is less than λ_s, creep instability has taken place.

5. Examples

The following examples illustrate the application of the described analysis.

a) Comparison with Test Results

Three test columns under different types of loads [9] were analysed according to the described method. The three columns had hinged ends on both sides and were of the same length and same cross section (Fig. 15). Due to the symmetry only one half of each column was considered. The column was divided in 6 elements.

Column 24 was loaded in a short time test up to failure (Fig. 15). The measured and the calculated load capacity of 24.2 t agreed favourably. The slightly overestimated middle deflection δ can be explained with the assumption of no tensile strength of the concrete.

Column 25 (Fig. 16) was loaded by a sustained load $P_s = 16.4$ t during 141 days. After this time the increase of deformation was very small. Also for this column the agreement of the measured and computed failure load in the final

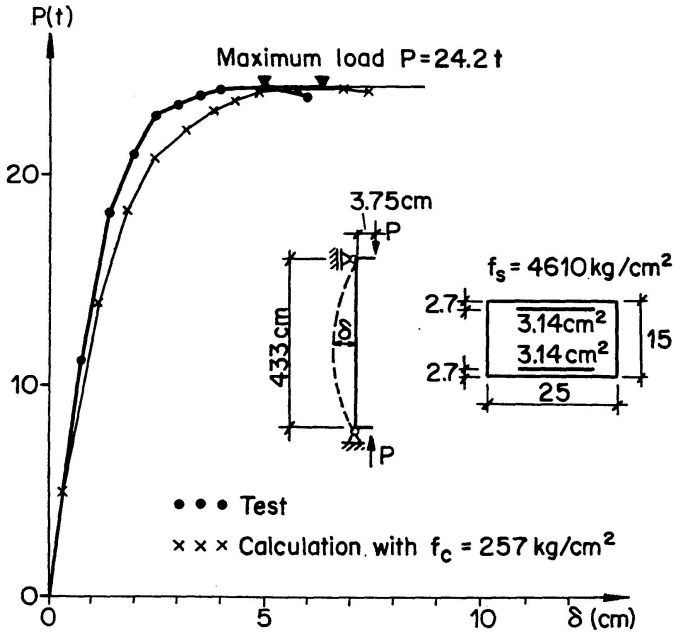

Fig. 15. Load-displacement curve (column 24).

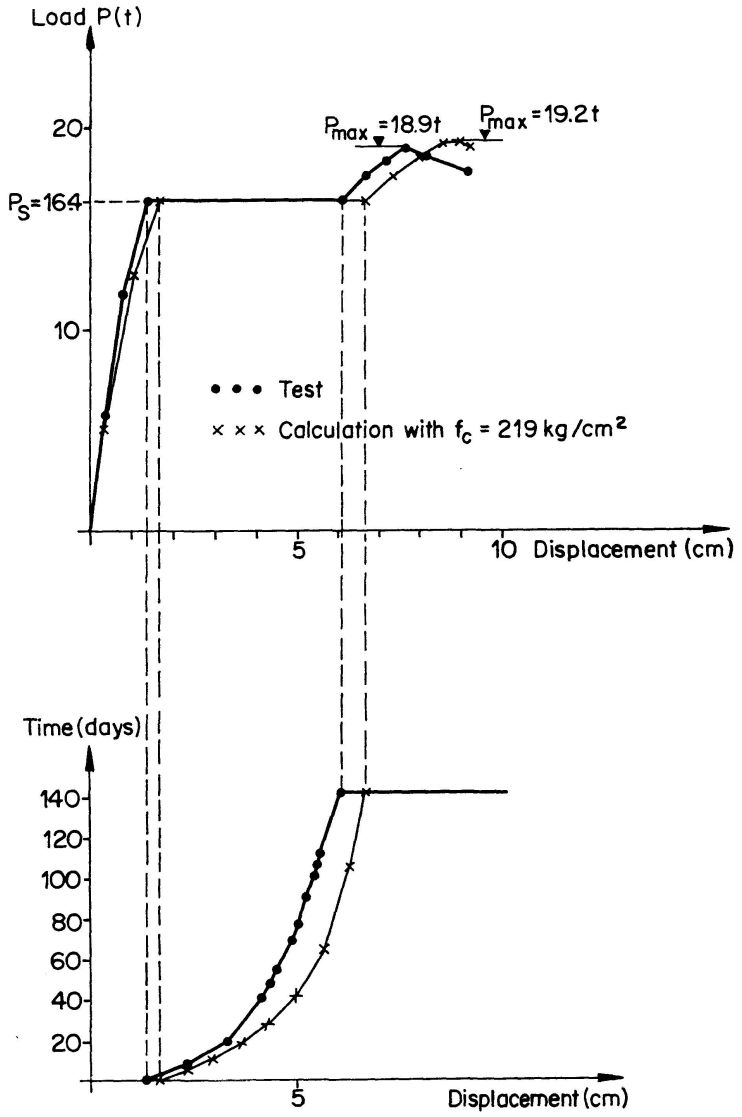

Fig. 16. Test under sustained load and final short time test (column 25).

short time test was good ($< 2\%$). The computed deflections both under sustained and under short time loads are too big due to the already mentioned reason. The relation between the middle deflection δ and the time is shown in the lower part of Fig. 16. The agreement of the two curves is satisfactory considering the big scattering which usually is involved in creep problems.

Fig. 17 shows a test under sustained load. The column failed due to creep buckling. The computed load-displacement curve is in good agreement with the measured one. With a middle deflection δ of 9 cm the column becomes unstable under the constant sustained load $P_s = 18.9$ t. The relation between the deflection δ and the time t agrees well up to $t = 61$ days. The computed time at failure is 185 days. The computation of the time depends very much on the assumed concrete strength. To illustrate this the computed time-displacement curve is also given in Fig. 17 for a concrete strength f_c 10% lower than

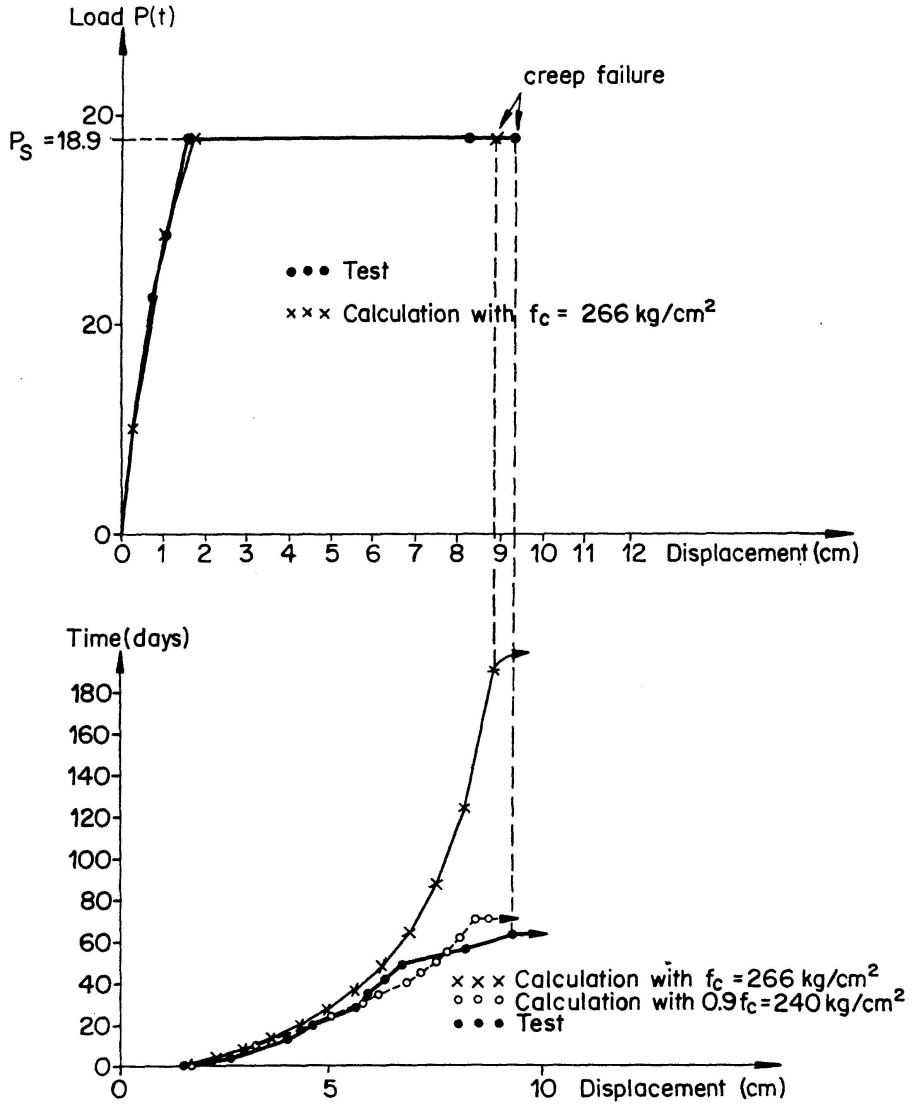

Fig. 17. Long time test up to creep failure (column 22).

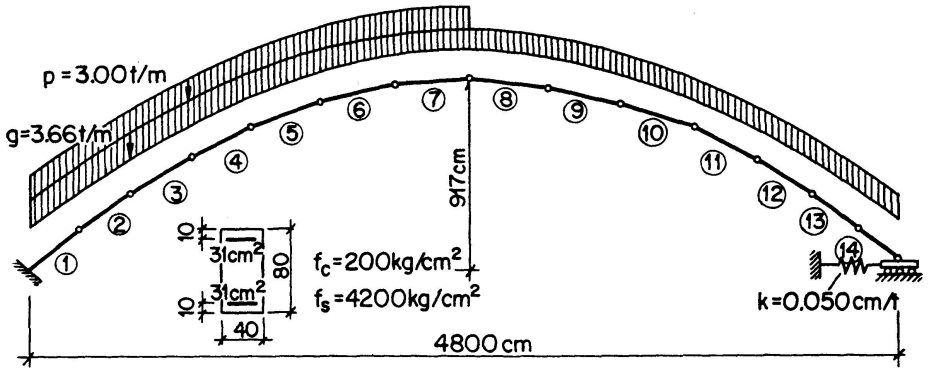

Fig. 18. System and loads.

the corresponding f_c of the test specimen. In this case the duration of time up to creep failure ($t = 68$ days) is reduced to one third.

b) Arch Under Snow Loads

The arch as shown in Fig. 18 is analysed. As an extreme loading a snow load of $\lambda \cdot 3.00$ t/m′ over half the span is assumed for the computation. The dead load $g = 3.66$ t/m′ is constant over the whole span. Fig. 19 shows the computed relation between the load factor λ and the maximum deflection at about one third of the span. The dotted line corresponds to a short time loading. In addition to that this relation is also given for a combined short-time and sustained loading. First, the load is increased up to $\lambda = 0.70$ and after a sustained load during 300 days the load is increased up to the maximum load capacity.

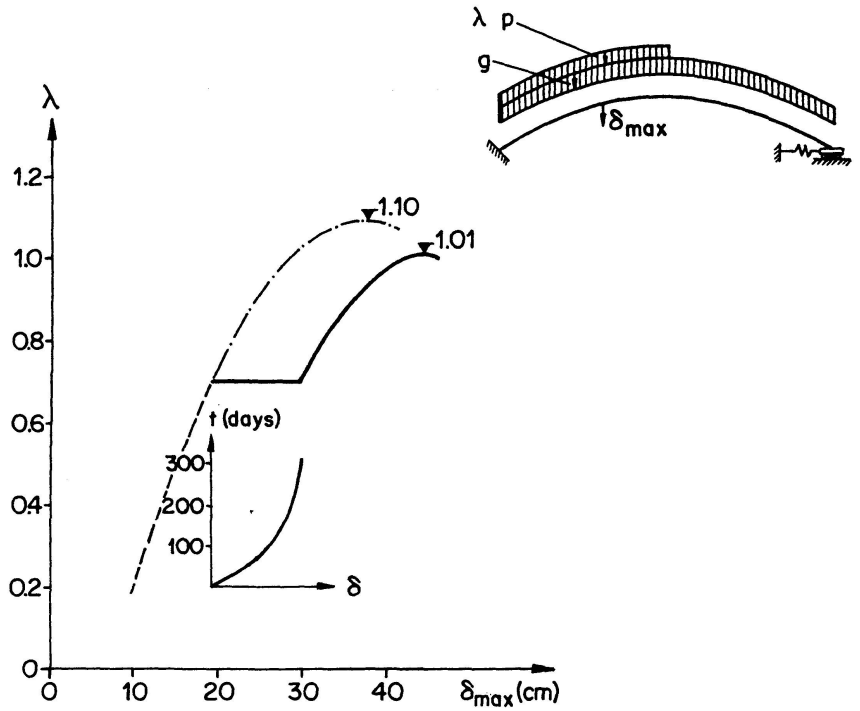

Fig. 19. Load-deflection behavior of an arch under short time and sustained loads.

Notation

M	moment
N	axial force
"i"	subscript "i" is used for reference to the cross sectional analysis
$\{P\}$	external loads
P_s	sustained load
λ	load factor for proportional loads

λ_s	load factor for sustained loads
$[K]$	stiffness matrix
$[K_1]$	first order stiffness matrix
$[K_2]$	non linear geometrical stiffness matrix
$[R]$	transformation matrix
$\{w\}$	nodal displacements
E	modulus of elasticity
A	area of cross section
l	length of element
EI	bending rigidity
EA	axial rigidity
σ	stress
f_s	yiel stress of steel
f_c	cylinder strength of concrete
ϵ	total strain
ϵ_c	"plastic" strain
ϵ_p	initial strain (e.g. due to prestressing)
ϵ_0	short-time strain
φ_∞	limiting creep factor
t	time
T	elapsed time until half of the limiting creep is reached

Acknowledgement

The study is based on results obtained in the course of a research project on the inelastic behavior of reinforced concrete columns under the direction of Prof. B. Thürlimann. The project was supported by the Swiss National Science Foundation (Schweizerischer National-Fonds).

References

1. Aas-Jakobsen, K. und Grenacher, M.: Berechnung unelastischer Rahmen nach der Theorie 2. Ordnung. Bericht Nr. 45, Institut für Baustatik, ETH Zürich.
2. von Karman, T. V.: Untersuchung über Knickfestigkeit. Mitteilung über Forschungsarbeiten auf dem Gebiet des Ingenieurwesens, No. 81, Berlin 1910.
3. Baumann, O.: Die Knickung der Eisenbeton-Säulen. Eidg. Materialprüfungsanstalt an der ETH in Zürich. Bericht Nr. 89, Zürich, Dezember 1934.
4. Broms, B.: Ultimate Strength of Long Reinforced Concrete Columns. Department of Theoretical and Applied Mechanics, University of Illinois, June 1956.
5. Pfrang, E. O. and Siess, C. P.: Analytical Study of the Behavior of Long Restrained Concrete Columns Subjected to Eccentric Loads. Civil Engineering Studies, Structural Research Series No. 215, University of Illinois, June 1961.
6. Breen, J. E.: The Restrained Long Concrete Column as a Part of a Rectangular Frame. Ph. D. Dissertation, University of Texas, Austin, Texas, 1962.

7. MANUEL, R. F. and MACGREGOR, J. G.: The Behavior of Restrained Reinforced Concrete Column under Sustained Load. Ph. D. Dissertation, Department of Civil Engineering, The University of Alberta, Canada, 1966.
8. BLAAWENDRAAD, J.: Realistic Analysis of Reinforced Framed Structures. Heron, Vol. 18, No. 4, 1972.
9. RAMU, P., GRENACHER, M., BAUMANN, M., THÜRLIMANN, B.: Versuche an gelenkig gelagerten Stahlbetonstützen unter Dauerlast. Bericht Nr. 6418-1, Institut für Baustatik, ETH Zürich, Mai 1969.

Summary

An approach to analyse reinforced concrete frames is outlined. The effects of second order and non linear material behavior are considered. The computational process described is based on the finite element method. The effective stiffnesses for each state of loading are determined by iteration. The influence of creep and shrinkage are taken into account. Two examples are given to demonstrate the possibilities of the proposed analysis.

Résumé

L'objet de ce rapport est la déscription d'une méthode de calcul selon le 2e ordre pour les structures composées de barres inélastiques. La méthode des éléments finis est à la base de ce calcul. Les rigidités flexionnelles sont calculées pour chaque état de charge par itérations. Les éffets du fluage et du retrait peuvent être considerés. On montre à l'aide de deux exemples les possibilités de cette méthode.

Zusammenfassung

Es wird eine Methode zur Berechnung von Rahmentragwerken aus Stahlbeton beschrieben. Dabei wird der Theorie 2. Ordnung, wie auch dem nicht linearen Materialverhalten, Rechnung getragen. Der beschriebene Rechnungsgang basiert auf der Methode der finiten Elemente. Die effektiven Biegesteifigkeiten für jeden Belastungszustand werden iterativ ermittelt. Langzeiteffekte, wie Kriechen und Schwinden, können berücksichtigt werden. Anhand von zwei Beispielen werden die Möglichkeiten des Rechenverfahrens gezeigt.

Leere Seite
Blank page
Page vide

The Fatigue Strength of Steel and Butt Welds in Definite Working Conditions

La limite de fatigue d'acier et de soudages bout à bout dans des conditions déterminées de service

Die Dauerfestigkeit von Stahl und Stumpfschweissungen unter festbegrenzten Betriebsbedingungen

WLADYSLAW BOGUCKI
Prof. Dr. inz.

ANDRZEJ NIEDZIELSKI
Doc. Dr. inz.

Technical University of Gdansk (Poland)

Introduction

In design of civil engineering structures such as bridges, crane beams etc., which are working under dynamic loading the fatigue strength is taken into account. The fatigue strength is usually taken from standard tests which are performed under conditions characterized by the testing equipment and not by the real dynamic loading of the structure.

To consider the real working conditions it was decided to take into account the cessations in the loadings. At the same time, by keeping up to fracture the investigated specimens in constant temperature, the influence of cooling is considered.

Description of Tests

The investigations were performed on specimens made of steel St 37 S with chemical composition: 0,11% C; 0,49% Mn; 0,04% Si; 0,032% P; 0,02% S, and average mechanical characteristics $R_e = 31{,}25\,\mathrm{kG/mm^2}$, $R_m = 52{,}95\,\mathrm{kG/mm^2}$, $a = 25{,}85\%$, $c = 38{,}63\%$. The shape and dimensions of the specimens were taken according to the instruction of Schenck-Pulsometer (Fig. 1).

In investigation specimens with 100 and 120 $\mathrm{mm^2}$ cross-sectional areas were used. The specimens were cut from plates of 10 mm thickness. The

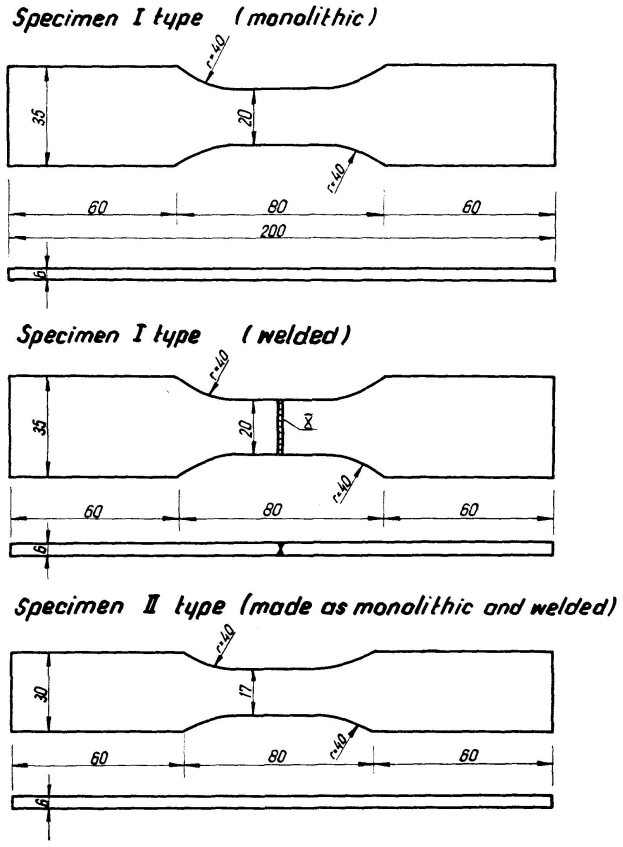

Fig. 1.

thickness of the part at which measurements were taken, was reduced to 6 mm within the accuracy of $\pm 0{,}05$ mm. The grinding was undertaken by a disk-type grinding wheel with intensive cooling by an adequate emulsion. Finally all the specimens were polished.

The butt welds were made by hand with the electrode EP 52-28. With the help of X-ray tests only specimens with defectless welds were chosen. In several cases the fatigue fractures showed minor defects (such as gas cavities, slag inclusions). The results from such tests were neglected in the analysis.

In spite of a very careful manufacturing the discrepancies from the theoretical values in the cross sectional areas were up to $\pm 1{,}5\%$, which was taken into account in the determination of the loading.

Three hundred fifty specimens were prepared (175 monolithic, 175 welded) and 336 were considered in the analysis.

The investigations under tensile pulsations with frequency 960 cycles/min were performed on a hydraulic testing machine manufactured by the Losenhausen Company. The investigations under tensile-compression pulsations with frequency 3000 cycles/min were performed on a resonance testing machine manufactured by Schenck of Darmstadt.

The temperature was measured with an accuracy of $\pm 1\%$ with the help of a special equipment made in the G.D.R.

In the investigations 5 minute cessations were applied at 15 minutes intervals. In the case of cooling the temperature was kept nearly at 18° C degrees.

The Results of Investigations

The results of investigations in the case of coefficient of uniformity of load $\kappa = 1{,}25 \left(\kappa = \frac{\sigma_m}{\sigma_a}\right)$ are given in Table I.

Table I

Types of specimens	Loading cessations	Z_{rj} kG/mm²	Standard deviation kG/mm²	R_r kG/mm²	Comparison of results*)
monolithic	without	33,50	±2,47877	52,95	100
welded	without	30,09	±1,60032	—	89,82
monolithic	with	34,31	±0,34275	52,95	102,44
welded	with	30,53	±1,67600	—	91,14

*) As 100% the strength Z_{rj} of monolithic specimens, equal to 33,50 kG/mm², is taken.

The table shows that the influence of cessations is advantageous, but very small. The increase in fatigue strength is 2,4% for monolithic and 1,5% for welded specimens. The influence of cooling was not considered because the increase of temperature was insignificant.

The results in the case of coefficients of uniformity of load $\kappa = 0$ are given in Table II.

Table II

Types of specimens	Loading cessations	Z_{rc} kG/mm²	Standard deviation kG/mm²	R_r kG/mm²	Comparison of results*)
monolithic	without	16,22	±0,63906	52,95	100
welded	without	15,06	±1,21669	—	92,88
monolithic	without and cooling	18,50	±0,69356	52,95	114,12
welded	without and cooling	17,42	±1,17644	—	107,46
monolithic	with	18,33	±1,01880	52,95	113,04
welded	with	16,97	±1,09279	—	104,66

*) As 100% the strength Z_{rc} of monolythic specimens, equal to 16,22 kG/mm², is taken.

In this case the introduction of cessations led to an increase of the fatigue strength equal to 13% for monolithic and 12,7% for welded specimens. The influence of cooling is of the same order and corresponds to 14,1% for monolithic and 15,7% for welded specimens.

The influence of the change of the velocity of loading (frequency) in the two cases was not considered.

In Fig. 2 and 3 the Wöhler diagrams are given the coefficients of uniformity of loading $\kappa = 1{,}25$ and $\kappa = 0$.

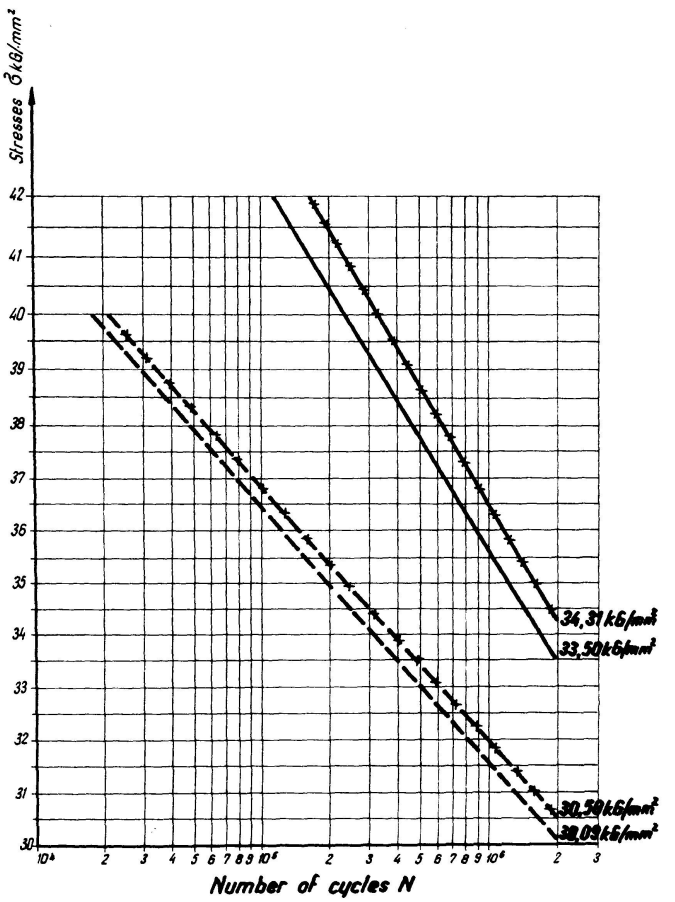

Fig. 2. Wöhler's diagrams for the coefficient $\kappa = 1{,}25$.

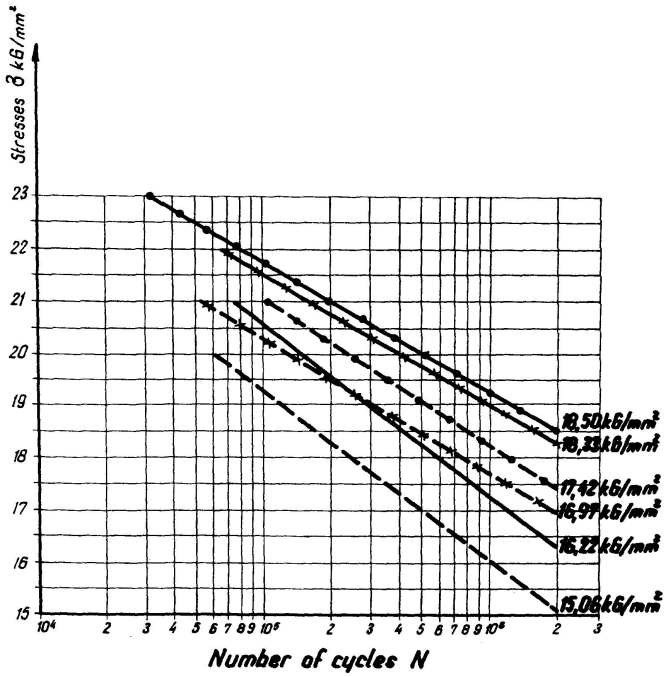

Fig. 3. Wöhler's diagrams for the coefficient $\kappa = 0$.

Conclusions

1. The results of standard fatigue tests do not correspond adequatly to the working conditions of civil engineering structures in view of the cessations in loading, and large surfaces which help to keep the structure at the ambient temperature.
2. The application of cessations in loadings increases the fatigue strength of steel and butt welds. For the same kind of steel the amount of increase depends upon the coefficient of uniformity of loading and the time of cessations.
3. The problem should be considered for other types of structural steels.
4. Based on further tests an adequate safety factor should be defined which takes into account the cessations in loading along with different factors such as shape, quality of manufacturing and material.

Summary

The paper presents the experimental results of the strength of butt welds subjected to cyclic loads corresponding to the working conditions of bridge structures.

The problem was discussed on the basis of research performed at the Chair of Steel Structures at the Technical University of Gdansk on specimens made of steel St 37 S.

Résumé

Ce travail traite les résultats expérimentaux de la résistance de soudages par rapprochement soumis à des charges cycliques correspondant aux conditions de service des constructions de ponts.

Le problème a été discuté sur la base de recherches entreprises à la chaire des constructions en acier de l'Université technique de Gdansk sur des spécimens en acier St 37 S.

Zusammenfassung

Die Arbeit vermittelt die experimentellen Ergebnisse der Festigkeit von Stumpfschweissungen gegenüber zyklischer Belastung entsprechend den Betriebsbedingungen von Brückenbauten.

Das Problem wurde auf der Basis von Untersuchungen beim Lehrstuhl für Stahlbau an der Technischen Universität Gdansk an Stahlproben St 37 S diskutiert.

Leere Seite
Blank page
Page vide

On Finite Strip Analysis of Continuous Plates

Analyse par bandes finies de plaques continues

Über die Finite-Streifen-Berechnung von Platten

A. GHALI
M. ASCE, Professor of Civil Engineering,

G. S. TADROS
Post-doctoral Fellow,

The University of Calgary, Calgary, Alberta, Canada

Introduction

Semi-analytical finite element procedures have been used to reduce drastically the number of equations and solution cost for two-dimensional and three-dimensional situations. In the application of these procedures to plates in bending, long elements or strips are used (Fig. 1a and b) and the transverse deflection of a strip is expressed in the form

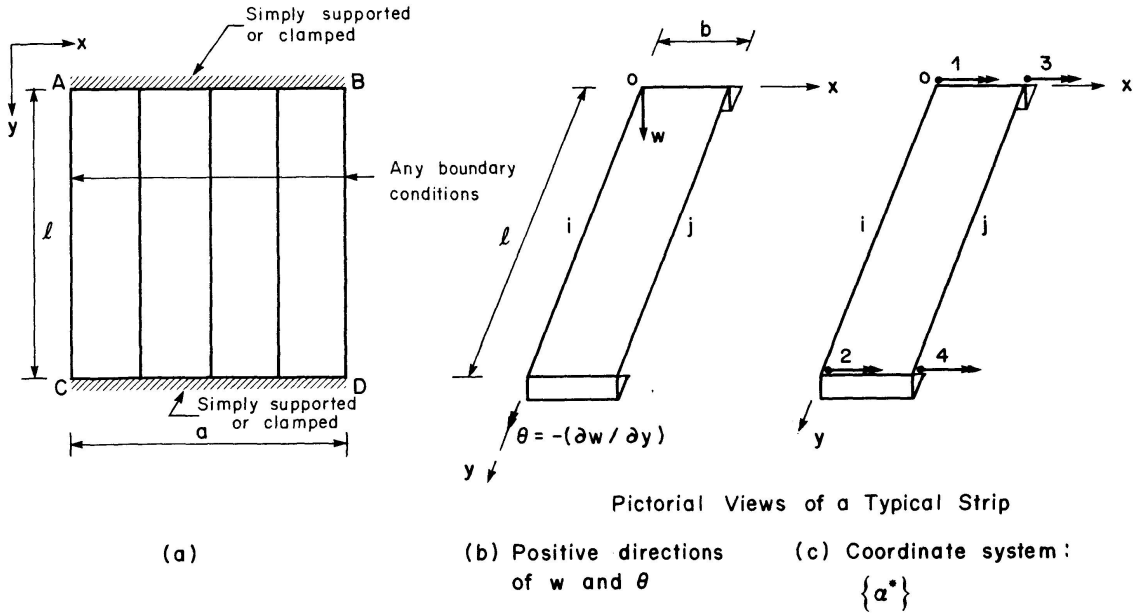

Fig. 1. Finite Strip Idealization.

$$w^* = \sum_{m=1}^{r} w_m^* = \sum_{m=1}^{r} f(x)\, Y_m, \tag{1}$$

where $f(x)$ is a polynomial of x only and Y_m are basic functions satisfying the end conditions in the y direction. When a third degree polynomial is used for $f(x)$, the unknown displacement parameters are two for each nodal line and for each term of the series: w_{im} and θ_{im}, where $\theta = -(\partial w/\partial x)$. This is the finite strip method, first developed by CHEUNG, for the analysis of simply-supported slabs [1] and later by CHEUNG and others for other structures idealized into strips subjected to in-plane as well as to bending forces. For the simply-supported slab, the basic function is a trigonometric series:

$$Y_m = \sin\frac{m\pi y}{l}. \tag{2}$$

Applied loads must also be resolved into series similar to the displacement function, and a load vector $\{F^*\}$ is then related to the nodal parameters. For the strip in Fig. 1 b, this relation takes the form:

$$[S^*]\{D^*\} = \{F^*\}, \tag{3}$$

where $[S^*]$ is a square matrix of order $4r$ representing the stiffness of the strip, and the displacement vector

$$\{D^*\} = \{\{D^*\}_1, \{D^*\}_2, \ldots, \{D^*\}_r\}, \tag{4}$$

where

$$\{D^*\}_m = \{w_i, \theta_i, w_j, \theta_j\}_m. \tag{5}$$

The stiffness matrix of the strip can be partitioned into $r \times r$ submatrices $[S^*]_{mn}$ corresponding to each term of the series. Due to the orthogonality of the chosen function Y_m and its derivatives, it can be shown that the submatrix $[S^*]_{mn} = [0]$ when $m \neq n$. Thus, Eq. (3) will actually uncouple, and for each term of the series we can write for one strip

$$[S^*]_{mm}\{D^*\}_m = \{F^*\}_m. \tag{6}$$

For each term of the series, a stiffness matrix of the plate $[S]_m$ of order $s \times s$ (where s is twice the number of nodal lines) is assembled from the stiffness matrices $[S^*]_{mm}$ of the individual strips. Adding the forces on each nodal line from the two adjacent strips, we obtain a load vector $\{F\}_m$. Solution of the equation

$$[S]_m\{D\}_m = \{F\}_m \tag{7}$$

gives the s displacement parameters for the mth term of the series. Thus, the uncoupling makes it necessary to solve r sets of s equations instead of one set of $r \times s$ equations. The half-band width of the matrix is reduced by a factor r; thus, the reduction in computer time due to uncoupling can be quite considerable.

CHEUNG [2] used the finite strip method with the basic function Y, other than trigonometric, to analyze plates with two other end conditions: simply-supported-clamped and clamped-clamped. Unfortunately, with these functions the uncoupling described above can not occur.

The object of the present paper is to use the trigonometric basic function of Eq. (2) for all the three boundary conditions described above. The effect of the fixing moment at the clamped edge is accounted for by superposition. Thus, in all cases benefit is obtained from the uncoupling of the equations.

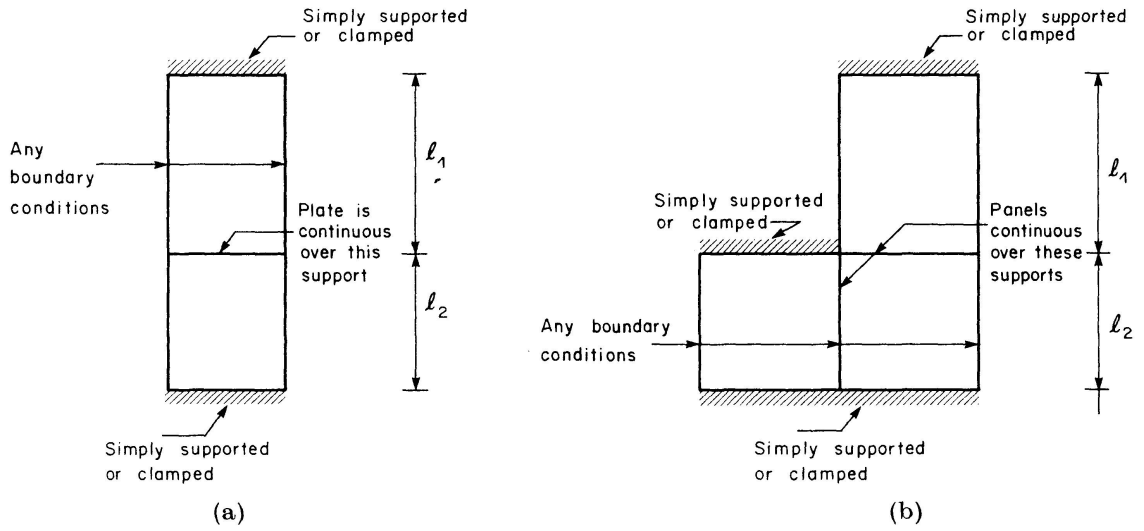

Fig. 2. Continuous plates in Bending.

Any of the plates of Fig. 2 continuous over a number of panels can be analyzed by the proposed method. Each panel is first analyzed with its two edges parallel to the x axis simply supported, then the compatibility of rotation at these edges is satisfied by the application of couples and the final result is obtained by superposition.

CHEUNG et al. [3] analyzed continuous bridges similar to the plate in Fig. 2a by solving a simply supported plate of span equals (l_1+l_2), and superposing the effect of concentrated transverse forces to bring the deflections at the intermediate support back to zero (force method of analysis). This approach may result in ill-conditioned equations when the plate is continuous over a number of spans and a large number of strips is used.

Procedure

The finite strip method for analysis of plates in bending is given in the references mentioned above and in more detail with simplified example in Ref. [4]. For this reason, the derivation of some of the equations which is available in these references is deleted from the following presentation.

The deflection of a strip (Eq. (1)) can be expressed in terms of the nodal parameters for its sides i and j. A general term of the series is

$$w_m^* = [L^*]_m \{D^*\}_m, \tag{8}$$

where

$$[L^*]_m = \left[\left(1 - \frac{3x^2}{b^2} + \frac{2x^3}{b^3}\right) \middle| \left(-x + \frac{2x^2}{b} - \frac{x^3}{b}\right) \middle| \left(\frac{3x^2}{b^2} - \frac{2x^3}{b^3}\right) \middle| \left(\frac{x^2}{b} - \frac{x^3}{b^2}\right)\right] Y_m. \tag{9}$$

Define a system of four coordinates for each strip: The rotation $(\partial w/\partial y)$ at the ends $y=0$ and $y=l$ of its nodal lines (Fig. 1 c).

$$\{\alpha^*\}_m = \left\{\left(\frac{\partial w_m^*}{\partial y}\right)_{x=0,y=0}, \left(\frac{\partial w_m^*}{\partial y}\right)_{x=0,y=l}, \left(\frac{\partial w_m^*}{\partial y}\right)_{x=b,y=0}, \left(\frac{\partial w_m^*}{\partial y}\right)_{x=b,y=l}\right\}. \tag{10}$$

Substitution of Eq. (8) into Eq. (10) gives

$$\{\alpha^*\}_m = [C^*]_m \{D^*\}_m, \tag{11}$$

where $[C^*]_m$ is the strip displacement transformation matrix for the mth term

$$[C^*]_m = \begin{bmatrix} [H]_m & [0] \\ [0] & [H]_m \end{bmatrix} \tag{12}$$

and

$$[H]_m = \frac{m\pi}{l} \begin{bmatrix} 1 & 0 \\ \cos m\pi & 0 \end{bmatrix}. \tag{13}$$

The edge bending moment normal to the short sides of the strip is assumed to vary linearly between nodal lines. Define a vector $\{Q^*\}$ of the four values of the moment (per unit length) at the ends of the nodal lines. The edge bending moments can be expressed in a form of trigonometric series of a transverse load of intensity

$$q = \sum q_m Y_m, \tag{14}$$

where

$$q_m = \frac{2m\pi}{l^2} \left[\frac{b-x}{b} \middle| \frac{b-x}{b} \cos m\pi \middle| \frac{x}{b} \middle| \frac{x}{b} \cos m\pi\right] \{Q^*\}. \tag{15}$$

The load vector (see Eq. (20.108) of Ref. [4]).

$$\{F^*\}_m = \int_0^l \int_0^b [L]_m^T q_m Y_m \, dx \, dy = [G^*]_m \{Q^*\}. \tag{16}$$

Substitution of Eqs. (9) and (15) in Eq. (16) gives the force transformation matrix

$$[G^*]_m = \frac{m\pi}{l} \left[\begin{array}{c|c|c|c} \frac{7b}{20} & \frac{7b}{20}\cos m\pi & \frac{3b}{20} & \frac{3b}{20}\cos m\pi \\ -\frac{b^2}{20} & -\frac{b^2}{20}\cos m\pi & -\frac{b^2}{30} & -\frac{b^2}{30}\cos m\pi \\ \frac{3b}{20} & \frac{3b}{20}\cos m\pi & \frac{7b}{20} & \frac{7b}{20}\cos m\pi \\ \frac{b^2}{30} & \frac{b^2}{30}\cos m\pi & \frac{b^2}{20} & \frac{b^2}{20}\cos m\pi \end{array}\right]. \tag{17}$$

For the assembled structure two vectors are derived: $\{\alpha\}_m$ and $\{Q\}$, each of order s. An element of $\{Q\}$ corresponding to one end of a nodal line is obtained by adding Q^* for the strips at its left and its right. In a similar way a transformation matrix $[G]_m$ of the structure (of order $s \times s$) can be assembled from the transformation matrices $[G^*]_m$ of the individual strips. Thus, for the assembled structure Eq. (16) becomes

$$\{F\}_m = [G]_m\{Q\}. \tag{18}$$

The rotation vector of the assembled structure is related to the nodal displacement parameter by the equation

$$\{\alpha\}_m = [C]_m\{D\}_m, \tag{19}$$

where

$$[C]_m = \begin{bmatrix} [H]_m & & \\ & [H]_m & \\ \text{submatrices} & \cdots & \\ \text{not shown are null} & & [H]_m \end{bmatrix}. \tag{20}$$

Combining Eq. (7) with Eqs. (19) and (18)

$$\{\alpha\}_m = [C]_m[S]_m^{-1}\{F\}_m \tag{21}$$

and

$$\{\alpha\}_m = [f]_m\{Q\}, \tag{22}$$

where

$$[f]_m = [C]_m[S]_m^{-1}[G]_m. \tag{23}$$

$[f]_m$ represents the contribution of the mth term to the "flexibility matrix relating $\{\alpha\}_m$ and $\{Q\}$. The "flexibility" matrix relating $\{\alpha\}$ and $\{Q\}$ is

$$[f] = \sum_{m=1}^{r} [C]_m[S]_m^{-1}[G]_m. \tag{24}$$

For an example of application of the above equations consider a one panel plate with the edges parallel to the x axis clamped. The bending moment normal to the clamped edges is of intensities $\{Q\}$ at the nodal lines ends. For compatibility the rotations due to $\{Q\}$ on a simply-supported slab $(=[f]\{Q\})$ must be equal and opposite to the rotations $\{\alpha\} = \sum\{\alpha\}_m$ due to actual loading; thus, combining this condition with Eq. (21) gives

$$\{Q\} = -[f]^{-1}\sum_{m=1}^{r}\{\alpha\}_m = -[f]^{-1}\sum_{m=1}^{r}[C]_m[S]_m^{-1}\{F\}_m. \tag{25}$$

It is to be noted that the above equation satisfies the compatibility condition $(\partial w/\partial y) = 0$ only at the ends of the nodal lines. The error resulting from this approximation is negligible and decreases as the width of the strips is decreased. (When $b \to 0$, the compatibility condition is satisfied at all points.)

The clamped plate can now be analyzed as a simply-supported one, subjected to the combined load $\{F\}_m$ and $\{Q\}$. The contribution of the mth term to the displacement parameters (see Eqs. (7) and (18)) for the clamped plate

$$\{\bar{D}\}_m = [S]_m^{-1}\{F\}_m + \sum_{n=1}^{p} [S]_n^{-1}[G]_n\{Q\}. \tag{26}$$

Choosing $p=r$, Eq. (26) becomes

$$\{\bar{D}\}_m = [S]_m^{-1}\{\bar{F}\}_m, \tag{27}$$

where

$$\{\bar{F}\}_m = \{F\}_m + [G]_m\{Q\}. \tag{28}$$

Thus, the analysis of a clamped plate is reduced to that of a simply-supported plate with the load vector $\{F\}_m$ replaced by $\{\bar{F}\}_m$.

Examples

To check the method of analysis for the effect of edge moments derived above, consider isotropic plates simply supported on four sides and subjected to uniform moment M_0 per unit length normal to the two sides AB and CD (see Fig. 1a and Table 1). Due to symmetry, half the plate is analyzed with $a/2$ divided into five strips. Table 2 gives the results of plates as in the first example but subjected to uniform load and the edges AB and CD clamped instead of simply supported. Poisson's ratio in both examples equals 0.3.

A study of convergence is made in Table 3 for one of the plats in Table 2 with $l/a=1.0$. Odd terms only contribute to the results. A somewhat large number of terms is required if high accuracy is desired. However, for the values considered the contribution of any two consecutive odd terms are of opposite signs, and the average of the answers with two consecutive odd terms is close to the exact solution. The results in Tables 1 and 2 are averages of solutions using 7 and 9 terms. For further study of convergence, see Ref. 6.

Table 1. Analysis of Plates Simply Supported on Four Sides and Subjected to Moments M_0 on Edges AB and CD (Fig. 1a)

l/a	Central Deflection	Central M_x	Central M_y	Source
2.0	1.746	0.156	−0.005	F. S.
	1.740	0.153	−0.010	Exact [5]
1.5	2.800	0.267	0.052	F. S.
	2.800	0.264	0.046	Exact
1.0	3.685	0.397	0.262	F. S.
	3.680	0.394	0.256	Exact
0.75	6.199	0.425	0.482	F. S.
	6.200	0.424	0.476	Exact
0.50	9.647	0.385	0.775	F. S.
	9.640	0.387	0.770	Exact
Multiplier	$M_0\,\xi^2/(100N)$ *)	M_0	M_0	

*) ξ is the smallest value of l and a.

Table 2. Analysis of Plates Clamped on Sides AB and CD, Simply Supported on the Two Other Sides Subjected to Uniform Load of Intensity q (Fig. 1a)

l/a	Central Deflection	Central M_x	Central M_y	M_y at Middle of AB	Source
0.5	0.00253	0.0135	0.0410	−0.0852	F. S.
	0.00260	0.0142	0.0420	−0.0842	Exact [5]
1.0	0.00186	0.0239	0.0325	−0.0718	F. S.
	0.00192	0.0244	0.0332	−0.0697	Exact
2.0	0.00834	0.0862	0.0475	−0.1269	F. S.
	0.00844	0.0869	0.0474	−0.1191	Exact
3.0	0.001162	0.1144	0.0421	−0.1370	F. S.
	0.001168	0.1144	0.0419	−0.1246	Exact
Multiplier	$q\,\xi^4/N$ *)	$q\,\xi^2$	$q\,\xi^2$	$q\,\xi^2$	

*) ξ is the smallest value of l and a.

Table 3. Study of Convergence. Uniformly Loaded Square Plate Clamped on Sides AB and CD, Simply Supported on the Two Other Sides (Fig. 1a)

Number of Terms in Series	Central Deflection		Central M_x		Average of Two Consecutive Solutions	
	Sum of Terms	Contribution of Last Term	Sum of Terms	Contribution of Last Term	Central Deflection	Central M_x
1	16.713	16.713	1.837	1.837		
					17.898	2.264
3	19.083	3.770	2.691	0.854		
					18.756	2.423
5	18.428	−0.655	2.155	−0.536		
					18.554	2.348
7	18.681	0.253	2.541	0.386		
					18.620	2.391
9	18.559	−0.122	2.240	−0.301		
					18.593	2.364
11	18.627	0.068	2.487	0.247		
					18.606	2.382
13	18.585	−0.042	2.277	−0.210		
					18.599	2.368
15	18.612	0.027	2.459	0.182		
					18.603	2.379
17	18.594	−0.018	2.299	−0.160		
					18.600	2.371
19	18.607	0.013	2.442	0.143		
					18.602	2.377
21	18.597	−0.010	2.312	−0.130		
..	...	...	...	...	...	...
					...	...
39	18.602	0.001	2.408	0.070		
					18.602	2.375
41	18.601	−0.001	2.342	−0.066		
Multiplier	$10^{-4}\,q\,l^4/N$		$10^{-2}\,q\,l^2$		$10^{-4}\,q\,l^4/N$	$10^{-2}\,q\,l^2$

Conclusion

The solution of plates simply supported on two opposite sides when analyzed by the finite strip requires solution of a small number of equations because of the orthogonal properties of the trigonometric basic functions used. If other functions are used to satisfy boundary conditions other than simply supported, the orthogonality does not occur and both the number of simultaneous equations to be solved and their half-band width are much increased. The method presented allows the use of trigonometric functions for all cases of clamped or continuous plates. The analysis is done for simply-supported panels and the compatibility of rotation at the clamped or continuous edges is achieved by the application of unknown "connecting" moments determined by the force method. The accuracy of the proposed method is demonstrated by examples.

Notation

$[C]$ = transformation matrix.
$\{D\}$ = displacement parameters.
$\{F\}$ = load vector.
$[f]$ = flexibility matrix.
$\{Q\}$ = intensity of end moment normal to the short sides of the strip. The positive directions of the end moments are the same as the directions of $\{\alpha\}$.
$[S]$ = stiffness matrix.
$\{\alpha\}$ = nodal line end rotation.
a = width of the plate.
b = width of the strip.
l = length of the strip.
N = flexural rigidity.
r = number of terms.
s = twice the number of the nodal lines.
Y_m = basic function.
w = transverse deflection.

Note: A star used as superscript refers to the strip while the absence of a star means that the symbol refers to the assemblage of strips.

Acknowledgement

This research was supported by a grant from the National Research Council of Canada, which is gratefully acknowledged.

References

1. Cheung, Y. K.: The Finite Strip Method in the Anlysis of Elastic Plates with Two Opposite Simply Supported Ends. Proc. Inst. Civ. Eng., 40, 1968, p. 1–7.
2. Cheung, Y. K.: Finite Strip Method of Analysis of Elastic Slabs. Proc. ASCE, 94, EM 6, 1968, p. 1365–1378.
3. Cheung, M. S., Cheung, Y. K. and Ghali, A.: Analysis of Slab and Girder Bridges by the Finite-Strip Method. Building Science, Vol. 5, Pergamon Press, 1970, p. 95–104.
4. Ghali, A. and Neville, A. M.: Structural Analysis: A Unified Classical and Matrix Approach. Intext E. Publishers, Scranton, Penn., 1972. (See p. 560–577, written in collaboration with the authors by Y. K. Cheung.)
5. Timoshenko, S. and Wojnowsky-Krieger, S.: Theory of Plates and Shells, 2nd. ed., McGraw Hill, New York, 1959, p. 180–188.
6. Tadros, G. S. and Ghali, A.: Convergence of Semianalytical Solution of Plates, Proc. ASCE, 99, EM 5, 1973, p. 1023–1035.

Summary

The finite strip solution for rectangular plates in bending is a semi-analytic procedure which reduces drastically the number of equations involved compared with the finite element method. This is particularly true in the case of a plate having two of its opposite edges simply supported, and the deflection variation perpendicular to these edges is expressed as a sum of basic trigonometric series. With other edge conditions, other basic functions must be used, which lack the orthogonality of the trigonometric functions and result in a large increase in the number of simultaneous equations and their half-band width. An alternative finite strip procedure is presented, in which using superposition, the trigonometric basic functions can be maintained for all edge conditions including clamped or continuous.

Résumé

La résolution par la méthode des bandes finies du problème des plaques rectangulaires soumises à la flexion est un procédé semi-analytique qui réduit considérablement le nombre des équations nécessaires comparé à la méthode des éléments finis. Ceci est particulièrement valable dans le cas de plaques dont deux côtés opposés sont simplement appuyés, et dont la variation de la flèche perpendiculairement à ces côtés est exprimée sous forme de somme de séries trigonométriques. Pour d'autres conditions aux limites, on devra utiliser d'autres fonctions de base, qui nuisent à l'orthogonalité des fonctions trigonométriques et impliquent une augmentation du nombre d'équations simultanées et de la largeur de leurs demi-bandes. On présente une méthode basée sur les

bandes finies alternatives pour lesquelles, par superposition, on peut conserver les fonctions trigonométriques de base pour toutes les conditions aux limites, y compris les encastrements ou les appuis continus.

Zusammenfassung

Die Finite-Streifen-Lösung für rechteckige Platten unter Biegung ist eine halbanalytische Methode, die die Anzahl Gleichungen, verglichen mit der Methode der finiten Elemente, wesentlich reduziert. Dies trifft besonders für den Fall einer Platte mit zwei entgegengesetzten frei aufliegenden Rändern zu, wo die Variation der Durchbiegung senkrecht zu diesen Rändern durch eine Summe fundamentaler trigonometrischer Reihen dargestellt werden kann. Andere Randbedingungen erfordern andere Grundfunktionen, die die Orthogonalität der trigonometrischen Funktionen nicht besitzen, und aus denen eine grosse Zunahme der Anzahl simultaner Gleichungen und deren Bandbreiten resultiert.

Alternativ wird eine andere mögliche Finite-Streifen-Methode beschrieben, bei der, durch Gebrauch von Superposition, die fundamentalen trigonometrischen Funktionen für alle Randbedingungen einschliesslich Einspannung und Auskragung beibehalten werden können.

Steel Structures Under Cyclic Unequal Deflections

Structures en acier soumises à des déflexions cycliques inégales

Stahlkonstruktionen unter zyklischer nicht konstanter Deformation

M. M. GHAMIAN
Research Student, Department of Civil Engineering, University of Waterloo, Waterloo, Ontario, Canada

S. KRISHNASAMY
Research Engineer, Ontario Hydro Research Division, Toronto, Ontario, Canada (associated with the University of Waterloo during this investigation)

A. N. SHERBOURNE
Professor of Civil Engineering and Dean of Faculty of Engineering, University of Waterloo, Waterloo, Ontario, Canada

Abstract

The behaviour of cantilever beams under the constraint of symmetrical and unsymmetrical cyclic deflections is investigated theoretically as well as experimentally. An analytical technique is developed to predict the behaviour of cantilever beams from cyclic moment-curvature relations derived from cyclic strain control tests. Twenty tests were conducted on rectangular structural steel sections under pure bending to establish these relations which couple the moment range and mean moment to curvature range. A linear nonlinear model is proposed which fits the moment range data; a tripartite model is suggested to fit the mean moment data. The models are capable of accommodating, in discrete form, the phenomena of hardening and softening of aggregation of fibers constituting a structural section as well as relaxation of the mean moment.

Nine tests were conducted on cantilever beams under completely and partially reversed tip deflections. The load range changed little with changes in mean deflection. The mean load, in general, relaxed with increasing cycling. The theory presented modelled the experimental behaviour fairly accurately. It also suggested that the behaviour may be comprised of

1. an elastic case, where mean load is proportional to load range,
2. an intermediate range where the effects of mean deflection cannot be ignored, and

3. the case of large inelastic cyclic deformation where the effects of mean deflection can be completely ignored except for associated changes in structural geometry and its secondary membrane effects.

Introduction

Cyclic loads have long been recognized as a cause of failure in structural elements such as aircraft components, pressure vessels, turbines, etc. These loads usually produce nominal (global) elastic stresses and highly localized plastic flow leading to conventional fatigue failure. Despite the fact that this topic has been the subject of extensive study, the phenomenon of fatigue is not yet fully understood from the engineering point of view. Low-cycle fatigue, on the other hand, deals with failure of components where the stress is in excess of the yield stress and the number of cycles necessary to promote failure ranges from one quarter of a cycle (monotonic failure) to 10^5. Failure at 10^6 cycles or more is considered to be the domain of conventional or high-cycle fatigue.

Most of the early work involving repeated loads on structures above the elastic limit concerned the shakedown problem. NEAL [1] proved that a structure can accumulate increasing deflections under a particular load cycle such that the structure becomes unserviceable. This kind of failure was designated "incremental collapse". Various experiments [2, 3] were conducted to establish the shakedown load leading to the proposition that theoretical predictions of shakedown loads are, in general, conservative. The main reason for such divergence between theory and experiment is that section behaviour is assumed to be invariant (elastic-plastic or static strain-hardening) regardless of cyclic history.

An altogether different approach to the same problem includes provision for the change in material response to cyclic loads and consideration of the highly non-linear nature of the problem.

The nature of the cyclic loading on structures is random, and consequently it is very difficult to study such a complex problem directly. The loading conditions can be divided simplistically into load and deformation control. At the structural, sectional and fiber level this corresponds respectively to load, moment and stress on the one hand, and deflection, curvature and elongation on the other.

ROYLES [4] suggested a moment-curvature relation derived from stable sectional behaviour under deformation control conditions. He predicted the behaviour of single and three-span continuous beams under completely reversed deflections, each subjected to a single concentrated load at the central section. Experiments were conducted on similar structures and the results were compared with theoretical predictions.

SHERBOURNE and KRISHNASAMY [5] suggested two models for the cyclic moment-curvature relation under deformation control: one model takes into account initial linear elastic behaviour and the other ignores it. They predicted the cyclic response of a cantilever beam under a single concentrated load at its tip. The tip deflection was cycled between two fixed symmetric values. Tests were carried out on the same beam configuration and experimental results were found to be in reasonable agreement with theoretical predictions.

A major shortcoming of the method after Royles was its inability to predict the behaviour of the structure at each cycle of loading. The theory developed by Sherbourne and Krishnasamy, however, can predict the response of a structure at every stage of loading.

TOPPER [6] suggested a derivation of the cyclic moment-curvature relation (for deformation control problem) from cyclic stress-strain data and section geometry. This idea was developed by other researchers (ROYLES [4], SHERBOURNE and KRISHNASAMY [5]) and proved acceptable.

A moment-curvature model under load control was suggested by KRISHNASAMY et al. [7]. It incorporates cyclic strain accumulation effects (creep) by introducing a cyclic (or time) dependent function into the moment-curvature relation. Using this expression one can predict the behaviour of a cantilever beam under completely reversed load applied at its tip. Experiments were performed on similar structures to verify theoretical predictions.

In the load and deformation control problems discussed above, only fully reversed (or alternating) conditions were considered. But it is seldom that a structural element will be subjected to alternating loading only and, here, it is necessary to investigate situations where mean loading is present.

The present work concerns mild steel beams under deflection control where the limits of cyclic deflection need not be symmetrical about the initial rest position. Obviously, unsymmetrical deflection limits will, in general, give rise to mean load, present at all times in the system; the relaxation of this mean load is also investigated. The theory postulated herein proposes that cyclic structural behaviour can be predicted from sectional behaviour where the latter is a function of cyclic material properties and sectional geometry. Hence, relevant moment-curvature models can also be developed under these ambient conditions.

Experimental

The experimental program is divided into two parts. The first consists of experiments on pure bending specimens to establish cyclic moment-curvature relations. The second part is concerned with the testing of a set of cantilever beams subjected to cyclic unsymmetric deflections. Both the pure bending and the cantilever beam specimens were made from the same material, received the same heat treatment and were tested under similar ambient conditions.

The specimens were machined from $^3/_8 \times 1^1/_2''$ hot-rolled, semi-killed, 1020 mild steel bars, the chemical composition of which is shown below.

Si	S	P	Mn	C	Ni	Cr	Mo	V	Cu	Fe
0.210	0.025	0.010	0.710	0.203	0.063	0.050	0.010	0.003	0.16	remainder

Fig. 1 shows a monotonic stress-strain curve obtained from a typical axially loaded coupon. The experiment was conducted in an Instron Universal Testing Machine and strains were measured by a clip-on extensometer mounted on the test section of the specimen.

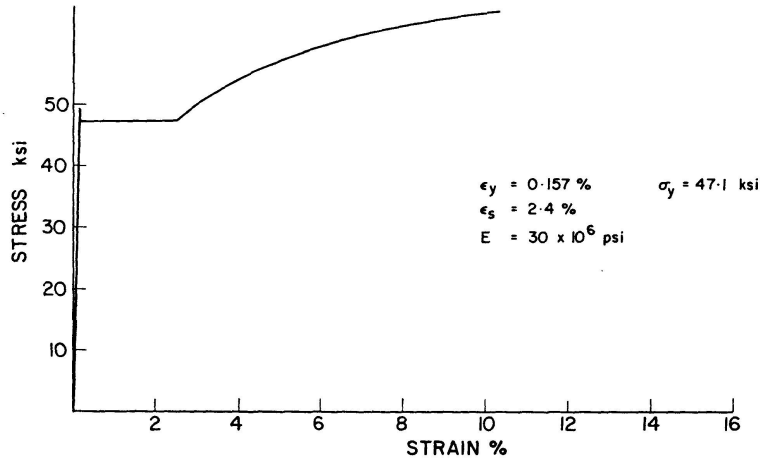

Fig. 1. Stress-Strain Curve.

All specimens were rough machined and then stress-relieved by retreating at 1600° F for a half hour and air cooling to room temperature. The final finish was carried out with care to minimize any residual stresses that might be induced.

The frequency of cycling for both kinds of tests (pure bending and cantilever) ranged between 6 and 15 cpm. Sufficient evidence is available to show that material response in this range can be considered as practically independent of frequency [8]. Moreover, the experiments were conducted under deformation control. KESHAVAN [8] showed that frequency plays a more significant role in load control than in deformation control. The wave shape used was sinusoidal throughout the experiments; the effects of wave shape are discussed elsewhere [8].

The test frame used employed a closed-loop servo-hydraulic (self-correcting) system, Fig. 2. A hydraulic actuator applied the load to the specimen and a load cell measured the load or reaction, depending upon the set-up of the testing fixture. The actuator ram displacement is measured electrically by means of a Linear Variable Differential Transformer (LVDT). Either the load or the ram displacement signal can be used as a control mechanism; thus one can obtain load or stroke control.

The pure bending device shown in Fig. 3 and used by previous researchers [9] is used in the present study. It makes use of the principle of four-point

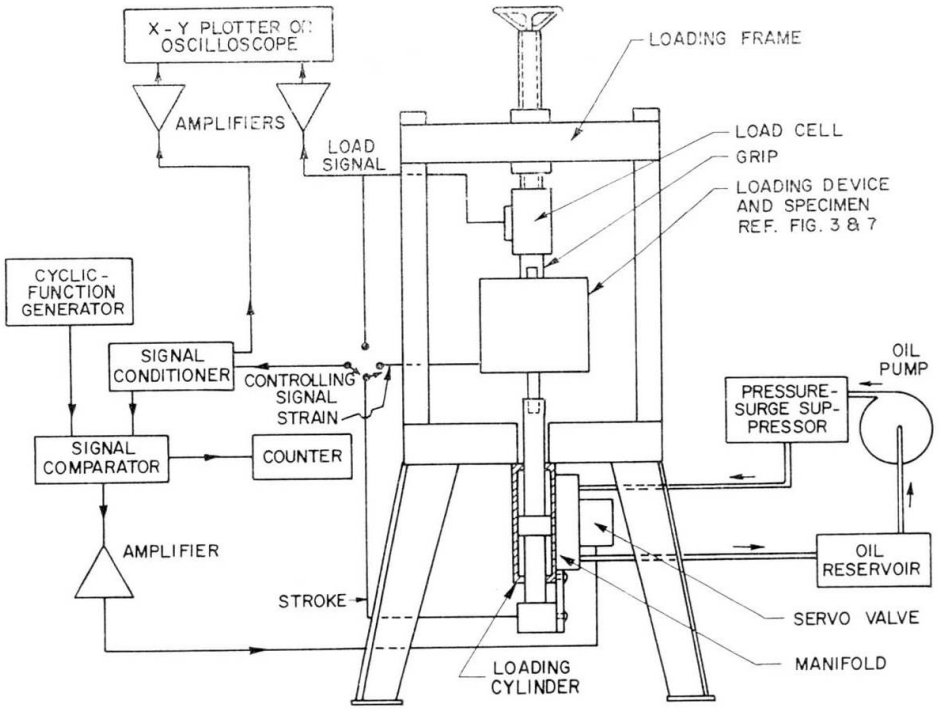

Fig. 2. Testing System.

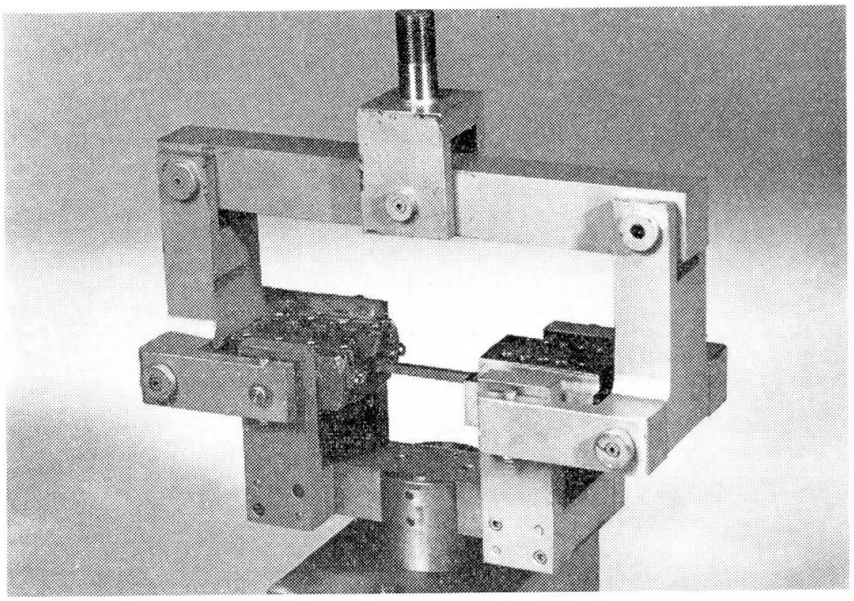

Fig. 3. Pure Bending Device.

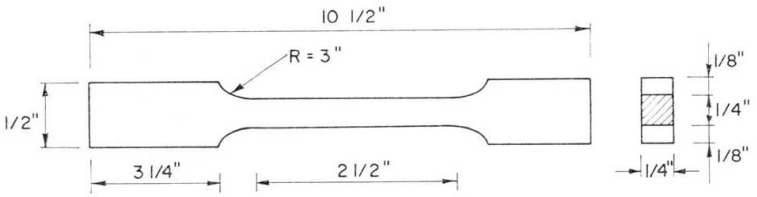

Fig. 4. Pure Bending Specimen.

loading which produces a region of uniform moment in which the bending specimen of Fig. 4 is placed. The device basically "converts the axial movement of the (test frame) ram into two equal and opposite rotations" at the ends of the bending specimen [9]. From the dimensions of the device, the uniform bending moment can be related to the load as measured by the load cell. The relation between ram displacement (stroke) and test section curvature was established experimentally as indicated in Fig. 5. The advantages of using stroke control (the case in the present work) over curvature control (measuring the extreme fiber strain by an extensometer) are indicated elsewhere [10].

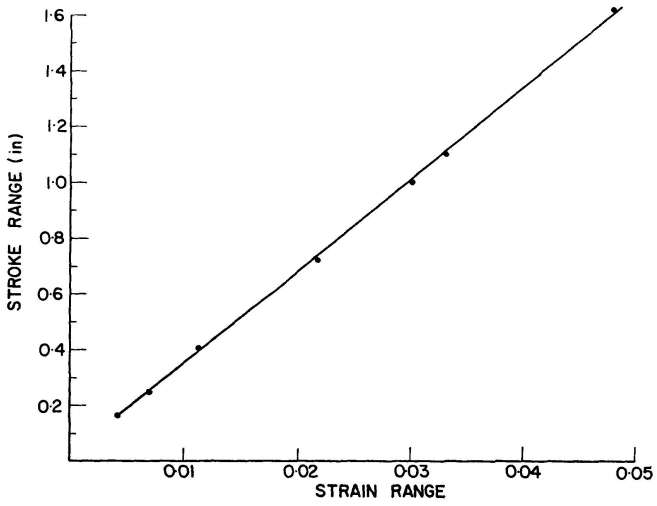

Fig. 5. Stroke Versus Strain Calibration Chart.

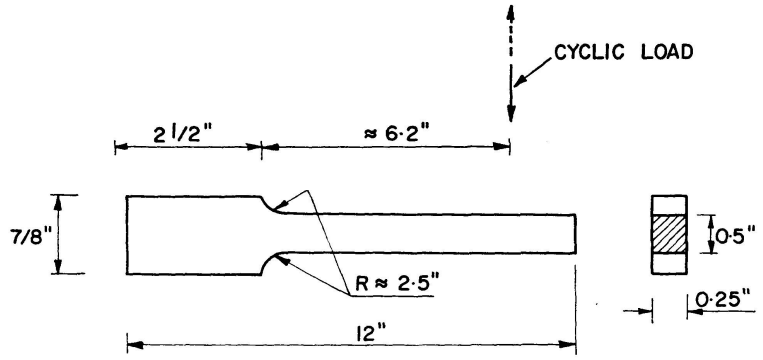

Fig. 6. Cantilever Beam Specimen.

The cantilever beam specimen is shown in Fig. 6. The depth of its haunched section is a function of the location and the two radii of fillet curvature (Appendix I). Each radius was measured accurately by means of an optical device. Simple measurements yielded the depth at consecutive sections along the beam length. The depth and width of these consecutive sections provide the input for a computer program, that will be presented later, to determine beam response.

The cantilever beam fixture shown in Fig. 7 was used previously [11] and is subject to minor modifications. The beam (1) is held at the "fixed end" by fixture (2) which, in turn, is fastened to the test frame hydraulic ram (3). The cyclic concentrated load, on the other hand, is applied to the beam at its "tip"

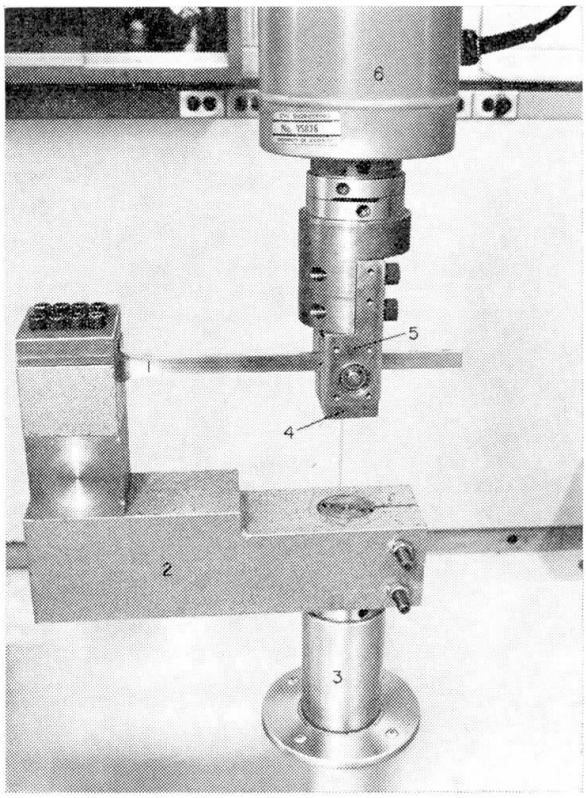

Fig. 7. Cantilever Beam Fixture.

by two rollers contained in a box (4). This box swings about an axis that connects it to a supporting element (5) attached to the load cell (6).

The load is measured by the load cell and the deflection of the beam's fixed end with respect to the free end is considered equal to the ram displacement. This implies that the test frame deformation is negligible as was verified experimentally.

Control Conditions

The trace of cyclic generalized force with respect to the corresponding generalized deformation yields a hysteresis loop that degenerates to a straight line when no plastic deformation is involved. At the sectional level this is a moment-strain loop. If the strain limits are fixed, any increase in the moment range is interpreted as hardening and any decrease as softening. Similarly, for fixed moment limits, an increase in strain range is softening; a decrease is hardening.

Other phenomena exhibited by the hysteresis loop are those of cyclic creep and relaxation. The first is an accumulation of strain (curvature) under load (moment) control; the second is a decrease in mean load (moment) under deformation (curvature) control. The pure bending tests discussed in the following section were conducted under exclusively constant strain control; hence, cyclic creep was not present.

Pure Bending

Moment Strain Relations

Fig. 8 shows the moment range versus cyclic state for a constant curvature range (or extreme fibre strain range). The moment range decreases with life, Fig. 8a. For larger strain ranges, however, the moment range remained practi-

Fig. 8a–g. Cyclic Variation of Moment Range and Mean Moment.

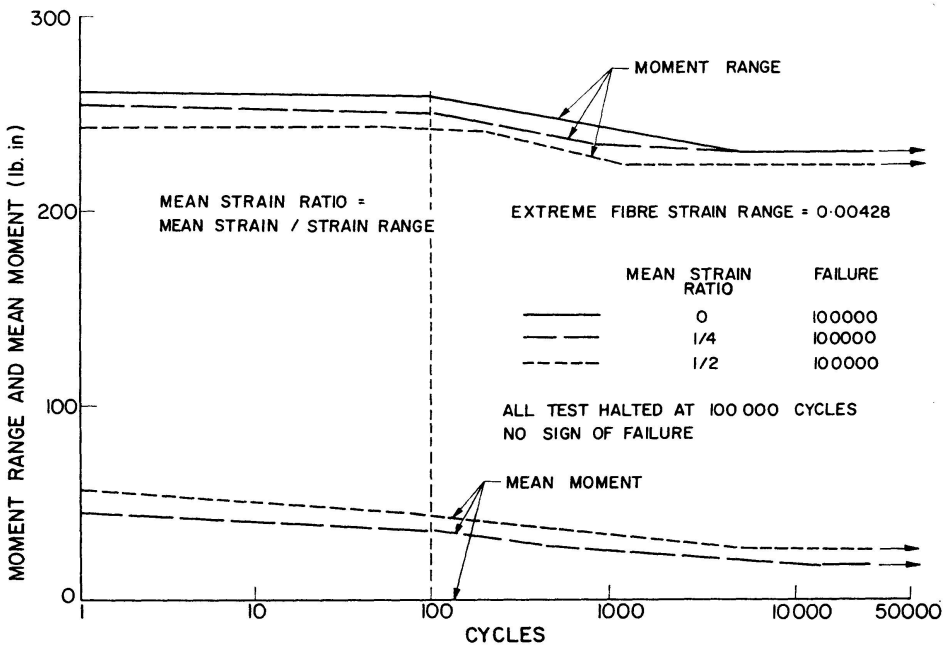

Fig. 8a.

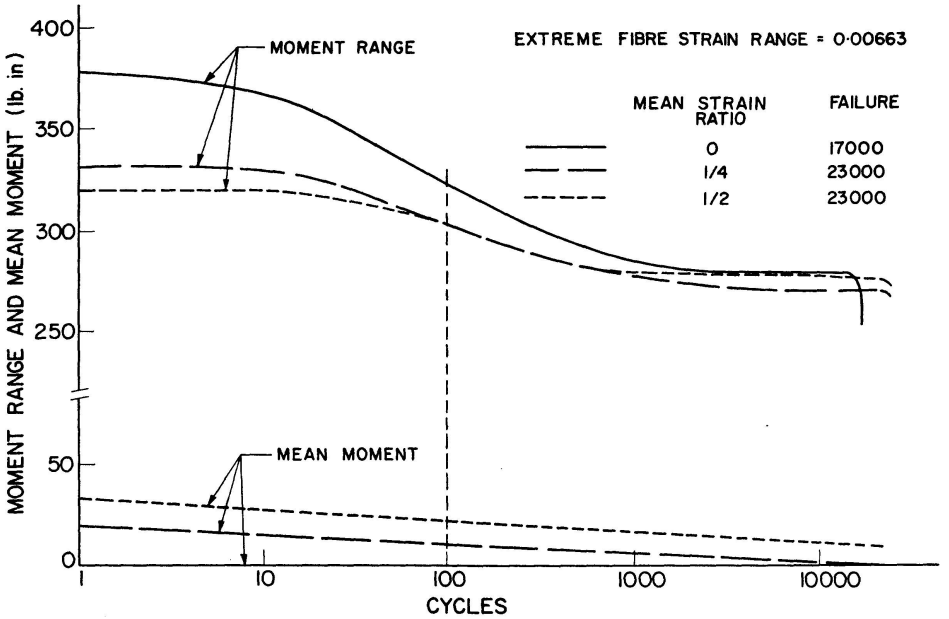

Fig. 8b.

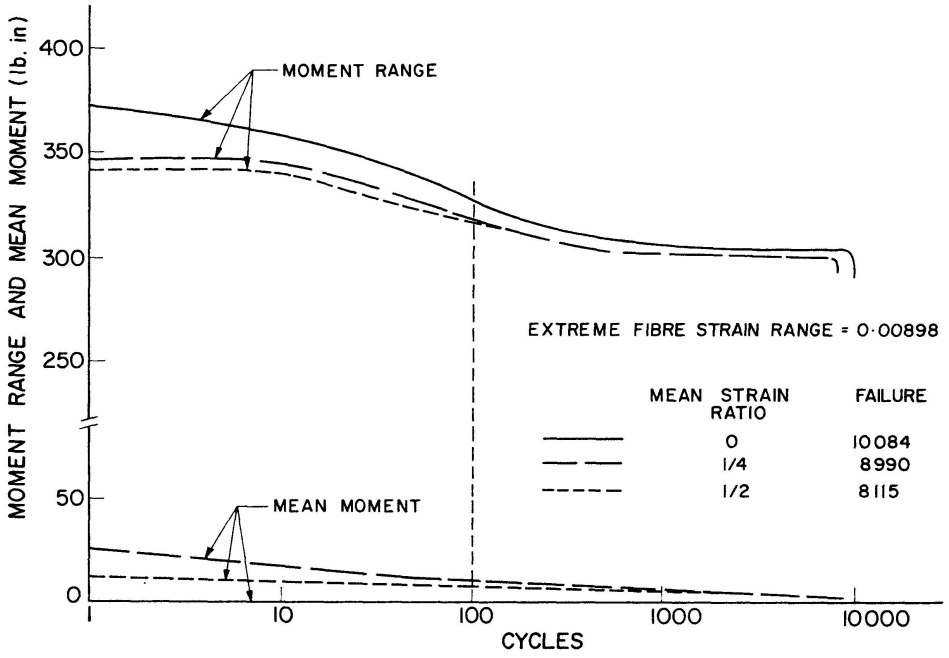

Fig. 8c.

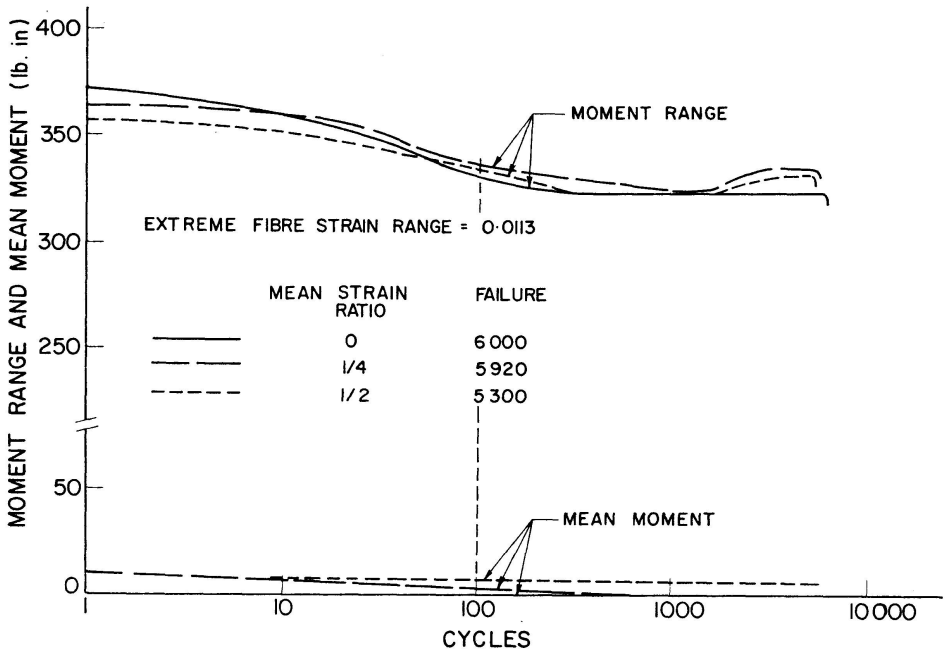

Fig. 8d.

cally constant or even increased, Figs. 8e, f, g. Hence the section as an aggregation of fibres, may be softening, stable or hardening depending upon the cyclic strain ranges involved in the individual elements.

The experimental results demonstrated that the moment range, for a certain strain range, varies little with the change in the mean strain value. Fig. 8d, for example, shows the moment range versus number of cycles for an extreme fiber strain range of 0.0113 and mean strain ratios of 0, 0.25 and 0.5. The maximum discrepency from the average value is less than 2%. For

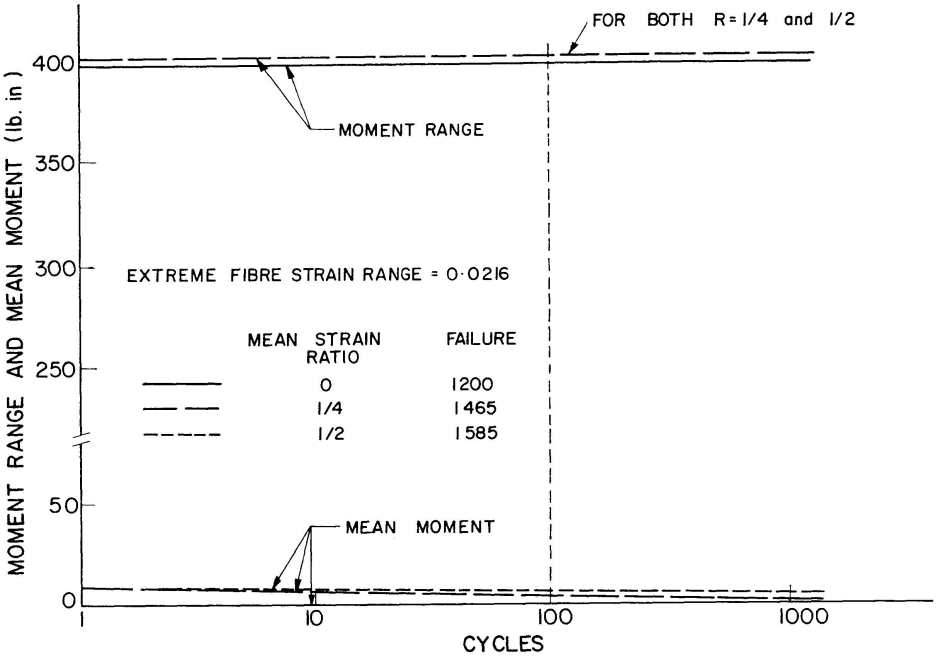

Fig. 8e.

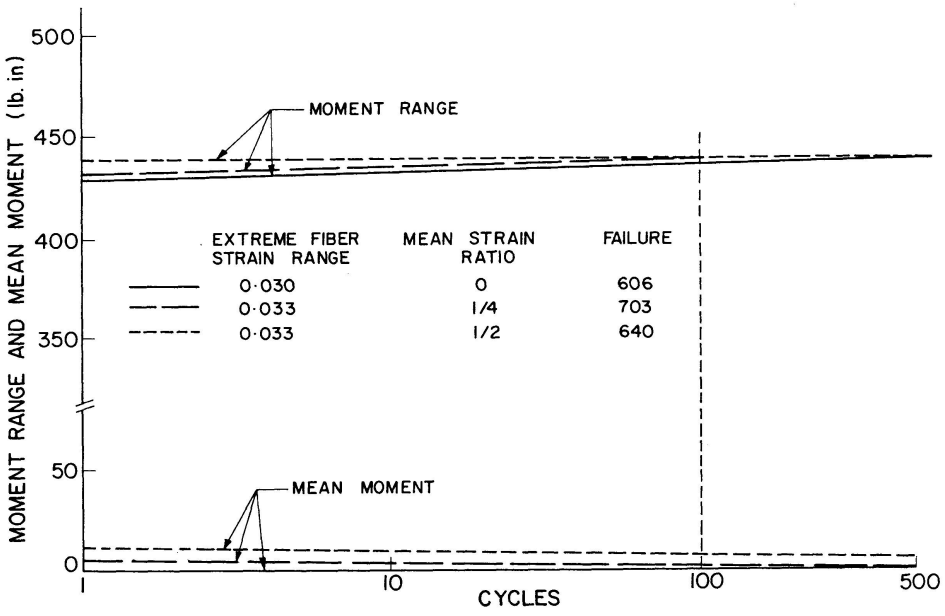

Fig. 8f.

this strain range the section softens during the initial 300 cycles or so then almost stabilizes for the remainder of its life.

The case where the mean strain has the greatest effect on moment range is depicted in Fig. 8b. This is due to the fact that the loop corresponding to zero mean strain and the given strain range has a small plastic strain component whereas that incorporating mean strain has a larger plastic component. This is illustrated in Figs. 9a and 9b. Nonetheless, for higher cycles, larger plastic strain would have developed within the total strain range of Fig. 9a, and the moment range approaches the value exhibited by the other specimens. The

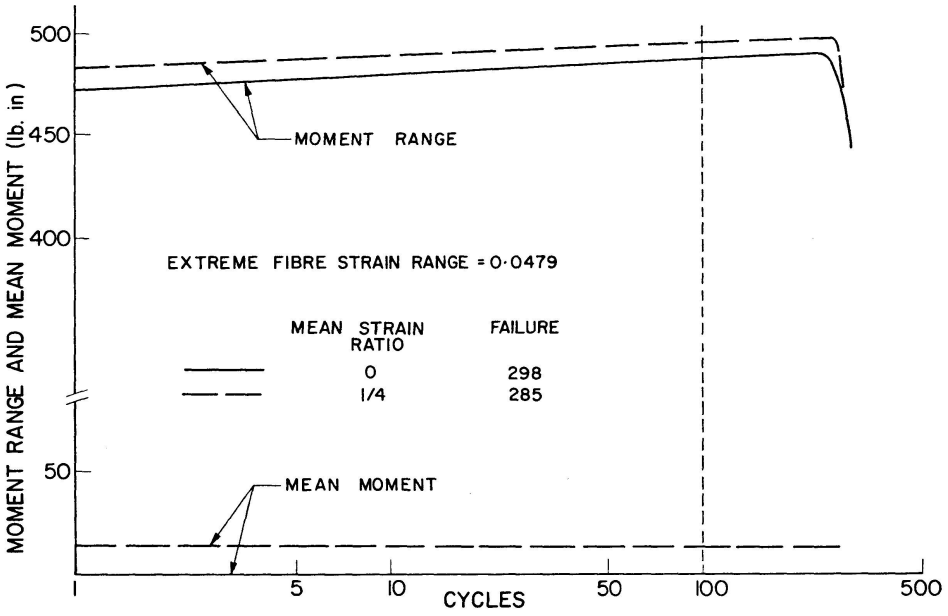

Fig. 8g.

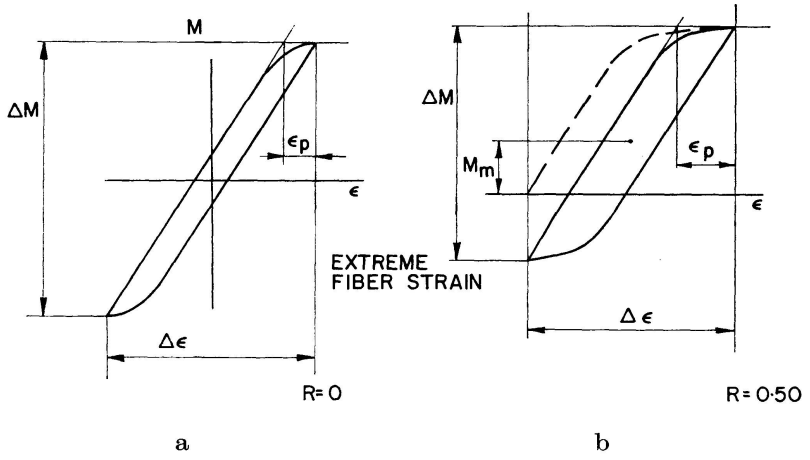

Fig. 9. Effect of Plastic Strain Component on Moment Range.

greatest discrepancy, however, is of the order of 15%. Such discrepancy will be ignored in the modelling suggested below, i.e., only an average moment range-strain range relation will be adopted for any cyclic stage regardless of the mean strain ratio. This may cause some predictive error only in the early stages of life of the structure. The significance of the error introduced will be discussed later.

The diagrams of Fig. 8, in addition to showing the moment range variation versus the number of cycles, show the relaxation of mean moment. It is clear that, for all strain ranges, the mean moment, in general, is a function of the mean strain.

Life span, on the other hand, did not seem to be significantly affected by mean strain. The tests, as a whole, did not show any definite trends in this

Fig. 10a–g. Discrete Cyclic Moment-Strain Relations.

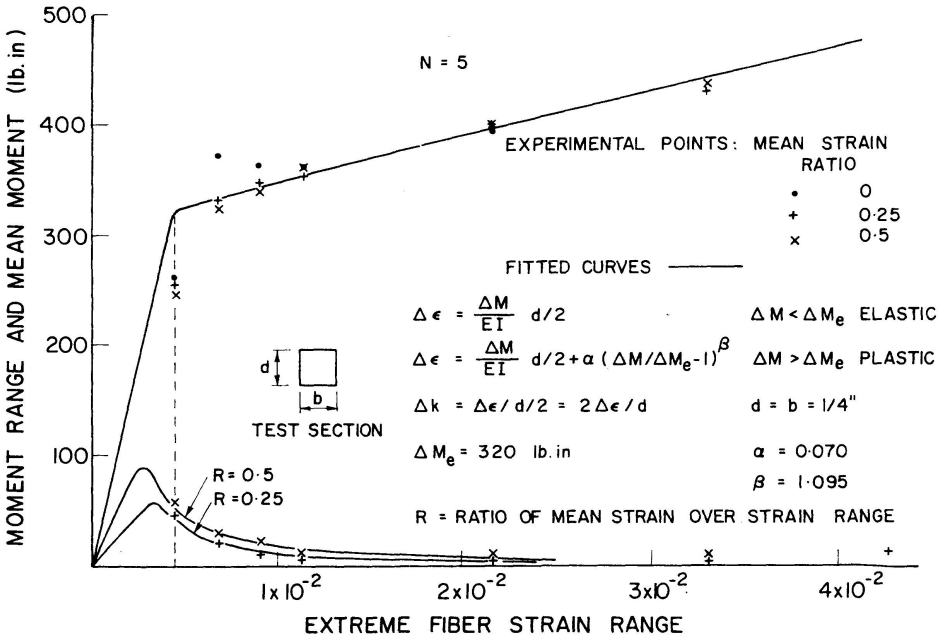

Fig. 10a.

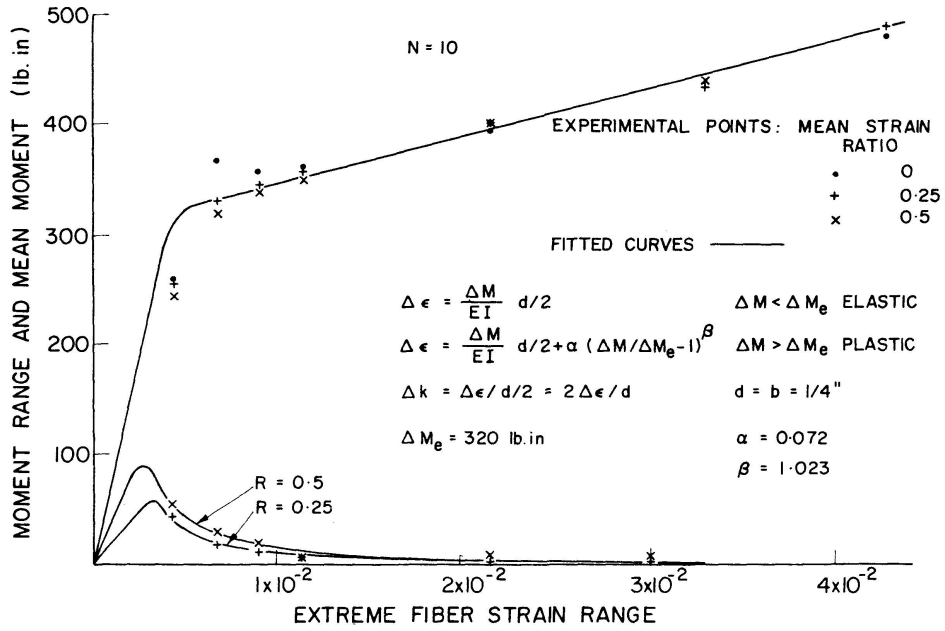

Fig. 10b.

direction and the lack of correlation can probably be accounted for by the scatter inherent in fatigue behaviour.

For a certain cyclic state, the compilation of moment range versus strain range data yields cyclic moment range-strain range relation as shown in Fig. 10. Similarly, the compilation of mean moment versus strain range yields corresponding cyclic mean moment-strain range relation. As an example, Fig. 10d

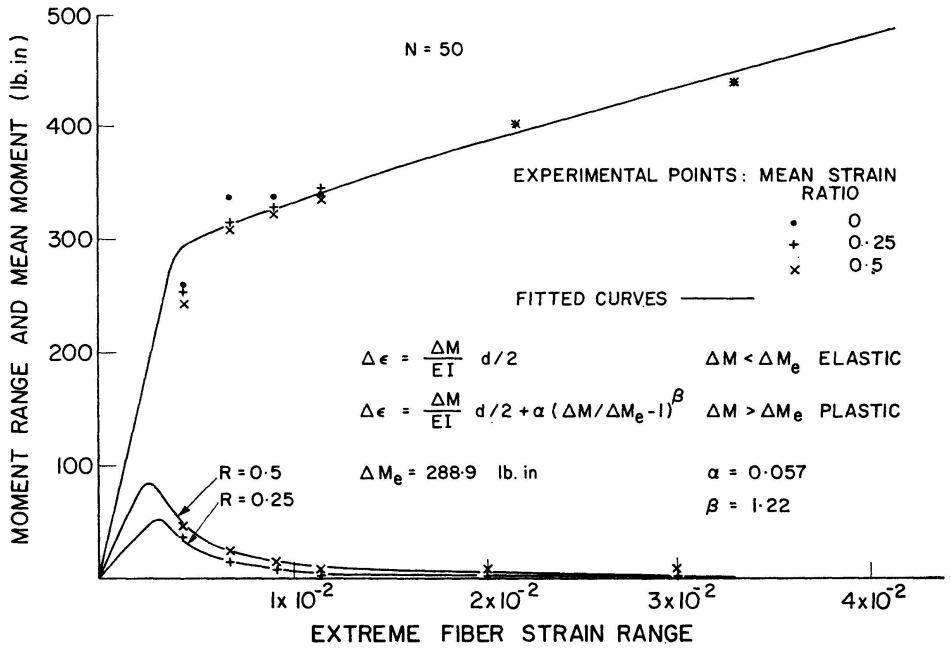

Fig. 10c,

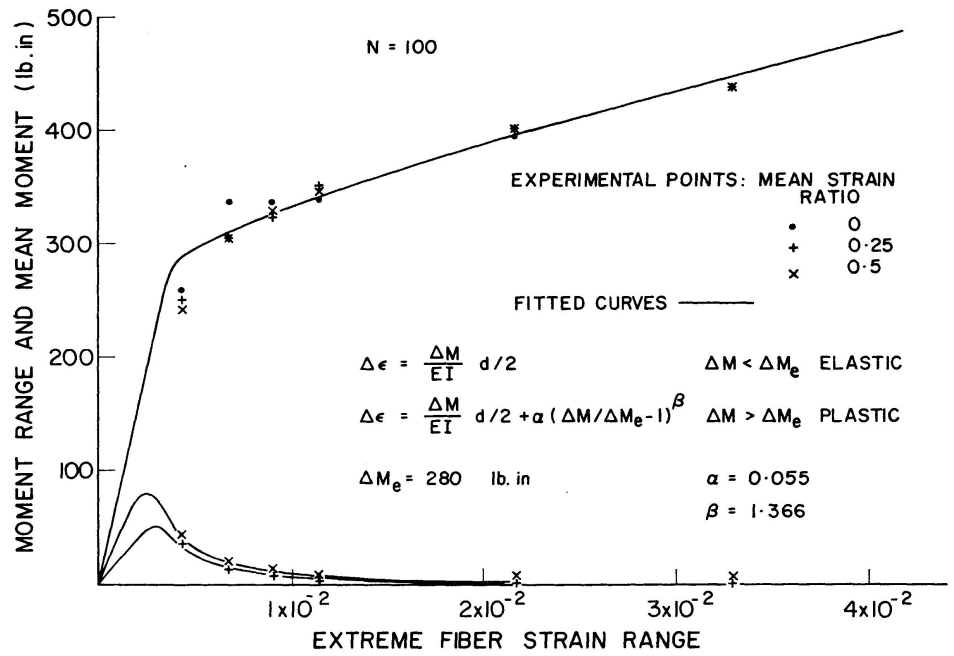

Fig. 10d.

is obtained by cross-plotting the data in Fig. 8 at $N = 100$. The other diagrams of Fig. 10 are derived in a similar way.

A two phase model of the type

$$\Delta\epsilon = \frac{\Delta M}{EI}\frac{d}{2} \qquad \text{for elastic behaviour,} \qquad \text{(I)}$$

$$\Delta\epsilon = \frac{\Delta M}{EI}\frac{d}{2} + \alpha\left(\frac{\Delta M}{\Delta M_e} - 1\right)^{\beta} \qquad \text{for inelastic behaviour} \qquad \text{(II)}$$

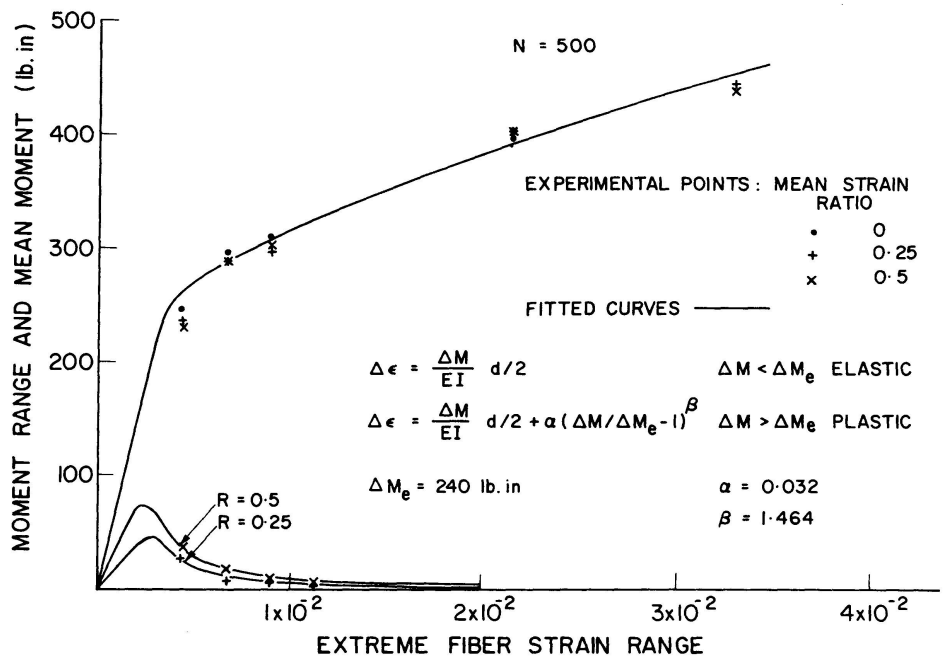

Fig. 10e.

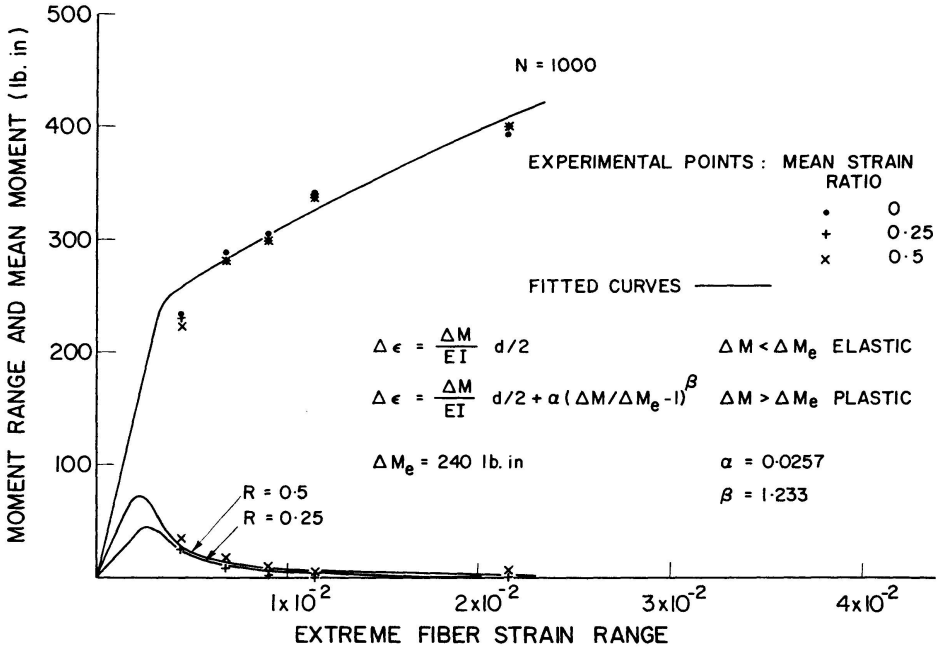

Fig. 10f.

is proposed as a fit to the moment range-strain range data where

$\Delta\epsilon$ = strain range,
ΔM = moment range,
ΔM_e = proportional moment range,
EI = flexural stiffness,
d = depth of section,
α, β = section and material constants.

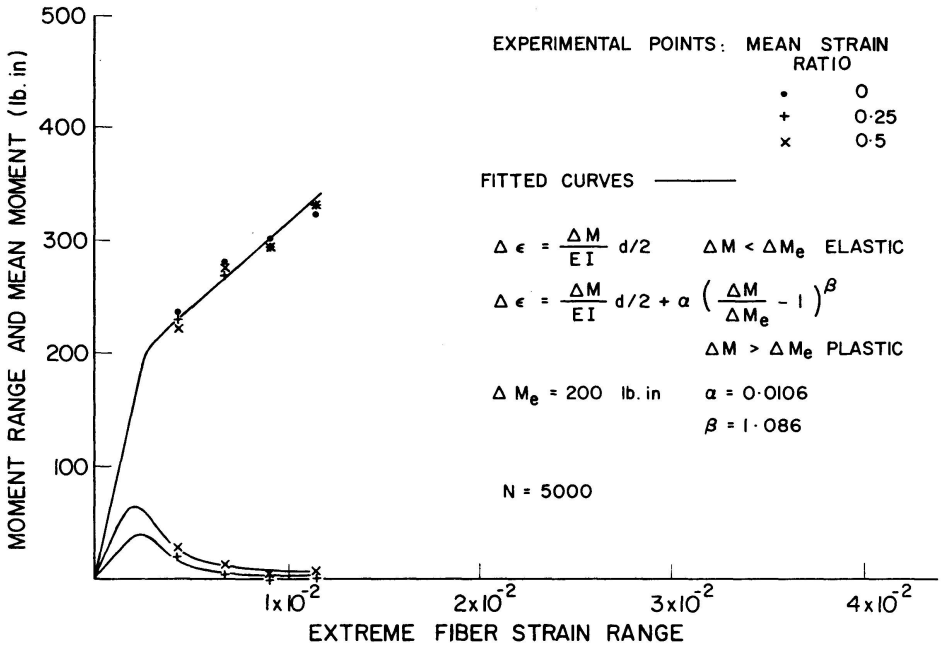

Fig. 10g.

This model is continuous and, as shown in Fig. 10 fits the data reasonably well. Dividing both sides of Eqs. (I) and (II) by $d/2$, leads to a cyclic moment-curvature relationship of the form:

$$\Delta k = \frac{\Delta M}{E I}, \tag{III}$$

$$\Delta k = \frac{\Delta M}{E I} + \frac{2}{d}\alpha\left(\frac{\Delta M}{\Delta M_e} - 1\right)^{\beta}. \tag{IV}$$

Since strain can be considered as dimensionless, the diagrams of Fig. 10 are semi-dimensional (only the moment axis has units) and can be easily employed for any rectangular structural section provided that the applied moment is adjusted by the appropriate ratio of the two section moduli, that of the section in Fig. 10 to that of the particular section under consideration.

The flexural stiffness, EI, for the test section was calculated theoretically from the section geometry and a value of 29.6×10^6 psi for E. The constants α, β and ΔM_e were established from a least squares curve fitting analysis. Thus, for each cyclic stage, a set of values for these constants was established (Appendix II).

The effect of mean strain on the moment range-strain range relation is shown in Fig. 11 for N equal 5 for which the discrepancy is largest. Four fitted curves are shown: three corresponding to the three mean strain ratios and the fourth to an average. The largest discrepancy corresponds to mean strain ratios of 0 and $\frac{1}{2}$ and a strain range of 0.00415. It is less than 15%. The deviation from the average curve, however, is about 8%. For larger strain range

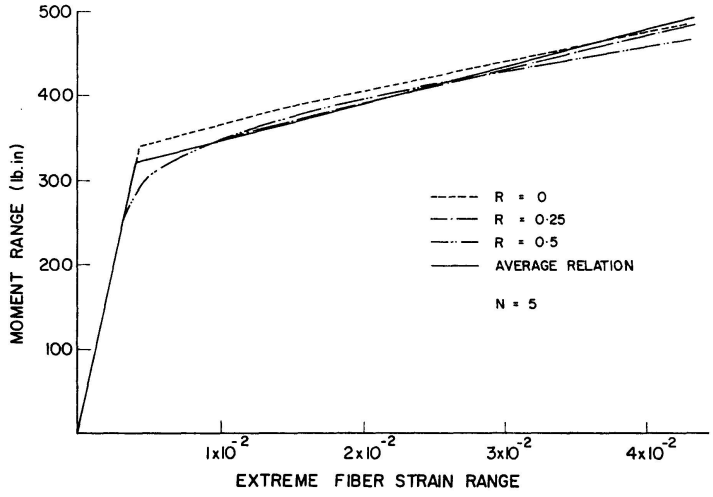

Fig. 11. Effect of Mean Strain on Moment Range-Strain Range Relation.

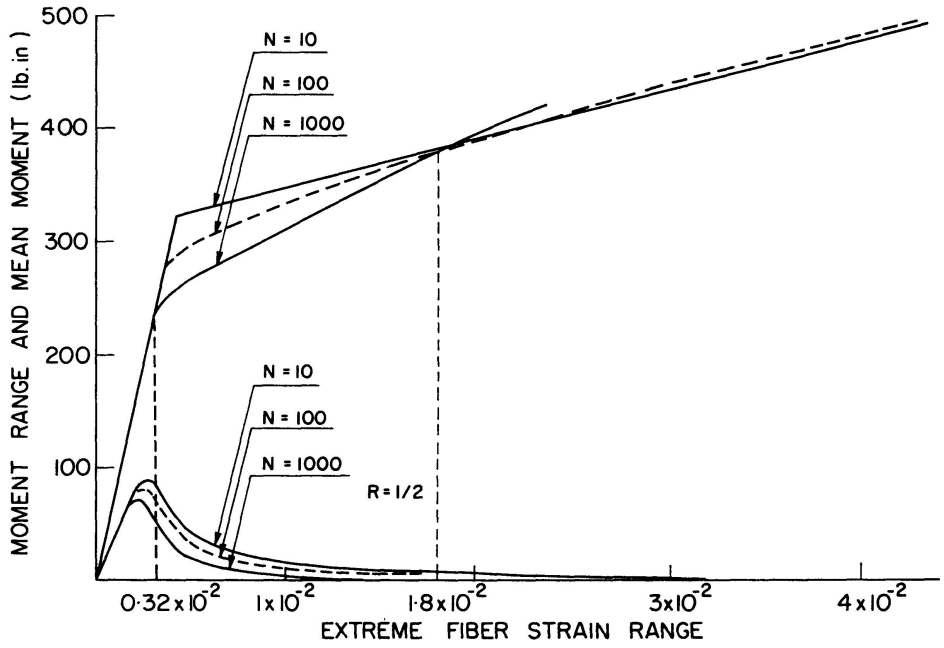

Fig. 12. Aggregated Cyclic Moment-Strain Relations.

value, the variation is not more than 5%. These variations become insignificant when N reaches large values, as discussed previously.

The cyclic softening and hardening characteristics of flexural sections can be visualized by examining the moment range-strain range relation at different cyclic stages. Such relations can be seen in Fig. 12 for $N = 10$ and $N = 1000$. The figure shows three different regions with respect to the extreme fiber strain range: from zero to 0,0032 where the all curves coincide; from 0.0032 to 0.018, where the curve for $N = 1000$ lies below that for $N = 10$, leading to cyclic softening within that range; and the region for strain range greater than about 0.018, where the section hardens with cycling. It is worth noting that, for the particular strain range value of 0.018, the section neither hardens nor softens but remains practically stable (or neutral) throughout its life. The

curves for N between 10 and 1000 cycles lie within the two limiting states of response. One such curve ($N=100$) is shown in dashed lines on the same figure.

Conversely, the mean moment versus strain range relationship poses a more difficult problem. A glance at Fig. 10 reveals that the curve required to fit the data for any mean strain ratio should have three regions: an initial straight line, an intermediate convex curve and finally a concave region where the curve asymptotically approaches zero for large values of curvature range. The slope of the initial straight part is simply equal to that of the initial portion of the $\Delta M - \Delta \epsilon$ relation times the mean strain ratio (ratio of mean strain over strain range). The latter region of the experimental data is modelled by an equation of the form:

$$M_m = \frac{\theta_1}{(\Delta \epsilon)^{\theta_2}}, \tag{V}$$

where M_m is the mean moment and θ_1 and θ_2 are constants to be established by least square analysis. The intermediate range is assumed to have the form:

$$M_m = C_1 + C_2 \Delta \epsilon + C_3 \Delta \epsilon^2 + C_4 \Delta \epsilon^3. \tag{VI}$$

This is a third degree polynomial with four arbitrary constants. From the continuity of the function and its slopes at the first transition point, i.e., between initial and intermediate regions, and the second transition point (between the intermediate and last regions) four equations will be obtained. Solving these equations simultaneously will establish the constants C_1 to C_4. Some approximation was used to locate these two transition points and Appendices III and IV deal with this concept in more detail. Fig. 10 shows the experimental data and the fitted curves.

Behaviour and Models

A total of twenty pure bending tests were conducted. The extreme fiber strain range assumed seven values: the smallest was 0.00428 or 1.36 times the monotonic yield strain range value; the largest was 0.0479 which is very close to the monotonic strain-hardening range value. At each level three tests, comprising a single set, were conducted except for the largest strain range where the set included only two tests. In each set, the first test involved no mean strain; the second included a mean strain equal to one-fourth the strain range; the third test had a mean strain equal to one-half the strain range.

The results of each set of tests were consistent within themselves. The moment range varied little with the introduction of mean strain. Thus, any inconsistency could have been readily identified. A maximum discrepancy of 15% of moment range in one set with a particular strain range is explained in terms of the proportion of plastic strain within the given total strain of the hysteresis loop. The mean moment, on the other hand, increased with the

increase in mean strain for small strain ranges. For large strain range values, however, the increase in mean moment was not that pronounced. In both cases, the experimental findings could be easily explained using the well-known rheological model [12]. The life observed for the tested specimens ranged from 300 cycles to above 100,000 cycles. Thus, most of the low cyclic fatigue range, pertinent to structural design, was covered.

The moment range versus the strain range obtained experimentally has been described by the two phase model of Eqs. (I) and (II). Fig. 10 shows that the suggested model fits the data reasonably well. The model could even be simplified to elastic strain hardening (bi-linear) without much loss of accuracy. However, this simplification was unnecessary since the structural calculations are computerized. The parameter ΔM_e decreased with cycles as did α; in contrast β did not show an amenable trend, hence the moment range-strain range was presented as a discrete function of cyclic life. Also, the mean moment-strain range relation was considered as such. Due to the tri-partite nature of the latter relation there were eight parameters to be established for each mean strain ratio: four in constant C, two in θ and two transition point strain values [Eqs. (V) and (VI)]. If the last two terms of Eq. (VI) were neglected, two parameters would be eliminated. However, the replacement of the third degree curve by a straight line would induce some unwarranted inaccuracy and two discontinuities in the model.

The experimental data revealed that the mean moment decreased rapidly as the strain range increased. Thus for $\Delta \epsilon$ equal to three times the maximum elastic strain range, the mean moment could be neglected, its value being less than 2% of the moment range. Therefore, the value of the mean moment-strain range model is confined to the intermediate domain of strain range, i. e., where the strain range is larger than the limit elastic strain range, for which linear classical theory applies, and smaller than the values associated with negligible mean moment.

Cantilever Beams

Bending Under Unequal Tip Deflection

The behaviour of the cantilever beam shown in Fig. 6 will be predicted theoretically and investigated experimentally in the present study. A single cyclic load is applied at its "tip" to cause cyclic deflections confined to two predetermined values, i. e., the beam is under deflection control. The deflection limits need not be symmetrical; the symmetrical case, however, is studied first in order to develop the method of calculation. The unsymmetrical case will be examined later.

The cantilever is under deflection control. If the associated load is well below the elastic limit of the material, there will be negligible softening or

hardening and section of the beam can be presumed as being under either moment or curvature control. If the load exceeds the linear limit, the sections are under neither moment control nor curvature control but under some mixed control condition. Nonetheless, it seems reasonable to predict cyclic structural behaviour, in this case, from a moment-curvature relationship based on controlled, fixed curvature limits [11]. The basic assumptions made in this investigations are as follows:

1. Inertia forces and weight of specimen are negligible.
2. The effects of shearing stresses can be ignored, arising from the geometry of the specimen as related to load position.
3. Variable cross sections can be idealized as a series of short, discrete segments each having a constant cross-section.
4. Plane sections before bending remain plane after bending.
5. Small deflection theory is applicable.
6. The normalized cyclic moment-curvature relation describes the behaviour of all geometrically similar cross-sections made of the same material.
8. Local and other kinds of buckling are prevented.

Analysis

As presented previously, the cyclic moment range-strain range relation can be regarded as independent of the mean strain. Hence, the cyclic load range-deflection range relationships can be expected to be independent of the mean deflection. The case of symmetrical deflection limits will first be presented and will be followed by consideration of the non-zero mean deflection case.

The method of predicting response is an iterative one; for a given deflection, a load range is assumed and the resulting deflection range is calculated. If this deflection range is equal to that specified, the assumed value of load range is the one sought; if not, the load range is adjusted and the entire process is repeated until convergence is obtained to within the desired error.

To obtain the deflection of the tip of the cantilever under an assumed concentrated load at the same point, the beam is divided into a number of segments. For each segment end and for the depth and width at that segment end, the curvature corresponding to the moment at that location is calculated from the cyclic moment-strain equation and section depth given as input data. Having established the curvatures at successive locations along the length of the beam, the "elastic curve" can be constructed. Elementary mathematics yield the deflection at any segment end of the beam. Appendix V presents the mathematical operations involved. Table I describes the main steps of a computer program based on the method presented herein.

For the cantilever beam under unequal deflection limits the method is a little more involved. The input data should include the mean deflection range.

Table I. Flow Chart

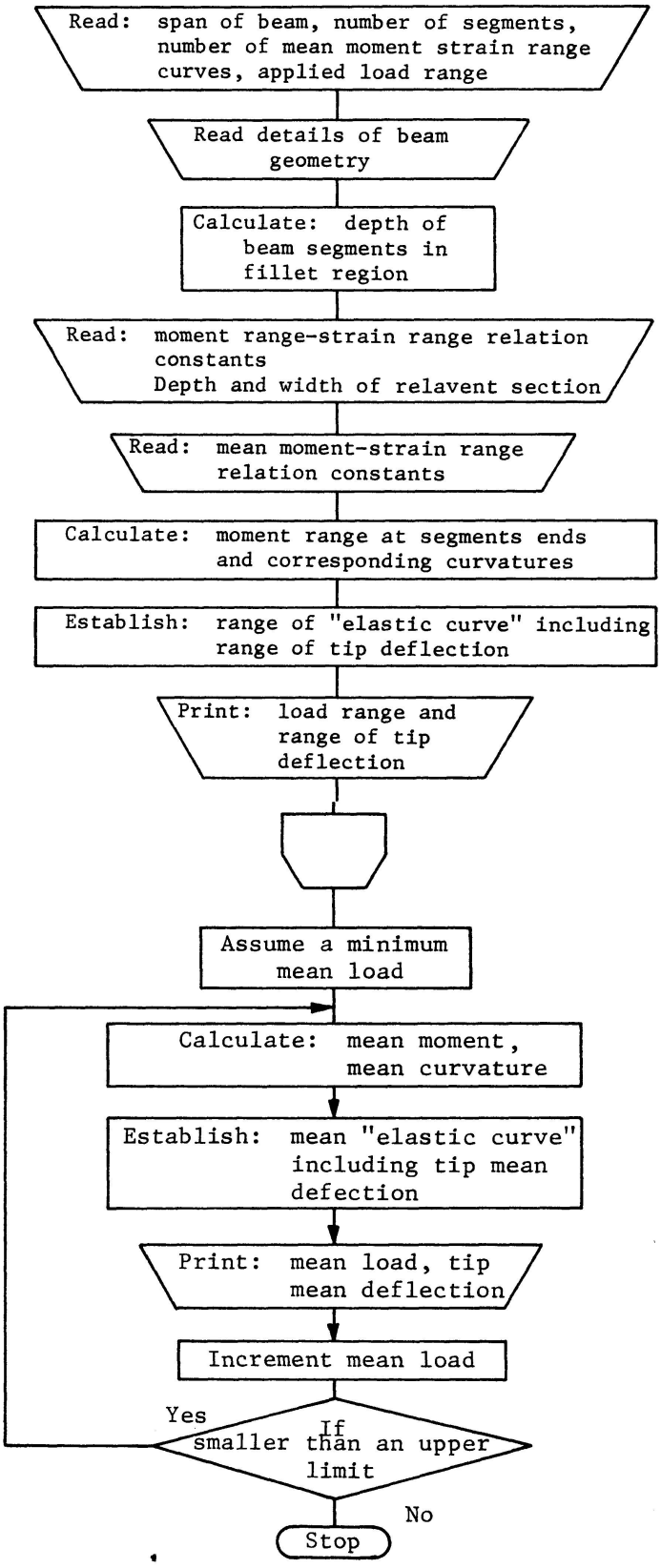

The desired values, on the other hand, are the corresponding load range and mean load. A trial mean load is first assumed and the corresponding mean deflection is calculated. If this mean deflection is equal to the specified mean deflection to within the tolerable error, the assumed value of load is accepted; otherwise, the assumed mean load is adjusted until the corresponding mean deflection converges to the specified value. The method presented for the calculation of deflection range is used again to calculate the mean deflection with one difference; the curvature range (or extreme fiber strain range) at the end of each beam segment is replaced by the mean curvature or mean strain at the same location.

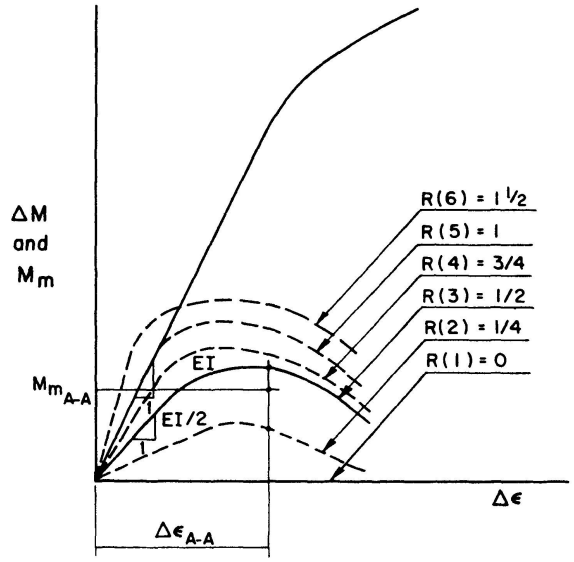

Fig. 13. Schematic Interpolation for Mean Strain.

For the calculation of this mean strain at a certain section, designated $A-A$, it is necessary to have at hand the strain range established from load range calculations and the mean moment calculated from the assumed mean load at the same section. These values are designated by $\Delta\epsilon_{A-A}$ and $M_{m_{A-A}}$ respectively. Fig. 13 shows the moment range and mean moment-strain range relations with the X axis distorted for the sake of clarity. Now, the mean moment value corresponding to a strain range of $\Delta\epsilon_{A-A}$ and a mean strain ratio equal to $R(I)$ is established, I being 2 for the first attempt. If the resulting mean moment is larger than $M_{m_{A-A}}$, the actual mean strain ratio is interpolated linearly between $R(I)$ and $R(I-1)$; if smaller, I is increased until the desired condition is met. Thus, the product of the interpolated mean strain ratio and strain range is an approximation to the desired mean strain. The mean curvature is simply the mean strain over half the beam depth.

Results and Discussion

Nine tests were conducted on cantilever beam, four pairs and a single. Each pair of beams had a single deflection range; one beam had no mean deflection

and the other had a mean deflection equal to about one eighth of the deflection range, i. e., completely and partially reversed deflections.

The deflection range for the first pair was 0.17″. The strain range at the critical section at the fifth cycle was, as obtained from the computer program, equal to 0.0034. This was less than the limiting linear strain range at the same cyclic state which was equal to 0.00415, Fig. 10a. Therefore, and since the material did not harden from the first to the fifth cycle for that strain range, the completely reversed deflection beam remained elastic up to at least the fifth cycle. Assuming the same conclusion was applicable to the partially reversed deflection case, the mean strain ratio would be equal to the mean deflection ratio, i. e., about one eighth. The maximum strain amplitude calculated on this basis, however, was found to be slightly higher than the maximum linear strain amplitude. Hence, the second beam has undergone some plastic deformation. This was readily observed from the hysteresis loop which was a straight line for the first beam and had some width for the second beam at the cyclic state under consideration.

As cycling progressed, the material softened. At $N = 5000$, for example, the limit linear strain range dropped to 0.00261 whereas the strain range at the critical section increased to about 0.0044. Naturally, both beams had undergone some plastic deformation although this was limited to small lengths along the beam. This conclusion was again supported by observations on the relevant hysteresis loops. The failure of the beam under zero mean deflection took place after 105,000 cycles; the test on the second beam was halted at

Fig. 14a–e. Experimental Versus Theoretical Results.

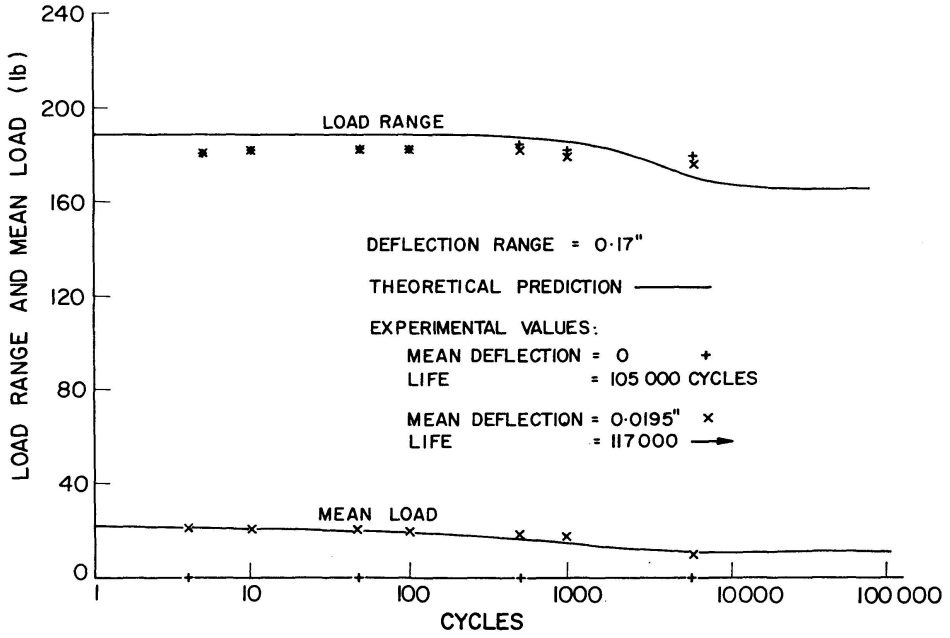

Fig. 14a.

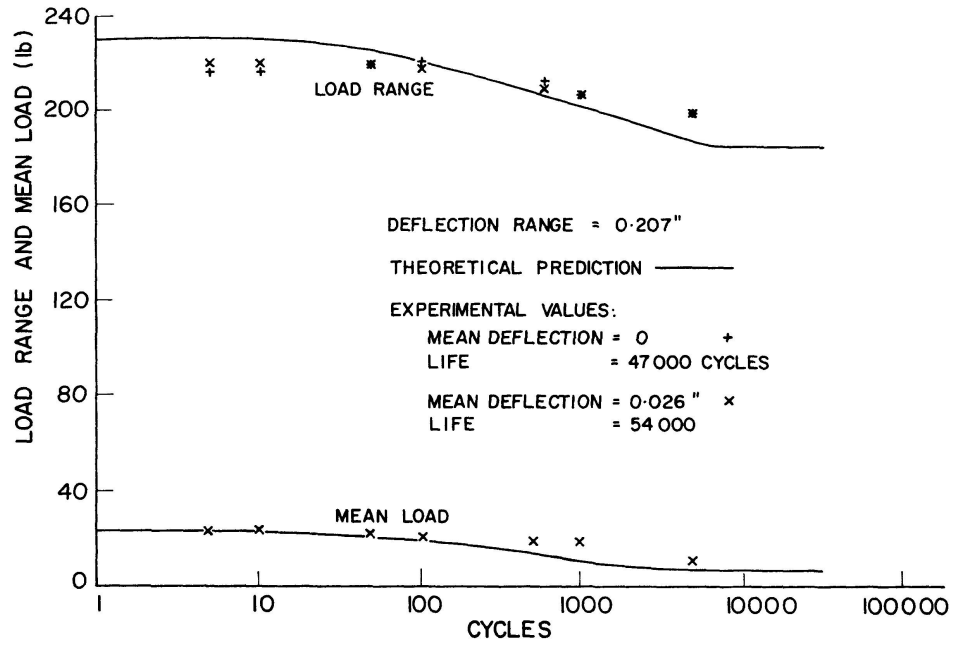

Fig. 14b.

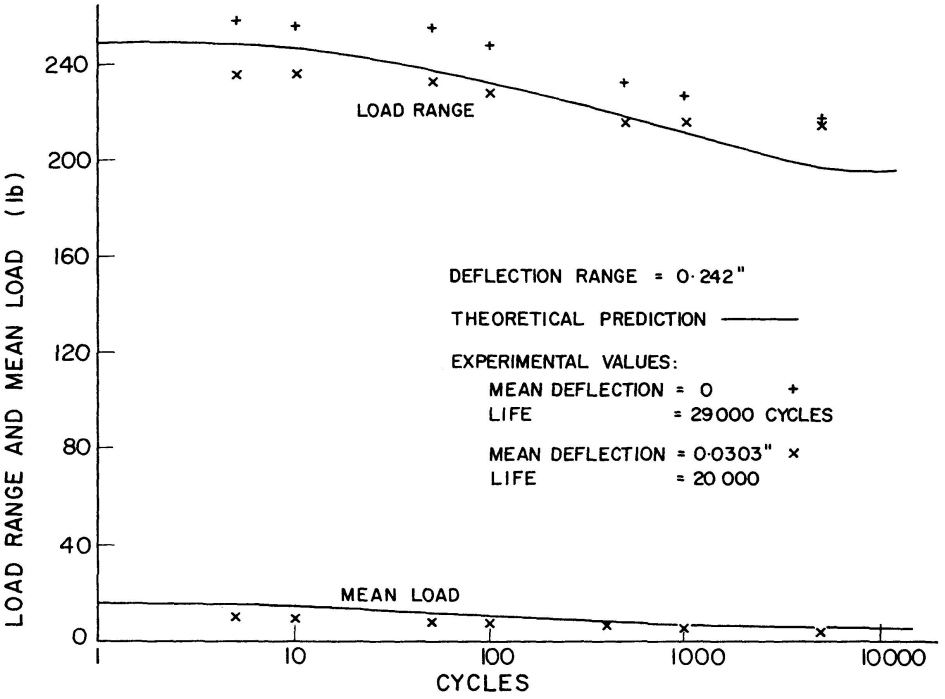

Fig. 14c.

117,000 cycles and failure was not attained. Hence, this deflection range may be considered to promote conventional fatigue.

For this deflection range Fig. 14a shows the theoretical load range and mean load versus cyclic life. The two solid lines were obtained by connecting discrete theoretical points corresponding to cycles 5, 10, 50, 100, 500, 1000 and 5000. The experimental results are also shown as discrete point at the above-mentioned cyclic states.

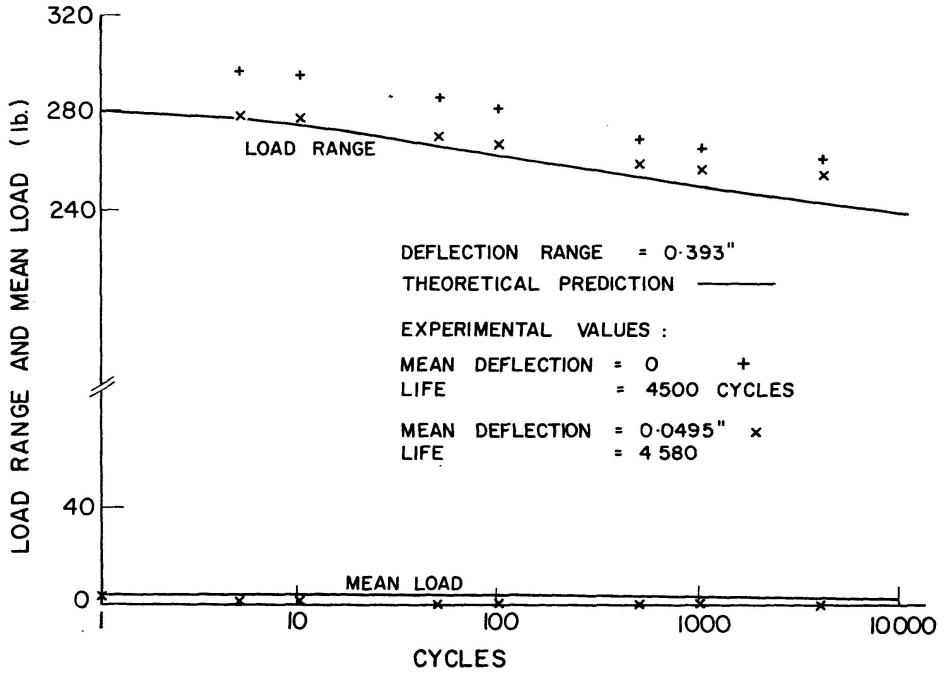

Fig. 14d.

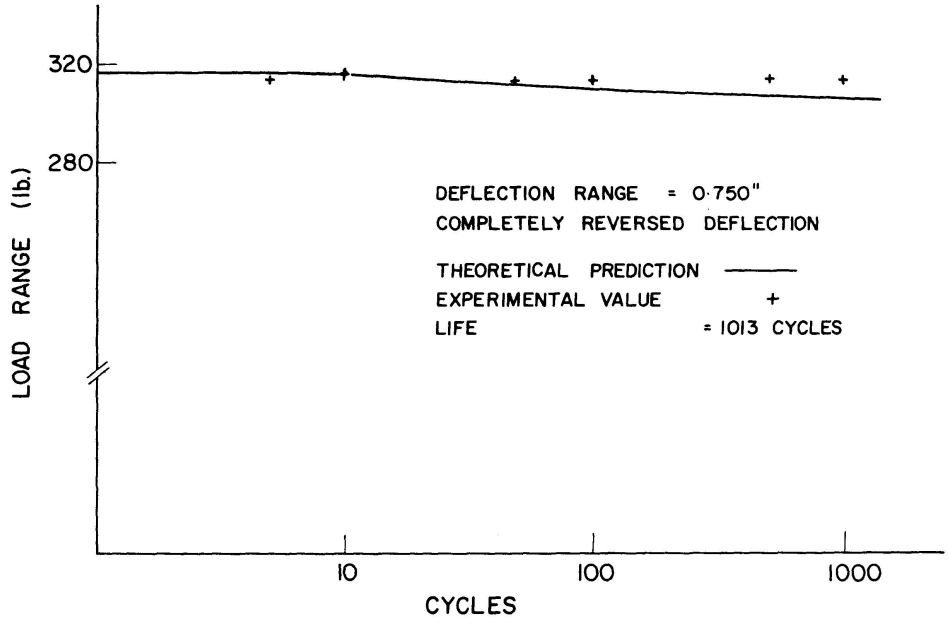

Fig. 14e.

In a similar manner, Figs. 14b, 14c, 14d and 14e show the theoretical and experimental results as well as life span for four larger deflection ranges equal to 0.207″, 0.242″, 0.393″ and 0.750″. It can be seen that the experimental load range associated with the smallest deflection range, Fig. 14a was not significantly influenced by mean deflection – the maximum relative discrepancy was about 3% at $N=5000$. Among all the deflection ranges, the maximum discrepancy occurred in the case of deflection range equal to 0.242″ and $N=5$. This discrepancy was 9% or a variation of less than 5% from the average

value. For the deflection ranges equal to 0.207″ and 0.242″, the variation was not more than 4% measures about the average. It is worth noting here that the experimental load range for zero mean deflection was, in general, larger than that for non-zero mean deflection. The discrepancy of 9% is less than the value of 15% presented previously in the discussion of the effect of mean strain on the moment-strain relation. This is due to the fact that the structural behaviour is an aggregate of sectional behaviour and that only at the critical section the mean strain ratio approaches the value of $\frac{1}{2}$ for the large deflection ranges.

For the largest deflection range of 0.75″, the maximum strain at the critical section was 0.034 at the fifth cycle and dropped to 0.023 at $N = 1000$. Both strain values are lower than the maximum value investigated under pure bending. Larger deflections, that will cause larger strain ranges, were not investigated as the effects of geometry change leading to membrane action cease to be insignificant for such deflections; the consideration of the effects of geometry change falls outside the domain of the current work.

The difference between the theoretical load range and the averaged experimental one, on the other hand, compared fairly well, the maximum difference being not more than 4% for any deflection range. It can be seen that the theoretical predictions are closer, in general, to the experimental results for non-zero mean deflection case than to the zero mean deflection one. This can be explained with reference to Fig. 11 which shows that the average moment range-strain range fits the partially reversed or repeated strain cases better than the completely reversed case. But since the error involved is fairly small, neglecting the effect of mean strain on moment range under pure moment and on load range under deflection control can be easily justified.

The theoretical and experimental mean load values, on the other hand, compare fairly well as shown in Fig. 14, especially when they are most significant, i.e., over the three lowest deflection ranges. When the mean load is added to and subtracted from half the load range, the maximum and minimum load limits are obtained, respectively. Simple calculations show that the relative error between theoretical prediction and experimental value for these limits is less than 5%.

Conclusions

Cyclic moment-strain relations, based upon deformation control tests conducted on rectangular structural steel sections were established. A model describing the moment range versus extreme fibre strain range, independent of the mean strain value, is presented. A second suggested model describes the mean moment versus the extreme fiber strain range for different ratios of mean strain over strain range at the same fiber. These models reduce cyclic flexural behaviour of sections to a pseudo-static representation amenable for

use in cyclic structural analysis. These models are capable of accommodating, in discrete form, the phenomena of hardening and softening of aggregations of fibres constituting a structural section as well as relaxation of mean moment.

A number of tests were conducted on cantilever beam specimens under tip deflection control. The behaviour under completely and partially reversed deflections was investigated. The load range was found to be little influenced by the mean deflection. Also, the mean load relaxed to an insignificant value in the first cycle when the deflection range was large enough to cause appreciable cyclic plastic deformation. For such cases, then, the beam could be considered as cycled under completely reversed deflection with a rest condition corresponding to the mean deflection position.

A theory was developed and presented for the prediction of the behaviour of such beams. It employs a discrete curvature-area method coupled with the cyclic moment-strain relations described above. The theoretical results agree fairly closely with experimental values. The theory also confirmed that the behaviour of simple structures under cyclic deformation can be divided into three cases, comprising: (1) an elastic case where the mean load is proportional to the load range; (2) an intermediate range where proportionality does not apply and the effect of mean deflection (mean load) cannot be ignored, and (3) the case of large, inelastic cyclic deformation where the effects of mean deflection can be completely ignored except for associated changes in structural geometry and its secondary membrane effects.

Notation

$\Delta \epsilon$	strain range.
ΔM	moment range.
ΔM_e	proportional moment range.
EI	flexural stiffness.
d	depth of section.
α, β	section and material constants.
Δk	curvature range.
M_m	mean moment.
$\theta_1, \theta_2,$ $C_1, \ldots C_4$	constants of mean moment-strain range relation.
R	ratio of mean strain over strain range or, ratio of mean curvature over curvature range.

Acknowledgements

This investigation was carried out in the Department of Civil Engineering at the University of Waterloo with financial assistance from the National Research Council of Canada under grant A-1582.

Appendix I. Depth of Cantilever Beam

Consider the cantilever beam specimen shown in Fig. I.1. Assuming that the upper fillet has a constant radius of curvature equal to R_1 it is required to determine the distance y in terms of x_1, x_2, R_1 and R_2.

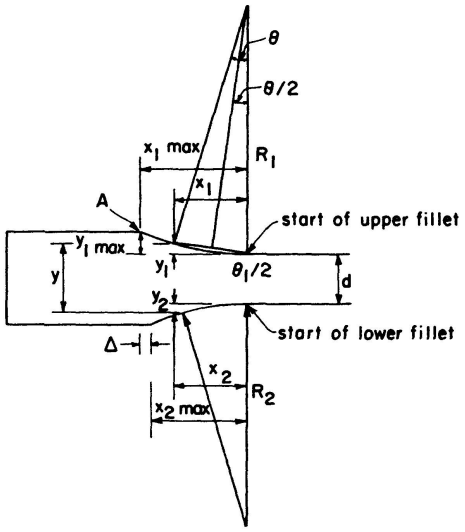

Fig. I.1. Cantilever Beam Fillet Depth.

From the Fig. I.1, obtain

$$x_1 = R_1 \sin\theta$$

or
$$\theta = \sin^{-1}\frac{x_1}{R_1},$$

also
$$y_1 = x_1 \tan\left(\frac{\theta}{2}\right),$$

then
$$y_1 = x_1 \tan\left(0.5 \sin^{-1}\frac{x_1}{R_1}\right). \tag{I.1}$$

Similarly,
$$y_2 = x_2 \tan\left(0.5 \sin^{-1}\frac{x_2}{R_2}\right)$$

and
$$y = y_1 + y_2 + d. \tag{I.2}$$

Hence, the depth of the section can be given as a function of the section location and the fillet radii.

The point where the fillet begins is usually difficult to establish by measurement accurately. Eq. (I.1) is used for this purpose as follows: for point A, y_{1max} can be easily measured. Assume a value for x_{1max} and calculate the corresponding y_1; if equal to the measured value of y_{1max}, the answer is obtained; if not, change the assumed value of x_{1max} until convergence is obtained. x_{2max} can be established similarly. A very short computer program facilitates such calculations.

For all specimen tested, R_1 and R_2 on the one hand and x_{1max} and x_{2max} on the other were close to each other. Also Δ was very small. In consequence, the assumption that the neutral axis of the untested specimen is a straight line is quite acceptable.

Appendix II. Determination of Coefficients (α, β, ΔM_e)

Assume a relationship of the form:

$$\Delta\epsilon = \frac{\Delta M}{EI}\frac{d}{2} \qquad \text{for the linear range where } \Delta M \leqq \Delta M_e \tag{II.1}$$

and

$$\Delta\epsilon = \frac{\Delta M}{EI}\frac{d}{2} + \alpha\left(\frac{\Delta M}{\Delta M_e} - 1\right)^{\beta} \qquad \text{for the non-linear range where } M > \Delta M_e. \tag{II.2}$$

The experiments provide a set of values $\Delta\epsilon$ and ΔM for each cycle, N. The coefficients will be evaluated so as to minimize the sum of the squares of the deviations of test points from an average curve. The curve fitting will be applied to the non-linear range only since the initial slope is considered fixed; but the limit of the linear range will be considered as a variable. The data point or points within the linear range will not be considered in the following step.

Eq. (II.2) can be rewritten in the logarithmic form as

$$\mathrm{Log}\left(\Delta\epsilon - \frac{\Delta M}{EI}\frac{d}{2}\right) = \mathrm{Log}\,\alpha + \beta\,\mathrm{Log}\left(\frac{\Delta M}{\Delta M_e} - 1\right)$$

or

$$y = K_1 + K_2 x, \tag{II.3}$$

where

$$y = \mathrm{Log}\left(\Delta\epsilon - \frac{\Delta M}{EI}\frac{d}{2}\right),$$

$$x = \mathrm{Log}\left(\frac{\Delta M}{\Delta M_e} - 1\right),$$

$$K_1 = \mathrm{Log}\,\alpha,$$

$$K_2 = \beta.$$

First ΔM_e is assumed constant. Thus, the problem is reduced to establishing two coefficients rather than three.

The least square analysis implies minimization of

$$E = \sum_{i=1}^{n} (y_i - K_2 x_i - K_1)^2.$$

Differentiating with respect to K_2 and K_1 for minima

$$\frac{\partial E}{\partial K_2} \rightarrow \sum_{i=1}^{n} (x_i y_i - K_2 x_i^2 - K_1 x_i) = 0,$$

$$\frac{\partial E}{\partial K_1} \rightarrow \sum_{i=1}^{n} (y_i - K_2 x_i - K_1) = 0$$

or
$$K_1 \sum_{i=1}^{n} x_i + K_2 \sum_{i=1}^{n} x_i^2 - \sum_{i=1}^{n} x_i y_i = 0, \tag{II.4}$$

$$K_1 \cdot 1 + K_2 \sum_{i=1}^{n} x_i - \sum_{i=1}^{n} y_i = 0, \tag{II.5}$$

where
$$K_1 \sum_{i=1}^{n} 1 = K_1 n.$$

The values of K_1 and K_2 are obtained by solving Eqs. (II.4) and (II.5).

$$K_2 = \frac{n \sum_{i=1}^{n} x_i y_i - \sum_{i=1}^{n} y_i \sum_{i=1}^{n} x_i}{n \sum_{i=1}^{n} x_i^2 - \sum_{i=1}^{n} x_i \sum_{i=1}^{n} x_i}$$

and
$$K_2 = \frac{\sum_{i=1}^{n} x_i^2 \sum_{i=1}^{n} y_i - \sum_{i=1}^{n} x_i \sum_{i=1}^{n} x_i y_i}{n \sum_{i=1}^{n} x_i^2 - \sum_{i=1}^{n} x_i \sum_{i=1}^{n} x_i}.$$

Having established K_1 and K_2, and, therefore α and β, the sum of the square of deviations can be given as

$$S = \sum_{i=1}^{n} \left[\Delta \epsilon - \frac{\Delta M_i}{E I} \frac{d}{2} - \left(\frac{\Delta M_i}{\Delta M_e} - 1 \right)^{\beta} \right]^2. \tag{II.5}$$

In this summation, all experimental data points should be included, be they below the elastic limit or above it, with due attention being paid to including or excluding the third term in Eq. (II.5).

Repeating the whole process but for a different value of ΔM_e, a new value for S is obtained, The best value of ΔM_e and the associated α and β are those which give the smallest value of S. The process, therefore, is complete when the minimum of $S = f(\Delta M_e)$ is obtained. This was programmed quite simply on a computer.

Appendix III. Location of First Transition Point

Assume the monotonic moment-curvature relation as given in Fig. III.1 where $\frac{\Delta M_e}{2}$ is the limit linear moment and k_0 is the corresponding curvature. When cycling with zero mean curvature, the loop will generally have a plastic component (and width) only if the curvature range exceeds $2k_0$. On the other hand, for a loop with constant mean curvature ratio, the mean moment will increase linearly with increase in curvature range as long as the absolute maximum curvature is less than k_0. Fig. III.2 illustrates such a case for mean curvature ratio of 1/2. Whenever the maximum curvature exceeds k_0, the mean moment ceases to increase linearly with curvature range. Therefore,

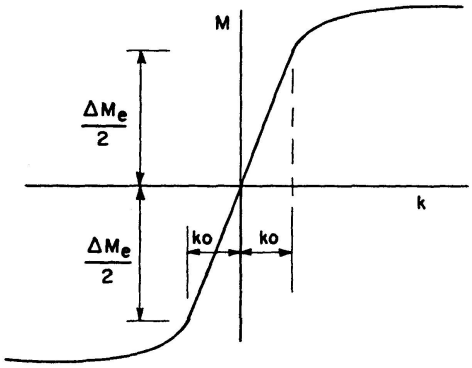

Fig. III.1. Maximum Linear Curvature.

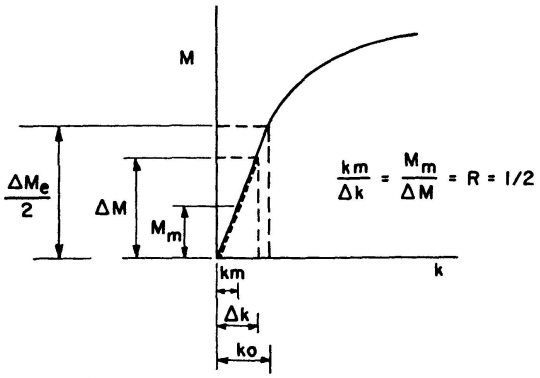

Fig. III.2. Calculation of Elastic Mean Moment Value.

the limit state is given by

$$k_{max} \leqq k_0 .$$

But

$$k_{max} = \frac{\Delta k}{2} + k_m ,$$

where Δk is curvature range and k_m is mean curvature

$$k_{max} = \frac{\Delta k}{2} + R \Delta k ,$$

where R is a ratio of proportionality

or

$$k_{max} = \Delta k \left(\tfrac{1}{2} + R\right),$$

$$\Delta k = \frac{k_{max}}{\tfrac{1}{2} + R},$$

when k_{max} assume its limit linear value, k_0, we obtain

$$\Delta k_{max} = \frac{k_0}{\tfrac{1}{2} + R}. \tag{III.1}$$

In other words, the maximum curvature range, for which the mean moment remains proportional to the mean curvature, is inversely proportional to $(\frac{1}{2} + R)$. The mean moment at this limit is designated the Maximum Linear Mean Moment (MLMM). Since it is at the limit of the linear range, it is given by:

$$\text{MLMM} = (\text{slope}) \cdot (\text{limit curvature}).$$

Since the slope is equal to $(E\,I\,R)$

$$MLMM = (E\,I\,R)\frac{k_0}{\tfrac{1}{2} + R} = \frac{\Delta M_e}{2}\frac{R}{\tfrac{1}{2} + R} \cdots \tag{III.2}$$

By solving Eq. (III.1) for R and substituting in Eq. (II.2), we obtain

$$R = \frac{k_0}{\Delta k_{max}} - \frac{1}{2}$$

and
$$MLMM = \frac{M_e}{2} \frac{\frac{k_0}{\Delta k_{max}} - \frac{1}{2}}{\frac{1}{2} + \frac{k_0}{\Delta k_{max}} - \frac{1}{2}} = \frac{\Delta M_e}{2}\left(1 - \frac{\Delta k_{max}}{2 k_0}\right) \qquad \text{(III.3)}$$

or
$$MLMM = A(1 - Bx),$$

where
$$A = \frac{\Delta M_e}{2}, \qquad B = \frac{1}{2 k_0}, \qquad x = \Delta k_{max}.$$

Eq. (III.3) describes a straight line passing through the points $\left(0, \frac{\Delta M_0}{2}\right)$ and $(2 k_0, 0)$ as shown in Fig. III.3.

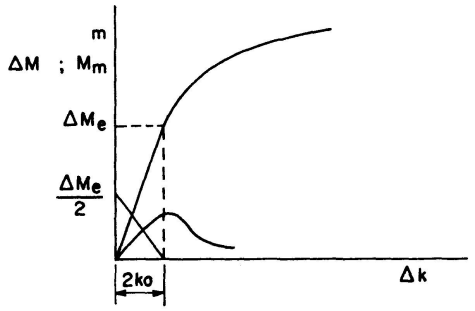

Fig. III.3. Limiting Linear Curvature.

The above discussion is applicable only to the case where ΔM_e is constant. However, as the specimen is cycled, the maximum linear moment range decreases due to the initiation of localized plastic strain. This will, in turn, cause the mean moment to decrease with cycling; therefore, the maximum linear mean moment will also decrease with cycling.

It does not seem unreasonable, then, to assume that the maximum linear mean moment locus will continue to be a straight line intersecting the curvature range axis at $2 k_{0n}$ and the moment axis at $\Delta M_{en}/2$ where k_{0n} and ΔM_{en} are similar to k_0 and ΔM_e but corresponding to cycle N. Therefore, this straight line locus will move parallel to itself with cycling.

Finally, what has been presented above can also be applied to the moment-strain relation with appropriate substitution of the curvature axis by the strain axis.

Appendix IV. Curve Fitting

The experimental data of the mean moment-extreme fiber relation will be fitted by a curve composed of three regions:

1. A straight line passing through the point of origin and having a slope equal to the product of the initial slope of the $M - \Delta\epsilon$ diagram and the mean strain ratio. The upper limit of this region is a point which has, as locus, a straight line as shown in Fig. IV.1 and explained in Appendix III.

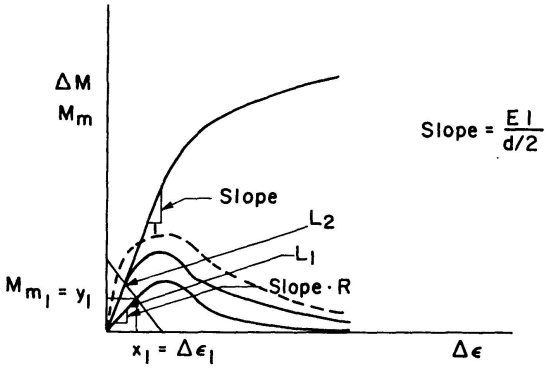

Fig. IV.1. Limiting Linear Mean Moment.

2. A third region where the value of the mean moment approaches zero asymptotically as the extreme fiber strain range reaches high values.
3. An intermediate region bridging the gap between the first and the last regions.

The first region has the form:

$$M_m = \Delta\epsilon \text{ slope } R,$$

where the slope is that of the initial $\Delta M - \Delta\epsilon$ curve $= \frac{EI}{d/2}$, and R is the mean strain ratio. Alternatively,

$$y = x \text{ slope } R, \tag{IV.1}$$

where

$$y = M_m,$$
$$x = \Delta\epsilon.$$

Hence

$$y' = \text{slope } R. \tag{IV.2}$$

The third region is fitted by a curve of the form:

$$M_m = \frac{\theta_1}{(\Delta\epsilon)^{\theta_2}}$$

or

$$y = \theta_1 x^{-\theta_2}, \tag{IV.3}$$

which is a hyperbola with two orthogonal asymptotes, the x and y axes. The two parameters, θ_1 and θ_2 are established using a library subroutine which performs a least squares curve fitting analysis on the input data. The data should include only those points that belong to the region under consideration. The input point with the minimum strain range value is considered common to both second and third regions. Since the fitted curve will not ordinarily pass through the data points, the transition point is considered a point on the fitted curve corresponding to the minimum input strain range value.

Having established the curve parameters and the transition point between the intermediate and third regions, the slope at this point can be calculated by differentiating Eq. (IV.3) with respect to x, i.e.,

$$y' = -\theta_2 \theta_1 x^{-\theta_2 - 1}. \tag{IV.4}$$

Similarly, there is another transition point between the first and intermediate regions. For the continuity of the entire curve, the intermediate range function is to satisfy four conditions, two from the function value at the two transition points and two from the slope at the same points. The third degree function given below has four parameters and can satisfy all four conditions:

$$y = a_0 + a_1 x + a_2 x^2 + a_3 x^3 \tag{IV.5}$$

and

$$y' = a_1 + 2a_2 x + 3a_3 x^2. \tag{IV.6}$$

A lower order function will not provide the desired continuity. Conversely, a higher order function will not be justified unless there are enough additional conditions (experimental data points in the intermediate region) and provided that the resulting curve is smooth and has single curvature.

To establish the first transition point, the intersection of lines L_1 and L_2 in Fig. IV.1 should be located as follows.

For L_1

$$y = x \,\text{slope}\, R. \tag{IV.1}$$

For L_2

$$y = \frac{\Delta M_e}{2} - \frac{x \,\text{slope}}{2}. \tag{IV.7}$$

The point of intersection will be given by

$$x \,\text{slope}\, R = \frac{\Delta M_e}{2} - \frac{x \,\text{slope}}{2}$$

or

$$x_1 = \frac{\Delta M_e}{\text{slope}} \quad \frac{1}{2\,(R+\frac{1}{2})}$$

and

$$y_1 = \frac{\Delta M_e}{\text{slope}} \frac{1}{2\,(R+\frac{1}{2})} \text{slope}\, R = \Delta M_e \frac{R}{2\,(R+\frac{1}{2})}. \tag{IV.8}$$

At x_1 and using Eqs. (IV.8) and (IV.5) obtain

$$a_0 + a_1 x_1 + a_2 x_1^2 + a_3 x_1^3 = \Delta M_e \frac{R}{2\,(R+\frac{1}{2})} \tag{IV.9}$$

and from Eqs. (IV.2) and (IV.6) obtain

$$a_1 + 2a_2 x_1 + 3a_3 x_1^2 = \text{slope}\, R. \tag{IV.10}$$

Similarly, at x_2, using Eqs. (IV.3) and (IV.5) obtain

$$a_0 + a_1 x_1 + a_2 x_1^2 + a_3 x_1^3 = \theta_1 x_1^{-\theta_2} \tag{IV.11}$$

and from Eqs. (IV.4) and (IV.6) obtain

$$a_1 + 2a_2 x_1 + 3a_3 x_1 = -\theta_1 \theta_3 x_2^{-\theta_2 - 1}. \tag{IV.12}$$

Hence, the four unknowns, a_0, a_1, a_2, a_3 can be established by solving Eqs. (IV.9), (IV.10), (IV.11), and (IV.12) simultaneously.

Appendix V. Deflection Calculations

Moment Range

For a load range applied at the tip of the cantilever, the moment range value at any section is equal to the load range times the (perpendicular) distance of the section from the load.

Curvature

The input moment range-extreme fibre strain range relation as shown in Eqs. (I) and (II) is for a rectangular section ($b_0 d_0$) whereas the beam, in general, has a section ($b_x d_x$) at any given location. The units of the left side of the Eqs. are moment units and those for the right side are strain units, i. e., in/in or dimensionless.

A moment range ΔM_x acting on a section ($b_x d_x$) is equivalent to a moment range $\Delta M_x (b_0 d_0^2)/(b_x d_x^2)$ acting on a section ($b_0 d_0$). The extreme fibre strain will be the same for both sections under the appropriate moments. The curvature range, Δk, is simply $(\Delta \epsilon_x)/(d_x/2)$.

Deflections

The curvature-area method will be used. The beam is divided into a suitable number of short segments for which the curvature diagram is assumed linear for each segment, Fig. V.1a, and is divided into two triangles as shown in Fig. V.1b. At the built end, the deflection and slope are zero. The deflection at the right end of each segment has, in general, three components as shown in Fig. V.2: the first is the deflection at the left end, the second is equal to the slope at that end times the segment length and the third is the tangential deviation of the right end with respect to a tangent at the left end. Thus,

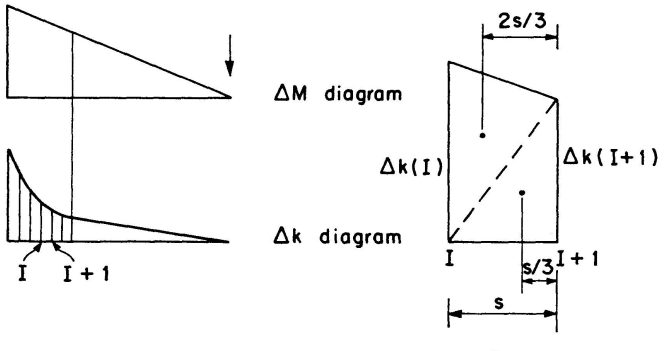

Fig. V.1. Curvature Distribution Diagram.

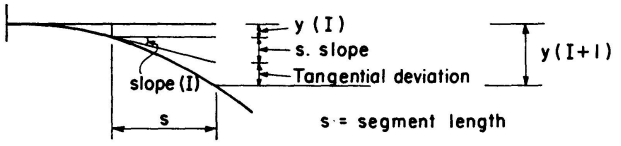

Fig. V.2. Slope and Deflection Calculations.

with the help of Figs. V.1b and V.2, the segment right end deflection and slope can be written as:

$$y(I+1) = y(I) + s\,\text{slope}(I) + \frac{\Delta k(I)\,s}{2}\frac{2}{3}s + \frac{\Delta k(I+1)\,s}{2}\frac{1}{3}s,$$

$$\text{slope}(I+1) = \text{slope}(I) + \frac{\Delta k(I)+\Delta k(I+1)}{2}s.$$

Starting at the extreme left end and moving to the right, discrete points on the "elastic curve" are established up to and including the cantilever tip.

References

1. Neal, B. G.: The Plastic Methods of Structural Analysis. Champan and Hall.
2. Neal, B. G., and Symunds, P. S.: Cyclic Loading of Portal Frames, Theory and Tests. Vol. 18, Pub. IABSE, Zurich, 1958.
3. Popov, E. P., and McCarthy, R. E.: Deflection Stability of Frames Under Repeated Loading. Journal of E. M. Division, ASCE, January, 1960.
4. Royles, R.: Fatigue of Ductile Structures in Reversed Bending. Ph. D. Thesis, Cambridge University, 1964.
5. Sherbourne, A. N., and Krishnasamy, S.: Moment-Curvature Models Under Reversed Cyclic Straining. Experimental Mechanics, Vol. 9, No. 1, 1969.
6. Topper, T. H.: Cyclic Plastic Loading of Mild Steel. Ph. D. Thesis, Cambridge University, 1962.
7. Krishnasamy, S., Sherbourne, A. N., and Khurana, K. K.: Deflection of Mild Steel Beams Under Symmetric Alternating Load. Presented at 1972 SESA Spring Meeting, Cleveland, Ohio, May 23–26.
8. Keshavan, S.: Some Studies on the Deformation and Fracture of Normalised Mild Steel under Cyclic Conditions. Ph. D. Thesis, University of Waterloo, 1967.
9. Jhansale, H. R., and Topper, T. H.: Equipment for Cyclic Deformation and Fatigue Studies in Pure Bending. Presented at 1970 SESA Fall Meeting, Boston, Mass., October 18–22.
10. Topper, T. H. et al.: Fatigue Testing Techniques for Conditions of Biaxial Stress, Stress Concentration, and Pure Bending. Journal of Materials, Vol. 6, No. 4, 1971.
11. Krishnasamy, S.: Beams Under Cyclis Alternating Deflection. Ph. D. Thesis, University of Waterloo, 1966.
12. Martin, J. F., Topper, T. H., and Sinclair, G. M.: Computer Based Simulation of Cyclic Stress-Strain Behaviour with Application to Fatigue. Materials Research and Standards, MTRSA, Vol. 11, No. 2, P. 23.

Summary

The response of simple mild steel cantilever beams to cyclic unequal deflections is investigated theoretically and experimentally following the derivation of appropriate moment-curvature models from strain control data involving the testing of specimens in pure bending. Different models are proposed

relating the curvature to moment range and mean moment; the models can accommodate hardening and softening of aggregations of fibres in the structural cross-section as well as mean moment relaxation with time. It is shown that behaviour is comprised of three stages involving elasticity, where mean load is proportional to load range, an intermediate state where the effects of mean deflection cannot be ignored and a terminal state of significant plastic deformation which is affected by geometry changes and secondary membrane action.

Résumé

On étudie théoriquement et expérimentalement le comportement de poutres-consoles simples en acier doux soumises à des déflexions cycliques inégales en suivant la courbe moment-courbure de modèles appropriés, déterminés à partir de contrôles des déformations effectués sur des spécimens soumis à la flexion pure. Différents modèles sont proposés mettant en relation la courbure avec les limites des moments ainsi qu'avec le moment principal; les modèles s'adaptent aux phénomènes de durcissement et d'adoucissement d'un ensemble de fibres dans la section ainsi qu'à la relaxation du moment principal dans le temps. On montre que le comportement peut se diviser en trois étapes; une étape élastique où la charge principale est proportionnelle aux limites entre lesquelles varient les charges, une étape intermédiaire où les effets de la déflexion principale ne peuvent être ignorés et une étape finale de déformations plastiques importantes qui est perturbée par des changements dans la géométrie et des effets secondaires de membrane.

Zusammenfassung

Die Reaktion von Kragarmen aus normalem Baustahl auf zyklische nicht konstante Verformung wird theoretisch und experimentell untersucht, unter Ableitung von Angaben über dehnungskontrollierte Versuche an entsprechenden Momenten-Krümmungsmodellen bei reiner Biegung. Verschiedene Modelle werden vorgeschlagen, bei denen die Krümmung zum Momentenbereich und zum Mittelmoment in Zusammenhang gebracht wird. Die Modelle können Verfestigung und Abnahme der Festigkeit der Fasern der Querschnitte wie auch Relaxation infolge des Mittelmomentes beinhalten. Es wird gezeigt, dass das Verhalten drei Stadien umfasst: Elastizität, wobei das Mittelmoment proportional zum Lastbereich ist, ein Zwischenstadium, wobei die Effekte der Verformung nicht mehr vernachlässigt werden dürfen, und ein Endstadium mit signifikanten plastischen Deformationen, welche Änderungen der Geometrie und sekundäre Membranwirkung nach sich ziehen.

Computer Analysis of Reinforced Concrete Sections Under Combined Bending and Compression

Analyse de sections en béton armé soumises à un effort normal avec flexion au moyen d'un calculateur électronique

Computer-Berechnung von Stahlbetonquerschnitten unter kombinierter Biegung und Druck

S. K. GHOSH
Adjunct Professor of Civil Engineering

M. Z. COHN
M. IABSE, Professor of Civil Engineering

University of Waterloo, Waterloo, Ontario, Canada

Introduction

The load-deformation characteristics of a reinforced concrete section subject to combined bending and axial load is significantly different from that of a section under pure flexure. The most critical difference may be the drastic reduction in sectional ductility which is caused by the presence of axial load.

Approximate load-moment interaction diagrams based on both the working stress [1] and ultimate strength [2] design theories are available for the design of square, rectangular and circular sections. However, the behaviour of reinforced concrete sections subject to combined bending and axial load in its generality, has been studied only to a very limited extent [3]–[8].

The purpose of this paper is to present some results of a comprehensive investigation into the subject [9]. In addition to providing a better understanding of inelastic action in reinforced concrete columns, these results suggest conditions under which inelastic analysis and design methods may be considered applicable to these members.

405 symmetrically reinforced rectangular concrete sections of identical dimensions, Fig. 1, but with varying *concrete strengths*, *steel grades*, and *reinforcement percentages*, and subject to varying *magnitudes of axial load* (Table 1), were analysed by using the sectional theory and the numerical method described in [8]. Reliable representations of the stress-strain properties of concrete and steel, proposed by SARGIN [10] and also described in [8], were

Table 1. Geometric and material properties of sections analysed

P/P_u =0.0	P/P_u =0.1	P/P_u =0.2	P/P_u =0.3	P/P_u =0.4	P/P_u =0.45	P/P_u =0.5	P/P_u =0.6	P/P_u =0.8	f'_c ksi	f'_c ksi	$p=p'$ %
Section no.											
1	46	91	136	181	226	271	316	361			0.5
2	47	92	137	182	227	272	317	362			1.0
3	48	93	138	183	228	273	318	363		45	1.5
4	49	94	139	184	229	274	319	364			2.0
5	50	95	140	185	230	275	320	365			3.0
6	51	96	141	186	231	276	321	366			0.5
7	52	97	142	187	232	277	322	367			1.0
8	53	98	143	188	233	278	323	368	3	60	1.5
9	54	99	144	189	234	279	324	369			2.0
10	55	100	145	190	235	280	325	370			3.0
11	56	101	146	191	236	281	326	371			0.5
12	57	102	147	192	237	282	327	372			1.0
13	58	103	148	193	238	283	328	373		75	1.5
14	59	104	149	194	239	284	329	374			2.0
15	60	105	150	195	240	285	330	375			3.0
16	61	106	151	196	241	286	331	376			0.5
17	62	107	152	197	242	287	332	377			1.0
18	63	108	153	198	243	288	333	378		45	1.5
19	64	109	154	199	244	289	334	379			2.0
20	65	110	155	200	245	290	335	380			3.0
21	66	111	156	201	246	291	336	381			0.5
22	67	112	157	202	247	292	337	382			1.0
23	68	113	158	203	248	293	338	383	4	40	1.5
24	69	114	159	204	249	294	339	384			2.0
25	70	115	160	205	250	295	340	385			3.0
26	71	116	161	206	251	296	341	386			0.5
27	72	117	162	207	252	297	342	387			1.0
28	73	118	163	208	253	298	343	388		75	1.5
29	74	119	164	209	254	299	344	389			2.0
30	75	120	165	210	255	300	345	390			3.0
31	76	121	166	211	256	301	346	391			0.5
32	77	122	167	212	257	302	347	392			1.0
33	78	123	168	213	258	303	348	393		45	1.5
34	79	124	169	214	259	304	349	394			2.0
35	80	125	170	215	260	305	350	395			3.0
36	81	126	171	216	261	306	351	396			0.5
37	82	127	172	217	262	307	352	397			1.0
38	83	128	173	218	263	308	353	398	5	60	1.5
39	84	129	174	219	264	309	354	399			2.0
40	85	130	175	220	265	310	355	400			3.0
41	86	131	176	221	266	311	356	401			0.5
42	87	132	177	222	267	312	357	402			1.0
43	88	133	178	223	268	313	358	403		75	1.5
44	89	134	179	224	269	314	359	404			2.0
45	90	135	180	225	270	315	360	405			3.0

utilized in these analyses. The results are presented in the form of moment-curvature, axial load-ultimate moment, axial load-ultimate curvature, and ductility factor-steel percentage diagrams under a broad range of combinations of the variables (italicized above).

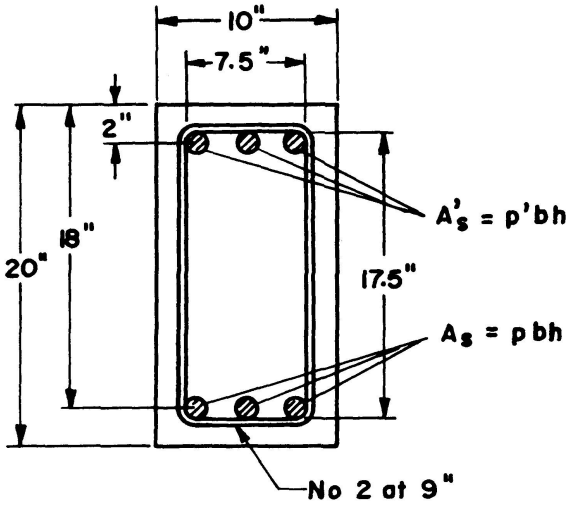

Fig. 1. Typical section used in analysis.

Effects of Axial Load on Moment-Curvature Diagrams

The M-ϕ diagrams of the sections analyzed are presented in Figs. 2 to 10. Each of these figures corresponds to a particular combination of concrete strength and steel grade and contains the diagrams corresponding to five different sectional reinforcement percentages. The curves in each diagram illustrate the effects of varying levels of axial load on nine identical sections.

The numerical values of moment and curvature at the stage of "yielding" and "sectional failure (ultimate)", associated with the M-ϕ diagrams in Figs. 2 to 10, the ratios of ultimate to yield moments, and of the corresponding curvatures, are important for subsequent discussion in this paper. It should be noted that, as in [8], the "yield" stage is defined as that at which the tension reinforcement in a section reaches its yield point stress and the "ultimate" stage is that at which the section reaches its moment carrying capacity (for a given axial load). This ultimate stage definition is different from the conventional one, according to which a section is assumed to have failed when the concrete strain in its extreme compression fibre reaches an arbitrary limiting value [3], [4], [5].

Tension, balanced and compression failures of a section are characterized by the yielding of tension reinforcement prior to, simultaneously with, and subsequent to the attainment of sectional moment carrying capacity, respectively. Sections subject to axial loading of magnitude below a certain level (corresponding to balanced failure) fail in tension. Figs. 2 to 10 indicate that the yield moments and curvatures of such sections increase with increasing levels of the axial loads. Both M_y and ϕ_y (corresponding to any given level of axial load) also increase with increasing steel percentages of the sections and with increasing reinforcement strengths. M_y increases somewhat, but ϕ_y remains unchanged, or decreases slightly, with increasing concrete strengths.

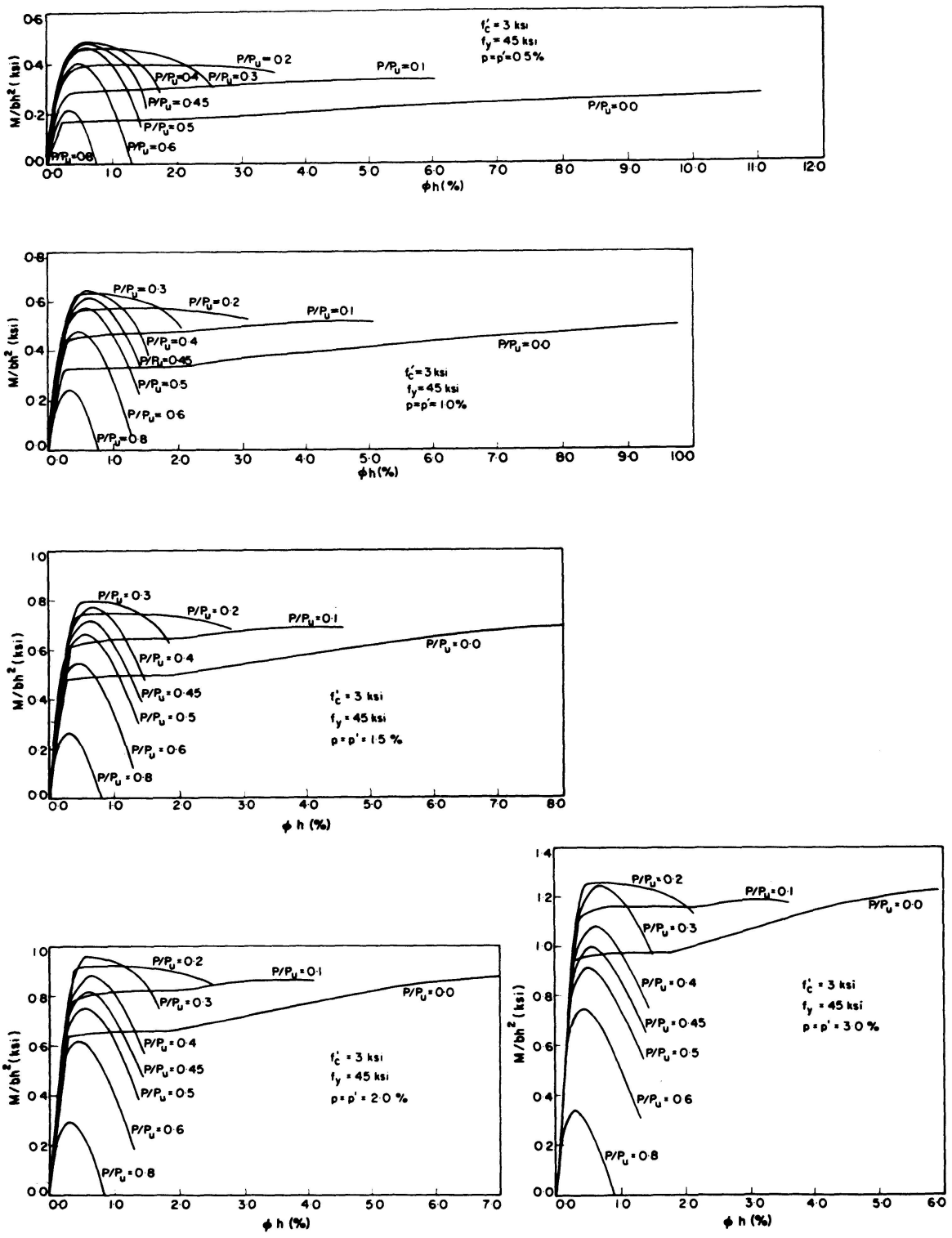

Fig. 2. M-ϕ diagrams, as affected by axial loads, for various concrete and steel grades and amounts of reinforcement ($f'_c = 3$ ksi, $f_y = 45$ ksi).

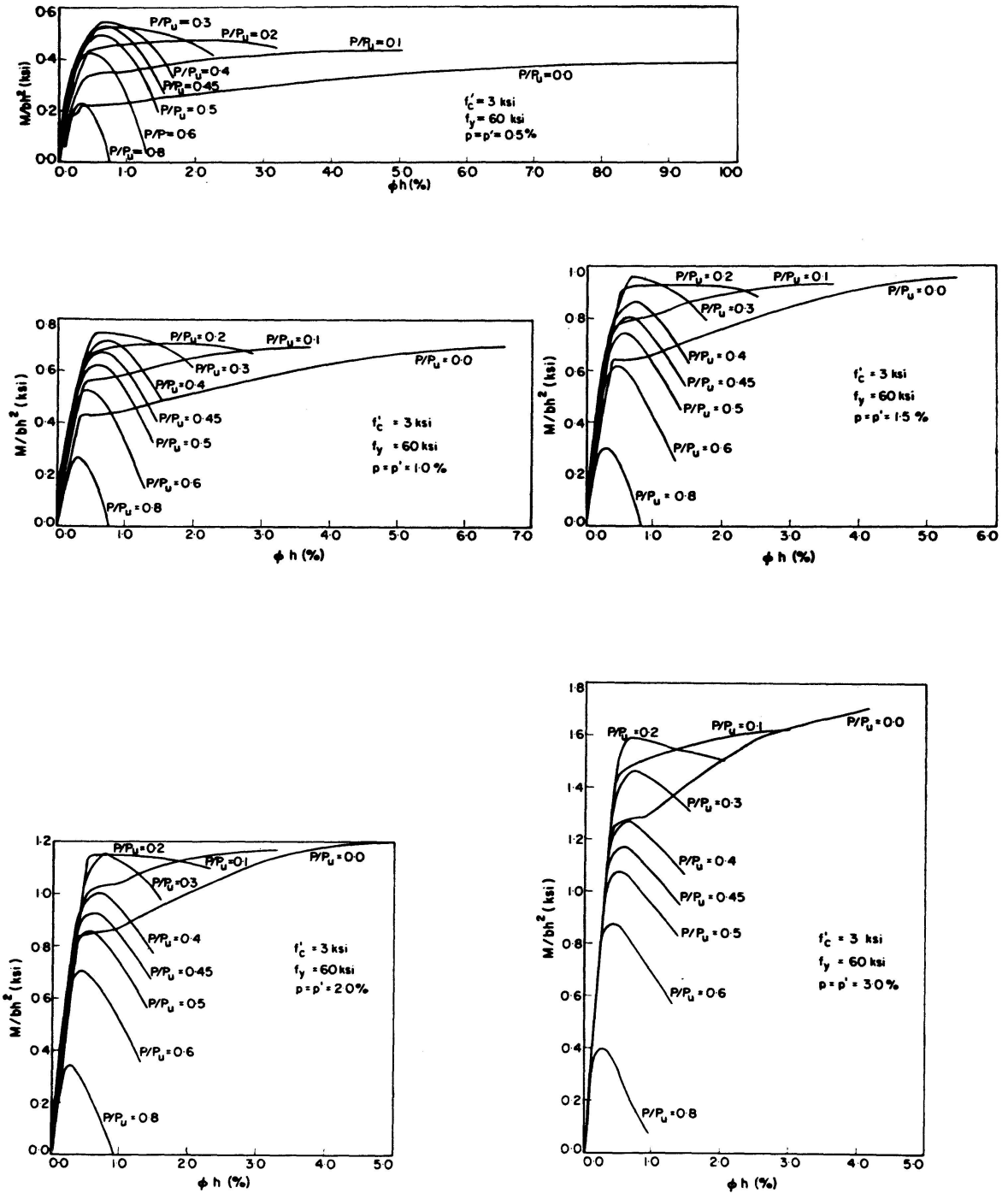

Fig. 3. M-ϕ diagrams, as affected by axial loads, for various concrete and steel grades and amounts of reinforcement ($f'_c = 3$ ksi, $f_y = 60$ ksi).

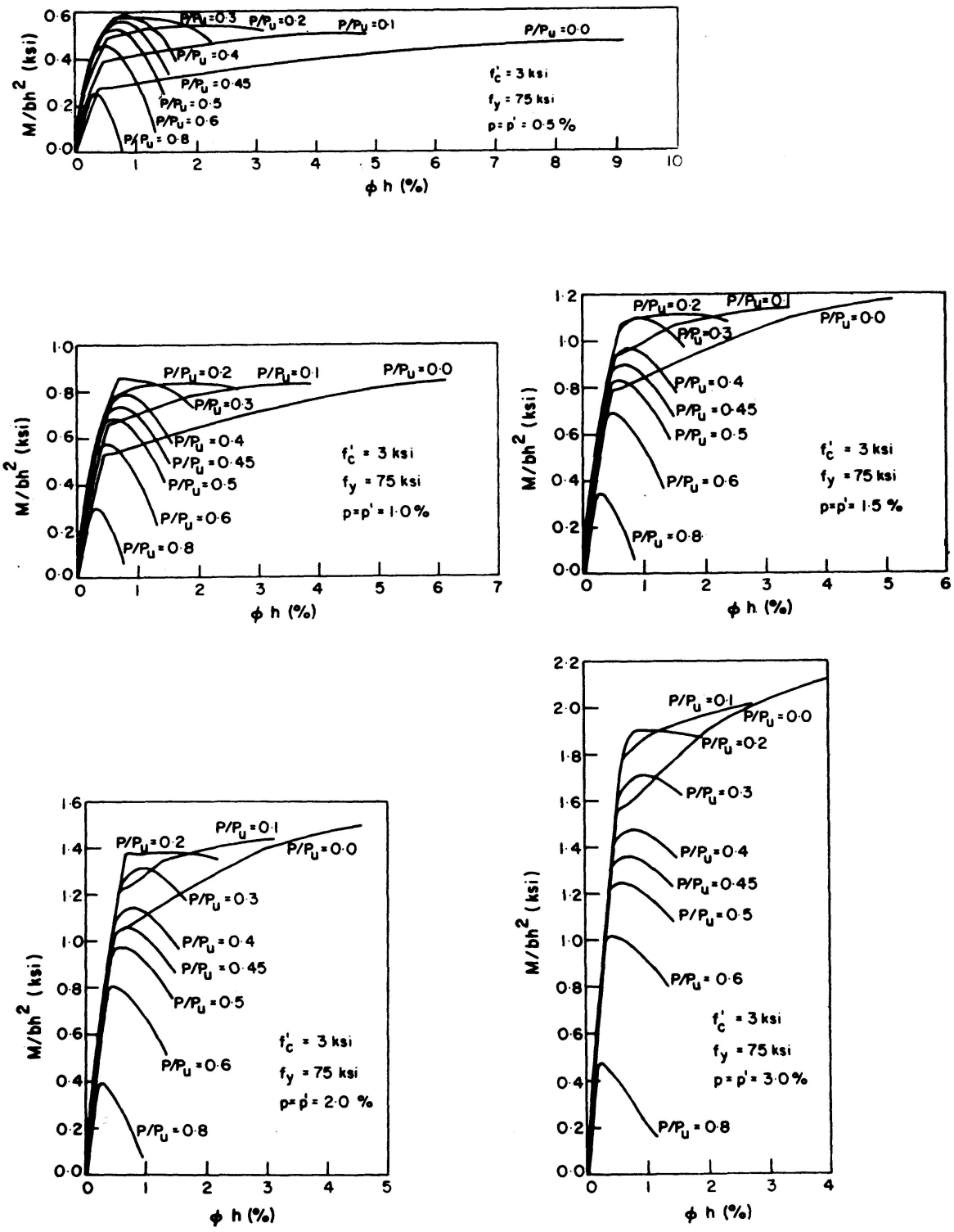

Fig. 4. M-ϕ diagrams, as affected by axial loads, for various concrete and steel grades and amounts of reinforcement ($f_c' = 3$ ksi, $f_y = 75$ ksi).

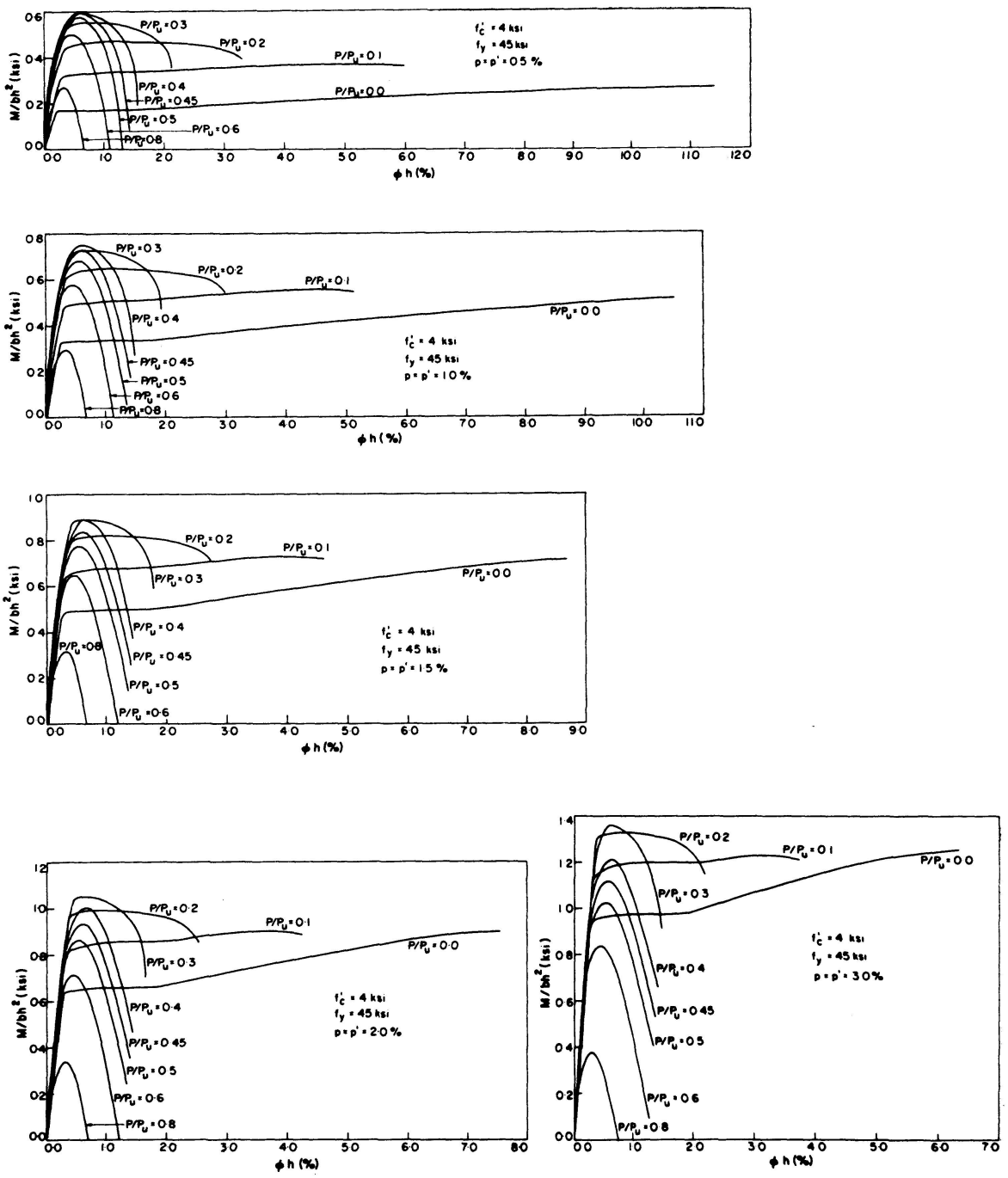

Fig. 5. M-ϕ diagrams, as affected by axial loads, for various concrete and steel grades and amounts of reinforcement ($f'_c = 4$ ksi, $f_y = 45$ ksi).

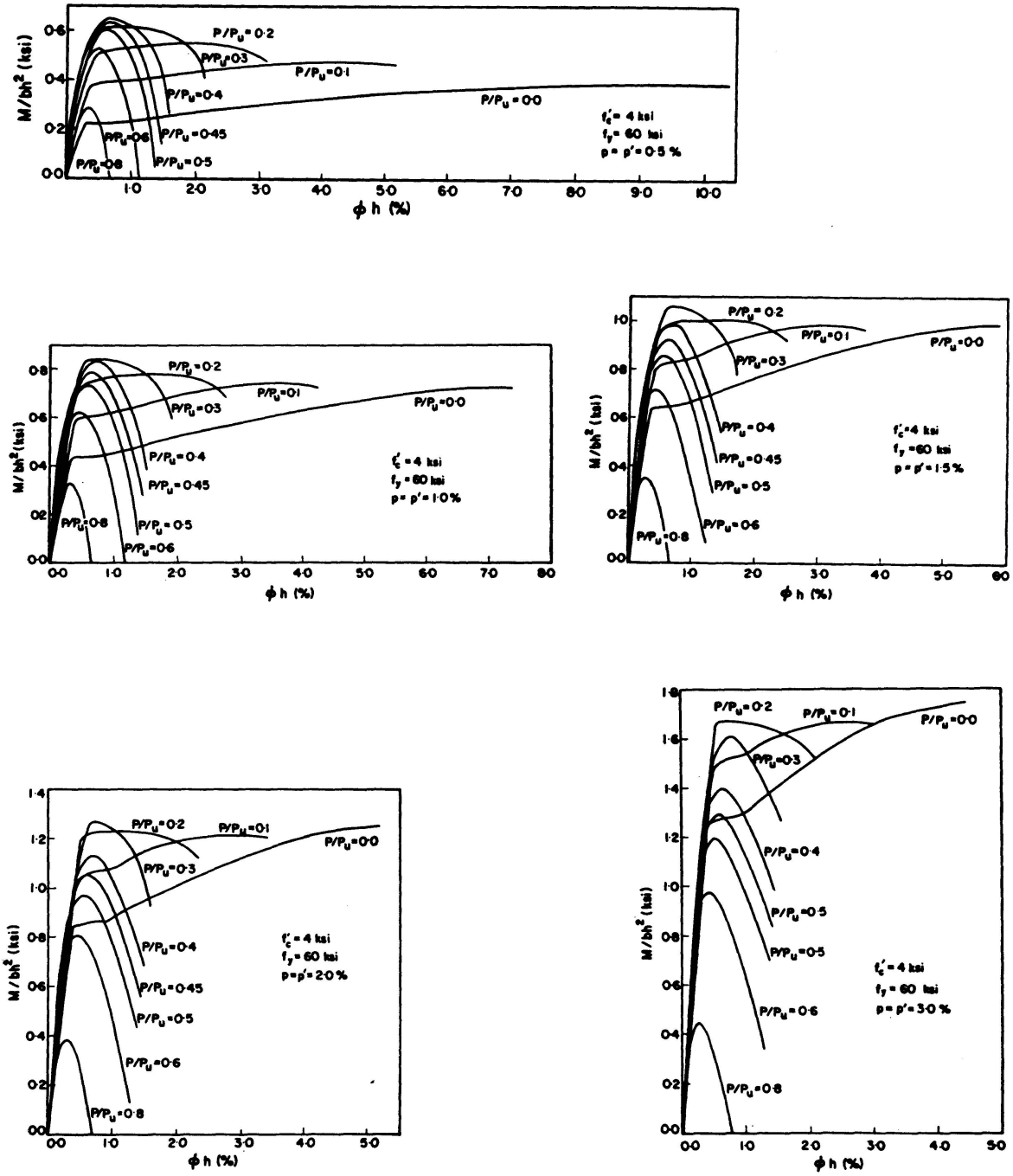

Fig. 6. M-ϕ diagrams, as affected by axial loads, for various concrete and steel grades and amounts of reinforcement ($f'_c = 4$ ksi, $f_y = 60$ ksi).

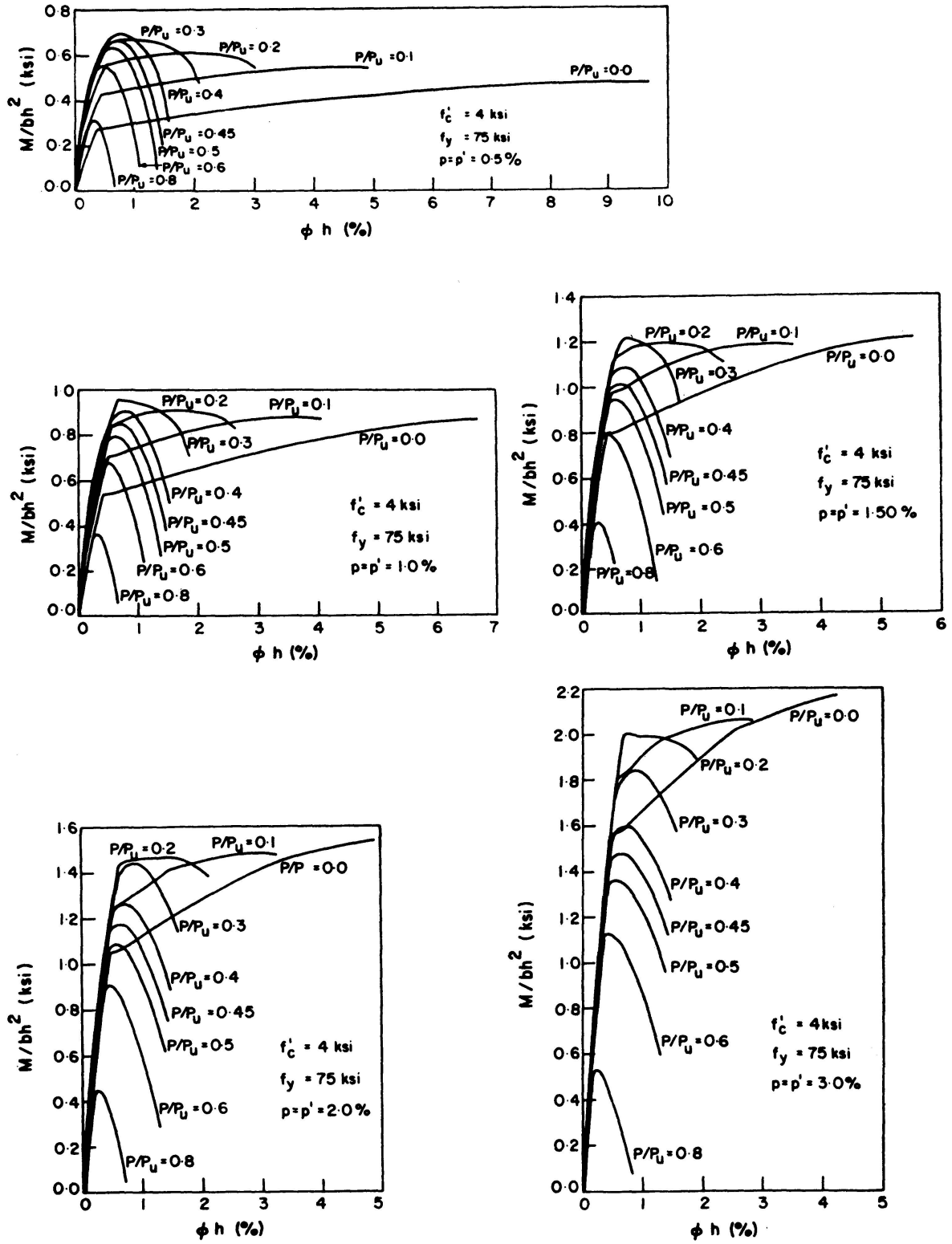

Fig. 7. M-ϕ diagrams, as affected by axial loads, for various concrete and steel grades and amounts of reinforcement ($f'_c = 4$ ksi, $f_y = 75$ ksi).

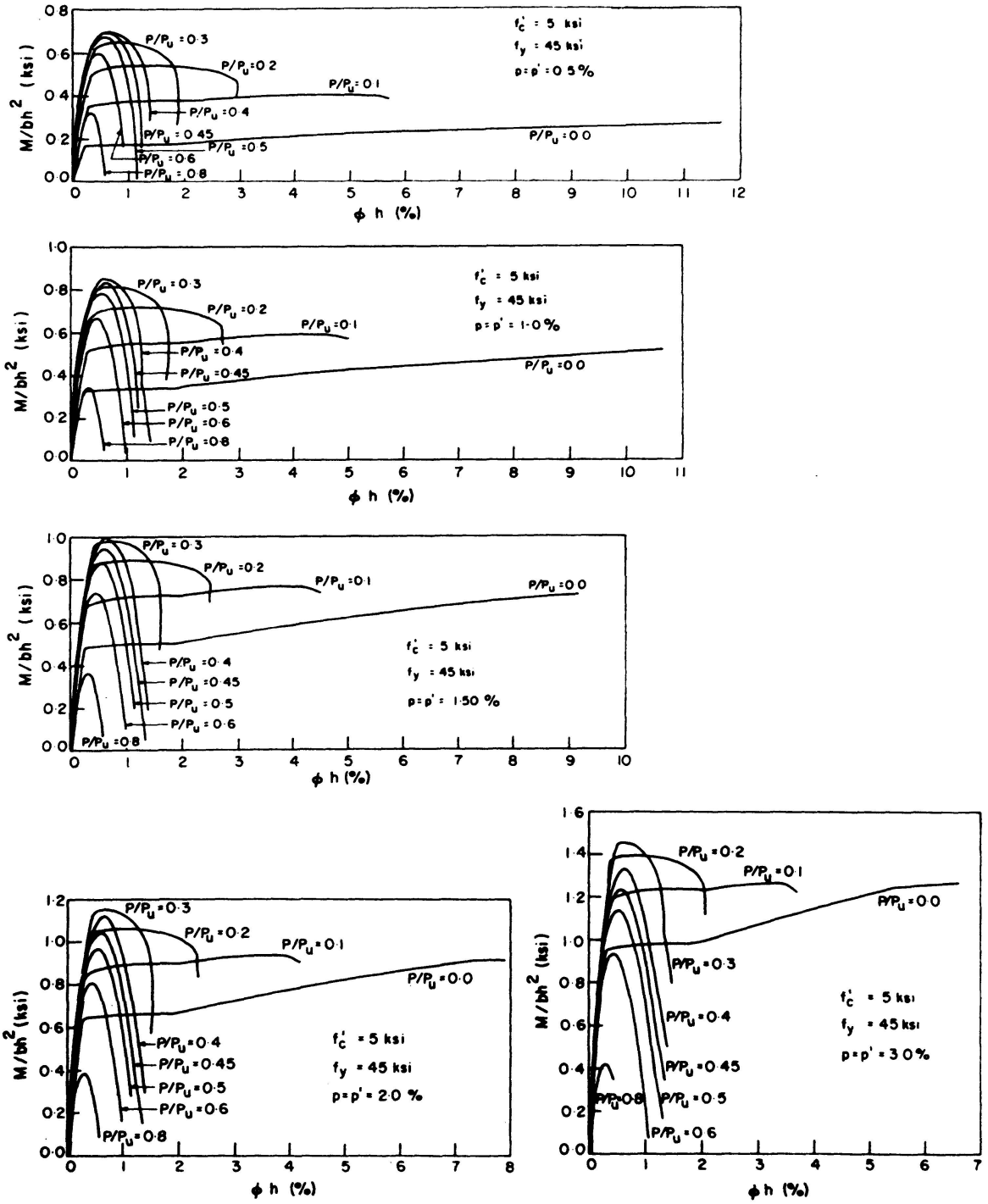

Fig. 8. M-ϕ diagrams, as affected by axial loads, for various concrete and steel grades and amounts of reinforcement ($f_c' = 5$ ksi, $f_y = 45$ ksi).

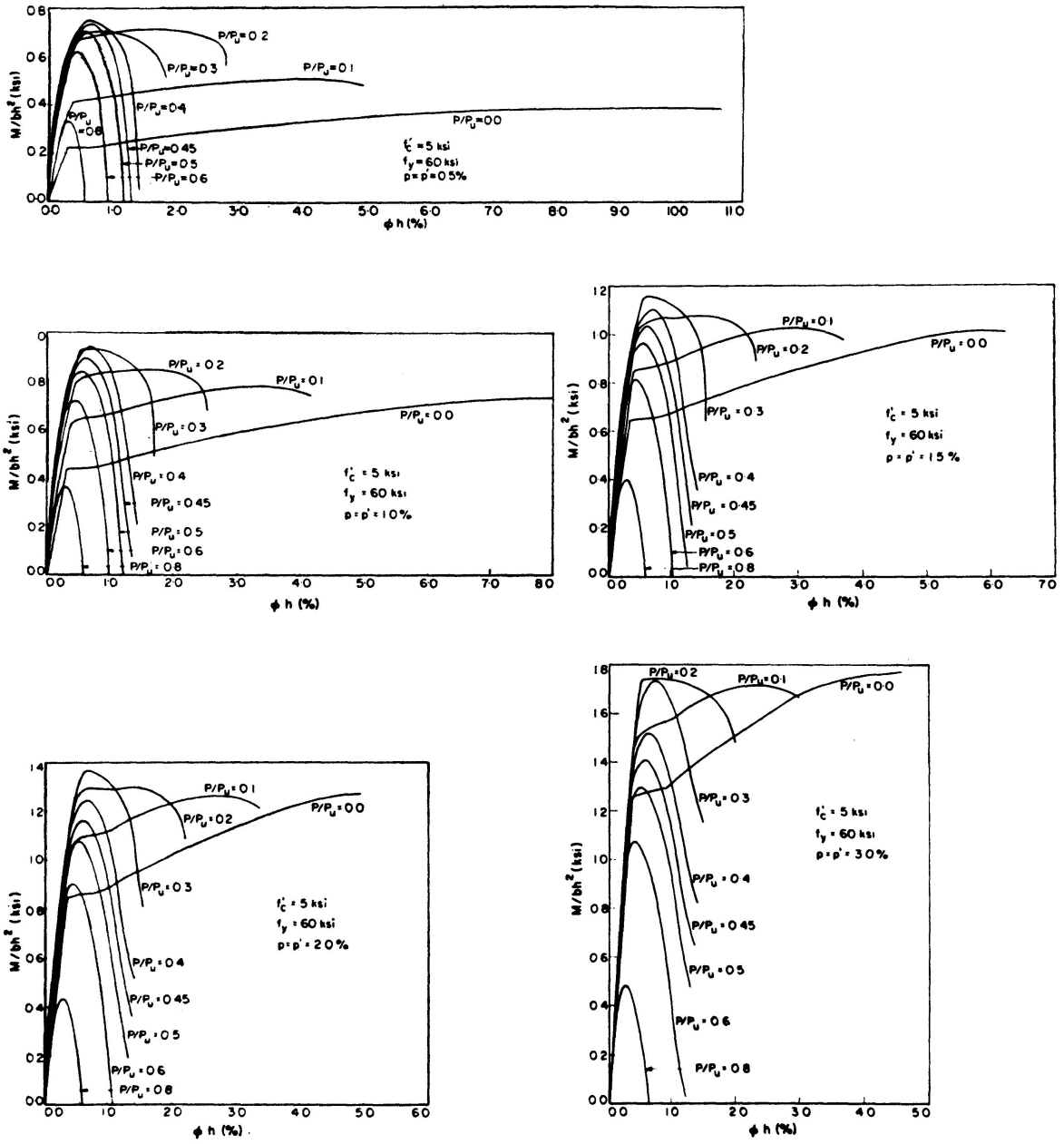

Fig. 9. M-ϕ diagrams, as affected by axial loads, for various concrete and steel grades and amounts of reinforcement ($f'_c = 5$ ksi, $f_y = 60$ ksi).

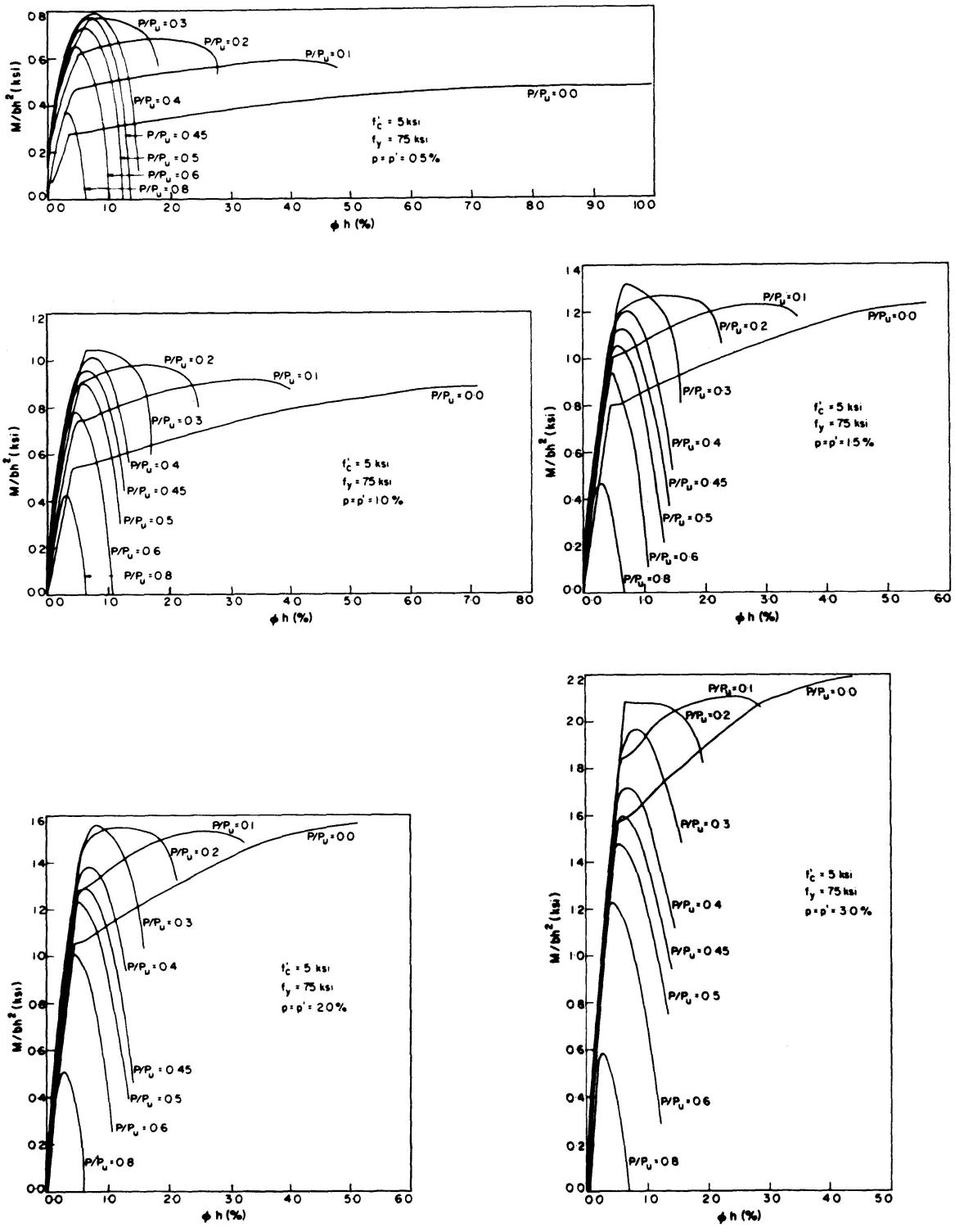

Fig. 10. M-ϕ diagrams, as affected by axial loads, for various concrete and steel grades and amounts of reinforcement ($f'_c = 5$ ksi, $f_y = 75$ ksi).

The effects of axial loading, of concrete and steel grades and amounts of reinforcement on M_u, ϕ_u, ϕ_u/ϕ_y and M_u/M_y are discussed in the next four sections.

Load-Moment Interaction Diagrams

The $P/P_u - M_u/b\,h^2$ interaction diagrams of Fig. 11 were plotted from the relevant data presented in Figs. 2 to 10. Fig. 11 consists of the diagrams corresponding to nine combinations of concrete and steel grades. Each of these diagrams contains the curves (in full lines) corresponding to five different sectional reinforcement percentages.

The break in each interaction diagram corresponds to the balanced failure conditions, above and below which are the compression and tension failure zones, respectively.

The shape of the interaction diagrams in the region corresponding to tension failure should be noted. This shape is a direct consequence of the ultimate stage definition adopted in this study. The interaction diagrams drawn in full lines change to the more familiarly shaped ones, indicated by dotted lines, if the ultimate stage is defined by the extreme compression fibre strain reaching a value of 0.3%.

From Fig. 11, it is apparent that the magnitude of the balanced load decreases with increasing steel percentages. This is contrary to an earlier finding by PFRANG et al. [4], who had concluded that the above magnitude was independent of reinforcement content. Fig. 11 also indicates that the balanced load decreases somewhat with increasing reinforcement strengths and decreases with increasing concrete strengths.

Fig. 11 shows that sectional moment capacity, corresponding to any given level of axial load, increases with increasing reinforcement percentage and steel and concrete strengths. If sectional failure is defined in a conventional manner (by a limiting compression concrete strain), the moment capacity of a section increases with increasing levels of axial load as long as failure is governed by tension, and thereafter decreases as the axial loads are further increased. The trend in the tension failure region changes if sectional failure is defined as in the present study, with moment carrying capacities under pure bending being larger than those under bending combined with low axial loads.

Axial Load-Ultimate Curvature Diagrams

The $P/P_u - \phi_u h$ diagrams in Fig. 12 were also plotted from the data presented in Figs. 2 to 10. To the left of each diagram (corresponding to a particular combination of steel and concrete grades) are the curves drawn according to the conventional definition of failure, and to the right are those plotted

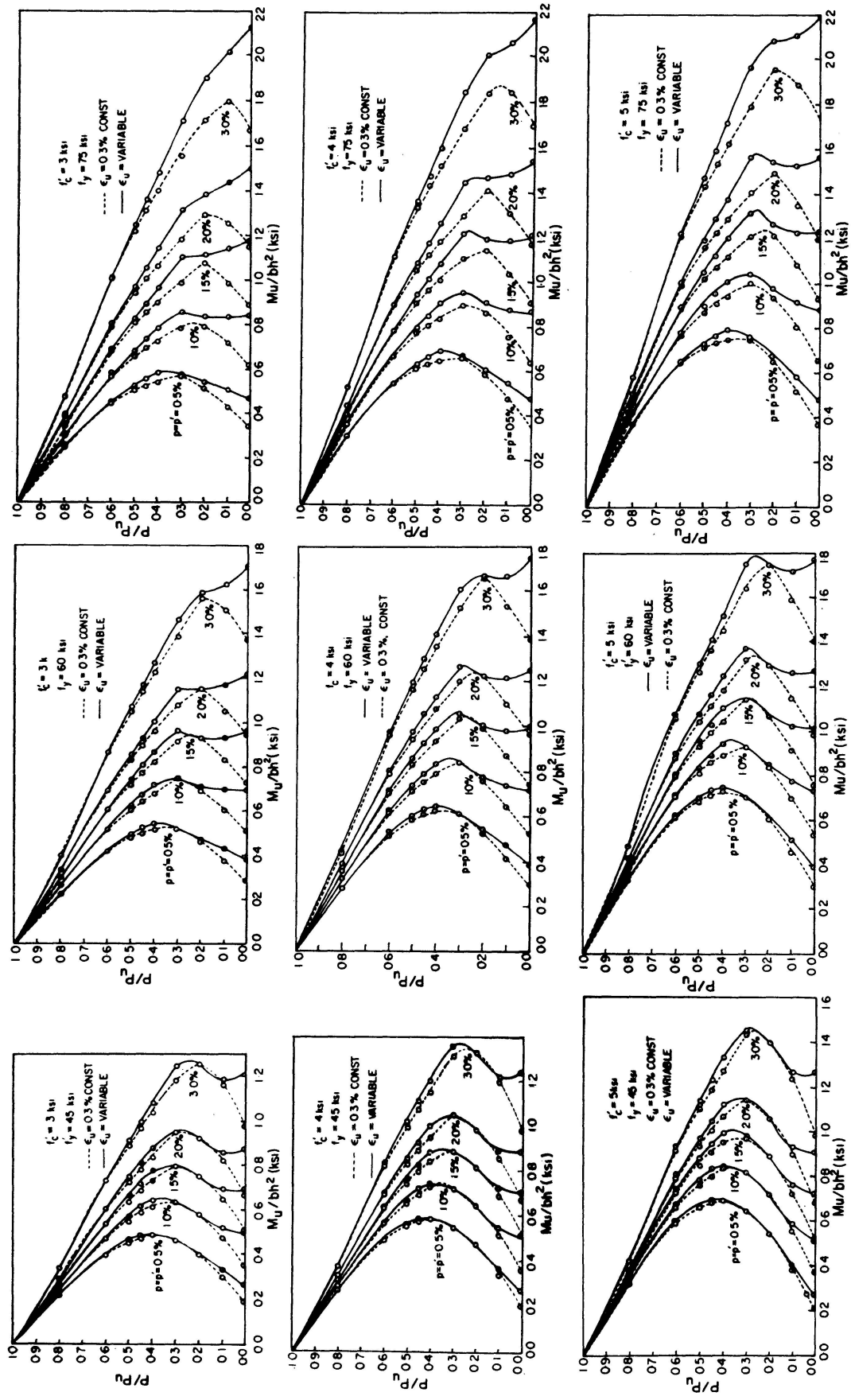

Fig. 11. Axial load-moment interaction diagrams for various concrete and steel grades, and amounts of reinforcement.

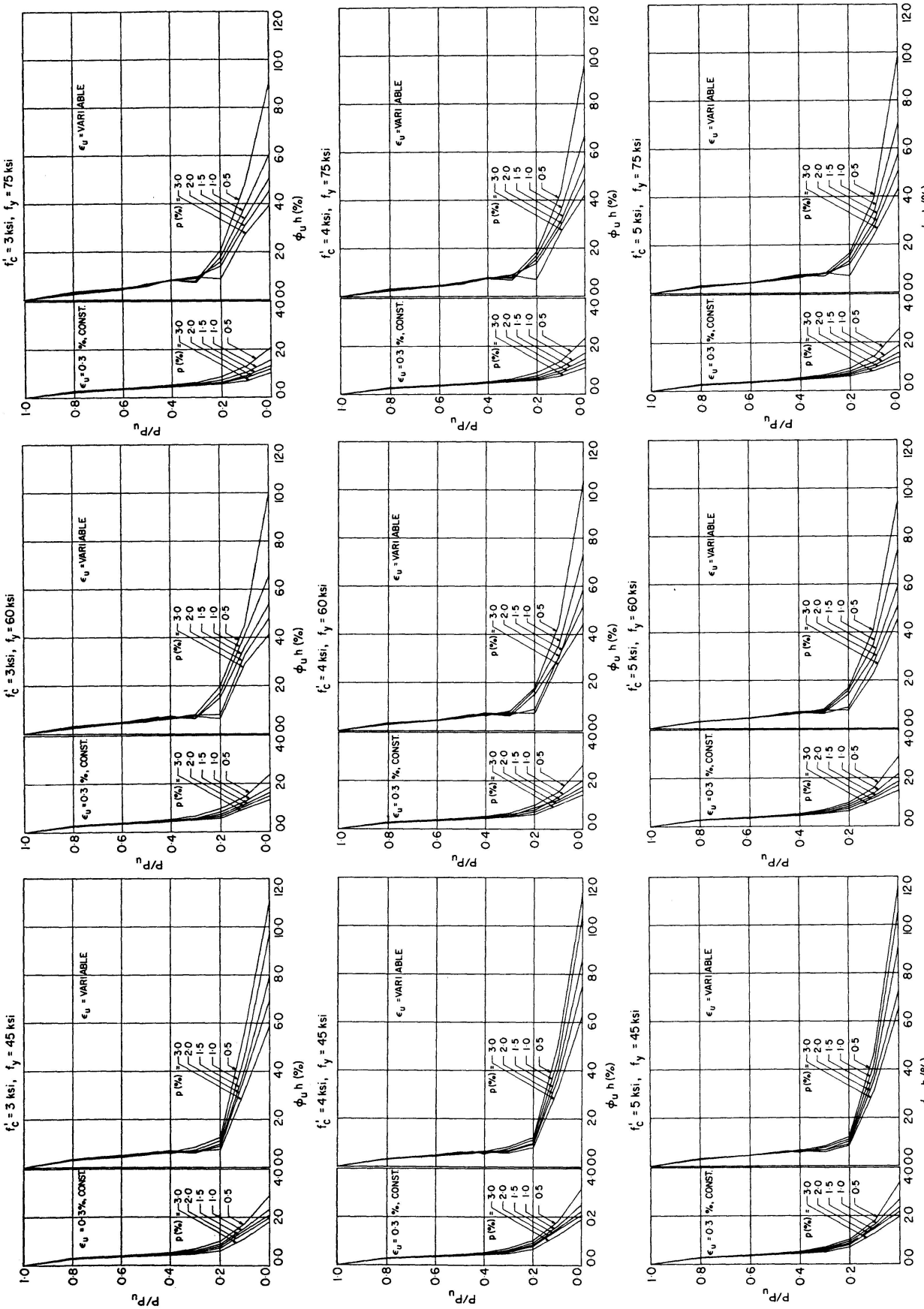

Fig. 12. Axial load-ultimate curvature diagrams for various concrete and steel grades, and amounts of reinforcement.

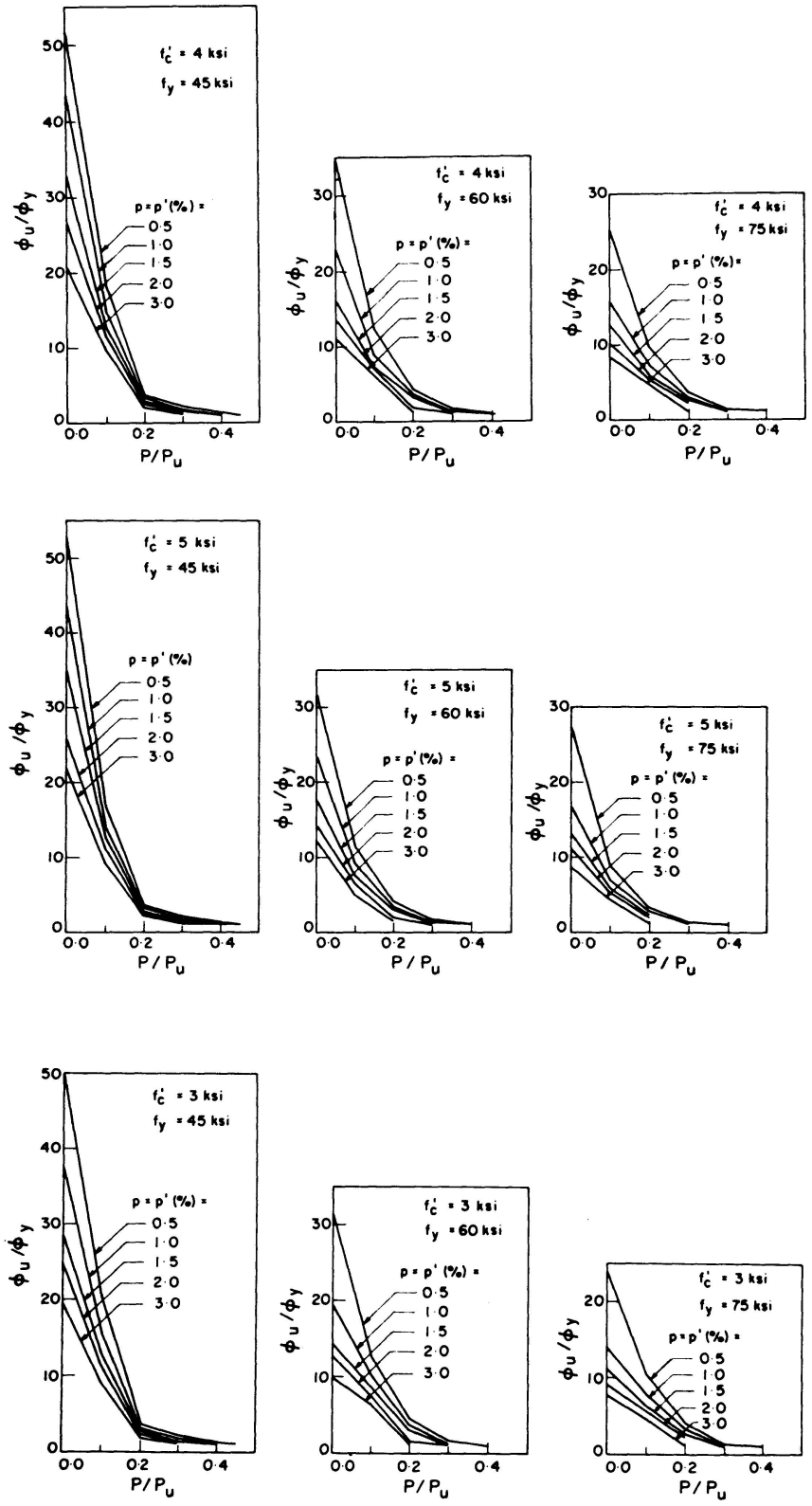

Fig. 13. Effects of axial loads on the ductility of reinforced concrete sections.

according to the failure definition of the present study (each curve corresponding to a particular sectional steel percentage). The conventional definition of failure, which provides a slightly conservative estimate of the moment capacity of a section (Fig. 11), obviously leads to a gross underestimation of its deformability. It is evident that the ultimate curvature decreases steadily with increasing levels of axial load, when failure is defined by a limiting strain. While this trend is generally true in case of the definition of failure adopted herein, some irregularities in the trend are observed around the balanced points. Ultimate curvatures (conforming to both definitions) are found to be extremely small in the regions of compression failure.

Fig. 12 shows that the ultimate curvature corresponding to any given axial load level decreases with increasing steel percentages of sections and with reinforcement strengths, and increases slightly with increasing concrete strengths.

Effects of Axial Load on Sectional Ductility

The ductility factor, defined as the ratio of ultimate to yield curvatures, ϕ_u/ϕ_y, is a satisfactory index of the ductility of reinforced concrete sections subject to pure and combined bending [8]. From the numerical data presented in Figs. 2 to 10, ductility ratio versus axial load curves corresponding to various reinforcement percentages are plotted in Fig. 13 for the nine combinations of steel and concrete grades considered. This figure and the tables indicate that as long as failure is governed by tension, a section is capable of mobilizing a certain amount of ductility, although this decreases drastically as the axial load on the section approaches the level corresponding to balanced failure. Fig. 13 also indicates that for the low levels of axial load usually carried by flexural members in reinforced concrete frames (not exceeding 10–15% of the axial load capacity), fairly high amounts of sectional ductility are always available.

It was observed in Ref. [8] that sectional ductility decreases with increasing steel percentages, increasing reinforcement strengths, and decreasing concrete strengths, a trend which is evident from Fig. 13.

Discussion of Results

a) Definition of Sectional Failure in Deformation Analysis

The ductility factor, defined as the ratio of ultimate to yield curvatures, ϕ_u/ϕ_y, is widely accepted as an index of the ductility of reinforced concrete sections subject predominantly to flexural action under static loading. However, while the yield curvature, ϕ_y, is generally defined as the curvature at which the tension steel reaches its yield point stress, several definitions of the

ultimate stage or the failure of a section, to which the curvature ϕ_u corresponds, are in use.

In most current codes of practice, ϕ_u is defined as the curvature at which a conventional limiting value of the concrete strain (corresponding presumably to the onset of crushing) is attained at the extreme compression fibre ($\epsilon_u = 0.3\%$ according to the ACI Code [11]). In this study ϕ_u has been defined as the curvature corresponding to the attainment of sectional moment capacity. A third definition of ϕ_u appears to be gaining increasing acceptance. "Many sections have considerable capacity for plastic rotation beyond the peak of the moment-curvature curve. It would seem reasonable to recognize some of this available deformation after maximum moment and to define ϕ_u as the curvature when the moment is reduced by some arbitrary amount after the maximum moment" [7]. ϕ_u was defined as the curvature corresponding to $0.9 M_u$ and M_y along the descending branch of the M-ϕ diagram in Refs. [7] and [12], respectively. The three definitions of ϕ_u discussed above are illustrated schematically in Fig. 14.

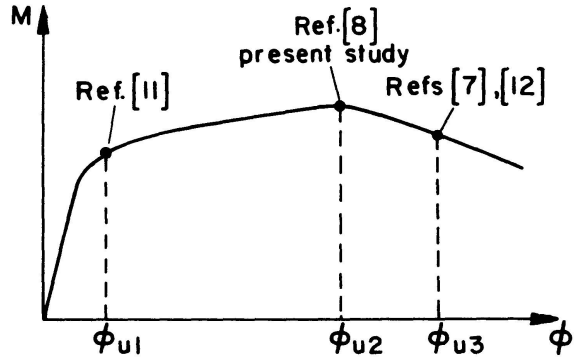

Fig. 14. Various definitions of ultimate curvature.

It has been noted earlier that the conventional definition of failure grossly underestimates the deformability of a section. Fig. 12 illustrates that the ratio ϕ_{u2}/ϕ_{u1} may be as large as 4–5 for sections failing in tension. A second disadvantage of this failure definition is that the limiting value of concrete strain at the extreme compression fibre has to be either arbitrarily fixed, or based on visual observations of the onset of crushing in experiments. The definitions of ϕ_u adopted in Refs. [7], [12] possibly account for the deformation capacity of a section to a fuller extent than the present study (depending upon sectional properties, ϕ_{u3} may be considerably larger than ϕ_{u2}). However, these definitions also are arbitrary. The failure of a section, as defined in the present study, corresponds to a mathematically well defined point, i.e. the peak of the M-ϕ diagram. The choice of this functional viewpoint is logical, noting that the primary purpose of a structural member is to carry loads. This definition is unlikely to prove unduly conservative in estimating the deformability of sections with current geometric and material properties. It is therefore recommended that, at least for the purposes of deformation analysis, sectional

failure be defined as the stage corresponding to the attainment of the maximum flexural capacity.

b) Definition of Sectional Failure in Strength Analysis

Fig. 11 shows that the strength of a section, unlike its deformability, is relatively insensitive to the definition of sectional failure. The dotted *P-M* interaction diagrams in Fig. 11, corresponding to the conventional definition of sectional failure (ultimate stage defined by $\epsilon_u = 0.3\%$), provide safe and only slightly conservative lower bounds on the moment capacities of sections subject to given levels of axial load.

It should be observed that the rather unusual shape of the tension failure regions of the *P-M* interaction diagrams for the definition of failure adopted in the present study (Fig. 11) was first noted by the authors [8]. The significance and implications of this shape are yet to be fully understood.

In view of the above, it is recommended that, pending further investigation, the conventional definition of failure be retained for strength analysis. It is hoped that future research will clarify all aspects of the functional definition of failure, leading to its wider acceptance. The arbitrariness of the conventional definition is not as much of a disadvantage in strength as in deformation analysis. The numerical value adopted for ϵ_u would normally have a relatively minor effect on sectional strength.

c) Estimate of Ductility Requirements in Design

Ductility governs the rotation capacity of hinging zones and the redistribution of moments in a structure; the adaptability of structures to foundation settlements and volume changes; and the energy absorption capacity of structures subject to dynamic (wind, earthquake, blast) loads. Ductility safeguards a structure against sudden overloads, impact and load reversals. For this reason it is necessary and desirable that structures be capable of mobilizing a reasonable level of ductility whenever actions such as those mentioned above are foreseen [8]. However, there have been very few attempts at determining the amount of ductility that may be required in structures designed to meet specific functional requirements. These limited attempts have largely been confined to the area of aseismic design.

A measure of the ductility of structures with regard to seismic loading is the displacement ductility factor defined as Δ_u/Δ_y, where Δ_u, Δ_y are the lateral deflections at the ultimate stage and at first yield, respectively. The commentary on the code of the Structural Engineers Association of California [13] indicates that the displacement ductility factor required in aseismic design may range from three to five. It is important to recognize the difference between the ratio Δ_u/Δ_y, and the index of sectional ductility, ϕ_u/ϕ_y. "Once

yielding has commenced in a frame the deformations concentrate at the plastic hinge positions and hence when a frame is deflected laterally in the post-elastic range the required ϕ_u/ϕ_y ratio at the plastic hinges is greater than the Δ_u/Δ_y ratio'' [7]. The following suggestion was offered in Ref. [7] *without* a rigorous basis: "Columns capable of reaching a curvature ductility factor ϕ_u/ϕ_y of at least 15, with ϕ_u defined as the curvature when the moment has reduced to 80–90 percent of the maximum moment, would appear to be a reasonably practical approach to column design for seismic resistance.'' It is obvious that the required ϕ_u/ϕ_y would be less than 15 if ϕ_u is defined as the curvature corresponding to M_u, rather than to $0.8\text{–}0.9\,M_u$.

A more precise estimate of the sectional ductility required in structures would require a considerable amount of further research, and is beyond the scope of the present study. The emphasis here is on determining the amounts of ductility that may be available in column sections with varying concrete and steel grades and amounts of reinforcement.

d) Amounts of Available Ductility

ACI 318-71 [11] requires that the column ends in ductile moment-resisting frames be provided with special transverse reinforcement when the column load exceeds 40% of the load corresponding to balanced failure. Therefore, $0.4\,P_b$ can be considered as the highest axial load to which a column section without any special lateral reinforcement may be subjected.

Table 2. Ratios of balanced to ultimate axial loads for various concrete and steel grades and reinforcement percentages

	f'_c = 3 ksi			f'_c = 4 ksi			f'_c = 5 ksi		
	f_y = 45 ksi	60 ksi	75 ksi	f_y = 45 ksi	60 ksi	75 ksi	f_y = 45 ksi	60 ksi	75 ksi
$p=p'=0.5\%$	0.40	0.35	0.30	0.40	0.37	0.32	0.40	0.40	0.35
$p=p'=1.0\%$	0.32	0.30	0.24	0.35	0.29	0.30	0.36	0.30	0.30
$p=p'=1.5\%$	0.30	0.25	0.20	0.30	0.27	0.20	0.33	0.28	0.24
$p=p'=2.0\%$	0.29	0.20	0.20	0.30	0.24	0.20	0.30	0.26	0.20
$p=p'=3.0\%$	0.20	0.20	0.10	0.24	0.20	0.15	0.27	0.20	0.20

The ratios P_b/P_u for the sections considered in the present investigation are listed in Table 2. These ratios were determined from the dotted interaction diagrams in Fig. 11, which correspond to sectional failure defined by $\epsilon_u = 0.3\%$. The amounts of ductility available in sections with varying combinations of the variables studied and subject to $P = 0.4\,P_b$ were determined from Fig. 13. Table 2 was used to convert the fixed P/P_b ratio of 0.4 to the appropriate P/P_u ratios. The results of this analysis are presented in Table 3. Table 3

Table 3. Ductility available in sections with varying concrete and steel grades and reinforcement percentages, and subject to 40% of balanced axial load

	f'_c = 3 ksi			f'_c = 4 ksi			f'_c = 5 ksi		
	f_y = 45 ksi	60 ksi	75 ksi	f_y = 45 ksi	60 ksi	75 ksi	f_y = 45 ksi	60 ksi	75 ksi
$p=p'=0.5\%$	10.5	9.5	9.0	9.5	8.4	8.0	8.8	7.0	6.5
$p=p'=1.0\%$	12.0	9.0	8.0	10.1	8.0	6.5	9.0	8.0	6.0
$p=p'=1.5\%$	11.0	8.5	7.3	10.7	7.0	7.5	9.5	7.0	6.2
$p=p'=2.0\%$	10.0	8.5	6.3	9.5	7.3	6.5	9.3	6.3	6.3
$p=p'=3.0\%$	11.0	7.0	6.5	10.0	7.0	6.0	8.7	6.5	5.0

shows that reinforced concrete sections, subject to the highest axial loads permitted by the ACI code [11], possess a minimum ductility ratio of 5 under the most adverse variable combinations studied. The ratio may be as high as 12 under more favourable combinations of the variables.

Conclusions

1. The magnitude of the balanced axial load, which separates tension from compression failure, decreases with increasing reinforcement percentages, increasing reinforcement strengths, and decreasing concrete strengths.

For the large number of section investigated, the above magnitude neither exceeded 40%, nor ever fell below 20% of the axial load capacities of the sections (these values are not unduly sensitive to the adopted definition of sectional failure).

2. If sectional failure is defined in a conventional manner in terms of limiting compression concrete strains, ultimate moments increase with increasing levels of axial load, as long as failure is governed by tension, and thereafter decrease as the axial loads are further increased. The corresponding curvatures decrease steadily with increasing levels of axial load.

If failure is defined, as in the present study, in terms of sectional moment capacity, two irregularities are found in the above trends, which otherwise remain generally valid. Firstly, moment capacities under pure bending are found to be larger than those under bending combined with low axial loads. Secondly, ultimate curvatures are sometimes found to increase with increasing axial loads around the balanced point.

3. It appears reasonable to define the failure of a section as the stage corresponding to the attainment of: (a) sectional moment capacity in deformation analysis, and (b) a limiting value of concrete strain at the extreme compression fibre in strength analysis.

4. Reinforced concrete sections without any special transverse reinforce-

ment, and subject to the highest axial loads permitted under the ACI code, i.e. $P=0.4P_b$, possess a ductility ratio of 5 under the most adverse, and of 12 under the most favourable, of the variable combinations studied.

5. Inelastic action, at least to an extent which would not require ductility in excess of the amounts indicated in Fig. 12, may be permitted in reinforced concrete column sections.

Notation

A_s = cross-sectional area of tension reinforcement.
A'_s = cross-sectional area of compression reinforcement.
b = width of section.
f'_c = standard cylinder strength of concrete.
f_y = yield strength of steel.
h = total depth of section.
M = sectional moment.
M_u = ultimate moment.
M_y = yield moment.
p = ratio of tension reinforcement area to gross area of section.
p' = ratio of compression reinforcement area to gross area of section.
P = axial load on section.
P_b = balanced axial load.
P_u = ultimate axial load.
Δ_u = lateral deflection in a structure at ultimate stage.
Δ_y = lateral deflection in a structure at yield stage.
ϵ_u = concrete strain in extreme compression fibre at ultimate stage.
ϕ = sectional curvature.
ϕ_u = curvature corresponding to ultimate moment.
ϕ_y = curvature corresponding to yield moment.

Acknowledgement

This paper is based on a portion of the doctoral dissertation of the first author and is part of an investigation on the "Inelastic Behaviour of Reinforced Concrete Structures" in progress in the Solid Mechanics Division and the Department of Civil Engineering, University of Waterloo, Waterloo, Ontario, Canada, under the direction of the second author.

The financial support of the National Research Council of Canada, under Grants A-4789 and D-10, is gratefully acknowledged.

References

1. American Concrete Institute: Reinforced Concrete Design Handbook. 3rd. Ed., ACI 317, Detroit, Mich., 1965.
2. Whitney, C. S., and Cohen, E.: Guide for Ultimate Strength Design of Reinforced Concrete. ACI Journal, Proceedings, Vol. 53, No. 5, November 1956, p. 455–490.
3. Blume, J. A., Newmark, N. M., and Corning, L. H.: Design of Multi-story Reinforced Concrete Buildings for Earthquake Motions. Portland Cement Association, Skokie, Ill., 1961.
4. Pfrang, E. O., Siess, C. P., and Sozen, M. A.: Load-Moment-Curvature Characteristics of Reinforced Concrete Cross Sections. ACI Journal, Proceedings Vol. 61, No. 7, July 1964, p. 763–778.
5. Newmark, N. M., and Hall, W. J.: Dynamic Behavior of Reinforced and Prestressed Concrete Buildings under Horizontal Forces and Design of Joints (Incl. Wind, Earthquake, Blast Effects). Preliminary Publication, 8th Congress, IABSE, New York, September 1968, p. 585–613.
6. Sampson, R. A.: Ductility of Reinforced Concrete Columns. Master of Engineering Report, Univ. of Canterbury, Christchurch, New Zealand, 1971, 51 p.
7. Park, R., and Sampson, R. A.: Ductility of Reinforced Concrete Column Sections in Seismic Design. ACI Journal, Proceedings, Vol. 69, No. 9, September 1972, p. 543–550.
8. Cohn, M. Z., and Ghosh, S. K.: Flexural Ductility of Reinforced Concrete Sections. Publications, IABSE, Vol. 32, Part II, Zürich, 1972, p. 53–83.
9. Ghosh, S. K.: Some Aspects of the Nonlinear Analysis of Reinforced Concrete Structures. Ph. D. Thesis, Univ. of Waterloo, Waterloo, Ont., Canada, September 1972.
10. Sargin, M.: Stress-Strain Relationships for Concrete and the Analysis of Structural Concrete Sections. Study No. 4, Solid Mechanics Division, Univ. of Waterloo, Ont., Canada, 1971.
11. American Concrete Institute: Building Code Requirements for Reinforced Concrete. ACI 318-71, Detroit, Mich., 1971.
12. Srinivasa Rao, P., Kannan, P. R., and Subrahmanyam, B. V.: Influence of Span Length and Application of Load on the Rotation Capacity of Plastic Hinges. ACI Journal, Proceedings Vol. 68, No. 6, June 1971, p. 468–471.
13. Structural Engineers' Association of California Seismology Committee: Recommended Lateral Force Requirements and Commentary. San Francisco, Calif., 1968 (with 1970 amendment).

Summary

An investigation into the effects of axial load on the load-deformation characteristics of reinforced concrete sections is reported. The variables studied, besides the level of axial loading, are the concrete strength, steel grade, and amount of sectional reinforcement. The approach used is a computer simulation of the behaviour of over four hundred sections under a broad range of combinations of the above variables. The results are presented in the form of moment-curvature, axial load-ultimate moment, axial load-ultimate curvature, and ductility factor-axial load diagrams. The study provides a broad understanding of inelastic action in reinforced concrete columns subject to combined bending and compression.

Résumé

On présente une étude sur les influences de l'effort normal sur les caractéristiques de déformation de sections en béton armé. Les variables étudiées sont, à côté de l'intensité de la charge, les tensions dans le béton, la qualité de l'acier et le degré d'armature. La méthode utilisée est une étude par simulation sur computer du comportement de plus de quatre cents sections soumises à un grand nombre de combinaisons des variables ci-dessus. Les résultats sont présentés sous forme de courbes «moment-courbure», «effort axial-moment de rupture», «effort axial-courbure à la ruine» et «coefficient de déformabilité-effort axial». L'étude a permis une meilleure compréhension des phénomènes inélastiques dans les colonnes en béton armé soumises à un effort normal avec flexion.

Zusammenfassung

Es wird eine Untersuchung der Effekte von Axiallast-Deformations-Charakteristiken an Stahlbetonquerschnitten beschrieben. Die Variablen, die neben der Grösse der Axiallast untersucht werden, sind der Betonwiderstand, die Stahlqualität und die Grösse des Bewehrungsgrades.

Die benützte Näherungsmethode ist eine Computer-Simulation des Verhaltens von mehr als 400 Querschnitten unter einem breiten Spektrum von Kombinationen der obengenannten Variablen. Die Resultate werden in Form von Momenten-Krümmungen, Axiallast-Fliessmoment, Axiallast-Fliesskrümmung und Duktilitätsfaktor-Axiallast-Diagrammen angegeben. Die Studie vermittelt ein breites Verständnis über das inelastische Verhalten von Stahlbetonstützen unter kombinierter Biegung und Druck.

Generalization of the Finite Strip Method for Solid Continua

Généralisation de la méthode des bandes finies pour les continus solides

Verallgemeinerung der Finite-Streifen-Methode für Festkörperkontinua

JACOB GLÜCK MENACHEM GELLERT
Department of Structures, Faculty of Civil Engineering
Technion-Israel Institute of Technology

Introduction

The object of this paper is to present a more general formulation of the finite strip method for solid continua, and discusses the cases where the use of the present approach is more advantageous compared with the finite element method.

In principle the finite element method in its present stage of development may be applied for analysis of any kind of plane or space structure. The problem which may arise is more of an economic kind as computer time, data preparation, interpretation of results etc. It is obvious that the finite element approach i.e. a discretization in three dimensions for the general case, is unavoidable for structures with geometric or physical irregularities in all three directions.

In a broad of structures especially in civil engineering the irregularities are not in all three directions for space structures nor in two directions for plane structures. For these cases the use of the finite element seems not to be the natural method of solution; it would be more rational to apply a method where the discretization is made only for the direction where irregularities appear. For the case of a three-dimensional body having irregularities in one direction, the basic element will be in the general case a curved plate with finite width and for two-directional irregularities a bar with deformable cross section, generally bounded with curved line segments.

This procedure leads essentially to the reduction of a three-dimensional problem to a two- or one-dimensional one. This idea was successfully applied

for two dimensional problems [1], [2] where by use of Fourier series expansion the problem was reduced to a one-dimensional one.

The formulation of the problem will be done for a three-dimensional body using the variational approach based on the principle of minimum total potential energy, but may be extended also to other energetic principles like generalized functionals by Lagrange multipliers or based on complementary energy or Reissner's principle [3]. For practical problems the most important case is that where the three-dimensional problem is reduced to a one-dimensional one, leading to the solution of a system of linear differential equations with variable coefficients. For such system well known procedures are known. The development here will be made for this case only. Small displacements and linear elasticity are assumed. The present approach will be exemplified for a plate in bending by neglection of the shear force energy.

Formulation of the Problem

The total potential energy of an elastic body may be expressed as

$$\pi = \int_V (\tfrac{1}{2} E^{ijkl} \epsilon_{ij} \epsilon_{kl} - \bar{F}^i u^i)\, dV - \int_{S_\sigma} \bar{T}^i u^i\, dS, \tag{1}$$

where E^{ijkl} = elastic constants, ϵ_{ij} = strain tensor component, $\bar{F}^i$ = prescribed body force component, u^i = displacement, V = volume, $\bar{T}^i$ = prescribed surface traction and S_σ = portion of S over which the surface tractions are prescribed.

The strain-displacement relation for small displacements has the form

$$\epsilon_{ij} = \tfrac{1}{2} (u^i_{,j} + u^j_{,i}). \tag{2}$$

When a solid is divided into a finite number of discrete strips V_n, the total potential energy may be written as

$$\pi = \sum_{n=1}^{m} [\int_{V_n} (\tfrac{1}{2} E^{ijkl} \epsilon_{ij} \epsilon_{kl} - \bar{F}^i u^i)\, dV_n - \int_{S_{\sigma_n}} \bar{T}^i u^i\, dS_n]. \tag{3}$$

The strips will be supposed to be along the x_1 axis, and with a finite surface into the x_2, x_3 plane. The unknown displacements may be expressed in this case as discrete values in the corners of the finite surface, and are functions along the x_1 axis only.

$$\boldsymbol{u}(x_1, x_2, x_3) = \boldsymbol{A}(x_1, x_2, x_3)\, \boldsymbol{q}(x_1), \tag{4}$$

where $\boldsymbol{A}$ = matrix containing the interpolation functions, and $\boldsymbol{q}$ = vector of displacements function at the corners of the finite surface.

The strain vector may be expressed now in the form

$$\boldsymbol{\varepsilon} = \boldsymbol{B}(x_1, x_2, x_3)\,\boldsymbol{q} + \boldsymbol{C}(x_1, x_2, x_3)\,\boldsymbol{q}', \tag{5}$$

where

$$\boldsymbol{q}' = \frac{d\boldsymbol{q}}{dx_1}. \tag{6}$$

In the case of theory of plates and shells where shear strain energy is neglected Eq. (5) includes also second derivatives of $\boldsymbol{q}$ with respect to x_1.

The bounding surfaces of a strip are defined by planes of the form $x_1 = \text{const.}$ and surfaces $x_2 = f(x_3)$. For $x_1 = \text{const.}$ the matrix $\boldsymbol{A}$ will be written in the form $\boldsymbol{A}_b(x_2, x_3)$, the load vector $\bar{\boldsymbol{T}}_b(x_2, x_3)$ and the unknown displacement in the form $\boldsymbol{q}_b$. For the surfaces $x_2 = f(x_3)$ by assuming that x_2 and x_3 may be curvilinear, i. e.

$$x_2 = g(S), \tag{7}$$

$$x_3 = h(S) \tag{8}$$

the matrix $\boldsymbol{A}$ will be written in the form $\boldsymbol{A}_s(x_1, S)$ and the load vector $\bar{\boldsymbol{T}}_s(x_1, S)$.

With the above mentioned notations Eq. (3) may be written as

$$\pi = \sum_{n=1}^{m} \iiint \left[\tfrac{1}{2}(\boldsymbol{B}\,\boldsymbol{q} + \boldsymbol{C}\,\boldsymbol{q}')^T \boldsymbol{E}(\boldsymbol{B}\,\boldsymbol{q} + \boldsymbol{C}\,\boldsymbol{q}') - \bar{\boldsymbol{F}}^T \boldsymbol{A}\,\boldsymbol{q}\right] dx_1\,dx_2\,dx_3$$
$$- \iint \bar{\boldsymbol{T}}_s^T \boldsymbol{A}_s\,\boldsymbol{q}_s\,dx_1\,ds - \iint \bar{\boldsymbol{T}}_b^T \boldsymbol{A}_b\,\boldsymbol{q}_b\,dx_2\,dx_3. \tag{9}$$

Denoting with

$$\boldsymbol{C}_{00}(x_1) = \iint \boldsymbol{B}^T \boldsymbol{E}\,\boldsymbol{B}\,dx_2\,dx_3, \tag{10}$$

$$\boldsymbol{C}_{01}(x_1) = \boldsymbol{C}_{10}^T(x_1) = \iint \boldsymbol{B}^T \boldsymbol{E}\,\boldsymbol{C}\,dx_2\,dx_3, \tag{11}$$

$$\boldsymbol{C}_{11}(x_1) = \iint \boldsymbol{C}^T \boldsymbol{E}\,\boldsymbol{C}\,dx_2\,dx_3, \tag{12}$$

$$\boldsymbol{Q}^T(x_1) = \iint \bar{\boldsymbol{F}}^T \boldsymbol{A}\,dx_2\,dx_3 + \int \bar{\boldsymbol{T}}_s^T \boldsymbol{A}_s\,ds, \tag{13}$$

$$\boldsymbol{P}^T = \iint \bar{\boldsymbol{T}}_b^T \boldsymbol{A}_b\,dx_2\,dx_3. \tag{14}$$

Eq. (9) may be expressed in the form

$$\pi = \sum_{n=1}^{m} \int \left[\tfrac{1}{2}(\boldsymbol{q}^T \boldsymbol{C}_{00}\boldsymbol{q} + \boldsymbol{q}^T \boldsymbol{C}_{01}\,\boldsymbol{q}' + \boldsymbol{q}'^T \boldsymbol{C}_{10}\boldsymbol{q} + \boldsymbol{q}'^T \boldsymbol{C}_{11}\,\boldsymbol{q}') - \boldsymbol{Q}^T \boldsymbol{q}\right] dx_1 - \boldsymbol{P}^T \boldsymbol{q}_b. \tag{15}$$

Not all unknown $\boldsymbol{q}$ are independent. Denoting with $\boldsymbol{d}$ the vector of independent unknowns the following relations may be written

$$\sum_{n=1}^{m} \boldsymbol{q} = \boldsymbol{J}\,\boldsymbol{d}, \tag{16}$$

$$\sum_{n=1}^{m} \boldsymbol{q}_b = \boldsymbol{J}\,\boldsymbol{d}_b, \tag{17}$$

where $\boldsymbol{J}$ is a transformation matrix.

Denoting

$$\boldsymbol{K}_{ij}(x_1) = \boldsymbol{J}^T \sum_{n=1}^{m} \boldsymbol{C}_{ij} \boldsymbol{J}, \quad i=0,1;\ j=0,1, \tag{18}$$

$$\boldsymbol{L}^T = \sum_{n=1}^{m} \boldsymbol{Q}^T \boldsymbol{J}, \tag{19}$$

$$\boldsymbol{X}^T = \sum_{n=1}^{m} \boldsymbol{P}^T \boldsymbol{J}, \tag{20}$$

$$\boldsymbol{d}' = \frac{d(\boldsymbol{d})}{dx_1}, \tag{21}$$

$$\boldsymbol{d}'' = \frac{d^2(\boldsymbol{d})}{dx_1^2}. \tag{22}$$

Eq. (15) may be expressed as function of the unknown vector $\boldsymbol{d}$ as follows:

$$\pi = \int [\tfrac{1}{2}(\boldsymbol{d}^T \boldsymbol{K}_{00} \boldsymbol{d} + \boldsymbol{d}^T \boldsymbol{K}_{01} \boldsymbol{d}' + \boldsymbol{d}'^T \boldsymbol{K}_{10} \boldsymbol{d} + \boldsymbol{d}'^T \boldsymbol{K}_{11} \boldsymbol{d}') - \boldsymbol{L}^T \boldsymbol{d}] dx_1 - \boldsymbol{X}^T \boldsymbol{d}_b. \tag{23}$$

Equating to zero of the variation of Eq. (23) and some integration by parts yields

$$\begin{aligned} \delta\pi = \int \delta \boldsymbol{d}^T [(\boldsymbol{K}_{00} - \boldsymbol{K}'_{10}) \boldsymbol{d} + (\boldsymbol{K}_{01} - \boldsymbol{K}_{10} - \boldsymbol{K}'_{11}) \boldsymbol{d}' - \boldsymbol{K}_{11} \boldsymbol{d}'' - \boldsymbol{L}] dx_1 \\ + \delta \boldsymbol{d}_b^T (\boldsymbol{K}_{10b} \boldsymbol{d}_b + \boldsymbol{K}_{11b} \boldsymbol{d}'_b - \boldsymbol{X}) = 0, \end{aligned} \tag{24}$$

where

$$\boldsymbol{K}'_{ij} = \frac{d\boldsymbol{K}_{ij}}{dx_1}, \tag{25}$$

$$\boldsymbol{K}_{ijb} = \boldsymbol{K}_{ij(x_1=const)}. \tag{26}$$

For existence of Eq. (24) for any variation δd^T the following equations must be satisfied:

$$-\boldsymbol{K}_{11} \boldsymbol{d}'' + (\boldsymbol{K}_{01} - \boldsymbol{K}_{10} - \boldsymbol{K}'_{11}) \boldsymbol{d}' + (\boldsymbol{K}_{00} - \boldsymbol{K}'_{10}) \boldsymbol{d} = \boldsymbol{L}, \tag{27}$$

$$\boldsymbol{K}_{11b} \boldsymbol{d}'_b + \boldsymbol{K}_{10b} \boldsymbol{d}_b = \boldsymbol{X}. \tag{28}$$

The Euler Eq. (27) represents a system of linear differential equations with variable coefficients with unknown vector function $\boldsymbol{d}$. Eq. (28) represents the natural boundary conditions which are mechanical conditions, the left side representing the interior forces at $x_1 = \text{const}$ and the right side the exterior in the region where exterior forces are prescribed.

Denoting

$$\boldsymbol{S}_2(x_1) = -\boldsymbol{K}_{11}, \tag{29}$$

$$\boldsymbol{S}_1(x_1) = \boldsymbol{K}_{01} - \boldsymbol{K}_{10} - \boldsymbol{K}'_{11}, \tag{30}$$

$$\boldsymbol{S}_0(x_1) = \boldsymbol{K}_{00} - \boldsymbol{K}'_{10} \tag{31}$$

the final form of Eq. (27) is obtained

$$\boldsymbol{S}_2 \boldsymbol{d}'' + \boldsymbol{S}_1 \boldsymbol{d}' + \boldsymbol{S}_0 \boldsymbol{d} = \boldsymbol{L}. \tag{32}$$

As example the plate bending problem with neglection of the shear strain energy (see Fig. 1) will be considered. By initial integration along x_3 the

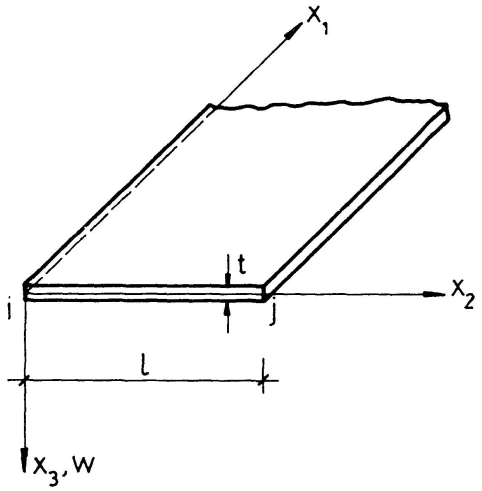

Fig. 1.

problem transforms to a two-dimensional one. The vector of unknowns for a single strip will be:

$$\boldsymbol{q}(x_1) = \{w_i, \theta_i, w_j, \theta_j\}^T, \tag{33}$$

where w_i and θ_i are the vertical displacement and rotation functions respectively along the ridge i, and w_j and θ_j are similar but for ridge j.

The displacements w and θ may be expressed as function of the ridge displacements as follows:

$$w = w_i - \frac{x_2}{l}\theta_i l + \frac{x_2^2}{l^2}(3w_j - 3w_i + 2\theta_i l + \theta_j l) + \frac{x_2^3}{l^3}(2w_i - 2w_j - \theta_i l - \theta_j l), \tag{34}$$

$$\theta = -\frac{\partial w}{\partial x_2} = \theta_i - \frac{2x_2}{l}\left(\frac{3w_j}{l} - \frac{3w_i}{l} + 2\theta_i + \theta_j\right) - \frac{3x_2^2}{l^2}\left(\frac{2w_i}{l} - \frac{2w_j}{l} - \theta_i - \theta_j\right). \tag{35}$$

The matrix $\boldsymbol{A}$ in this case is a function of x_2 only

$$A = \left\{1 - 3\frac{x_2^2}{l^2} + 2\frac{x_2^3}{l^3} \;\middle|\; -x_2 + \frac{2x_2^2}{l} - \frac{x_2^3}{l^2} \;\middle|\; \frac{3x_2^2}{l^2} - \frac{2x_2^3}{l^3} \;\middle|\; \frac{x_2^2}{l} - \frac{x_2^3}{l^2}\right\}. \tag{36}$$

The generalized strain vector $\boldsymbol{\varepsilon}$ may be expressed as function of the curvatures

$$\boldsymbol{\varepsilon} = \begin{Bmatrix} -\dfrac{\partial^2 w}{\partial x_1^2} \\ -\dfrac{\partial^2 w}{\partial x_2^2} \\ -2\dfrac{\partial^2 w}{\partial x_1 \partial x_2} \end{Bmatrix}. \tag{37}$$

Denoting with w', θ', $\boldsymbol{q}'$ the first derivative and with w'', θ'', $\boldsymbol{q}''$ the second derivative of w, θ and q respectively with respect to x_1, the components of the vector $\boldsymbol{\varepsilon}$ may be expressed in the form

$$-\frac{\partial^2 w}{\partial x_1^2} = -w_i'' + \frac{x_2}{l}\theta_i'' l - \frac{x_2^2}{l^2}(3w_j'' - 3w_i'' + 2\theta_i'' l + \theta_j'' l) - \frac{x_2^3}{l^3}(2w_i'' - 2w_j'' - \theta_i'' l - \theta_j'' l), \tag{38}$$

$$-\frac{\partial^2 w}{\partial x_2^2} = -2\left(\frac{3w_j}{l^2} - \frac{3w_i}{l^2} + \frac{2\theta_i}{l} + \frac{\theta_j}{l}\right) - \frac{6x_2}{l}\left(\frac{2w_i}{l^2} - \frac{2w_j}{l^2} - \frac{\theta_i}{l} - \frac{\theta_j}{l}\right), \tag{39}$$

$$-2\frac{\partial^2 w}{\partial x\,\partial y} = 2\theta_i' - \frac{4x_2}{l}\left(\frac{3w_j'}{l} - \frac{3w_i'}{l} + 2\theta_i' + \theta_j'\right) - \frac{6x_2^2}{l^2}\left(\frac{2w_i'}{l} - \frac{2w_j'}{l} - \theta_i' - \theta_j'\right). \tag{40}$$

Eq. (37) may now be expressed in the form

$$\boldsymbol{\varepsilon} = \boldsymbol{B}\boldsymbol{q} + \boldsymbol{C}\boldsymbol{q}' + \boldsymbol{D}\boldsymbol{q}'', \tag{41}$$

where $\boldsymbol{B}$, $\boldsymbol{C}$, and $\boldsymbol{D}$ are matrices, the components of which are functions of x_2 only.

$$\boldsymbol{B} = \left[\begin{array}{c|c|c|c} 0 & 0 & 0 & 0 \\ \frac{6}{l^2} - \frac{12x_2}{l^3} & -\frac{4}{l} + \frac{6x_2}{l^2} & -\frac{6}{l^2} + \frac{12x_2}{l^3} & -\frac{2}{l} + \frac{6x_2}{l^2} \\ 0 & 0 & 0 & 0 \end{array}\right], \tag{42}$$

$$\boldsymbol{C} = \left[\begin{array}{c|c|c|c} 0 & 0 & 0 & 0 \\ 0 & 0 & 0 & 0 \\ \frac{12x_2}{l^2} - \frac{12x_2^2}{l^3} & 2 - \frac{8x_2}{l} + \frac{6x_2^2}{l^2} & -\frac{12x_2}{l^2} + \frac{12x_2^2}{l^3} & -\frac{4x_2}{l} + \frac{6x_2^2}{l^2} \end{array}\right], \tag{43}$$

$$\boldsymbol{D} = \left[\begin{array}{c|c|c|c} -1 + \frac{3x_2^2}{l^2} - \frac{2x_2^3}{l^3} & x_2 - \frac{2x_2^2}{l} + \frac{x_2^3}{l^2} & -\frac{3x_2^2}{l^2} + \frac{2x_2^3}{l^3} & -\frac{x_2^2}{l} + \frac{x_2^3}{l^2} \\ 0 & 0 & 0 & 0 \\ 0 & 0 & 0 & 0 \end{array}\right]. \tag{44}$$

The total potentional energy of the plate may be expressed as follows:

$$\pi = \sum_{n=1}^{m} \iint \left(\tfrac{1}{2}\boldsymbol{\varepsilon}^T \boldsymbol{E}\boldsymbol{\varepsilon} - p\,w\right) dx_1\,dx_2 - \int \left(\bar{Q}_s w + \bar{M}_s \theta\right) dx_1 - \int \left(\bar{Q}_b w_b - \bar{M}_b w_b'\right) dx_2, \tag{45}$$

where p = the normal load on the plate, Q_s and M_s = shear force and bending moment respectively acting on the boundaries x_2 = const. where forces are prescribed, Q_b and M_b = shear forces and bending moments respectively acting on the boundaries x_1 = const. where forces are prescribed, and $\boldsymbol{E}$ = the elasticity matrix.

Substituting in Eq. (45) the expressions for $\boldsymbol{\varepsilon}$, w, θ, w_b and w_b' as given above yields

$$\pi = \sum_{n=1}^{m} \iint \left[\tfrac{1}{2}(\boldsymbol{B}\boldsymbol{q} + \boldsymbol{C}\boldsymbol{q}' + \boldsymbol{D}\boldsymbol{q}'')^T \boldsymbol{E}(\boldsymbol{B}\boldsymbol{q} + \boldsymbol{C}\boldsymbol{q}' + \boldsymbol{D}\boldsymbol{q}'') - p\,\boldsymbol{A}\boldsymbol{q}\right] dx_1\,dx_2 - \int \left(\bar{Q}_s \boldsymbol{A}_s - \bar{M}_s \frac{\partial \boldsymbol{A}_s}{\partial x_2}\right) \boldsymbol{q}\,dx_1 - \int \boldsymbol{A}\left(\bar{Q}_b \boldsymbol{q}_b - \bar{M}_b \boldsymbol{q}_b'\right) dx_2. \tag{46}$$

Denoting

$$\boldsymbol{C}_{00} = \int \boldsymbol{B}^T \boldsymbol{E}\, \boldsymbol{B}\, dx_2, \tag{47}$$

$$\boldsymbol{C}_{01} = \boldsymbol{C}_{10}^T = \int \boldsymbol{B}^T \boldsymbol{E}\, \boldsymbol{C}\, dx_2, \tag{48}$$

$$\boldsymbol{C}_{02} = \boldsymbol{C}_{20}^T = \int \boldsymbol{B}^T \boldsymbol{E}\, \boldsymbol{D}\, dx_2, \tag{49}$$

$$\boldsymbol{C}_{11} = \int \boldsymbol{C}^T \boldsymbol{E}\, \boldsymbol{C}\, dx_2, \tag{50}$$

$$\boldsymbol{C}_{12} = \boldsymbol{C}_{21}^T = \int \boldsymbol{C}^T \boldsymbol{E}\, \boldsymbol{D}\, dx_2, \tag{51}$$

$$\boldsymbol{C}_{22} = \int \boldsymbol{D}^T \boldsymbol{E}\, \boldsymbol{D}\, dx_2, \tag{52}$$

$$\boldsymbol{Q}^T(x_1) = \int p\, \boldsymbol{A}\, dx_2 + \bar{Q}_s\, \boldsymbol{A}_s\, \bar{M}_s \frac{\partial \boldsymbol{A}_s}{\partial x_2}, \tag{53}$$

$$\boldsymbol{P}^T = \int \bar{Q}_b\, \boldsymbol{A}\, dx_2, \tag{54}$$

$$\boldsymbol{M}^T = \int \bar{M}_b\, \boldsymbol{A}\, dx_2. \tag{55}$$

For non-anisotropic plates, matrices $\boldsymbol{C}_{01}$, $\boldsymbol{C}_{10}$, $\boldsymbol{C}_{12}$, $\boldsymbol{C}_{21}$ vanish. In this case Eq. (46) may be written in the form:

$$\pi = \sum_{n=1}^{m} \int [\tfrac{1}{2}(\boldsymbol{q}^T \boldsymbol{C}_{00}\, \boldsymbol{q} + \boldsymbol{q}^T \boldsymbol{C}_{02}\, \boldsymbol{q}'' + \boldsymbol{q}'^T \boldsymbol{C}_{11}\, \boldsymbol{q}' + \boldsymbol{q}''^T \boldsymbol{C}_{20}\, \boldsymbol{q} + \boldsymbol{q}''^T \boldsymbol{C}_{22}\, \boldsymbol{q}'') - \boldsymbol{Q}^T \boldsymbol{q}]\, dx_1 - \boldsymbol{P}^T \boldsymbol{q}_b + \boldsymbol{M}^T \boldsymbol{q}_b'. \tag{56}$$

The expressions for the matrices $\boldsymbol{C}_{00}$, $\boldsymbol{C}_{02}$, $\boldsymbol{C}_{11}$, $\boldsymbol{C}_{20}$ and $\boldsymbol{C}_{22}$ for the case of isotropic plates are given in the appendix.

The generalized displacement vector $\boldsymbol{q}$ and its derivatives may now be expressed by adding the independent displacement vector $\boldsymbol{d}$ using Eq. (16) and (17). With the notations based on Eqs. (18), (19) and (20), Eq. (56) may be expressed as follows:

$$\pi = \int [\tfrac{1}{2}(\boldsymbol{d}^T \boldsymbol{K}_{00}\, \boldsymbol{d} + \boldsymbol{d}^T \boldsymbol{K}_{02}\, \boldsymbol{d}'' + \boldsymbol{d}'^T \boldsymbol{K}_{11}\, \boldsymbol{d}' + \boldsymbol{d}''^T \boldsymbol{K}_{20}\, \boldsymbol{d} + \boldsymbol{d}''^T \boldsymbol{K}_{22}\, \boldsymbol{d}'' - \boldsymbol{L}^T \boldsymbol{d}]\, dx_1 - \boldsymbol{X}^T \boldsymbol{d}_b + \boldsymbol{Y}^T \boldsymbol{d}_b'. \tag{57}$$

The condition of vanishing of the variation of the total potential energy, after some integrations by parts, yields

$$\delta\pi = \int \delta \boldsymbol{d}^T [\boldsymbol{K}_{22}\, \boldsymbol{d}'''' + (\boldsymbol{K}_{02} - \boldsymbol{K}_{11} + \boldsymbol{K}_{20})\, \boldsymbol{d}'' + \boldsymbol{K}_{00}\, \boldsymbol{d} - \boldsymbol{L}]\, dx_1 + \delta \boldsymbol{d}_b^T [-\boldsymbol{K}_{22}\, \boldsymbol{d}_b''' + (-\boldsymbol{K}_{20} + \boldsymbol{K}_{11})\, \boldsymbol{d}_b' - \boldsymbol{X}] + \delta \boldsymbol{d}_b'^T (\boldsymbol{K}_{22}\, \boldsymbol{d}_b'' + \boldsymbol{K}_{20}\, \boldsymbol{d}_b + \boldsymbol{Y}) = 0. \tag{58}$$

From the requirement of arbitrary possible variations the following conditions result:

— equations of equilibrium expressed in the form of a system of nonhomogeneous linear differential equations with constant coefficients:

$$\boldsymbol{K}_{22}\, \boldsymbol{d}'''' + (\boldsymbol{K}_{02} - \boldsymbol{K}_{11} + \boldsymbol{K}_{20})\, \boldsymbol{d}'' + \boldsymbol{K}_{00}\, \boldsymbol{d} = \boldsymbol{L}. \tag{59}$$

— natural boundary conditions at $x_1 = \text{const}$

$$-\boldsymbol{K}_{22}\, \boldsymbol{d}_b''' + (-\boldsymbol{K}_{02} - \boldsymbol{K}_{11})\, \boldsymbol{d}_b' = \boldsymbol{X}, \tag{60}$$

$$-\boldsymbol{K}_{22}\, \boldsymbol{d}_b'' - \boldsymbol{K}_{20} \boldsymbol{d}_b = \boldsymbol{Y}. \tag{61}$$

Eq. (60) is the boundary condition for prescribed shear force at cross sections $x_1 = \text{const.}$, and Eq. (61), for prescribed bending moment at the same sections.

Solving the system of differential Eqs. (59) under boundary conditions (60), (61), the interior forces may be obtained for each strip as shown for the general approach.

The system of differential equations with variable coefficients may be solved for example using finite differences. This method of solution will lead to a system of linear algebraic equations. Essentially the accuracy of the solution and amount of numerical calculations will be approximately the same as in the case application of standard finite element approach, but the finite difference solution is less satisfactory owing to the fact, that boundary conditions are not automatically satisfied as in finite element approach. If the first derivative of the unknowns is represented by finite differences and substituted in Eq. (23), direct minimalization of the functional with respect to the discrete unknowns leads to the Euler's method. This method is similar to the finite element method and the coefficient matrix is of the same order of magnitude. Automatic fulfillment of mechanical boundary conditions is achieved.

Another way for solution of the system of differential equations may be obtained by means of infinite power series. A new non-dimensional variable will be chosen:

$$\xi = \frac{x_1}{x_{1\,max}}, \qquad |\xi| \leqq 1, \tag{62}$$

where $x_{1\,max}$ is an arbitrary length. Expanding the right side of Eq. (32) into an infinite power series

$$\boldsymbol{L} = \boldsymbol{N}\boldsymbol{\xi}, \tag{63}$$

where

$$\boldsymbol{N} = \begin{bmatrix} N_{1,0} & N_{1,1} & \dots & N_{1,\infty} \\ N_{2,0} & N_{2,1} & \dots & N_{2,\infty} \\ N_{m,0} & N_{m,1} & \dots & N_{m,\infty} \end{bmatrix}, \tag{64}$$

$$\boldsymbol{\xi} = \{1, \xi, \xi^2, \xi^3, \dots \xi^\infty\}^T. \tag{65}$$

m being the number of unknown displacement functions. The solution of Eq. (32) may be selected also in the form of an infinite power series

$$\boldsymbol{d} = \boldsymbol{G}_0 \boldsymbol{\xi}, \tag{66}$$

where $\boldsymbol{G}_0$ is an $m \times \infty$ coefficient matrix to be determined.

Differentiating Eq. (66) results

$$\boldsymbol{d}' = \boldsymbol{G}_1 \boldsymbol{\xi}, \tag{67}$$

$$\boldsymbol{d}'' = \boldsymbol{G}_2 \boldsymbol{\xi}, \tag{68}$$

where the element (i,j) of the matrices $\boldsymbol{G}_1$ and $\boldsymbol{G}_2$ respectively have the form

$$G_{1_{i,j}} = \frac{1}{x_{1\,max}} j\, G_{0_{i,j+1}}, \tag{69}$$

$$G_{2_{i,j}} = \frac{1}{x_{1\,max}^2} (j+1)\, j\, G_{0_{i,j+2}}. \tag{70}$$

Substituting Eqs. (63), (66), (67) and (68) into Eq. (32) the following equation will be obtained:

$$\boldsymbol{S}_2 \boldsymbol{G}_2 \xi + \boldsymbol{S}_1 \boldsymbol{G}_1 \xi + \boldsymbol{S}_0 \boldsymbol{G}_0 \xi = \boldsymbol{N} \xi . \tag{71}$$

Generally the elements of matrices $\boldsymbol{S}_1$, $\boldsymbol{S}_2$ and $\boldsymbol{S}_0$ may be functions which can be expanded into power series. The following relation may be written

$$\boldsymbol{S}_k \boldsymbol{G}_k = \sum_{n=0}^{\infty} \xi^n \bar{\boldsymbol{T}}_{k,n}, \quad (k = 0, 1, 2). \tag{72}$$

The elements of the matrices $\bar{\boldsymbol{T}}_{k,n}$ are constants. For convenience the columns of these matrices will be shifted to right with n steps, and zeros will be placed in the corresponding n columns. The new matrices will be denoted $\boldsymbol{T}_{k,n}$ and the following notation will be introduced

$$\boldsymbol{T}_k = \sum_{n=0}^{\infty} \boldsymbol{T}_{k,n} . \tag{73}$$

Multiplying on both sides by ξ, Eq. (72) may now be written

$$\boldsymbol{S}_k \boldsymbol{G}_k \xi = \boldsymbol{T}_k \xi . \tag{74}$$

Denoting

$$\boldsymbol{M} = \boldsymbol{T}_2 + \boldsymbol{T}_1 + \boldsymbol{T}_0 . \tag{75}$$

Eq. (71) yields

$$\boldsymbol{M} \xi = \boldsymbol{N} \xi . \tag{76}$$

This equation must exist separately for each power of ξ which means that the respective columns in the matrices $\boldsymbol{M}$ and $\boldsymbol{N}$ must be equal.

$$\boldsymbol{M}_j = \boldsymbol{N}_j . \tag{77}$$

Eq. (77) is a recursive equation which relates the coefficients $G_{0_{i,n}} (n \geqq 3)$ with the coefficients of lower index. For example for $j = 1$

$$\boldsymbol{M}_1 = \boldsymbol{N}_1 \tag{78}$$

is a system of m equations which relates the coefficients $G_{0_{i,3}}$, $G_{0_{i,2}}$ and $G_{0_{i,1}}$ assuming that the last two are known. Solving this system the coefficients $G_{0_{i,4}}$ may now be calculated from the system

$$\boldsymbol{M}_2 = \boldsymbol{N}_2 . \tag{79}$$

The procedure is continued until the coefficients $G_{i,n}$ are small enough to be neglected, remembering that $0 \leqq |\xi| \leqq 1$.

Since the constants $G_{0_{i,1}}$ and $G_{0_{i,2}}$ are not known the recursive equation must be solved for all homogeneous cases ($\boldsymbol{N} = \boldsymbol{0}$) assuming one of the constants equal to 1 while all other coefficients equal zero. Let us denote with $\boldsymbol{H}^{i1}$ the matrix $\boldsymbol{G}_0$ which is obtained by assuming $G_{0_{i,1}} = 1$ and all other constants with index smaller than 3 equals zero, and with $\boldsymbol{H}^{i2}$ the matrix $\boldsymbol{G}_0$ obtained by assuming $G_{0_{i,2}} = 1$ and all other constants with index smaller

than 3 equals zero. Similarly the coefficients obtained in the same way for the first derivative of $\boldsymbol{d}$ with respect to x_1 will be denoted by $\boldsymbol{R}^{i1}$ respective $\boldsymbol{R}^{i2}$

$$H_{i,j}^{k1} = G_{0_{i,j}}, \tag{80}$$

$$R_{i,j}^{k1} = \frac{j}{x_{1\,max}} G_{0_{i,j+1}} \tag{81}$$

with $G_{0_{k,1}} = 1$, $G_{0_{k,2}} = G_{0_{i,2}} = G_{0_{i,1}} = 0$ and $1 \leqq i < k$ and $k < i \leqq m$.

$$H_{i,j}^{k2} = G_{0_{i,j}}, \tag{82}$$

$$R_{i,j}^{k2} = \frac{j}{x_{1\,max}} G_{0_{i,j+1}} \tag{83}$$

with $G_{0_{k,2}} = 1$, $G_{0_{k,1}} = G_{0_{i,1}} = G_{0_{i,2}} = 0$ and $1 \leqq i < k$ and $k < i \leqq m$.

A particular solution will be obtained assuming all the constants $G_{0_{i,1}}$ and $G_{0_{i,2}}$ vanish and solving the nonhomogeneous Eqs. (77). Denoting the corresponding matrix $\boldsymbol{G}_0$ by $\boldsymbol{H}^0$ and the coefficients of the first derivative of $\boldsymbol{d}$ by $\boldsymbol{R}^0$ the unknown vector $\boldsymbol{d}$ and its first derivative may be written in the form

$$\boldsymbol{d} = \sum_{i=1}^{m} (G_{0_{i,1}} \boldsymbol{H}^{i1} + G_{0_{i,2}} \boldsymbol{H}^{i2}) \xi + \boldsymbol{H}^0 \xi,$$

$$\boldsymbol{d}' = \sum_{i=1}^{m} (G_{0_{i,1}} \boldsymbol{R}^{i1} + G_{0_{i,2}} \boldsymbol{R}^{i2}) \xi + \boldsymbol{R}^0 \xi.$$

For solution of the unknowm coefficients $G_{0_{i,1}}$ and $G_{0_{i,2}}$, $2m$ equations will be necessary. These equations are obtained for the boundary conditions at two sections $x_1 = \text{const}$. The boundary conditions may be geometric or mechanical and may be different for each ridge. The equations are obtained by substituting the values of $x_1 = \text{const}$ ($\xi = \text{const}$) in the corresponding row of $\boldsymbol{d}$ in Eq. (84) or in Eq. (28), using both Eqs. (84) and (85). It is obvious that in order to avoid rigid body motions a minimum number of geometric boundary consitions will be necessary. Knowing the coefficients $G_{0_{i,1}}$ and $G_{0_{i,2}}$ the vector d is known. The displacement vector $\boldsymbol{q}$ may then be calculated from Eq. (16) and the displacement from Eq. (4) and the strains from Eq. (5). Finally the stresses will be calculated from $\boldsymbol{\sigma} = \boldsymbol{E}\,\boldsymbol{\varepsilon}$.

An important class of problems leads to a system of differential equations with constant coefficients.

A particular and very frequent case is the one where boundary conditions enable the use of orthogonal functions as Fourier series.

The solution by differential equations may also be very advantageous in the case of specific problems where no boundary conditions have to be satisfied in x_1 direction as in the case of axisymmetric problems.

In conclusion, the present approach may be applied successfully and economically for a broad class of practical problems encountered especially in civil engineering.

Appendix

$$\boldsymbol{C}_{00} = \frac{E t^3}{12\,(1-\mu^2)} \begin{bmatrix} \frac{12}{l^3} & -\frac{6}{l^2} & -\frac{12}{l^3} & -\frac{6}{l^2} \\ & \frac{4}{l} & \frac{6}{l^2} & \frac{2}{l} \\ & & \frac{12}{l^3} & \frac{6}{l^2} \\ \text{Sym.} & & & \frac{4}{l} \end{bmatrix},$$

$$\boldsymbol{C}_{11} = \frac{E t^3}{24\,(1+\mu)} \begin{bmatrix} \frac{24}{5l} & -\frac{2}{5} & -\frac{24}{5l} & -\frac{2}{5} \\ & \frac{8l}{15} & \frac{2}{5} & -\frac{2l}{15} \\ & & \frac{24}{5l} & \frac{2}{5} \\ \text{Sym.} & & & \frac{8l}{15} \end{bmatrix},$$

$$\boldsymbol{C}_{02} = \boldsymbol{C}_{20}^T = \frac{\mu E t^3}{12\,(1-\mu^2)} \begin{bmatrix} -\frac{6}{5l} & \frac{1}{10} & \frac{6}{5l} & \frac{1}{10} \\ \frac{11}{10} & -\frac{2l}{15} & -\frac{1}{10} & \frac{l}{30} \\ \frac{6}{5l} & -\frac{1}{10} & -\frac{6}{5l} & -\frac{1}{10} \\ \frac{1}{10} & \frac{l}{30} & -\frac{11}{10} & -\frac{2l}{15} \end{bmatrix},$$

$$\boldsymbol{C}_{22} = \frac{E t^3}{12\,(1-\mu^2)} \begin{bmatrix} \frac{13l}{35} & -\frac{11l^2}{210} & \frac{9l}{70} & \frac{13l}{420} \\ & \frac{l^3}{105} & -\frac{13l^2}{420} & -\frac{l^3}{140} \\ & & \frac{13l}{35} & \frac{11l^2}{210} \\ \text{Sym.} & & & \frac{l^3}{105} \end{bmatrix}.$$

References

1. Cheung, Y. K.: Finite strip method of analysis of elastic slabs. Proc. Am. Soc. Civ. Eng., *94*, EM 6, 1365–1378, 1968.
2. Zienkiewicz, O. C.: The Finite Element Method in Engineering Science. McGraw-Hill, 1971.
3. Washizu, K.: Variational Methods in Elasticity and Plasticity. Pergamon Press, 1968.

Summary

The present paper is a more general formulation of the finite strip method for solid continua, and discusses the advantages compared with finite element method. The formulation is done for a three-dimensional body using the variational approach based on the principle of minimum total potential energy. As an application the particular case where the three-dimensional problem is reduced to an one-dimensional one is presented in more detail, leading to a system of linear differential equations with variable coefficients for which an infinite series solution is proposed. Small displacements and linear elasticity are assumed. The one-dimensional case is exemplified for a plate in bending by neglecting shear force energy.

Résumé

Ce travail présente un énoncé plus général de la méthode des bandes finies pour les continus solides, et discute les avantages comparés à la méthode des éléments finis. Cet énoncé est étudié pour un corps à trois dimensions en utilisant le calcul des variations basé sur le principe du minimum de l'énergie potentielle totale. Comme application on présente en détail le cas particulier où le problème à trois dimensions est réduit à un problème unidimensionnel, conduisant à un système d'équations différentielles linéaires avec coefficients variables pour lequel une solution aux séries infinies est proposée. On admet de petits déplacements et une élasticité linéaire. On montre comme exemple le cas unidimensionnel d'une plaque soumise à la flexion en négligeant l'énergie des efforts tranchants.

Zusammenfassung

Der vorliegende Artikel ist eine allgemeinere Formulierung der Finite-Streifen-Methode für Festkörperkontinua und bespricht deren Vorteile, verglichen mit der Finite-Elemente-Methode. Die Formulierung erfolgt anhand eines dreidimensionalen Körpers unter Anwendung der Variationsnäherung, die auf dem Prinzip der minimalen potentiellen Energie beruht. Als Anwendung wird ein spezieller Fall näher behandelt, bei dem das dreidimensionale Problem auf ein eindimensionales reduziert wird; es führt auf ein System linearer Differentialgleichungen mit variablen Koeffizienten, für welches eine Lösung mit infiniten Reihen vorgeschlagen wird. Kleine Deformationen und lineare Elastizität werden vorausgesetzt. Der eindimensionale Fall wir anhand einer Biegeplatte erläutert, wobei die Querkraftenergie vernachlässigt wird.

Buckling of Welded Beams and Girders

Flambement de poutrelles soudées

Kippen geschweisster Balken und Träger

D. A. NETHERCOT
B. Sc., Ph. D., Department of Civil and Structural Engineering,
University of Sheffield, England

1. Notation

a	distance from point on cross section to shear centre.
B_y	minor flexural rigidity.
b_f	width of flanges.
C_T	torsional rigidity.
C_w	warping rigidity.
c	width of assumed rectangular stress block.
d	depth of section between flanges.
$\bar{K} = \int_A \sigma a^2 dA$	property of cross section.
k	effective length factor.
L	span.
L_y	span for which $M_{cr} = M_y$.
M_{cr}	critical moment.
M_p	fully plastic moment.
M_y	moment at which section starts to yield, the effects of residual stresses being neglected.
M_{yr}	moment at which section starts to yield, the effects of residual stresses being included.
r_y	minor radius of gyration.
$s_w = \frac{2c}{d}$	proportion of web containing tensile residual stresses.
t_f	thickness of flanges.
t_w	thickness of web.

σ stress.
σ_{rc} compressive residual stress.
σ_y yield stress.

2. Introduction

Failure of laterally unsupported steel beams usually occurs by lateral-torsional instability, the fully plastic moment M_p being attainable only for very short spans. Over most of the range of practical slenderness ratios (span/minor radius of gyration) buckling will not occur until parts of the cross section have yielded under the action of the applied major axis loading system. When residual stresses are present, as they will be in most practical situations, the consequent reduction in the value of the applied load necessary to initiate yielding M_y, extends this inelastic range. Studies [1–5] of the buckling of beams containing patterns of residual stresses typical of those found in hot rolled sections have shown that, since yielding can occur at applied loads corresponding to less than one half of M_p, the range of spans for which buckling is inelastic may be at least twice that for a similar stress free section and that within this range the critical moment may be reduced by over forty per cent as a direct result of the presence of the residual stresses. Moreover, this range of spans comprises a major portion of the range of slenderness commonly used in practice.

Measurements of the residual stresses present in welded I and H shapes [6–9] have shown these to be significantly different to those found in hot rolled sections and an example for each type of section is given in Fig. 1. Because of the considerable influence of residual stresses on inelastic buckling strength it is to be expected that the behaviour of welded sections will be rather different to that of geometrically similar rolled sections.

In this paper theoretical studies of the inelastic buckling of bisymmetrical I section beams containing welding type residual stresses are reported. From

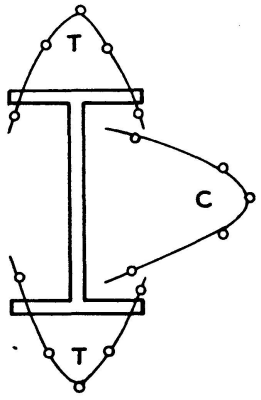

$10 \times 5\frac{3}{4}$ UB 21 hot rolled [6].

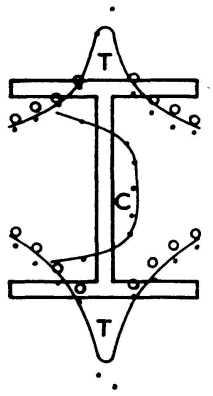

9×9 welded, universal mill plates [8].

Fig. 1. Typical measured residual stress patterns (not to scale, refer to original refs. for details).

the results obtained a simple method of approximating the beam buckling curve is suggested and compared favourably with available experimental results. In order to be able to compare directly the behaviour of welded and rolled beams, standard cross-sectional shapes have been used in the numerical examples.

3. Method of Analysis

The beam is assumed to be of doubly symmetric I section and to be loaded in the plane of the web by equal end moments, the critical value of which is given by:

$$M_{cr} = \frac{\pi}{kL}\left[B_y C_T\left(1+\frac{\bar{K}}{C_T}\right)\right]^{1/2}\left[1+\frac{\pi^2 C_w}{K^2 L^2 C_T\left(1+\frac{\bar{K}}{C_T}\right)}\right]^{1/2}, \tag{1}$$

where B_y is the minor flexural rigidity,
C_T is the torsional rigidity,
C_w is the warping rigidity,

$$\bar{K} = \int_A \sigma a^2 dA,$$

where a is the distance from the shear centre to the point where the total stress σ acts

and k is an effective length factor whose value depends upon the degree of restraint at either end.

In the numerical examples that follow the value of k has been taken as unity which corresponds to supports at both ends that prevent lateral deflexion and twist but offer no restraint to either lateral bending or warping. The treatment of other support conditions is discussed later in the paper.

For inelastic buckling the values of the stiffnesses B_y, C_T, C_w and $\bar{K}$ must be modified in accordance with the degree of plasticity present in the beam i.e. the value of $\frac{M_{cr}}{M_p}$. When residual stresses are present yielding occurs as a result of the combined effects of the residual stress system and the applied stress system and a convenient technique for tracing the spread of yield through the section is to consider it as being composed of a large number of small regions each of which, depending upon the value of the total i.e. residual plus applied, strain at its centroid, may be either elastic or plastic. The stiffness terms B_y etc. are then obtained by summing the contributions of all the regions and, since a different value of residual strain may be specified in each region, almost any residual stress pattern may be accommodated. Inelastic material behaviour was modelled using the suggestions of TRAHAIR and KITIPORNCHAI [10]. Briefly, these consist of replacing E by its strain hardening value E_{st} when calculating B_y and C_w, using the concept of a two phase material to determine the effective value of C_T and tracing the movement of the shear

centre of the effective section when calculating $\bar{K}$ and C_w. Once relationships between the effective values of each of the stiffnesses have been established, Eq. (1) may be solved for the span L corresponding to a compatible set of values of M_{cr}, B_y, C_T, C_w and $\bar{K}$. Fuller details of the complete approach, including assessments of its numerical accuracy, have been reported elsewhere [5]. Convergence tests for the present examples have indicated the use of 200 elements for one half of the section to be adequate and this mesh has been used in all the numerical examples.

4. Results

a) Rectangular Stress Block

Measurements of residual stresses in welded sections (6–9) have consistently shown the areas adjacent to the welds to be stressed up to yield in tension, the remainder of the section containing smaller, balancing compressive stresses. Theoretical investigations at Cambridge [11] supported by tests [6] have produced a simple method of relating the width of the (assumed) rectangular tension block c, see Fig. 2, to either the heat input or the size of the weld(s). Using this process residual stress distributions for a series of geometrically

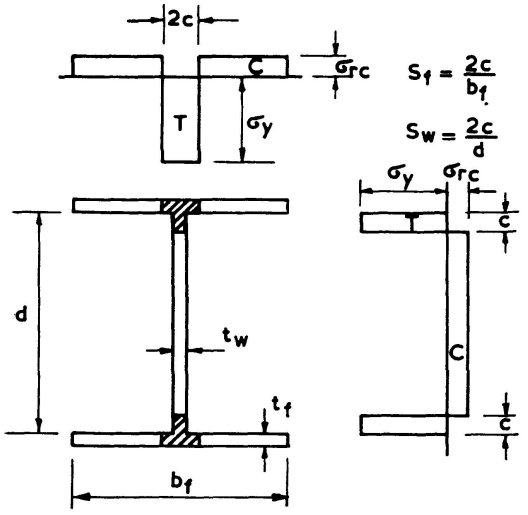

Fig. 2. Rectangular residual stress block (6).

different sections have been determined for use in the beam buckling analysis described above. Variations in the severity of welding have been included by using a number of values of s_w, a measure of the width of the tension block. Although axial equilibrium of the patterns has been checked, no subsequent adjustments have been made to try and ensure torsional equilibrium [5].

Two complete beam buckling curves for a $10 \times 5^3/_4\, U\, B$ section are illustrated in Fig. 3, values of s_w of 0.2 and 0.05 corresponding approximately to "moderate" and "light" welding respectively having been used in the calculations. Inclusion of the effects of residual stresses causes the critical moment to fall

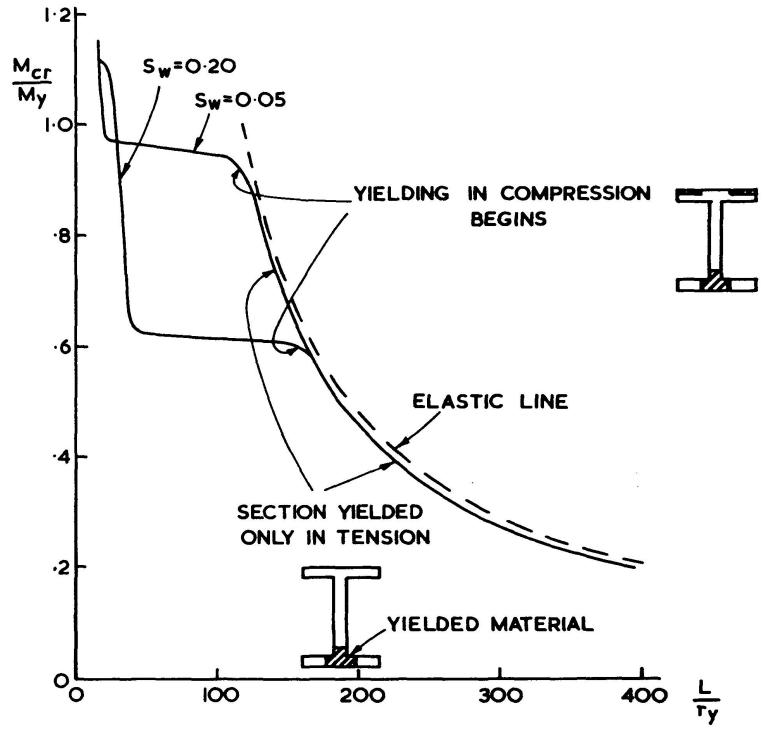

Fig. 3. Buckling curves for welded $10'' \times 5\frac{3}{4}''$ UB 21 sections.

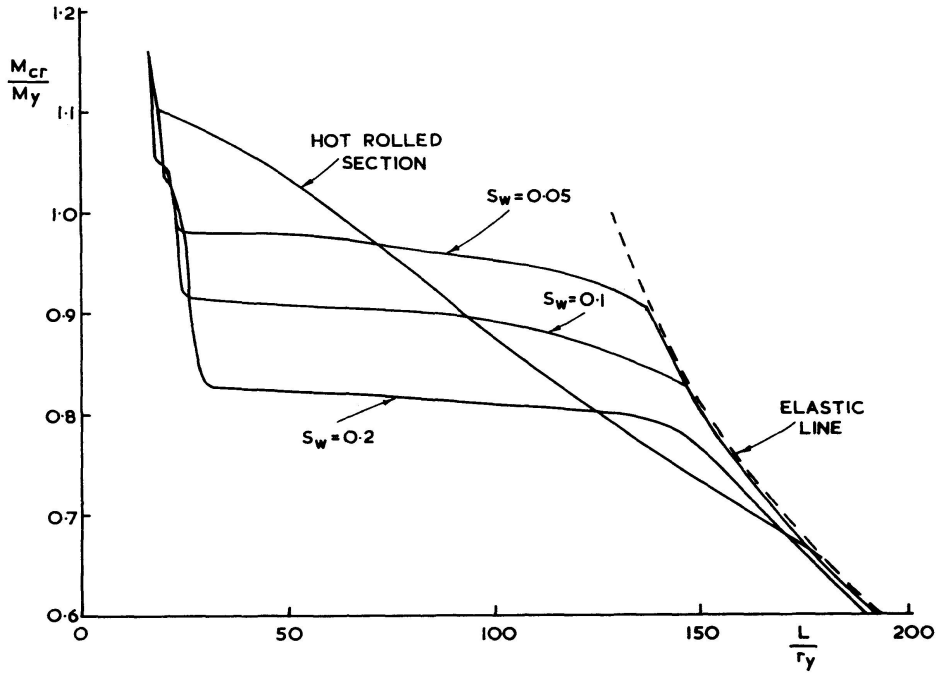

Fig. 4. Buckling curves for $8'' \times 8''$ UC 31 section.

below that based upon wholly elastic behaviour even for very long beams. This is a result of tensile yielding in the region of the web to tension flange junction which occurs immediately any load is applied. However, its effect upon the section's stiffness is small and the corresponding decrease in M_{cr} amounts to only a few per cent. On the other hand, when yield of the outer parts of the compression flange occurs, it is accompanied by a major reduction

in stiffness with the result that the buckling curve dips sharply below the elastic line. Eventually progressive yielding of the web causes the section to become almost completely strain hardened and the fully plastic moment M_p is attainable for sufficiently short spans.

Figs. 4 and 5 show portions of the buckling curves for two further shapes, a compact "column type" shape and a slender "beam type" shape. Taking British UB and UC sections as a representative set, for a given value of s_w, the balancing compressive residual stresses in all UC sections are very similar, whilst the 12×4 UB represents a beam section in which they are particularly high and the $10\times5\frac{3}{4}$ UB a beam section in which they are particularly low. The three sections considered in Figs. 3–5 therefore cover a wide range. For the 12×4 section slightly different elastic curves are obtained for different values of s_w due to differences in the value of the $\bar{K}$ term for the residual stresses acting alone. This is a consequence of their not indentically satisfying the condition $\bar{K}=0$ and is discussed more fully in ref. [5]. For the two other

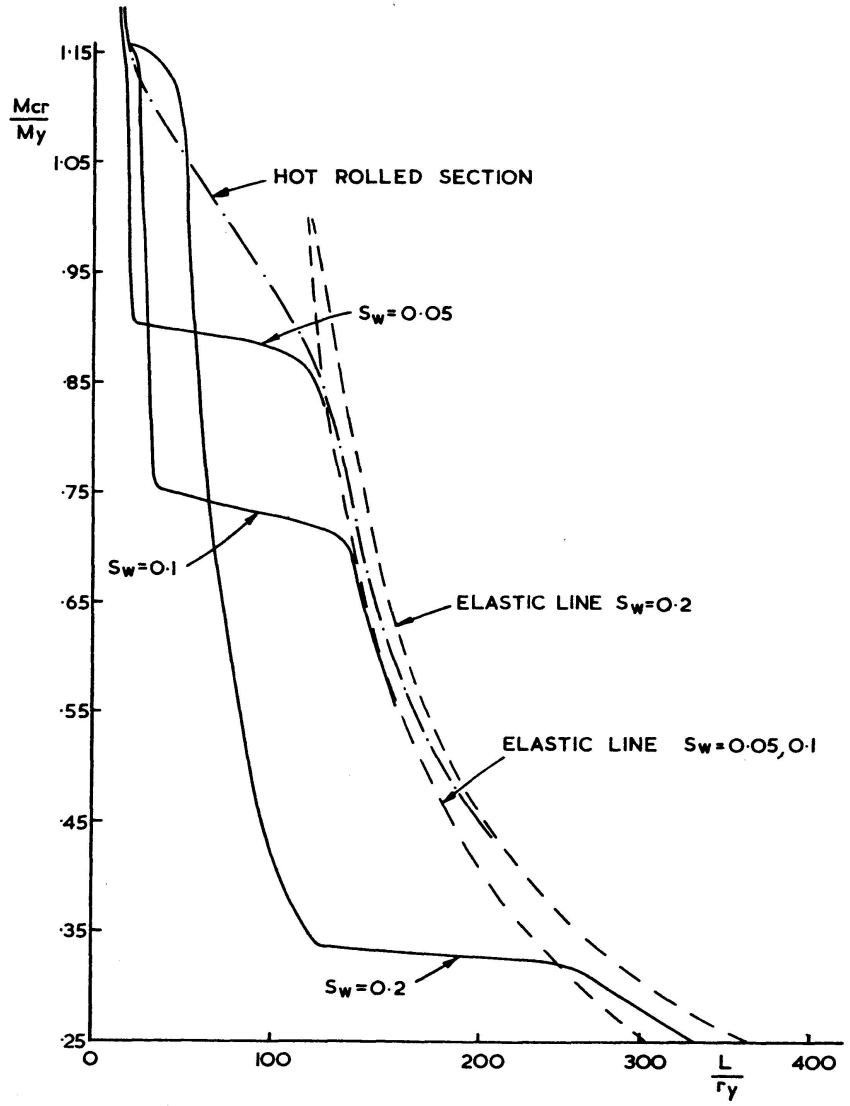

Fig. 5. Buckling curves for $12''\times4''$ UB 19 section.

sections this effect is sufficiently small that only one elastic curve need be plotted.

Figs. 4 and 5 also contain inelastic buckling curves for the equivalent hot rolled sections, YOUNG's [6] parabolic residual stress patterns having been employed in the generation of these curves. In both cases the differences between this curve and the set for the geometrically identical welded section clearly demonstrate the important role played by residual stresses in beam buckling. Whereas sections containing cooling type patterns lose stiffness gradually with increasing load, welded beams suffer a much more rapid decrease in stiffness due to the sudden loss of a considerable portion of the compression flange.

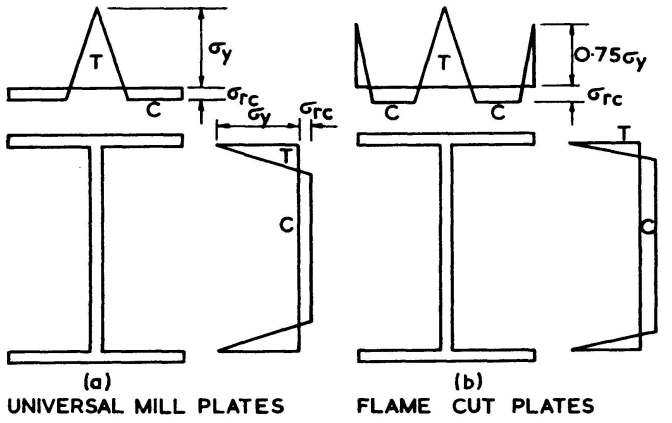

Fig. 6. Triangular residual stress block [12].

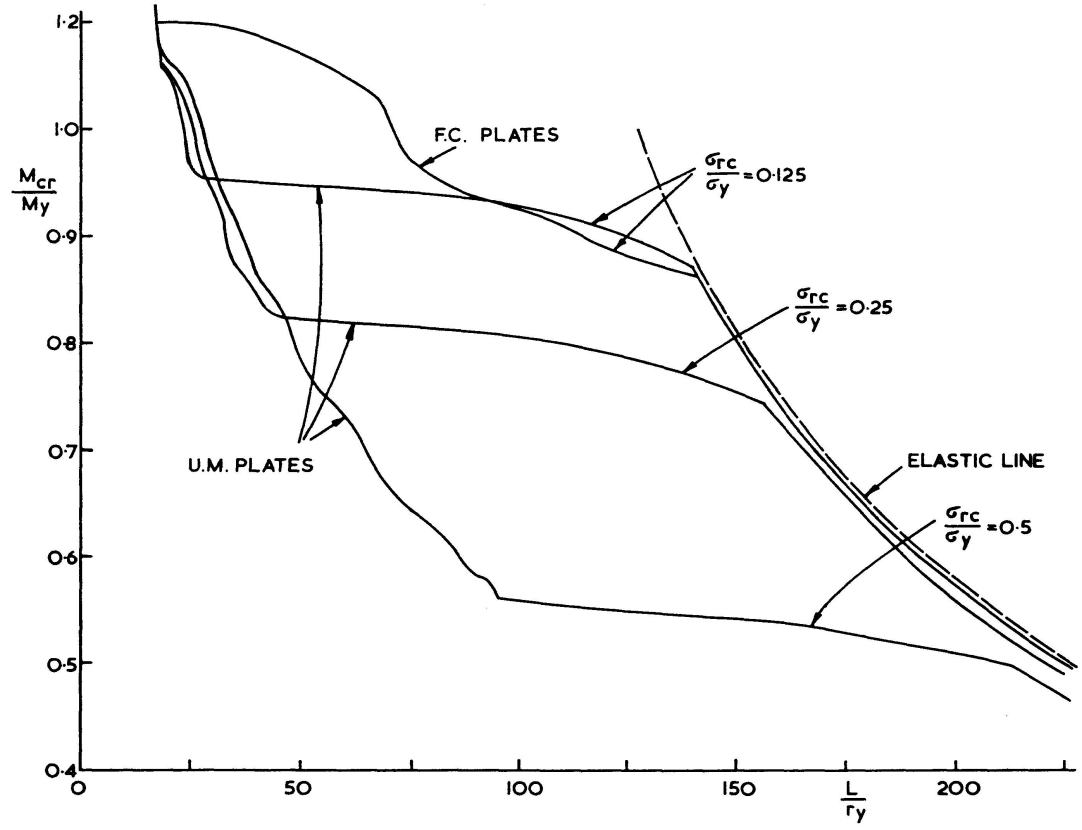

Fig. 7. Buckling curves for $8'' \times 8''$ UC 31, triangular stress block, UM or FC plates.

b) Triangular Stress Block and Flame Cut Sections

Opinions differ as to the actual shape of the tensile residual stress block and TALL and his co-workers at Lehigh prefer a triangular shape [12], see Fig. 6. Beam buckling curves calculated on the basis of this alternative residual stress pattern are given in Figs. 7 and 8. Over most of their range the shape of these curves is very similar to that corresponding to the use of the rectangular stress block for the same value of compressive residual stress in the flanges. For very short spans, however, since the proportion of the compression flange containing residual compression is smaller, the curves approach the fully strain hardened state more gradually, although the span at which M_p is reached is about the same. Therefore, for a given value of compressive residual stress, the assumption of a triangular stress block rather than a rectangular one leads to a slightly higher beam buckling curve in the region of very short spans.

Until now it has been assumed that the plates from which the section is fabricated are cut to size by mechanical means. Unless these plates are very

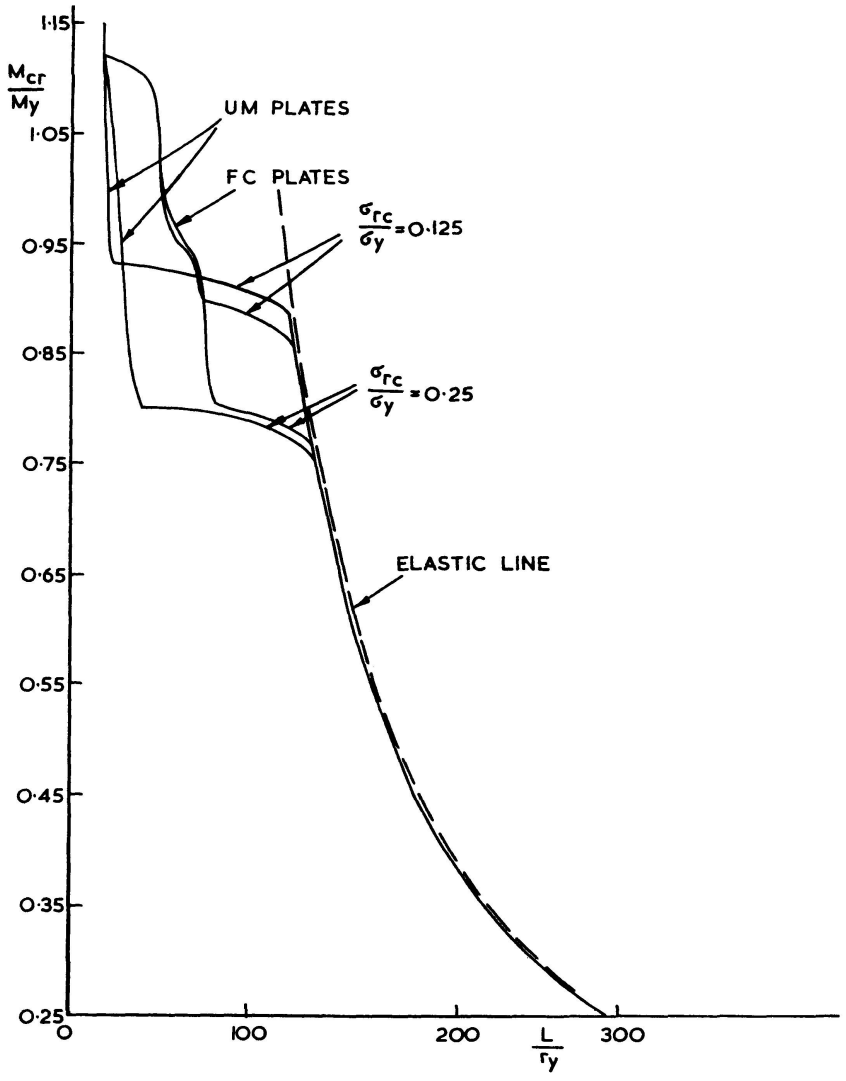

Fig. 8. Buckling curves for 12″×4″ UB 19 section triangular stress block and UM or FC plates.

thick (greater than about 25 mm) any residual stresses contained in them prior to welding will be comparitively small [13], and will be absorbed into the final residual stress pattern. However, plates with flame cut edges contain considerable tensile residual stresses in the vicinity of the cut [7]. For the web plate of a I section these will be absorbed into the stress block associated with the welding but at the flange tips a tensile stress block will remain. Some actual measurements are reported in ref. [7] and the type of pattern that has previously been used in column calculations [12] is shown in Fig. 6.

Using this pattern results have been obtained for the lateral buckling of the 8×8 and 12×4 sections and these are shown in Figs. 7 and 8. Since a balance of axial forces is required this type of pattern can only exist with fairly low values of compressive flange residual stress. For a similar value of σ_{rc} the section built up from flame cut plates possess a higher beam buckling curve than a similar section fabricated from universal mill plates. This is hardly surprising since the tensile stresses at the edges of the flanges produced by flame cutting postpone the yielding of that region which contributes most to the section's lateral stability; the compression flange tips.

c) Plate Girders

Few measurements of the residual stresses present in plate girders have been reported. OWEN [14], in Australia, has measured the stresses in two fairly small girders with unstiffened webs and has found that these conform to the expected pattern of stresses in welded I-sections. Using this data, beam buckling curves have been obtained for both of Owen's sections and these are shown in Figs. 9 and 10. These curves are similar to those derived previously for the more compact sections, although for the 24×6 girder in parti-

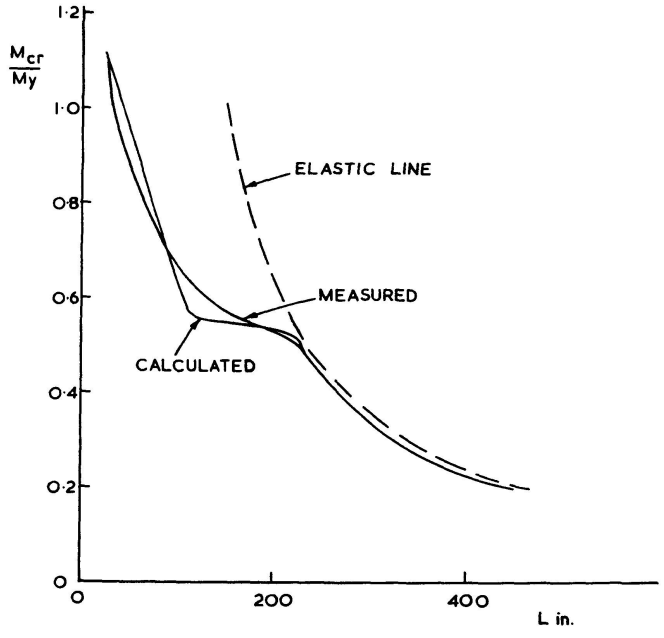

Fig. 9. Buckling curves for a $24''\times 6''$ plate girder [14].

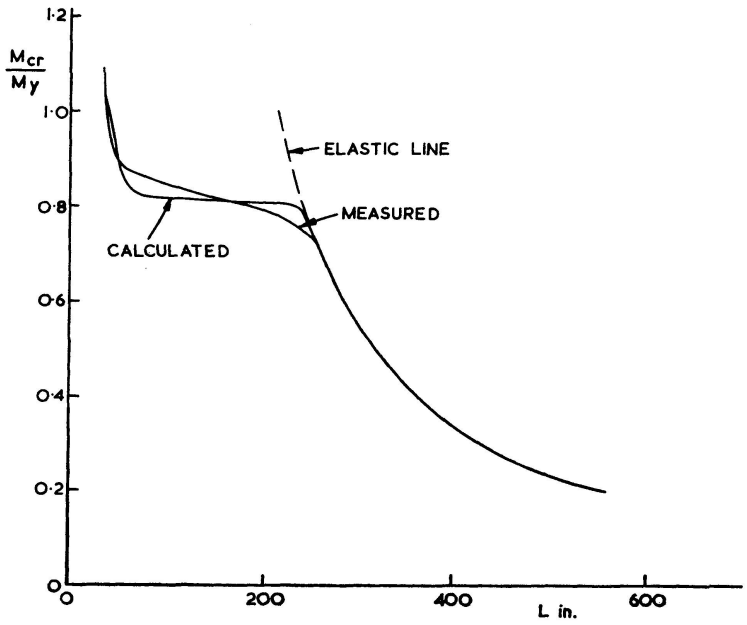

Fig. 10. Buckling curves for a $36'' \times 9''$ plate girder [14].

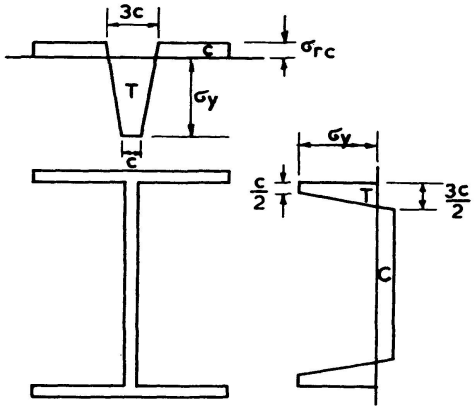

Fig. 11. Modified trapezoidal stress block [15].

cular, a slightly less rapid drop in stiffness at the point corresponding to the initiation of compressive yielding is indicated. This is a result of the actual variations in residual stresses over the cross section being somewhat smoother than the abrupt variations assumed in the patterns of Figs. 2 and 6.

Recently DWIGHT [15] has suggested that for column work it is preferable to modify the rectangular stress block of Fig. 2 into the trapezoidal shape of Fig. 11. Using the welding data given by OWEN [14], together with this variant of the Cambridge approach, theoretical residual stress distributions have been obtained for both of Owen's sections and the resulting beam buckling curves are shown on the appropriate figures. Agreement between the two curves is, in both cases, excellent.

5. Simplified Approach and Comparison with Experimental Results

In ref. [5] it was shown that, for hot rolled sections, a close approximation to the actual beam buckling curve could be obtained from a knowledge of the moment required to initiate yielding at the tips of the compression flange

M_{yc} together with the elastic buckling curve. Moreover, values of M_{yc} calculated from simple bending theory neglecting the effects of any tensile yielding elsewhere in the section were shown to be sufficiently accurate for use with this process.

The shape of the buckling curve for welded beams also suggests an approximation of this type. In this case, however, it is not appropriate to join the point on the elastic curve corresponding to M_{yc} to the point $(M_p, 0.15\,L_y)$ i.e. the limiting span for which M_p may be attained, but rather to use the construction shown in Fig. 12.

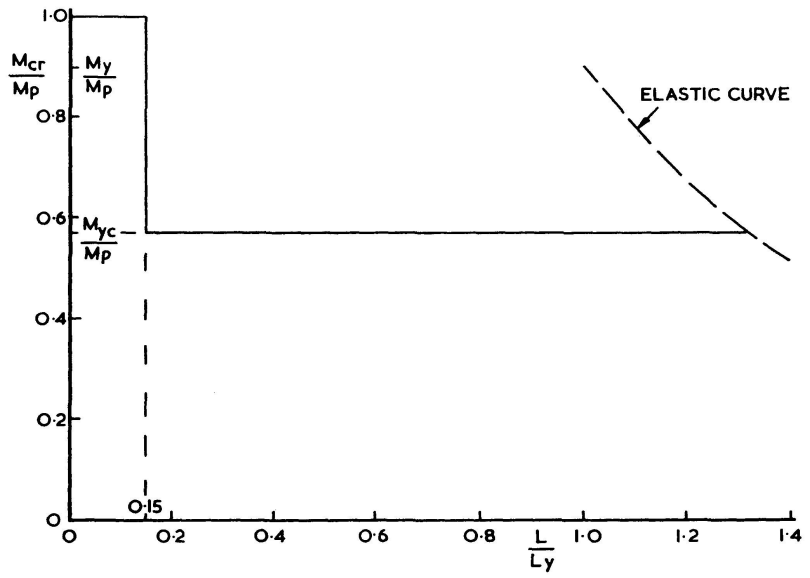

Fig. 12. Construction of approximate buckling curve for a welded beam.

Although the numerical examples considered previously were all for simply supported ends, ref. [4] showed that, providing L_y was calculated on the basis of the actual support conditions provided, this type of approach could be applied to beams with other forms of end support. The approximate curve of Fig. 12 is therefore applicable to welded beams with any degree of end fixity.

Inspection of the spans at which M_p is attained for each of the examples considered earlier suggests an average value of $0.15\,L_y$, where L_y is the span at which $M_{cr} = M_y$, the effects of residual stresses being neglected. The approximate curve is therefore obtained by combining a vertical line passing through this point $(M_p, 0.15\,L_y)$ with a horizontal line through the point on the elastic buckling curve at which compressive yielding is initiated. Table 1, which compares actual values of M_{yc} taken from the examples in the paper with the approximate values shows that good approximations to this point may readily be calculated. Since the value of residual flange compressive stress in the section may be calculated from a knowledge of the welding parameters using the Cambridge approach [6, 15], the approximate curve may be directly related to the severity of welding.

Table 1. Comparison of approximate and exact Values of $\frac{M_{yc}}{M_y}$

Section	Calculated Value of $\frac{M_{yc}}{M_y}$	"Exact" Value of $\frac{M_{yc}}{M_y}$	Calculated Value of $\frac{M_{yc}}{M_y}$	"Exact" Value of $\frac{M_{yc}}{M_y}$	Calculated Value of $\frac{M_{yc}}{M_y}$	"Exact" Value of $\frac{M_{yc}}{M_y}$
Value of s_w	0.2		0.1		0.05	
8×8 UC 31	0.78	0.77	0.83	0.83	0.95	0.94
12×4 UB 19	0.37	0.33	0.76	0.72	0.89	0.88
10×5¾ UB 21	0.61	0.60	0.84	0.84	0.93	0.91
Value of $\frac{\sigma_{rc}}{\sigma_y}$	0.125		0.25		0.50	
8×8 UC 31 } UM	0.87	0.87	0.75	0.74	0.50	0.50
12×4 UB 19 } plates	0.87	0.89	0.75	0.76	—	—
8×8 UC 31 } FC	0.87	0.87	—	—	—	—
12×4 UB 19 } plates	0.87	0.86	0.75	0.76	—	—
Plate girder	Measured residual stresses		Calculated residual stresses			
36×9	0.76	0.74	0.76	0.79		
24×6	0.53	0.50	0.53	0.51		

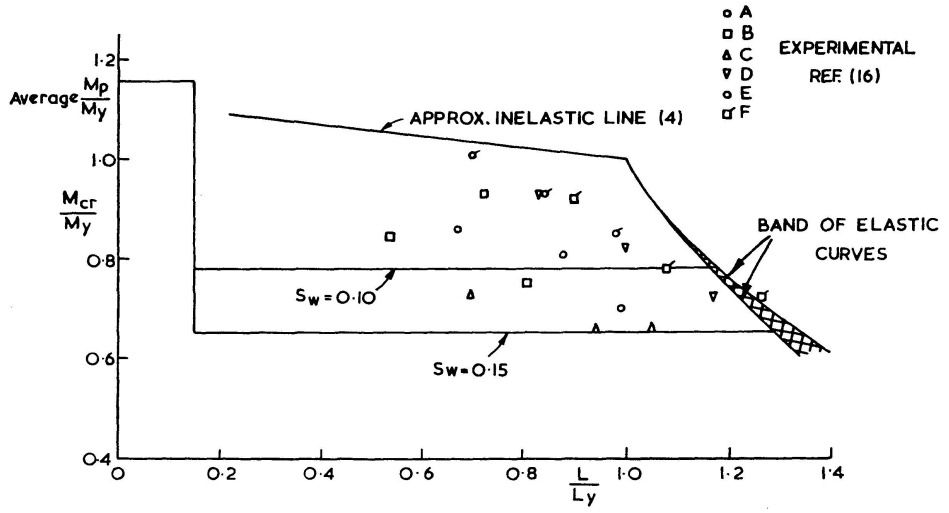

Fig. 13. Comparison of approximate buckling curves with test results [16].

Fig. 13 compares this approach with the results of a series of Japanese tests [16]. Complete fixity was provided at both ends of the test beams and the values of L_y used in plotting the results have therefore been modified accordingly. Since only limited welding data was available it has not been possible to use the above process to calculate values of M_{yc} for each section. Instead, average lines corresponding to values of s_w of 0.10 and 0.15 have

been used. These may be considered appropriate for the "moderate" welding conditions suggested by the data given in ref. [16]. The scatter of the test results reflects the variability of the residual stresses developed in geometrically similar sections even for apparently similar welding conditions. With this in mind, agreement between the test points and the approximate theoretical lines $s_w = 0.1$, representing an average curve, and $s_w = 0.15$, representing an approximate lower bound, may be regarded as satisfactory. Unfortunately, no results for tests on short welded beams could be found, although experiments on rolled sections [17] tend to support the view that $0.15\,L_y$ is a reasonable limiting span for the development of M_p.

6. Conclusions

The influence of the residual stresses produced during the fabrication of welded I sections on the lateral buckling strength of such beams has been investigated.

Even for long spans the yielding which occurs as a result of the presence of tensile residual stresses approaching the material yield stress in magnitude causes a reduction in buckling strength but, since this yielding is confined to a portion of the section which contributes little to its lateral stiffness, such reductions are small. Compressive yielding, however, as in the case of rolled beams, causes a more rapid decrease in stiffness. Indeed, for welded sections the sudden loss of a large part of the compression flange means that the inelastic curve diverges very rapidly from the elastic curve, decreases in stability of the order of fifty per cent being possible in heavily welded sections.

Studies of the effect on the buckling curve of the exact shape of the assumed residual stress pattern have shown this to be small except in the range of very short spans. What is of importance, however, is the magnitude of the balancing compressive stress in the flanges, which is itself dependent upon the size of the tension block. Use of the Cambridge method of relating the size of this tension block to the welding data has been shown to yield buckling curves in close agreement with those determined from measured residual stress patterns.

Sections fabricated from flame cut plates have been shown to possess higher buckling curves than geometrically similar sections fabricated from mechanically prepared plates due to the beneficial effect of the additional tension blocks at the flange tips.

From the numerical results a simple method of constructing beam buckling curves for welded sections has been proposed. These curves, which make due allowance for the severity of welding and the end fixity of the member, have been checked against available test results.

References

1. Galambos, T. V.: Inelastic Lateral Buckling of Beams. Proc. ASCE, J. Struct. Div., Vol. 89, No. ST 5, Oct. 1963, p. 217.
2. Massey, P. C.: Effect of Residual Stresses on the Lateral Stability of Steel I Beams. N. Z. Engng., Vol. 19, No. 9, Sept. 1964, p. 338.
3. Faella, C., and Mazzolani, F. M.: Instabilità Flesso-torsionale Inelasticà di Travi Metalliche Sotto Carichi Trasversali. Construzioni Metalliche, No. 6, 1972.
4. Nethercot, D. A.: Factors Affecting the Buckling Stability of Partially Plastic Beams. Proc. ICE, Vol. 53, Sept. 1972, p. 285.
5. Nethercot, D. A.: Residual Stresses and their Influence upon the Lateral Buckling of Rolled Steel Beams. The Struct. Eng. Vol. 52, No. 3, March, 1974, p. 89.
6. Young, B. W. and Dwight, J. B.: Residual Stresses and their Effect on the Moment-Curvature Properties of Structural Steel Sections. CIRIA Tech. Note 32, 1971.
7. McFalls, R. K., and Tall, L.: A Study of Welded Columns Manufactured from Flame-Cut Plates. Welding Journal, 48 (4) April 1969, Research Suppl. p. 141-s.
8. Beedle, L. S., and Tall, L.: Basic Column Strength. Proc. ASCE, J. Struct. Div., Vol. 86, No. ST 7, July 1960, p. 139.
9. Nagaraja Rao, N. R., and Tall, L.: Residual Stresses in Welded Shapes. Welding Journal, 43 (7) July 1964, Research Suppl., p. 295-s.
10. Trahair, N. S., and Kitipornchai, S.: Buckling of Inelastic I Beams Under Uniform Moment Proc. ASCE, J. Struct. Div., Vol. 98, No. ST 11, Nov. 1972, p. 2551.
11. Dwight, J. B., and Moxham, K. E.: Welded Steel Plates in Compression. The Struct. Eng., Vol. 47, No. 2, Feb. 1969, p. 49.
12. Yu, C. K., and Tall, L.: Significance and Application of Stub Column Test Results. Proc. ASCE, J. Struct. Div., Vol. 97, No. ST 7, July 1971, p. 1841.
13. Nagaraja Rao, N. R., and Tall, L.: Residual Stresses in Welded Plates. Welding Journal, 40 (10), Oct. 1961, Research Suppl., p. 468-s.
14. Owen, R.: Welding Residual Stresses in Plate-Web Girders. Civ. Eng. Trans., Instn. Engrs. Aust., Vol. CE 11, No. 2, Oct. 1969, p. 157.
15. Dwight, J. B.: Prediction of Residual Stresses Caused by Welding. Proc. Colloquium on Centrally Compressed Structs, Paris, Nov. 1972.
16. Fukumoto, Y., Fujiwara, M., and Watanabe, N.: Inelastic Lateral Buckling Tests on Welded Beams and Girders. Proc. Jap. Soc. Civ. Engrs., Paper 189, May 1971, p. 39.
17. Dibley, J. E.: Lateral Torsional Buckling of I Sections in Grade 55 Steel. Proc. ICE, Vol. 43, Aug. 1969, p. 599.

Summary

The inelastic lateral buckling of I beams loaded in uniform bending and containing patterns of residual stresses typical of those found in welded sections is studied. Variations in the assumed shape of the residual tension block are shown to be less important than the magnitude of the balancing compressive stresses and the beneficial effects of using flame cut plates are examined. The rapid construction of approximate beam buckling curves for welded sections, including the use of the Cambridge relationships between welding parameters

and residual stresses, is discussed and compared against available rest results. Such curves are therefore directly related to weld severity.

Résumé

On étudie le flambement latéral inélastique de poutres en double Té soumises à une flexion uniforme et contenant des tensions résiduelles telles que l'on en trouve dans les sections soudées. On montre que les variations dans la forme admise pour la répartition des tensions résiduelles sont moins importantes que l'amplitude des tensions de compression équilibrantes et on examine les effets bénéfiques de plaques découpées au chalumeau. On discute la construction de courbes de flambage pour des sections soudées, en tenant compte des relations de Cambridge entre les paramètres de soudure et les tensions résiduelles et on compare les résultats obtenus par essais. De telles courbes sont ainsi directement en relation avec la rigueur de la soudure.

Zusammenfassung

Die Arbeit untersucht das unelastische Kippen von I-Balken, die durch konstantes Biegemoment belastet sind und typische Eigenspannungen wie die in geschweissten Querschnitten aufweisen. Es wird gezeigt, dass Variationen der angenommenen Form der Eigenspannungszugzone weniger wichtig sind als die Grösse der ausgewogenen Druckspannung; die vorteilhaften Effekte bei Anwendung heiss zugeschnittener Platten werden untersucht. Das schnelle Konstruieren angenäherter Balken-Kippkurven für geschweisste Querschnitte, einschliesslich des Gebrauchs der Cambridge-Beziehung zwischen Schweiss-Parametern und der bleibenden Eigenspannungen, wird diskutiert und mit vorhandenen Test-Resultaten verglichen. Solche Kurven stehen somit in direkter Beziehung zur Schweisshärte.

Leere Seite
Blank page
Page vide

Die Kragschalenkonstruktion des Stadions Lehen in Salzburg

The Cantilever Roof Construction of the Lehen Stadium at Salzburg, Austria

La construction du toit en porte-à-faux du stade de Lehen à Salzbourg, Autriche

WOLFGANG OBERNDORFER
Dr. Dipl.-Ing., Linz

A. Allgemeines

Beim Neubau des Stadions Lehen im Herzen von Salzburg in den Jahren 1969 bis 1971 wurde beschlossen, die Zuschauertribünen zum grössten Teil zu überdachen. Der Entwurf sah hierfür eine Kragschalenkonstruktion vor, die je Spielplatzseite aus 9 nebeneinanderliegenden zylindertonnenähnlichen einmanteligen Teilen eines liegenden Rotationshyperboloids besteht (Fig. 1).

Fig. 1. Modell des Stadions.

Würde eine derartige Form rein als einmanteliges Hyperboloid ausgebildet, ergäbe sich an den seitlichen Begrenzungen ein gekurvter Rand. Die Architekten sahen jedoch – wie bein Tribünendach des Hippodroms in La Zarzuela (Spanien) von E. Torroja, das in vielfacher Hinsicht Vorbild war – am Kämpfer einen geradlinig verlaufenden Rand vor. Um eine solche Form zu erreichen, wurde eine sich zum Einspannende hin verbreiternde Kämpferzone vorgesehen, die jedoch in der Vorderansicht des Tribünendaches nicht in Erscheinung tritt, da sie hier in ihrer Breite fast auf Null ausläuft.

Das Schalendach besteht aus der eigentlichen Schale, die eine Stärke von 16 cm über der Stütze und 6 cm am Kragrand aufweist, und dem sog. Kehlträger, der den Zwickel zwischen den Schalenrändern monolithisch ausfüllt und von 1,50 m auf 0,15 m Höhe abnimmt (Fig. 2). Die Kragweite beträgt

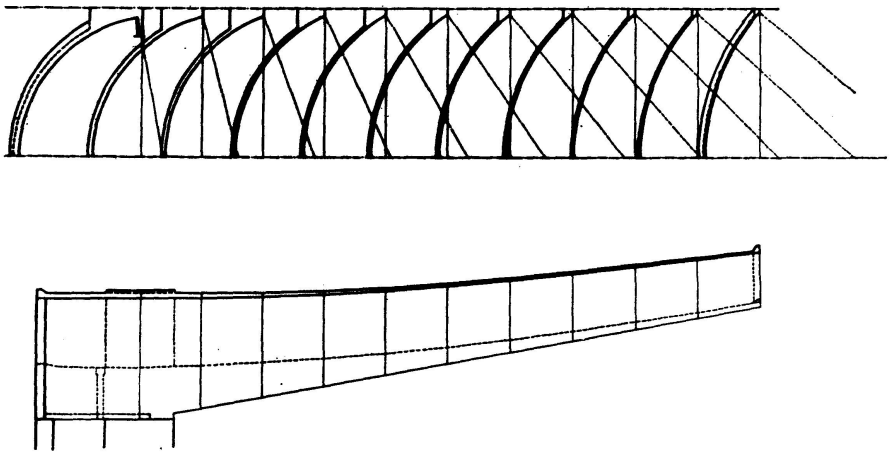

Fig. 2. Schalplan einer Regelschale (Querschnitt in den 1/10-Punkten und Längsschnitt).

18 m und die Schalenbreite (Achsabstand der Kehlträger) 8,70 m. Der 1. Hauptkrümmungsradius des Rotationshyperboloides nimmt von der Einspannstelle zum Kragrand hin von 4,15 auf 6,59 m, der 2. von 73 auf 284 m zu. Das rückwärtige Ende des Kehlträgers ist durch Spannstäbe in den Rahmenstiel, der das Tribünendach und die Zuschauerstufen trägt, niedergespannt. Die Ableitung der Schalenkräfte an der Stützstelle in die Stiele übernimmt eine Stützrippe, deren Stärke von 24 cm im Scheitel auf 36 cm am Kämpfer ansteigt. Das rückwärtige (also spielfeldabgewendete) Ende der Dachkonstruktion wird durch eine 25 cm starke Binderscheibe, die gleichzeitig die Schale aussteift und damit ihre Form erhält, abgeschlossen.

B. Theoretische Grundlagen der Schalenberechnung

Die charakteristischen Schalenparameter für die Stützstellen und den Kragrand sind:

$$\alpha = \frac{S}{L} = R\frac{y}{2K}, \qquad 1 : 8{,}1 \text{ bzw. } 1 : 8{,}0,$$

$$\beta = \frac{t}{R}, \qquad 1 : 26 \text{ bzw. } 1 : 110.$$

Zur Berechnung standen folgende Methoden zur Diskussion:

Fast strenge Berechnung nach [5].
Annäherungsberechnung als Kreiszylinderschale.
Elektronische Berechnung nach einer finiten Elementmethode.
Näherungsberechnung nach LUNDGREN [6].

Nach den bisherigen Erkenntnissen, die in der Theorie der Tonnendächer erarbeitet wurden, liegt hier der Fall einer sog. «langen» Schale vor, die mittels einer Näherungsmethode berechnet werden kann. Es wurde die Lundgrensche Methode ob ihrer Anschaulichkeit gewählt, jedoch waren einige theoretische Überlegungen zur Ermittlung der spezifischen Schubkräfte notwendig [7]. Lundgren betrachtete nämlich in seinem Werk nur den Träger mit konstantem Trägheitsmoment, während hier durch die Geometrie der Schale ein Differentialquotient der Steifigkeitsabnahme von 0,50 m 4/m vorhanden war. Dementsprechend wurde die spezifische Schubkraft nach der Formel

$$\frac{\partial N_{xy}}{\partial x} = \frac{\partial^2}{\partial x^2}\left(M_{xx}\frac{S(x,y)}{I_{xx}} + N_{xx}\frac{T(x,y)}{F_{xx}}\right)$$

berechnet, wobei:

N_{xy}	Schalenschubkraft	[Mp/m]
M_{xx}	Trägerlängsmoment	[Mpm]
N_{xx}	Trägerlängsnormalkraft	[Mp]
$S(x,y)$	stat. Moment des Teilquerschnittes	[m³]
$T(x,y)$	zugeh. Fläche des Teilquerschnittes	[m²]
I_{xx}	Trägheitsmoment des Gesamtquerschnittes	[m⁴]
F_{xx}	Fläche des Gesamtquerschnittes	[m²]

Als Gesamtquerschnitt des Trägers in Kragrichtung wurde eine Schale mit den zugehörigen Hälften des linken und rechten Kehlträgers angesehen.

Die Spannungen in Längsrichtung wurden also nach der Trägermethode ermittelt. Eine Bogenrechnung in Querrichtung ergab die Querbiegemomente, -normalkräfte und Schubkräfte in der Schale. Der Vorteil dieser Näherungsmethode liegt darin, dass jede Querschnittslamelle, für die die Bogenrechnung

durchgeführt wird, im Gleichgewicht ist und dass auf die Veränderlichkeit der Schalenstärke, Radius und Öffnungswinkel eingegangen werden kann.

C. Konstruktive Einzelheiten

Das Schalendach wird nach dem System DYWIDAG mit Spanngliedern ⌀ 12,2 St 140/160 formtreu vorgespannt. Die Spannglieder verlaufen trajektorienförmig von der Spannstelle am rückwärtigen Schalenrand im Scheitel hinunter in den Kehlträger, wo sie miteinander verankert sind (Fig. 3). Zur

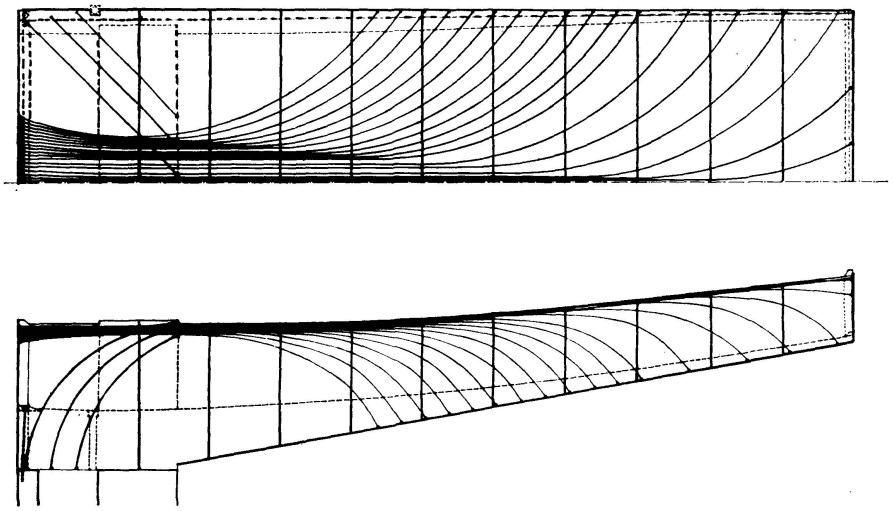

Fig. 3. Spannkabelplan (Grundriss und Längsansicht).

Abdeckung der Quermomente sind UNIDIM-Baustahlmatten mit variabler Stärke an der Ober- und Unterseite durchgehend verlegt. Der Schalenbeton hat eine Würfelfestigkeit von 4500 Mp/m². Der Kragrand ist mit einer Rippe, die einen Querschnitt von 14×14 cm² aufweist, zur Erhaltung der Schalenform versteift.

Da die 9 Schalen einer Tribünenseite nicht am Scheitel, sondern mit einem Randträger enden, werden Horizontalkräfte frei, die durch Vorspannung des Randträgers aufgenommen werden. Dies wurde so durchgeführt, dass der Randträger zunächst für sich allein betoniert und so vorgespannt wurde, dass er infolge eben dieser Vorspannung und der Horizontalkräfte für den Lastfall $g + \frac{p}{2}$ momentenfrei wurde.

Die diesem Spannungszustand entsprechende seitliche Verformung wurde durch ein sehr steifes Gerüst verhindert. Nach dem Anbetonieren und Vorspannen der 1. Schale wurde der Randträger und die im Gerüst gespeicherte verhinderte Verformungsenergie freigesetzt und kompensierte den nun freiwerdenden Horizontalschub. Die für die Lastfälle g bzw. $g+p$ auftretenden zusätzlichen Quermomente wurden überschlägig berechnet.

Der von der Stützrippe herrührende Horizontalschub wird über eine waagrechte Aussteifungsplatte in den Endfeldern in die Ebene der Binderscheibe übergeleitet. Die Binderscheibe läuft über alle 9 Felder kontinuierlich durch und ermöglicht durch ihre Vorspannung mit 2 DYWIDAG-Spanngliedern ⌀ 32, St 85/105, eine Insichverhängung des Horizontalschubes. Im Bereich der Überleitung der Niederhaltekraft zur Stützrippe sind die Schubspannungen so hoch, dass noch vorgespannte Schubnadeln ⌀ 12,2 eingelegt werden, die die Einhaltung der zulässigen Hauptzugspannungen gemäss DIN 4227 gewährleisten. Die Niederspannung, ebenfalls mit DYWIDAG-Spanngliedern ⌀ 32, ist so bemessen, dass für die Last $g+\frac{p}{2}$ der Rahmenstiel gerade momentenfrei ist. Ihr hauptsächlichster Zweck ist der, die Verformungen aus Schnee möglichst hintanzuhalten (Fig. 4).

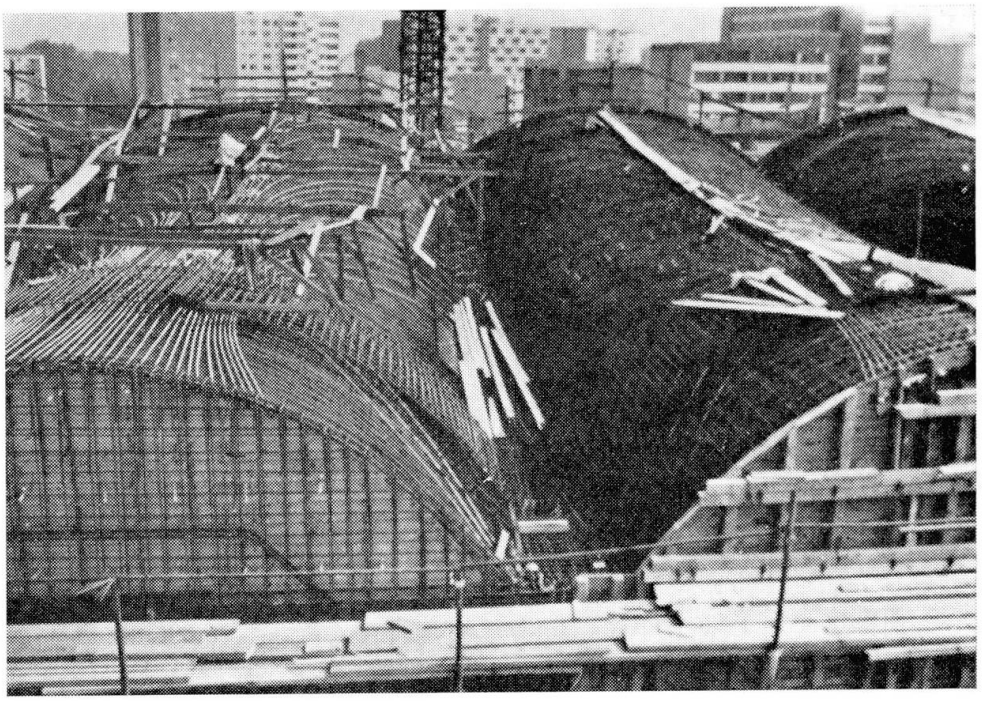

Fig. 4. Spanngliedverlegung und Bewehrung eines Schmetterlingträgers.

Literaturverzeichnis

1. E. Torroja: Logik der Form, S. 113.
2. Joedicke: Schalenbau, S. 167/168.
3. Hart: Kunst und Technik der Wölbung, S. 204/205.
4. Strangmann: Das Hippodrom von La Zarzuela in Madrid. Bautechnik 26 (1969), Heft 12, S. 381.
5. Aas Jakobson: Zylinderschalen mit veränderlichem Krümmungshalbmesser und veränderlicher Schalenstärke. Bauingenieur 18 (1937), S. 418–422 und 436–444.
6. Lundgren: Cylindrical Shells, Cylindrical Roofs. Vol. 1, S. 60–110.
7. W. Oberndorfer: Schubspannungen in Stäben mit veränderlicher Steifigkeit und eine Erweiterung des Lundgrenschen Verfahrens. Bauingenieur 47 (1972), Heft 4, S. 136–140.

Zusammenfassung

Es werden die statischen und konstruktiven Eigenheiten bei Entwurf und Berechnung eines vorgespannten Hyperboloid-Kragschalendaches aus Spannbeton zur Überdachung einer Stadiontribüne beschrieben.

Summary

The report deals with the static and design criteria that were applied on the outlay and calculation of a prestressed hyperboloid concrete cantilever shell roofing over a stadion's gallery.

Résumé

La contribution décrit les particularités statiques et constructives au projet et calcul d'un toit hyperbolique en porte-à-faux et en béton précontraint pour la tribune d'un stade.

On Improving the Aerodynamic Stability of H and Channel Sections

De l'augmentation de la stabilité aérodynamique de sections en double Té et en U

Über die Verbesserung der aerodynamischen Stabilität von H-förmigen und Kanalquerschnitten

ALI SABZEVARI
Dept. of Mech. Eng.
Pahlavi University,
Shiraz, Iran

ERIK HJORTH-HANSEN
Dept. of Civ. Eng.
The Norwegian Institute of Technology,
Trondheim, Norway

Introduction

After the dramatic failure of Old Tacoma Narrows suspension bridge on November 7, 1940 major steps have been taken by engineers towards the construction of aerodynamically stable (within the expected range of velocities at the site) suspension bridges of various lengths and forms. All the countermeasures taken so far against the aerodynamic instability in wind fall in the following categories:

1. The modern suspension bridge structures are designed for higher torsional stiffness when compared to that of earlier designs such as the Old Tacoma Narrows bridge. In the case of truss-stiffened bridge decks the increase in the torsional rigidity is achieved by means of stiffening and lateral trusses. In such structures the ratio of the principal natural torsional frequency to that of vertical bending is generally more than 2 compared to only 1.3–1.5 for the Old Tacoma Narrows [1].
2. The geometrical form of the bridge decks has been greatly improved and made more favourable as far as fluid flow over the deck and the consequent aerodynamic stability are concerned. Thus the simple plate-girder designs have almost become outdated and the more elaborate truss-girder and recently box-girder versions appear to be the most common forms of today's suspension bridge decks.

Notable in these advancements are the early work of FARQUHARSON [2], VINCENT [3] and BLEICH [4] in U.S.A., SCRUTON [5] in U.K., SELBERG [6] in

Norway, HIRAI [7] in Japan, KLÖPPEL [8] in Germany and STÜSSI [9] in Switzerland. Scores of later contributions can be found in Refs. [10], [11] and [12].

Of course the improvements achieved in the aerodynamic stability of suspension bridges by means of increasing the stiffness of structure, especially those of torsional modes of oscillations and designing the deck form to be less susceptible to aerolastic vibrations have led to much heavier and more elaborate structures than what is necessary to withstand static loadings including static wind load. Consequently the increase in steel mass and elaborations in the deck configuration have increased the cost of structures drastically. Furthermore, the modern constructional techniques and fabrications have resulted in rather low structural damping values compared to that in earlier constructions, see SELBERG's damping measurements on some Norwegian suspension bridges [13].

Although the departure from the simple plate-girder design has been necessary in the case of long span bridges, the economical attractions of such a simple design, at least for small span suspension bridges, are inevitable.

It is therefore the aim of the present work to revisit the aerodynamic stability of simple H and channel sections and examine the possibility of improving the aeroelastic stability by means of attaching simple suitable fairings to both the front and back faces of deck. Such a procedure may prove to provide a sufficient degree of stability to some decks so that any drastic increase in cost may be avoided. Such fairings of course are not meant to carry any significant load and can be fabricated from any conveniently available material as "dummy" structural elements. Furthermore the effect of bottom plates and horizontal flow-splitters in addition to fairings are to be examined in the wind tunnel.

It has to be mentioned that artificial dynamic stabilizers or vibration detuners of either passive or active type may also prove to be effective means of detuning some of the aeroelastic oscillations encountered in suspension bridges. This possibility is presently under investigations.

In general, two distinct types of aeroelastic oscillatory motions are expected in the wind tunnel:

1. Low amplitude uncoupled vertical and or rotational vibrations occuring at usually narrow ranges of low wind speed beyond which stability is restored.
2. Flutter *) oscillations either in single degree or in the bending-torsion coupled form.

---

*) The word flutter used in this work means the diverging oscillations of any non-rigid object exposed to a fluid stream and extracting its oscillatory energy from that stream. The stability is not restorable after the flutter on-set by increasing the fluid speed and the non-rigid body referred to in this paper is a deck model section.

In this report we are concentrating on the feasibility of improving the catastrophic oscillatory motion of the latter type. Nevertheless it must be mentioned that in any study concerning an actual bridge deck the former type of oscillation must also be seriously considered. It is interesting to note that fairings have in fact been used on the Long's Creek bridge in Canada for reducing oscillatory motions of former type [14].

Section Models and Test Arrangements

The two types of basic cross-sections considered in this work are shown as section Nos. 10 and 20 in Fig. 1. The channel section model is a simplified form of the first draft for Lokkaren suspension bridge to be constructed in Norway. A linear scale factor of 36 was chosen. The mass of the model was 5.9 kg/m corresponding to nearly 8000 kg/m on the prototype.

The second model, which is basically an H-section, represents a simplified version of the Old Tacoma Narrows. The linear scale factor being 37.5 in this case resulting in a model mass of 5.9 kg/m as in the previous case. This mass was infact maintained throughout the test programme including the section models with fairings.

The variety of configurations tested is shown in Fig. 1. Fairings were attached either in continuous or alternating fashion as suggested in Fig. 2. The channel section was also tested with some propellers attached to the side faces as illustrated in Fig. 3.

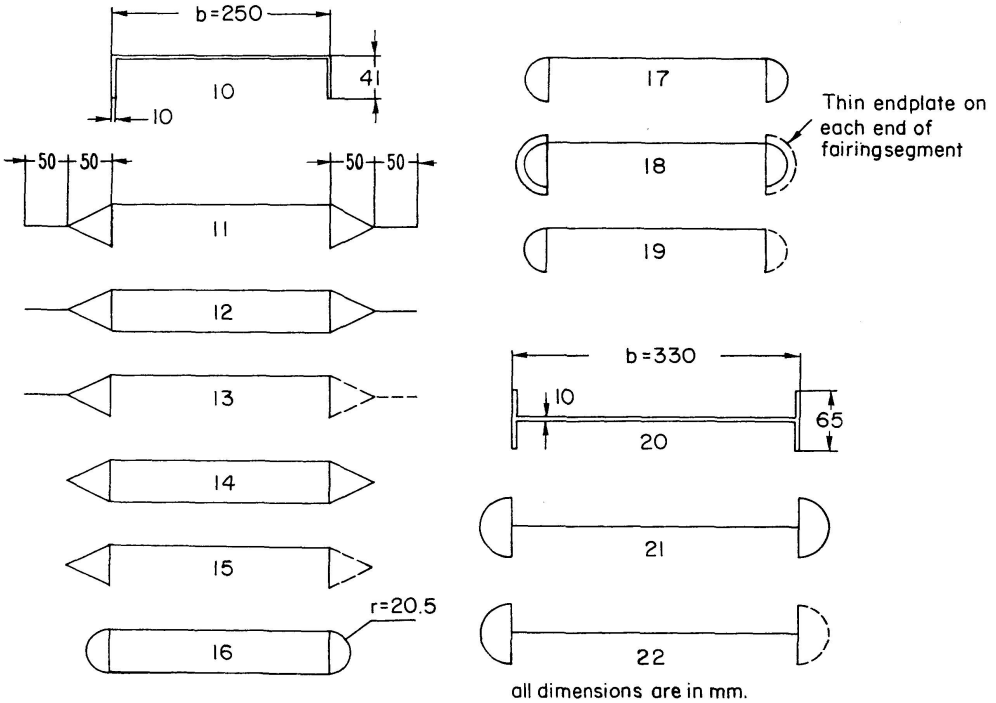

Fig. 1. Section models. When both fairings are drawn in full line then the continuous arrangement of Fig. 2a is employed, otherwise the alternating type of fairings, Fig. 2b is used.

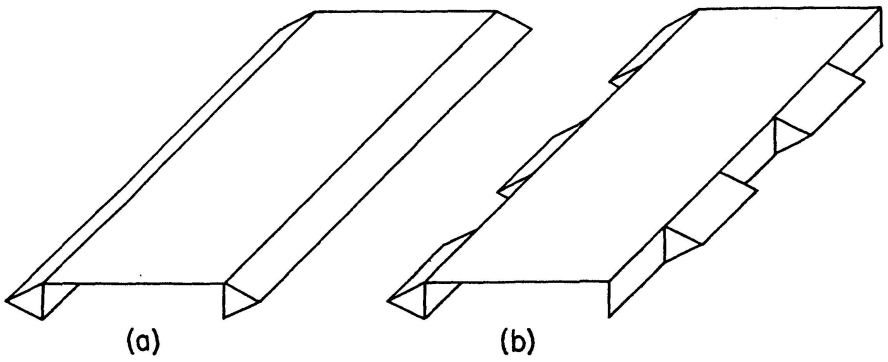

Fig. 2. Continuous and alternating forms of fairing attachment.

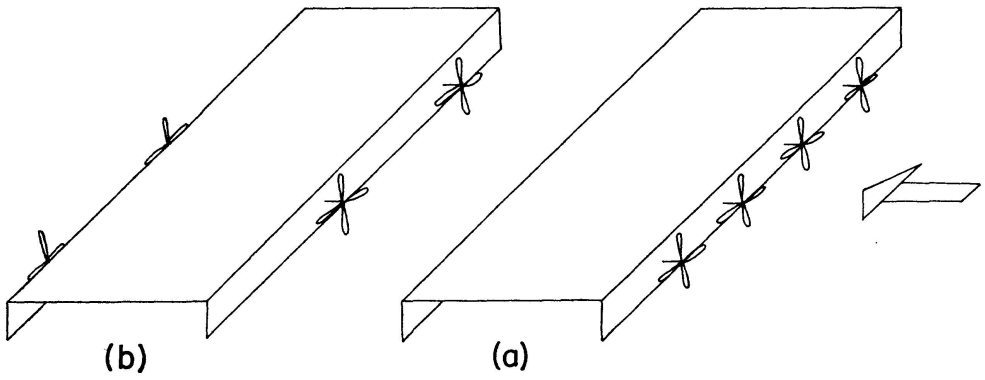

Fig. 3. Models with propellers.

Section models of length 1.06 m were tested in the low-speed wind-tunnel of NTH, Trondheim, with a working section of 1.1 m wide and 1.2 m long. The capacity of the tunnel being approximately 20 m/s.

Each section model was supplied with end-plates to assure the two-dimensional character of air flow. These end-plates were 250×530 mm^2 on channel sections and 250×500 mm^2 on H sections with rounded corners.

Models were stayed with guy wires at an elevation corresponding to the assumed shear-centre location of the prototype. This was taken to be the point of symmetry on H-sections and midchord point on the upper surface of channel-sections.

The rigid section models were suspended by the conventional coil spring rig systems with half the number of springs being located at each end and equidistant from the chord centre line. The supporting system was placed completely outside the airstream.

The distance between the coil springs at each end was adjusted for the correct frequency ratio (N_T/N_V), where N_T and N_V designate the principal torsional (rotational) and bending (vertical) natural frequencies respectively. Frequency ratios of 1.3 and later 1.7 (in a few cases 1.8) were selected. The selection of these specific values is for the following reasons:

The ratio 1.3 corresponds to the extremely torsionally weak (and dangerous) girder-stiffened designs in which there is only one lateral stiffening system. In

such a design the deck contributes very little to torsional stiffness. The frequency ratio 1.7 (or 1.8) was chosen to represent a lower estimate of the frequency ratio obtained when two lateral systems are used. That is, addition of horizontal trusses along the bottom part for the channel section say. Such a truss system would probably have small effect on the deck aerodynamics and hence it is not produced on the model.

The entire experimental programme for the comparative study was executed with models suspended by the so-called "flexible rig" which permitted large amplitudes of the order of 0.2 radian to develop for the rotational oscilla-

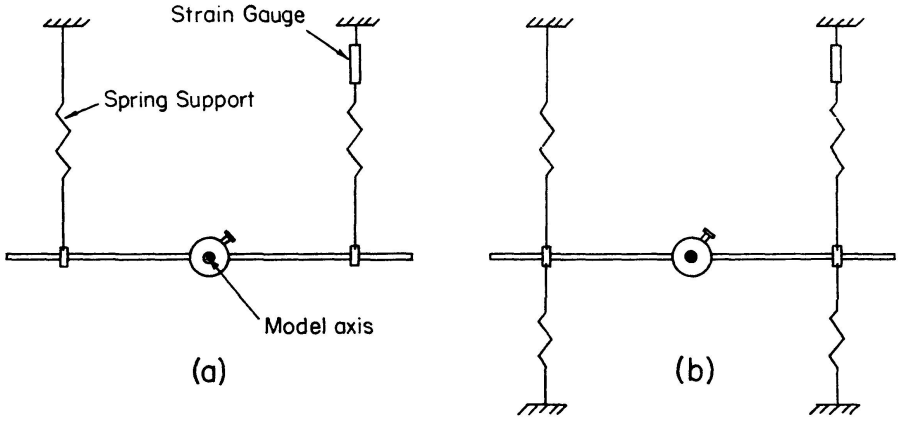

Fig. 4. Supporting systems, (a) flexible rig, (b) stiff rig.

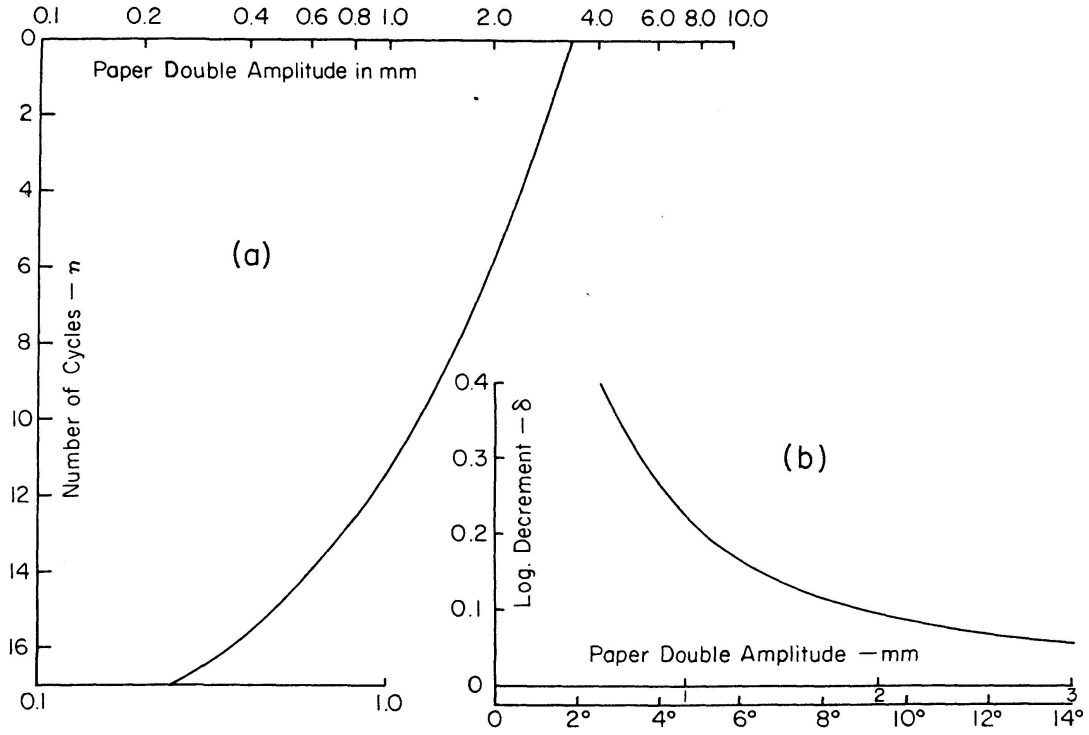

Fig. 5. Mechanical damping of the flexible rig.
(a) n vs. $\ln \alpha_0$, (b) δ vs. $2\alpha_0$.

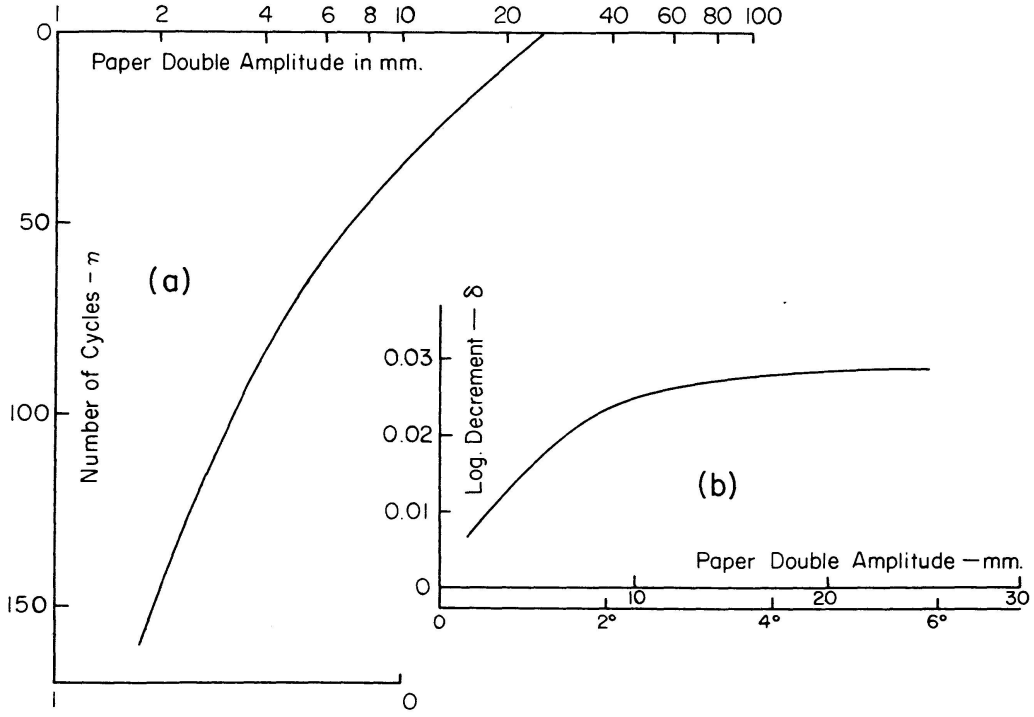

Fig. 6. Mechanical damping of the stiff rig.
(a) plot of n vs. $\ln \alpha_0$, (b) plot of δ vs. $2\alpha_0$.

tions. Parts of the model tests were repeated with the so-called "stiff rig". These two rigs are schematically shown in Fig. 4.

The major difference between the two supporting systems (rigs) is not only the different stiffnesses but also the great difference between the values of the torsional damping (measured in still air). There is greater damping capacity in the flexible rig than stiff rig as revealed by damping curves in Figs. 5 and 6. The difference in vertical damping was less pronounced. The typical logarithmic decrement of vertical oscillation was 0.01 for flexible and 0.006 for stiff rig respectively.

Attention is drawn to Fig. 5 and to the fact that the flexible rig exhibits a logarithmic decrement curve resembling dry friction at low amplitudes. This was some kind of unwanted surprise during the data reduction period.

Discussions of Test Results

Channel Sections

The torsional response curves for all the channel sections are presented in Fig. 7 about which the authors are quite enthusiastic. There are a number of interesting points to be observed:

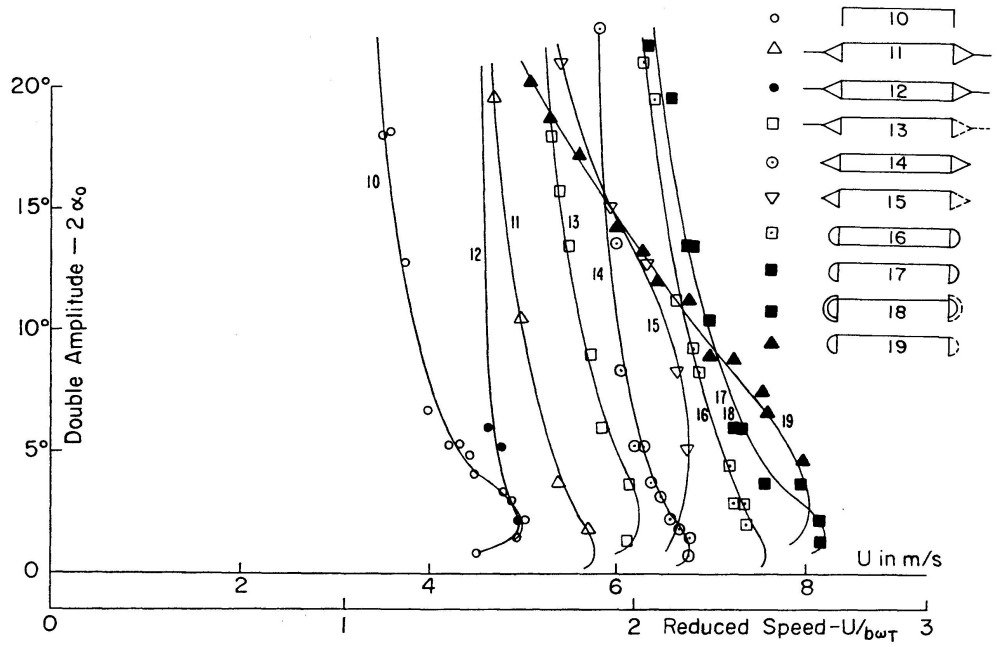

Fig. 7. The flutter torsional response. Models tested with the flexible-rig, $N_T/N_V = 1.7$.

1. A number of sections with fairings and without bottom plate yielded better results than the two box configurations (section Nos. 12 and 14) which are the only two models (in this work) for which airfoil classical theory may nearly hold.
2. All amplitude response curves are of the lean-back type. This is mainly attributed to the amplitude dependency of the system's damping as demonstrated in Fig. 5.
3. The alternating form of fairings attachment proved to provide as good, if not better, response results compared to those of the continuously attached fairings case.
4. Perhaps the most unexpected fact is that the basic channel section (No. 10) behaved as good as it did. According to Selberg's systematic tests (reference [6]) on similar sections one should expect a monotonically increasing response curve (not lean-back) and further the starting velocity would be only about half of the value obtained in the present tests. In all the tests the velocity of no return (when unlimited amplitudes are developed) was surprisingly high compared to section No. 14 which is commonly accepted as having excellent form quality.

All tests were carried out at three angles of attack. While the results for the case of zero angle are presented in Fig. 7 those of $+5$ and -5 degrees are tabulated in Table 1.

Sections 11 and 12 exhibited considerable static tilt (resembling divergence phenomenon) at relatively low wind velocities. The static tilting under the

Table 1. Catastrophic Flutter Speeds, Models Tested with Flexible-Rig, High Damping

Section Model		Flutter velocity m/s Angle of attack $+5°$	Angle of attack $-5°$	Angle of attack $0°$	% of improvement for $0°$ angle of attack
Section Model	No. 10*)	3,9		5,1	—
„	No. 11*)	4,5	4	5,85	14
„	No. 12	4,4	4	5,1	0
„	No. 13	4,8	7,2	6,5	27
„	No. 14	6,15	5,4	6,95	36
„	No. 15	4,65	8,4	6,85	34
„	No. 16	4,8	4,85	7,65	50
„	No. 17	4,8	6,25	8,25	61
„	No. 18	4,9	6,20	8,30	62
„	No. 19	5,20	8,2	8,05	58

*) All section models are numbered in Fig. 1.

wind load basically increased the effective angle of attack which caused the onset of flutter at an unusually low wind velocity for such sections. This is mainly due to the extra large value of the section width as it has been pointed out early by FRANDSEN [15].

As the primary object of the tests was to find simple means of improving stability, only the two best sections, Nos. 17 and 19, with the basic section No. 10 were tested also in the stiff rig, the results of which are presented in Fig. 8. The response curves in Fig. 8 are rather disappointing in the respect that the reduced damping has caused the models to oscillate at lower reduced velocities compared to the corresponding values obtained from the flexible

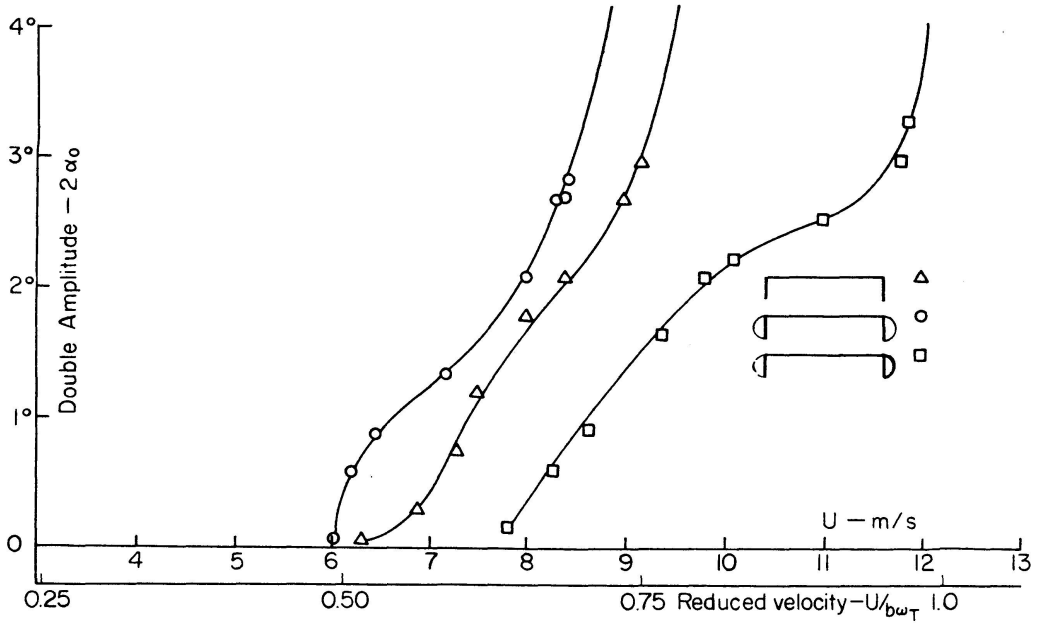

Fig. 8. The flutter torsional response. Model tested with stiff rig, $N_T/N_V = 1.7$.

rig. Furthermore the response curves of Fig. 8 are all of monotonicly increasing type. For the basic section, this is in agreement with Selberg's results, see reference [6].

An important conclusion to be drawn from the comparison of the previous two figures is the revealing fact that damping is one of the primary factors in the aerodynamic stability of unstreamlined objects.

Comparison of Figs. 7 and 8 with those presented in reference 6 indicates that the damping level in that reference, which is as a matter of fact not stated by Selberg, has been fairly low. It is therefore not unexpected that a series of old Norwegian girder-stiffened suspension bridges (with apparently high structural damping values) behave much better in reality than predicted by Selberg. It is to be feared that the damping in modern, "clean" and composite structures is fairly low which has a consequent reverse effect in the stabilizing effort.

The damping capacity of a structure is a perfidious quantity. It is hard to predict, and most complicated to improve, at least within the topological frame of the original structure.

It is felt that Selberg's damping results [13] of a series of the Norwegian short span bridges should be regarded with sound scepticism when speaking of modern structures.

The relative merits of the alternating type of fairings are maintained in the results of Figs. 8 and 9. This indicates that fairings might be the life-saver for channel sections provided the improvement asked for is not more than say 30%.

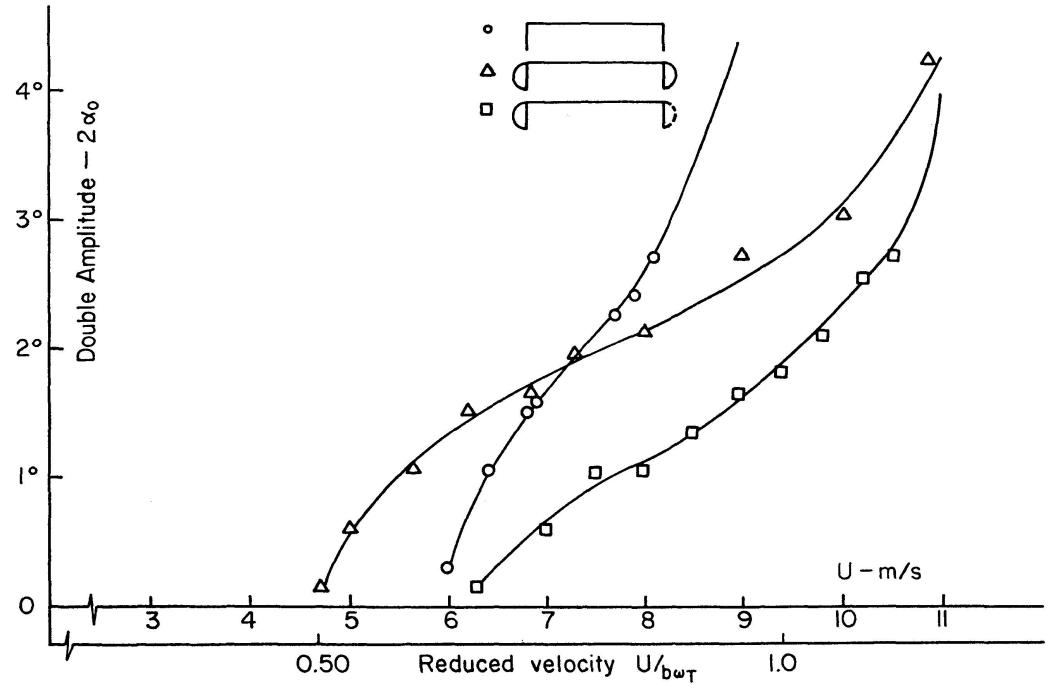

Fig. 9. The flutter torsional response. Models tested with stiff rig, $N_T/N_V = 1.3$.

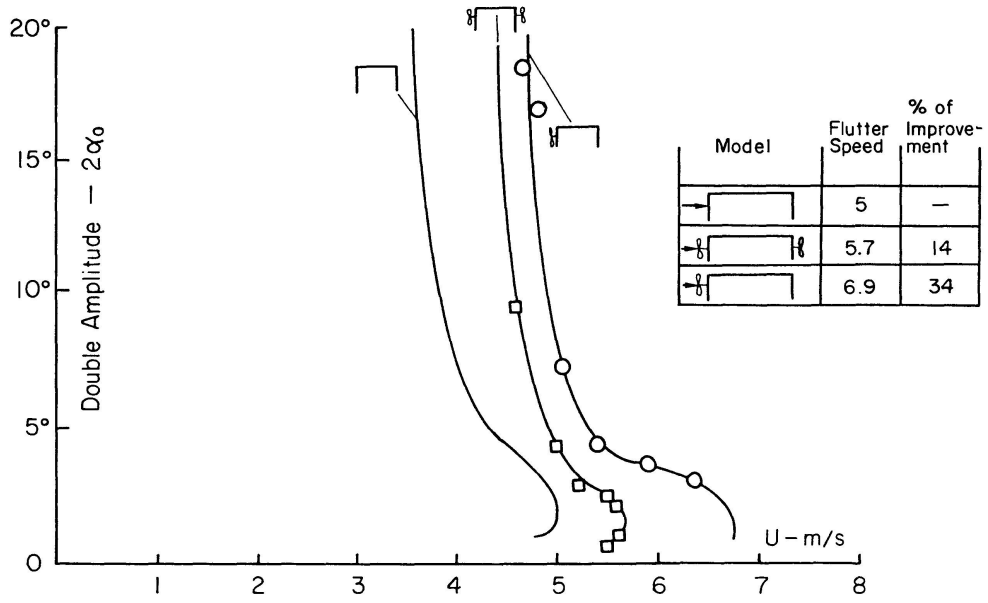

Fig. 10. Effect of propellers on the torsional response.

Response curves obtained with propellers are given in Fig. 10. The results show the benefit of modifying the flow pattern over the deck. The best of the two propeller arrangements gives approximately the same contribution to stabilization as the alternating type of fairings did.

It is however doubtful that a designer would be convinced, at this stage, about possible advantages of stabilizing propellers. They took funny, not least from the fact that the model versions (4 blades, outside diameter 100 mm i. e. more than twice the depth of the girder itself) resembled closely the propellers made by children playing with paper origami in jolly moments.

The response curves given for the family of sections derived from the channel form are those for the torsional oscillation which in fact was dominating. However it should be mentioned that in many cases some coupling with the vertical mode was observed.

The degree of coupling was indicated by the shift in the apparent axis of rotation. The shift of axis relative to longitudinal axis was quite high for section Nos. 11, 12, 14 and 16 on one extreme and very small for the basic channel section on the other hand.

H-Sections

While addition of suitable fairings to the channel section improved the aerodynamic stability to a marked extend, this beneficial effect is proved to be less pronounced when the basic section is of an *H*-form as shown in Figs. 11 and 12. Moreover, the reduced wind velocities obtained for the three members of the *H*-section family are so low compared to the corresponding channel section results that no motivation for further improvement of the *H*-section is found in this work.

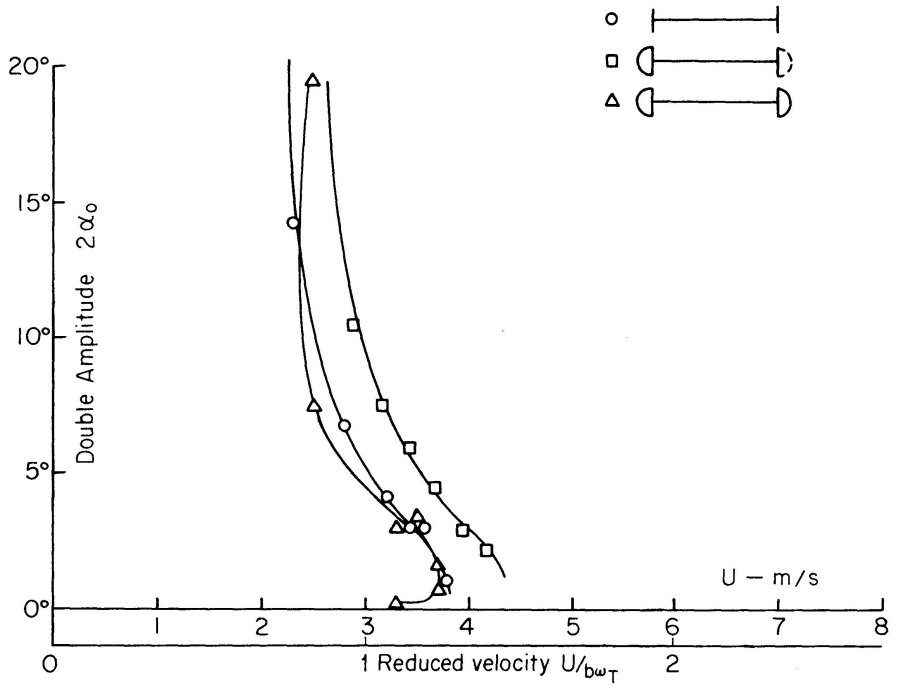

Fig. 11. The flutter torsional response. Models tested with flexible rig, $N_T/N_V = 1.8$.

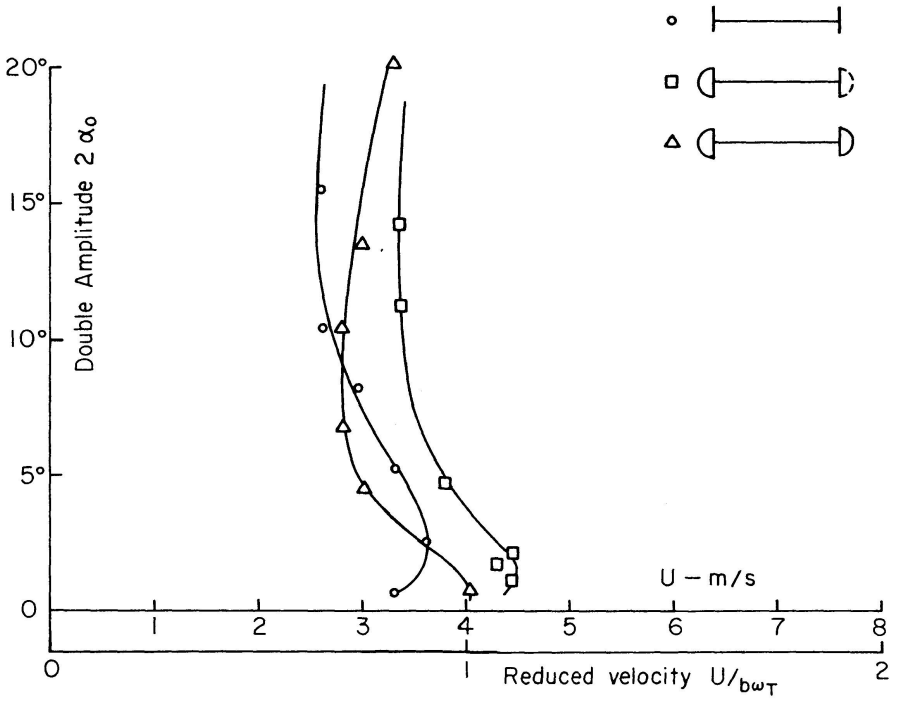

Fig. 12. The flutter torsional response. Model tested with flexible rig, $N_T/N_V = 1.3$.

Comments on Extrapolation of Model Results from one Level of Damping to Another

In two earlier papers [16], [17] SCANLAN and SABZEVARI proposed the following mathematical model for analysing the suspension bridge flutter problem:

$$\ddot{h} + 2\zeta_h \omega_h \dot{h} + \omega_h^2 h = H_1 \dot{h} + H_2 \dot{\alpha} + H_3 \alpha, \tag{1}$$

$$\ddot{\alpha} + 2\zeta_\alpha \omega_\alpha \dot{\alpha} + \omega_\alpha^2 \alpha = A_1 \dot{h} + A_2 \dot{\alpha} + A_3 \alpha, \tag{2}$$

where the vertical and rotational displacements are represented by h and α respectively. ζ_r is mechanical damping ratio with respect to critical (in $r = h$ or α degree of freedom) and ω_r denotes natural undamped frequency ($r = h$ or α).

H_i and A_i ($i = 1, 2, 3$) are aerodynamic coefficients to be evaluated experimentally for each bridge deck model as a function of reduced velocity. Due to inherent nonlinearities in the aerodynamics involved these coefficients are also amplitude dependent, but for the present time those values appropriate for the on-set of flutter instability are considered. A catalogue of such coefficients is given by SCANLAN and TOMKO [18].

The attention is now drawn to the problem of predicting the changes in flutter velocity due to any change in the mechanical damping value. This discussion is limited to cases where damping plays an important role such as the case of the basic H- or channel sections dealt with experimentally in this work. From the experiences with these two sections it is correct enough to put $h = 0$, $A_1 = 0$ (case of no bending flutter) and $A_3 = 0$ (because of no significant deviation in torsional frequency from that of no wind conditions). Hence Eqs. (1) and (2) are reduced to:

$$\ddot{\alpha} + 2\left(\zeta_\alpha - \frac{A_2}{2\omega_\alpha}\right)\omega_\alpha \dot{\alpha} + \omega_\alpha^2 \alpha = 0. \tag{3}$$

Hence the effective damping of the model motion with wind blowing and that of the prototype are respectively:

$$\gamma_{model} = \left(\zeta_\alpha - \frac{A_2}{2\omega_\alpha}\right)_{model} \tag{4}$$

and

$$\gamma_{prototype} = \left(\zeta_\alpha - \frac{A_2}{2\omega_\alpha}\right)_{prototype}. \tag{5}$$

Combining Eqs. (4) and (5) as to eliminate the aerodynamic term, thus resulting in:

$$\gamma_{prototype} = \gamma_{model} + [(\zeta_\alpha)_{prototype} - (\zeta_\alpha)_{model}] \tag{6}$$

or in terms of the corresponding logarithmic increment (or decrement) we will have:

$$\delta_{prototype} = \delta_{model} + [(\delta_\alpha)_{prototype} - (\delta_\alpha)_{model}]. \tag{7}$$

Expression (7) indicates that the logarithmic decrement (or increment) of the prototype is that experienced in the tunnel with model mechanical damping being subtracted and the prototype damping substituted. Of course the same argument is also valid for uncoupled bending flutter provided the corresponding values of vertical damping are substituted in Eq. (7).

So by such a procedure it is possible to predict the horizontal shift of points of the response curve on $2\alpha_0 - \frac{U}{b\omega}$ plots caused by not fulfilling of the similarity requirement of having identical damping values between model and prototype, see SCRUTON [5] and SELBERG [13].

The prediction of the behaviour of the basic channel section at $+5$ degrees angle of attack and for higher level of damping is made from the measurement of logarithmic increment on the same configuration but at a much lower damping value. The plot of logarithmic increment for section No. 10 tested at $+5°$ angle of wind incident is presented in Fig. 13. The amplitude level for which the plot of Fig. 13 is valid is about 2 degrees double amplitude.

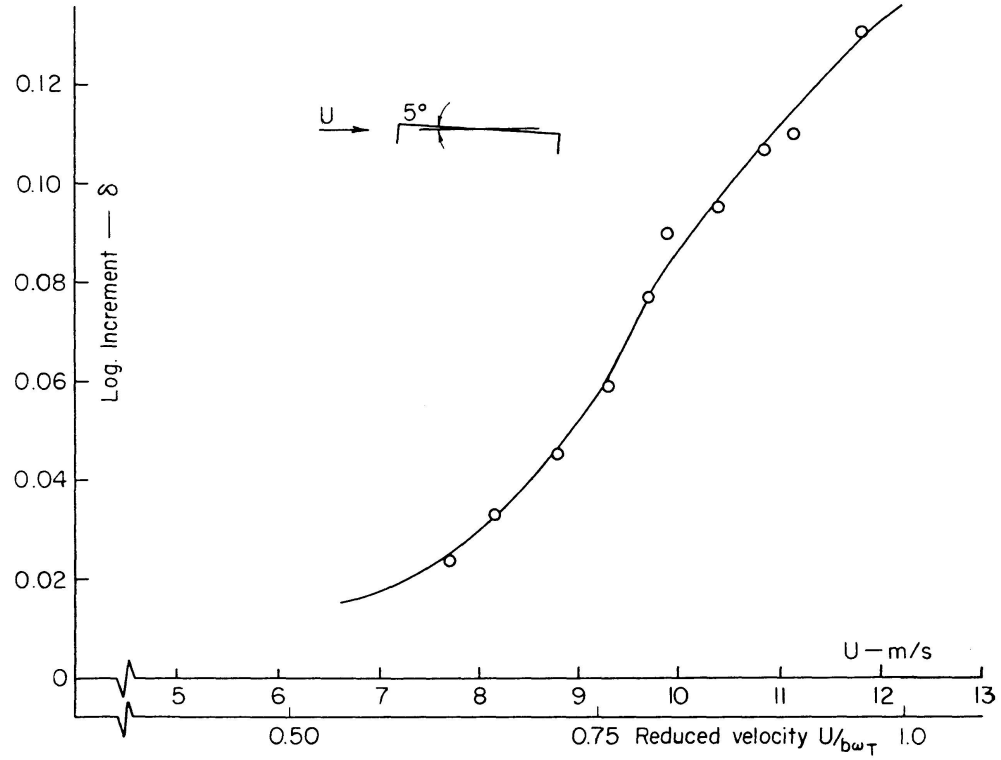

Fig. 13. Plot of logarithmic increment vs. velocity for the channel section at 5° angle of attack.

Conclusions

The following conclusions are drawn from the investigations carried out in this work.

1. The aerodynamic stability of simple channel sections can significantly be improved by attachment of suitable fairings to its side faces. While fairings, within the range of frequency ratios considered in this work, proved to render stabilizing effects to channel section, round- or sharp-edge fairings did not have marked effect on that of the *H*-section.

2. For even the fairings to be effective, the bridge deck must be torsionally sound, that is, bridges with very small torsional stiffness ($N_T/N_V = 1.3$) have little chance of withstanding to even moderate wind velocities. Thus for any type of girder-stiffened design where the lateral stiffening structure lies essentially in one plane, addition of a second set of lateral stiffeners for increasing the torsional resistance is unavoidable. This conclusion is in conformity with the well documented records of aeroelastic oscillations of Old Tacoma Narrows and the Golden Gate suspension bridges.
3. It is interesting to observe that the addition of fairings in small lengths in an on-and-off pattern has yielded equally good, if not better, results as compared to those with continuous fairings.
4. A simple technique is described for estimating the on-set of flutter (single degree) for a prototype from the model tests with damping values not necessarily equal to that of the prototype.

Notation

A_i Aerodynamic coefficient.
b Deck cord of basic sections No. 10 or 20.
H_i Aerodynamic coefficient.
h Vertical displacement.
n Number of cycles.
N_i Frequency ($i = T, V$).
U Wind velocity.
α Rotational (torsional) displacement.
δ Logarithmic decrement or increment.
ζ_r Mechanical damping ratio with respect to critical ($r = h$ or α).
γ_r Recorded damping ratio (r = model, prototype).

Acknowledgements

The authors wish to thank Professor Arne Selberg for his worthwhile comments and suggestions during the course of this work. The Royal Norwegian Council for Applied and Industrial Research (NTNF) is acknowledged with gratitude for the research followship offered to Dr. Ali Sabzevari for carrying out this study. Assistance of Mr. Olav Haldorsen in preparing the models and the careful typing of Mrs. Thuri Mathisen are also acknowledged.

References

1. SMITH, F. C., and VINCENT, G. S.: Aerodynamic Stability of Suspension Bridges, Part II, Mathematical Analysis, Bulletin No. 116, Part 2, p. 14–20, University of Washington Engineering Experiment Station, Oct. 1950.
2. FARQUHARSON, F. B., VINCENT, G. S. and SMITH, F. C.: Aerodynamic Stability of Suspension Bridges, Bulletin No. 116, Parts 1–5, University of Washington Engineering Experiment Station, 1949–1954.
3. VINCENT, G. S.: Summary of Laboratory and Field Studies in U.S. on Wind Effects on Suspension Bridges, Symp. Wind Effects on Buildings and Structures, N.P.L., England, paper 20, 1965.
4. BLEICH, F. et al: The Mathematical Theory of Vibration in Suspension Bridges, Bureau of Public Roads, 1950.
5. SCRUTON, C.: Experimental Investigation of Aerodynamic Stability of Suspension Bridges with Special Reference to Proposed Severn Bridge, Proc. Institution of Civil Engineers, London, Vol. 1, Part 1, No. 2, March 1952.
6. SELBERG, A.: Oscillation and the Aerodynamic Stability of Suspension Bridges, Acta Polytechnica Scandinavia, Ci 13, 1961.
7. HIRAI, A.: Aerodynamic Stability of Suspension Bridges Under the Influence of Wind Load, Bauingenieur, Berlin, Vol. 31, No. 11, Nov. 1956.
8. KLÖPPEL, K. und WEBER, G.: Teilmodelversuche zur Beurteilung des aerodynamischen Verhaltens von Brücken, Der Stahlbau, Berlin, Heft 3 und 4, 1963.
9. STÜSSI, F. und ACKERET, J.: Zum Einsturz der Tacoma-Hängebrücke. Schweiz. Bau, No. 117, 1941.
10. Proceedings of International Symposium on Wind Effects on Buildings and Structures, N.P.L. 26–28 June 1963, Teddington, England.
11. Prooceedings of International Symposium on Suspension Bridges, Laboratório Nacional de Engenharia Civil, 7–10 November 1966, Lisbon, Portugal.
12. Proceedings of Third International Conference on Wind Effects on Building and Structures, Tokyo University, 6–11 September 1971, Tokyo, Japan.
13. SELBERG, A.: Damping Effect in Suspension Bridges, IABSE Publication, Vol. 10, 1950.
14. WARDLAW, R. L.: Some Approaches for Improving the Aerodynamic Stability of Bridge Road Decks, Proc. 3. International Conference on Wind Effects on Buildings and Structures, Tokyo, Paper IV-28, September 1971.
15. FRANDSEN, A. G.: Wind Stability of Suspension Bridges, Application of the Theory of thin Airfoils, International Symposium on Suspension Bridges, paper No. 43, Lisbon 1966.
16. SABZEVARI, A. and SCANLAN, R. H.: Aerodynamic Instability of Suspension Bridges, Proc. ASCE Journal of Engineering Mechanics Division, Vol. 94, No. EM 2, April 1968.
17. SCANLAN, R. H. and SABZEVARI, A.: Experimental Aerodynamic Coefficients in the Analytical Study of Suspension Bridge Flutter, Journal of Mechanical Engineering Science, Vol. 11, No. 3, June 1969.
18. SCANLAN, R. H. and TOMKO, J. J.: Airfoil and Bridge Deck Flutter Derivatives, Proc. ASCE Journal of Engineering Mechanics Division, December 1971.

Summary

The aeroelastic behaviour of simple girder-stiffened suspension bridges is revisited. It is shown that while attachment of round- or sharp-edge fairings to wind and leeward sides could improve the aerodynamic stability of channel sections, fairings would not affect that of H-sections, at least within the frequency ratio range of $N_T/N_V = 1.3 - 1.8$.

Extrapolation of a bridge deck behaviour from that of the corresponding model tested at a different level of damping in the wind tunnel is discussed.

Résumé

On revoit dans ce travail le comportement aérodynamique des ponts suspendus à poutre raidissante simple. On montre que l'emploi de carénages arrondis ou aigus pour le côté exposé au vent et pour le côté abrité du vent peut augmenter la stabilité aérodynamique des sections en U, alors que pour les sections en double Té, elle n'est pas influencée par les carénages, du moins pour le domaine des rapports de fréquence $N_T/N_V = 1{,}3 - 1{,}8$.

On discute ensuite l'extrapolation pour le comportement d'un tablier de pont à partir d'essais sur modèles testés en soufflerie à différents niveaux d'amortissement.

Zusammenfassung

Das aeroelastische Verhalten einfacher trägersteifer Hängebrücken wird neuerlich untersucht. Es wird gezeigt, dass die Anbringung runder oder scharfkantiger Enden an den Wind- und Leeseiten die aerodynamische Stabilität von Kanalquerschnitten verbessern konnte, während sie für H-förmige Querschnitte nicht beeinflusst wird, zumindest nicht innerhalb des Frequenzverhältnisses von $N_T/N_V = 1{,}3 - 1{,}8$.

Es wird dann die Extrapolation des Verhaltens einer Brückenfahrbahn gegenüber jenem eines entsprechenden Modells bei Versuchen von verschiedenen Dämpfungsniveaus im Windkanal diskutiert.

On the Shear Capacity of Girder Webs

De la capacité de cisaillement des âmes de poutres

Über die Schubkapazität von Trägerstegen

ARNE SELBERG
Professor, The University of Trondheim, Norway

The post critical shear capacity of webs has been known for a long time [1, 2, 3]. However, a simple calculation was first started by BASLER [4, 5] when he introduced the shear capacity as the sum of the shear taken by shear stress in the web and the shear taken by a tension diagonal. There has been raised some critic against Basler's equations, for instance by FUJII [9]. Considerable work has been done on improvements of Basler's equations, notably by ROCKEY and ŠKALOUD [6, 7, 8].

In the following will be demonstrated some errors made by BASLER. Further on a more general deduction will be given, which includes the corrected Basler equations and the Rockey-Škaloud equations.

In Fig. 1 is given a girder with tension field due to shear load into the post critical range. BASLER's idea that the shear capacity is the sum:

$$V_u = V_\tau + V_d \tag{1}$$

is generally accepted. V_τ is the shear force taken by the shear stresses in the

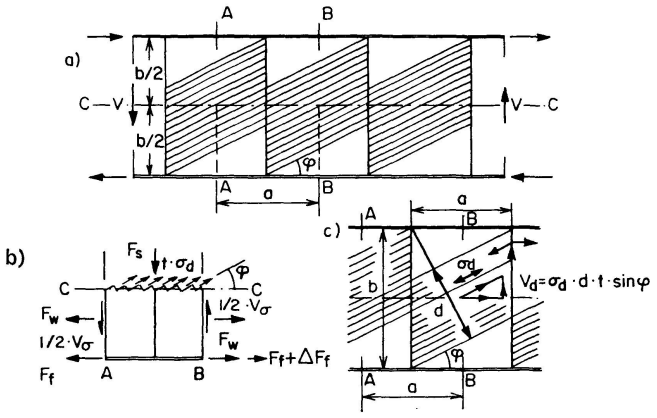

Fig. 1. Equilibrium due to shear force V.

web and V_d is the shear force taken by the tension diagonal or tension field, see Fig. 1.

For the V_τ BASLER postulates:

$$V_\tau = \tau_c b t, \tag{2}$$

where τ_c is the critical shear buckling stress:

$$\tau_c = \tau_{cE} = \frac{\pi^2 E}{12(1-\nu^2)}\left(\frac{t}{b}\right)^2 k_s \tag{2a}$$

for an elastic material. $\qquad k_s = 5{,}34 + 4\left(\frac{1}{\alpha}\right)^2.$

BASLER assume that the development of a tension field has no effect on the value of τ_c. Accordingly the ultimate capacity corresponds to the angle ϕ giving max V_u or V_d:

$$\frac{dV_u}{d\phi} = \frac{dV_d}{d\phi} = 0. \tag{3}$$

As will be seen from Fig. 1c we have

$$V_d = \sigma_d d t \sin\phi, \tag{4}$$

where

$$d = b\cos\phi - a\sin\phi \tag{4a}$$

and

$$\frac{dV_d}{d\phi} = 0 = \frac{d}{d\phi}(\sigma_d dt\sin\phi) = \sigma_d t\frac{d}{d\phi}(b\cos\phi\sin\phi - a\sin^2\phi). \tag{5}$$

BASLER neglects obviously that σ_d will be a function of ϕ, as seen from Eq. (8). However, this error will be small, as easily controlled.

The error may in rare cases mean up to 5% of V_d and is consequently of no importance.

Eq. (5) gives:

$$\operatorname{tg}\phi = \sqrt{1+\alpha^2} - \alpha; \qquad \alpha = \frac{a}{b} \tag{6}$$

and

$$V_d = \sigma_d t b \frac{1}{2(\sqrt{1+\alpha^2}-\alpha)} = \frac{1}{2}\sigma_d t b(\sqrt{1+\alpha^2}-\alpha) = \frac{1}{2}\sigma_d t b \operatorname{tg}\phi. \tag{7}$$

BASLER deduced the equation:

$$V_d = \sigma_d t b \frac{1}{2\sqrt{1+\alpha^2}}.$$

This result is due to the incomplete picture of forces in Fig. 1b used by BASLER in his deductions [9].

As readily seen, Eq. (7) give results well below the Basler equation.

Between σ_d and τ we have the following equation due to the deviation yield hypothesis:

$$\sigma_d = \sqrt{\sigma_y^2 - \tau_c^2\left[3 - \left(\frac{3}{2}\sin 2\phi\right)^2\right]} - \frac{3}{2}\tau_c \sin 2\phi . \tag{8}$$

As given by BASLER, the following equation:

$$\sigma_d \approx \sigma_y - \sqrt{3}\,\tau_c \tag{8a}$$

may be used without any important loss of accuracy. However, we shall here use the complete Eq. (8).

Introducing this we get for V_u:

$$V_u = \sigma_d t b \tfrac{1}{2} \operatorname{tg}\phi + \tau_c t b \tag{9}$$

or $$V_u = \sigma_y t b\left\{\frac{1}{2}\operatorname{tg}\phi\left[\sqrt{1 - \left(\frac{\tau_c}{\sigma_y}\right)^2\left(3 - \frac{3}{2}\sin 2\phi^2\right)} - \frac{3}{2}\left(\frac{\tau_c}{\sigma_y}\right)\sin 2\phi\right] + \frac{\tau_c}{\sigma_y}\right\}. \tag{9a}$$

The angle ϕ is given by Eq. (6) and τ_c is known from (2a) for an elastic material. For stresses above the proportionality limit we may introduce.

$$\tau_c = \tau_y - \left(\frac{1}{\kappa} - 1\right)\frac{\tau_p^2}{\tau_{cE}}, \tag{10}$$

where $\tau_y = \frac{1}{\sqrt{3}}\sigma_y$; $\tau_p = \kappa\tau_y$ is the proportionality limit.

For most structural steel $\kappa \approx 0.8$, but due to welding stresses, out of planes of the web etc. $\kappa = 0.5$ is a better value for technical use. In the diagrams, Figs. 2 and 7, the value $\kappa = 0.8$ is used.

Fig. 2 gives the values of $\frac{V_u}{V_y} \approx \frac{\tau_u}{\tau_y}$ for webs with varying $b/t = \beta$ values and $a/b = \alpha$ values 1.0 and 2.0.

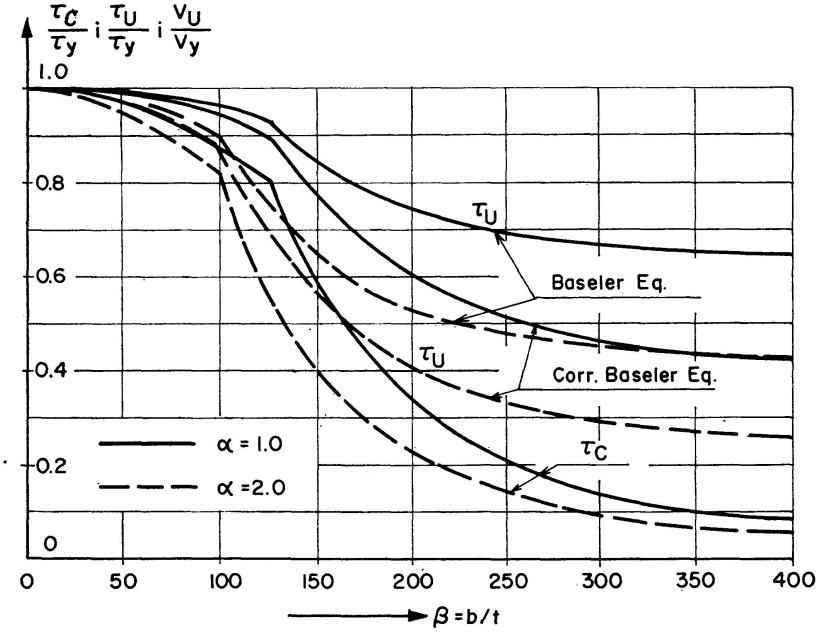

Fig. 2. Diagram of V_u/V_y for $\alpha = a/b$ values 1.0 and 2.0 and web slenderness $\beta = b/t$, giving original and corrected Basler results.

As will be seen from Fig. 2 the corrected Basler equation (9) gives considerably less shear capacity than the original Basler equation. Especially will it be so for thin webs $\beta < 200$. Eq. (9) is also given by FUJII [9].

The original Basler equations give results which are in good agreement with experiments, especially for α values between 1 and 1.5. With the error in V_d corrected a V_u corresponding to the experiments will only be possible with an increased shear force V_τ, and it is little reason to believe that τ_c will not be affected by a tension field or tension diagonal across the web, which in turn gives a raise to V_τ.

In Fig. 3 is given a diagram for the shear buckling τ_s' as effected by a uniform tension in one direction [10, 11]. As will be seen from Fig. 3 the "critical" shear stress may be considerably greater than given by (2a).

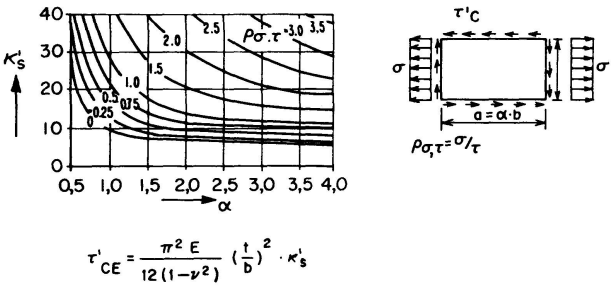

Fig. 3. Effect of uniform tension on shear buckling stress τ_{cE}.

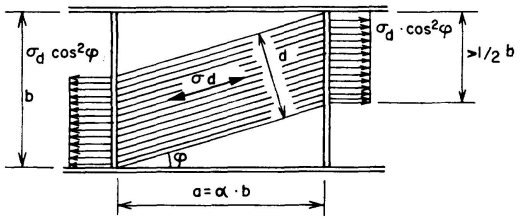

Fig. 4. Tension field or diagonal in shear loaded web.

In Fig. 4 is drawn for a comparison a sketch of the tension field or diagonal. It is readily seen that the effect must be very much the same as in Fig. 3.

We may for instance assume the following expression for the shear buckling stress τ_c.

$$\tau_c = \tau_{c4} + f(\sigma_d; \beta; \alpha),$$

where τ_{c4} is the critical shear stress in a rectangular plate without any tension field. σ_d is given by Eq. (8).

However, just to demonstrate the arbitrariness of the Basler assumption concerning τ_c, we shall handle it in a different manner.

The tension field, see Fig. 4, will act as an elastic support on the web, like a hammock. As a simplification we consider this effect as equal to a support which follows the middle of the tension field, see Fig. 5. We have then two trapezoidal plates AEE'D and BEE'C instead of the original plate ABCD. The effect of this support might increase τ_{cE} up to 4 times the previous value, as will be seen by substituting the two trapezoids by two rectangles.

However, it will emphasize the arbitrariness better to calculate the critical shear load of triangular plates AEF and CE'F' [12]. The stiffeners, BE and DE' will have some effect, but a calculation of critical shear stress τ_c as for a triangle is a simplification on the conservative side. With d and ϕ known,

Eqs. (4a) and (6), we get:

$$l = \tfrac{1}{2}(b \operatorname{cotg}\phi + a); \qquad e = \tfrac{1}{2}(b \operatorname{cotg}\phi - a) \tag{11}$$

and

$$\tau_{cE} = \frac{\pi^2 E}{12(1-\nu^2)}\left(\frac{t}{l}\right)^2 k_s', \tag{12}$$

where k_s' is given by:

$$k_s' \approx 5.34(1.0+\xi^2) + \frac{1.8\,\xi^2}{1.0+\xi}; \qquad \xi = \operatorname{cotg}\phi. \tag{13}$$

Eq. (13) is an approximation of the results given in [12]. Within the elastic range $\tau_c = \tau_{cE}$, in the post proportionality range τ_c is given by Eq. (10).

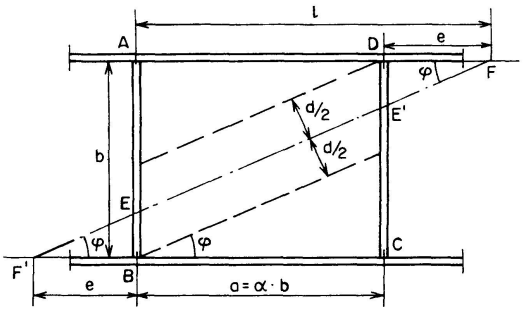

Fig. 5. Effect of tension field substituted by a support CC'.

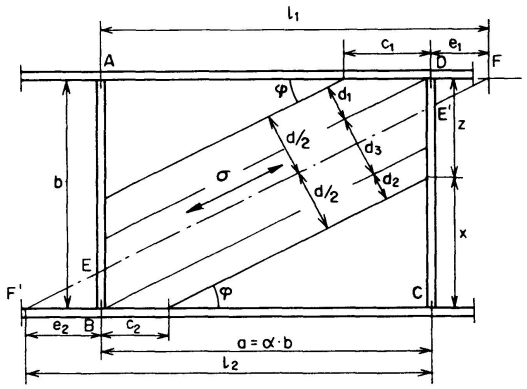

Fig. 6. Tension field with different stiffness of flanges.

With τ_c given, σ_d is found from Eq. (8) and V_u from Eq. (9). In Fig. 7 is given the results for a calculation with α values 1.0 and 2.0. The curves to be compared with the results in Fig. 2 are marked with $c/a = 0$.

In a series of publications [6, 7, 8] ROCKEY and ŠKALOUD have made investigations on the shear capacity of webs. They introduced a tension field which is symmetrical about the diagonal, and the width of which is given by the stiffness of the upper and lower flanges. The angle ϕ is given by $\operatorname{tg}\phi = b/a$.

This model is an unnecessary limitation on the tension diagonal. We shall here investigate the conditions shown in Fig. 6. c_1 and c_2 are defined by the stiffness of the flanges, see Eq. (23).

The tension diagonal d is devided in 3 strings. We have:

$$\begin{aligned} d &= d_1 + d_2 + d_3, \\ d_1 &= c_1 \sin\phi; \quad d_2 = b\cos\phi - a\sin\phi; \quad d_3 = c_2 \sin\phi \end{aligned} \tag{14}$$

and for the shear capacity V_d.

$$V_d = \sigma_d t\left\{c_1\left(1-\frac{c_1}{2a}\right)\sin^2\phi + b\cos\phi\sin\phi - a\sin^2\phi + c_2\left(1-\frac{c_1}{2a}\right)\sin^2\phi\right\}$$

or

$$V_d = \sigma_d t\, b\{\cos\phi\sin\phi - \alpha_c \sin^2\phi\}; \qquad \alpha_c = \frac{a}{b}\left(1 - \frac{c_1+c_2}{a} + \frac{c_1^2+c_2^2}{2a^2}\right) \tag{15}$$

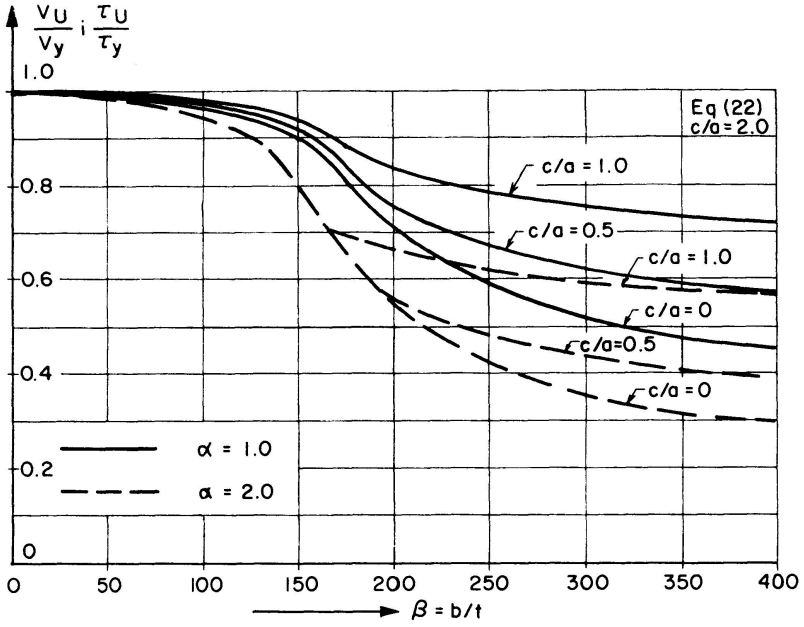

Fig. 7. V_u/V_y diagram $\alpha = 1$ and 2; $\beta = b/t$; $c/a = 0$; 0.5 and 1.0, due to Eq. (19).

with further modification:

$$V_u = \sigma_d t b \frac{(1 - \alpha_c \operatorname{tg}\phi)\operatorname{tg}\phi}{1 + \operatorname{tg}^2\phi} + \tau_c t b. \tag{16}$$

The deduction of Eqs. (14)–(16) imply $\operatorname{tg}\phi \leqq b/a$. However, it can be proved that the equations are valid for $\operatorname{tg}\phi \lesseqgtr b/a$.

The special situation investigated by ROCKEY and ŠKALOUD [6, 7, 8] and others is given by $c_1 = c_2$ and $\operatorname{tg}\phi = b/a$. If we introduce this in Eqs. (15) or (16), we get the Rockey solution:

$$V_u = 2\sigma_d t c \sin^2\phi \left(1 - \frac{c}{2a}\right) + \tau_c t b. \tag{17}$$

The relation between σ_d and τ_c is given by Eq. (8).

If we, like BASLER, neglect the influence of ϕ on the stresses σ_d and τ_c we get from Eq. (16):

$$\frac{dV_u}{d\phi} = \frac{dV_d}{d\phi} = 0; \quad \text{and} \quad \operatorname{tg}\phi = \sqrt{1 + \alpha_c^2} - \alpha_c; \quad \alpha_c = \frac{a}{b}\left(1 - \frac{c_1 + c_2}{a} + \frac{c_1^2 + c_2^2}{2a^2}\right) \tag{18}$$

and the following simple formula is deduced:

$$V_u = \sigma_d t b \tfrac{1}{2} \operatorname{tg}\phi + \tau_c t b, \tag{19}$$

which is identical to formula (9); the value ϕ beeing different. τ_c is given by Eqs. (12) and (10); σ_d by Eq. (8).

In Fig. 8 is shown the results of calculations with Eqs. (16) and (19). The values given by Eq. (19) are given in the centre of the diagrams, and then Eq. (16) is solved for different ϕ values, $\phi + \Delta\phi$. As will be seen Eq. (19) is

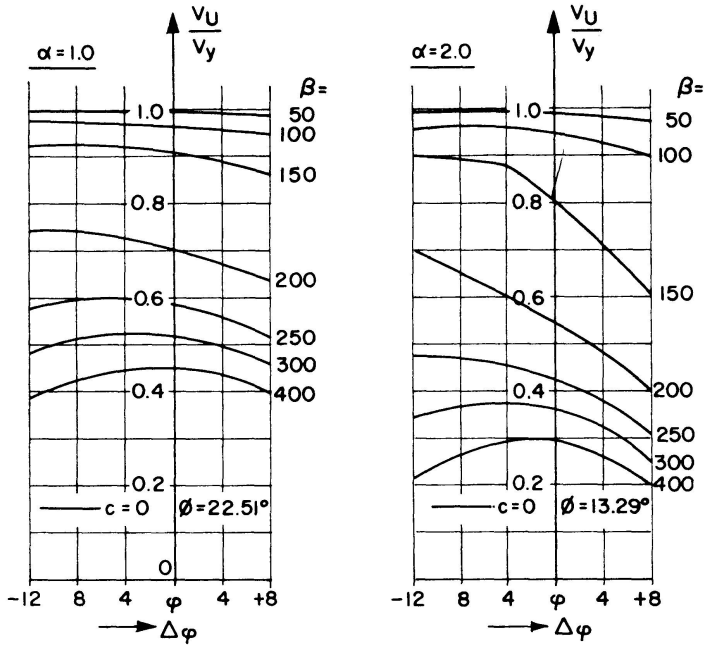

Fig. 8. Comparison of results from Eqs. (16) and (19). $\alpha = 1.0$ and 2.0; $c/a = 0$.

fairly good in most cases, the maximum value of V_u are always greater than given by Eq. (19).

In Fig. 7 is given the results V_u/V_y for $\alpha = 1.0$ and 2.0 and $c/a = 0$; 0.5; 1.0; with $c_1 = c_2$ we have $c = 2c_1$; with $c_1 \leqq c_2$ we have:

$$c = 2a - \sqrt{2}\sqrt{(a-c_1)^2 + (a-c_2)^2} \tag{20}$$

with absolute stiff flanges we get $c_1 = c_2 = a$, $c = 2a$, $\operatorname{tg}\phi = 1$ and

$$V_d = \tfrac{1}{2}\sigma_d t b, \tag{21}$$

which result was obtained by WAGNER [2], and the ultimate capacity for a very thin web, $\beta > 400$, with stiff flanges is:

$$V_u = V_d = \frac{1}{2}\sigma_y t b \quad \text{or} \quad \frac{V_u}{V_y} = \frac{\frac{1}{2}\sigma_y}{\tau_y} = \frac{\sqrt{3}}{2} = 0.865. \tag{22}$$

The bending moment in the flanges may be controlled by the following equations, see Fig. 9.

$$c_1^2\left(1 - \frac{c_1}{2a}\right)^2 = \frac{4M_{Fy}}{t\sigma_d \sin^2\phi} \tag{23}$$

and the yield hinge in the flange is placed at

$$x = c_1 - \frac{c_1^2}{2a}. \tag{23a}$$

Normally the flanges and in consequence the yield moment in the flange M_{Fy} is known, and c_1 is found by a trial and error method as σ_d will be a function of c_1.

In general the c_1 and c_2 values will be small compared to a. However, in some structures as for instance composite beams one of them may be of considerable importance, see Fig. 10.

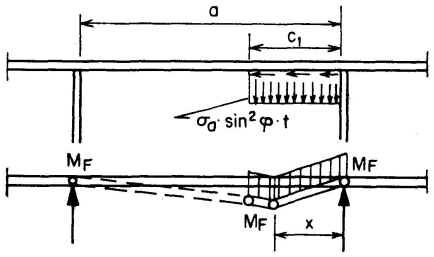

Fig. 9. Bending of flange.

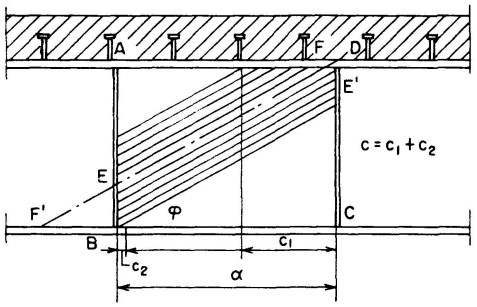

Fig. 10. Bending of flanges in a composite beam.

In this situation the triangles AEF and CE'F are different in size, and a mean value:

$$\tau_{cE} = \sqrt{\tau_{cE_1}\tau_{cE_2}} \tag{24}$$

is better used for calculating V_τ.

The triangles are defined by the following expressions, see Fig. 6:

$$\begin{aligned} e_1 &= \frac{d}{2}\frac{1}{\sin\phi} - c_1; \qquad l_1 = a + e_1, \\ e_2 &= \frac{d}{2}\frac{1}{\sin\phi} - c_2; \qquad l_2 = a + e_2. \end{aligned} \tag{25}$$

d is given by Eq. (14).

The method demonstrated above is compared to a number of tests with astonishing good results, which in itself is really interesting compared to the arbitrariness in the assumptions leading to the method.

In the following shall only be referred the results from two tests H_1 and H_2 in [13].

The relation V_{exp}/V are for this beams:

	Basler	Corr. Basler	Fujii	[13]	This method	Rockey
$H_1\ V_{exp}/V$ =	1.05	1.24	1.09	1.00	1.09	2.85
$H_2\ V_{exp}/V$ =	1.04	1.26	1.02	0.95	1.03	2.16

V_{exp} is the shear capacity observed by the experiment. V is the calculated capacity when the moment effect is considered as well. In the control is the effect of the moment except for the Rockey method handled as suggested by Basler [15]. The beams are characterized by the following data:

$$H_1: \quad \alpha = 2.0;\ \beta = 249; \qquad H_2: \quad \alpha = 3.0;\ \beta = 242.$$

In Fig. 11 is given the load deflection diagram for this beams. As will readily be seen the ultimate loads are connected with great deformations. In reality a structure will be destroyed before deformations of this magnitude can take place.

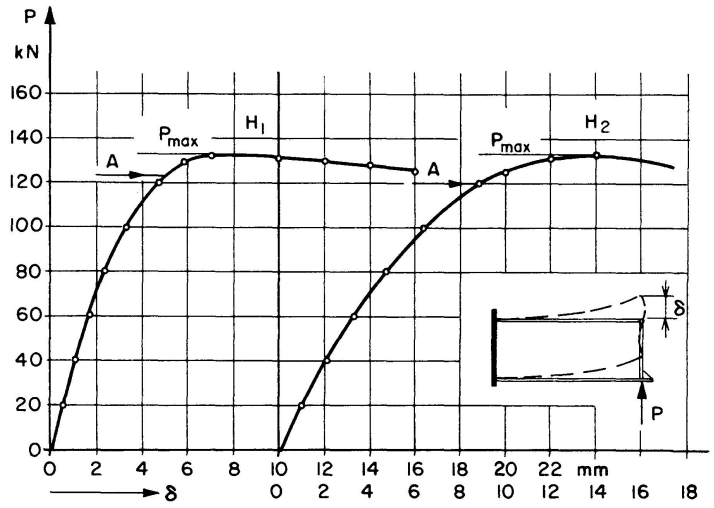

Fig. 11. Load deflection of test beams H_1 and H_2 |13|.

For design work the load capacities at the beginning of the really great deformations, f. inst. points A in Fig. 11, are the important ones. A design procedure founded on the theory of plates with large deformations as f. inst. given by [14] or [16] seems to fulfil the purpose. A load limit where the first yielding take place in the middle plane of the plate will satisfy any design purpose, and the large deflection elastic plate theory will still be sufficiently valid. It may be well to keep in mind that the web failure always is a result of yield in tension, the web "stability" is not the main problem, stability failures are due to failure in f. inst. the flanges which is quite a different problem.

Notation

a = Length of web panel, distance between vertical stiffeners.
b = Distance between flanges.
$c_{1,2}$ = Length of tension field action on upper resp. lower flange.
$c \approx c_1 + c_2$. Eq. (20).
d = Width of tension field.
$e_{1,2}$ = Where center line of tension field cross the flanges.
t = Web thickness.
$\alpha = a/b$.
$\beta = b/t$.
$\kappa = \tau_p/\tau_y$.
σ_d = Stress in tension field.

τ_c = Critical shear stress.
τ_{cE} = Critical shear stress, elastic material.
ϕ = Angle between tension field and flanges.
V = Shear force. Index u, y, d, τ refer to ultimate, yield, tension diagonal and shear tension.

References

1. Rode, H. H.: Beitrag zur Theorie der Knickerscheinungen. Eisenbau 1916.
2. Wagner, H.: Ebene Blechwandträger mit sehr dünnem Stegblech. Zeitschr. f. Flugtechnik u. Motorluftschiffahrt 1929.
3. Bergmann, S. G. A.: Behaviour of Buckled Rectangular Plates under the Action of Shearing Forces. Stockholm 1948.
4. Basler, K.: Strength of Plate Girders. Ph. D. Thesis, Lehigh Univ. 1959.
5. Basler, K.: Strength of Plate Girders in Shear. ASCE, Proc. October 1961.
6. Rockey, K. C.: The influence of flange stiffness upon the post buckled behaviour of web plates subjected to shear. Engineering, Dec. 1957.
7. Rockey, K. C., Škaloud, M.: Influence of Flange Stiffness upon the Load Carrying Capacity of Webs in Shear. Final Report 8th Congress IABSE, New York 1968.
8. Rockey, K. C., Škaloud, M.: The Ultimate Load Behaviour of Plate Girders Loaded in Shear. The Structural Engineer, Jan. 1972.
9. Fujii, T.: On an Improved Theory for Dr. Basler's Theory. Final Report 8th Congress, IABSE, New York 1968.
10. Klöppel, K., Sheer, J.: Beulwerte ausgesteifter Rechteckplatten. Wilh. Ernst & Sohn, Berlin 1960.
11. Sheer, J.: Der stabilisierende Einfluss von Zugspannungen auf die Beulung schubbeanspruchter, unausgesteifter Rechteckplatten. Der Stahlbau, H. 8, 1962.
12. Wakasugi, S.: Buckling of a Simply Supported Triangular Plate, having inner Angles of 30, 60 and 90 Degrees. Bulletin of JSME, Vol. 4, No. 13, 1961.
13. Huslid, J., Aasen, B.: The Strength of Plate Girder Webs. Report, Div. of Steel Structures, The Univ. of Trondheim, The Norwegian Inst. of Technology.
14. Huslid, J.: Postbuckling Behaviour of Shear Loaded Plates. Report. Div. of Steel Structures, The University of Trondheim, The Norwegian Inst. of Technology.
15. Basler, K.: Strength of Plate Girders under Combined Bending and Shear. ASCE, Proc. October 1961.
16. Wolmir, A. S.: Biegsame Platten und Schalen. VEB. Berlin 1962.

Summary

Some errors are discussed and corrected in the Basler method, especially the effect of the tension field. The corrected value gives a considerable reduction in shear capacity compared to the Basler equations. The main point is however the arbitrariness of the assumption, made by Basler, Rockey and others, that the critical shear stresses of the web are not affected by the tension field.

To demonstrate this point, a method is presented where the effect of the tension field is substituted by a simple lateral support. The method gives

results which for slender webs ($\beta > 200$) are in very good agreement with experiments. All methods give reasonable results for stout webs ($\beta < 100$).

However, the ultimate loads are connected with deformations of such a magnitude that actual structures, f. inst. bridges, will be destroyed before this load limit. A design method based on large deflection theory of elastic plates and taking the first yielding in the middle plane of the plate as the ultimate load limit will serve the purpose and be more realistic to conditions in actual structures.

Résumé

On corrige des fautes dans la méthode de Basler, en particulier l'effet du champ de tension. Les valeurs corrigées donnent une réduction considérable de la capacité de cisaillement. Le point capital est pourtant l'objection contre la supposition faite par Basler, Rockey et d'autres comme quoi la tension critique de cisaillement dans l'âme ne serait influencée par le champ de tension.

Pour illustrer ce point on présente une méthode où l'effet du champ de tension est remplacé par un simple support latéral. Pour des âmes élancées ($\beta > 200$) les résultats correspondent très bien aux valeurs d'essai. Tous les procédés donnent des résultats raisonnables pour des âmes épaisses ($\beta < 100$).

Pourtant la charge ultime est associée à des déformations de sorte que des structures existantes, p. ex. des ponts seront détruits avant la charge limite. Une méthode de calcul fondée sur la théorie des plaques élastiques, en tenant compte des grands déplacements est donc plus convenable et plus réaliste pour des structures existantes. La charge critique est alors atteinte à l'écoulement de la fibre moyenne de la section de la plaque.

Zusammenfassung

Es werden Fehler der Methode von Basler korrigiert, speziell der Einfluss des Zugfeldes. Die Korrekturwerte ergeben eine beachtliche Reduktion der Schubkapazität. Wesentlich ist aber der Einwand gegen die willkürliche Annahme von Basler, Rockey und anderen, wonach die kritische Schubspannung im Steg nicht vom Zugfeld beeinflusst wird.

Zur Illustration dient ein Verfahren, bei dem der Einfluss des Zugfeldes durch eine einfache Festhaltung ersetzt wird. Die Ergebnisse stimmen für schlanke Stege ($\beta > 200$) sehr gut mit den Versuchswerten überein. Sämtliche Verfahren ergeben vernünftige Resultate für dicke Stege ($\beta < 100$).

Zur kritischen Last gehören so grosse Verformungen, dass bestehende Konstruktionen (z. B. Brücken) vor Erreichen derselben zerstört werden. Ein auf der elastischen Plattentheorie beruhendes Berechnungsverfahren unter Berücksichtigung der grossen Verschiebungen ist deshalb zweckmässig und für bestehende Tragwerke realistischer. Die kritische Last wird dann beim Fliessen der mittleren Faser des Plattenquerschnitts erreicht.

Leere Seite
Blank page
Page vide

Mild Steel Beams: Behaviour and Failure Under Cyclic Alternating Loads

Poutres en acier doux: comportement et ruine sous l'influence de charges cycliques alternatives

Flussstahl-Balken: Verhalten und Versagen unter zyklischer Wechselbelastung

A. N. SHERBOURNE
Professor of Civil Engineering and Dean of Faculty of Engineering, University of Waterloo, Waterloo, Ontario, Canada

S. KRISHNASAMY *)
Research Engineer, Research Division, Ontario Hydro, 800 Kipling Avenue, Toronto, Ontario, Canada

Introduction

The importance of studying the behaviour of structural components subjected to low-cycle fatigue conditions, as an extension of simple plastic theory, has been described by the authors in earlier publications [1–4]; a technique to predict the behaviour of structural components under alternating deflections has been formulated. The investigation, however, will be incomplete unless it is extended to cover the behaviour of components under a constant load range. As most of the studies reported on this subject are inconclusive, the present investigation is aimed at examining the behaviour and failure of mild steel beams under alternating load and deflection conditions. A brief account is presented of the fatigue machine, fixtures for pure bending, and cantilever tests.

Cyclic moment curvature models which are discrete functions of the instantaneous cyclic history, are generated from cyclic tests on beams under pure bending. These models are then employed to predict the behaviour of cantilever beams under deformation and load control and are compared with experiments.

A failure criterion for estimating the life of structural components is established by coupling strain range and number of cycles to failure from the

---

*) Dr. S. Krishnasamy was associated with the University of Waterloo during the course of this investigation.

tests on beams under pure bending. The above criterion is then employed to predict the life of cantilever beams subjected to alternating tip loads and the results are compared with experiments.

Test Equipment and Procedure

The experiments were carried out in a servo-controlled testing machine. The system was augmented by special bending fixtures and transducers suitable to control either load or deformation. The testing machine and the various fixtures are fully explained elsewhere [1, 2].

For the pure bending tests described here the fixtures shown in Figs. 1a and 1b were used. The rig in Fig. 1b is a modified version of the fixture in Fig. 1a. Curvature was measured by a transducer shown in Fig. 2.

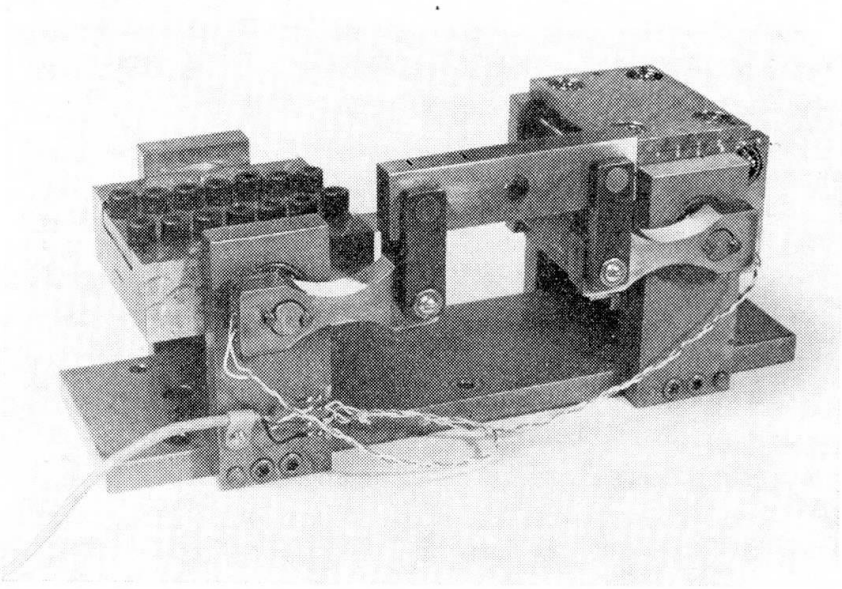

Fig. 1a.
Pure-bending fixture.

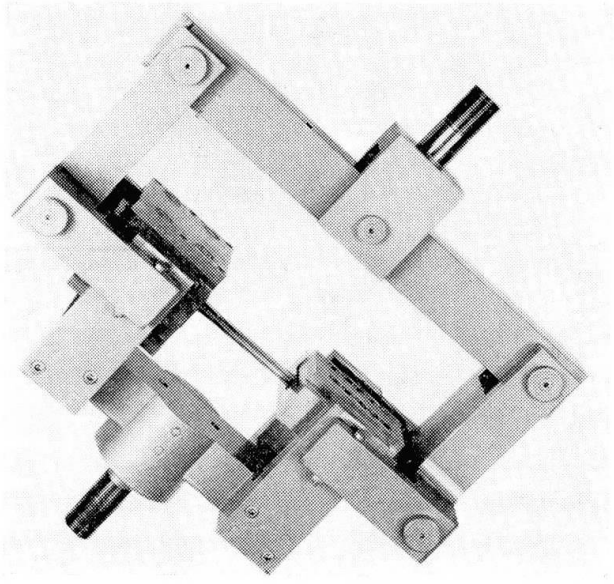

Fig. 1b.
Modified version of the fixture in Fig. 1a.

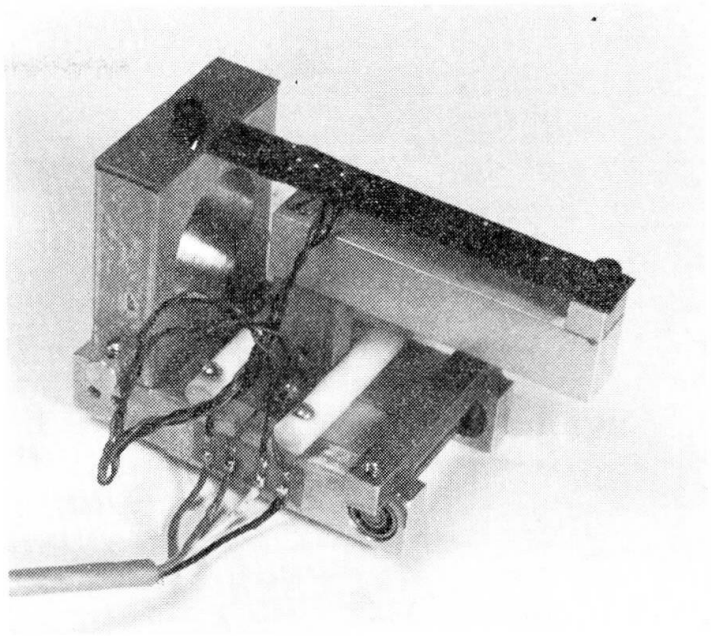

Fig. 2. Curvature meter.

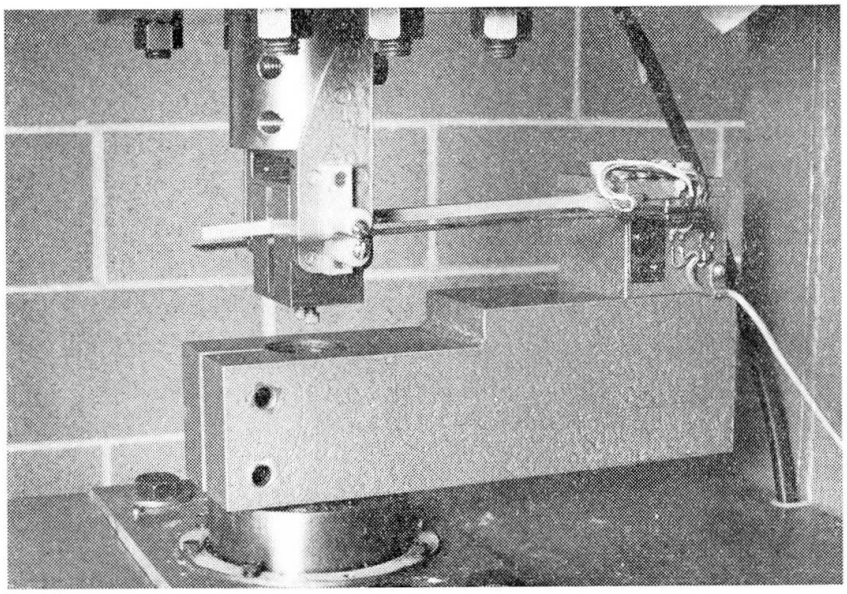

Fig. 3.
Cantilever fixture.

The fixture in Fig. 3 was used to test the cantilever specimens. The load on the specimen was measured by the load cell and the measurement of the deflection was achieved by an LVDT (Linear Voltage Displacement Transducer), which is an integral part of the testing system. A strip-chart recorder and X-Y plotter were used to record the load and deformation, respectively.

Material Properties and Test Specimens

Fully killed 1020 steel was used in making the pure bending and cantilever beam specimens. The chemical properties are tabulated below:

Si	S	P	Mn	C	Cr	Fe
0.037	0.025	0.004	0.47	0.143	0.01	Remainder %

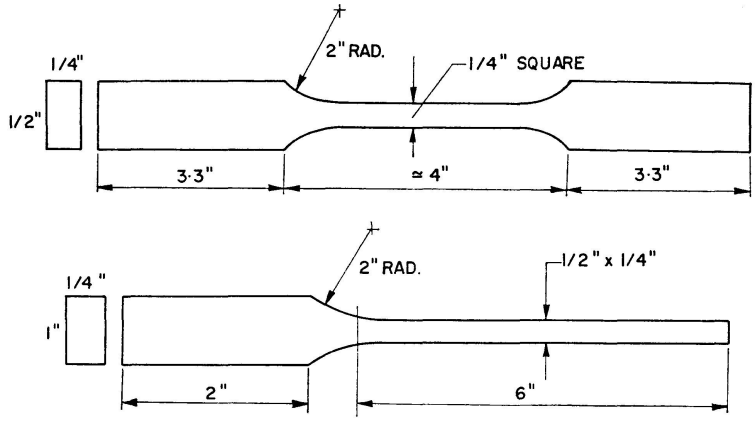

(a) Pure bending specimen.

(b) Cantilever specimen

Fig. 4. Test specimens.

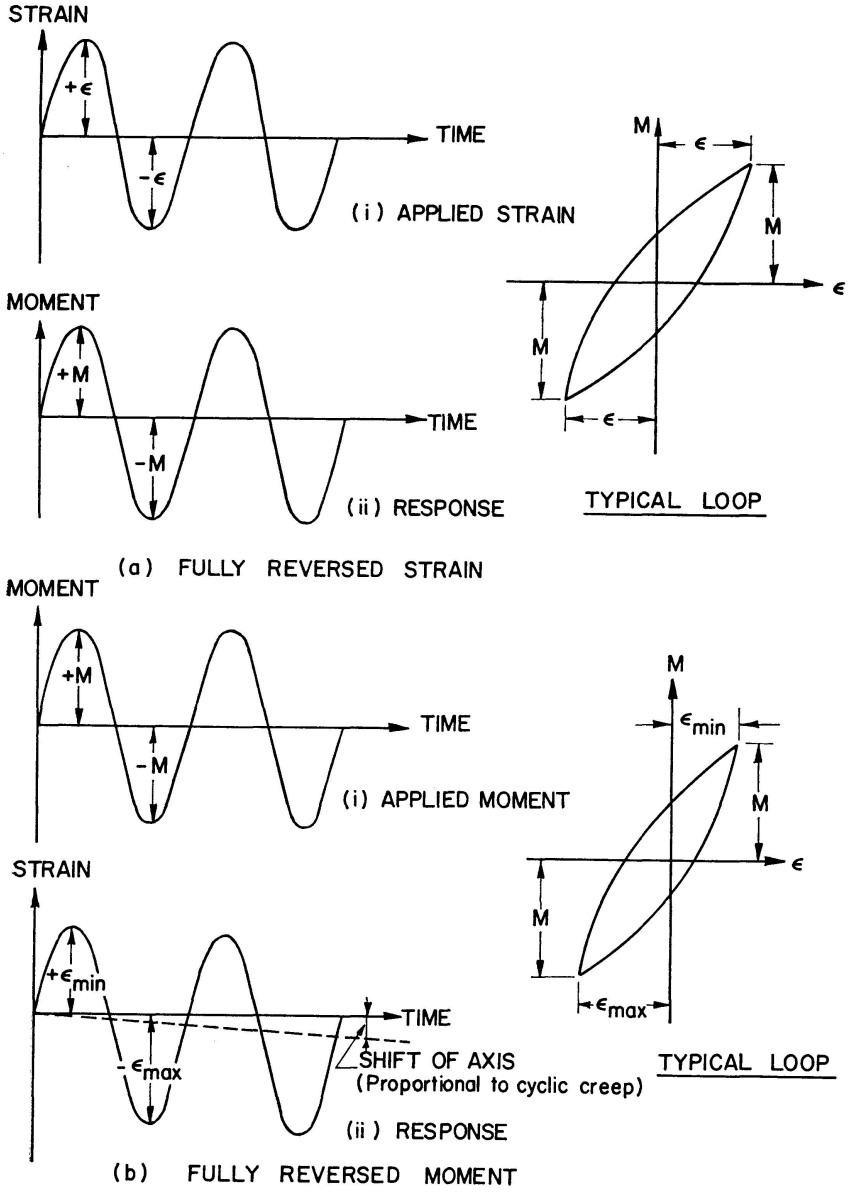

Fig. 5. Loading scheme: Strain and moment control.

The pure bending and cantilever specimens used in the cyclic tests are sketched in Fig. 4. The pure bending test piece had a uniform section $\frac{1}{4}''$ square and approximately 4″ long about the middle section; the two ends were larger in cross-section. The transition from the middle section to the end was uniform and smooth to avoid stress concentrations. The cantilever beam specimens were approximately 12″ long and $\frac{1}{2}'' \times \frac{1}{4}''$ in cross-section. The built-in end of the beam was $2\frac{1}{2}''$ long and $\frac{1}{2}'' \times 1''$ in cross-section. The smooth transition between these two portions reduces stress concentration. The span of the cantilever beam is $6\frac{1}{2}''$.

The specimens were cut roughly to the required size. They were then soaked at 1600° F for about 30 minutes and allowed to cool in air. Great care was taken in machining to reduce the contact stresses. A finish of four micro-inches was attained in order to achieve a fairly correct estimate of life.

The lower yield stress of the material is found to be 33.3 ksi from static bending tests. The Elastic Modulus and the yield strain of the material from static tension tests are determined as 29.85×10^6 psi and 0.14% respectively.

Moment-Curvature Characteristics

Fig. 5 shows the type of loading and control imposed on the test specimens. The results of pure bending tests on specimens subjected to both strain and moment control are shown in Figs. 6 and 7. The cyclic moment-curvature relations for the analysis of structural components can be formulated from these plots as explained below.

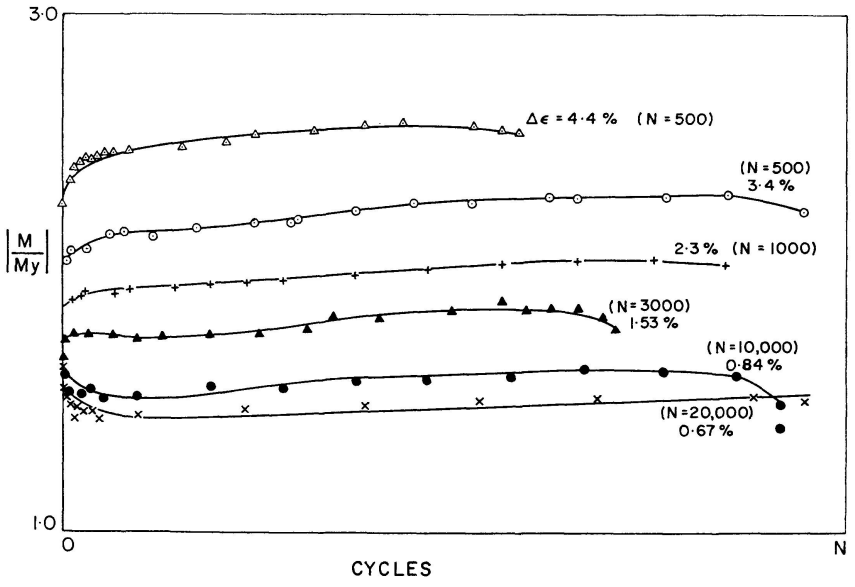

Fig. 6. Cyclic variation of moment amplitude under constant strain range.

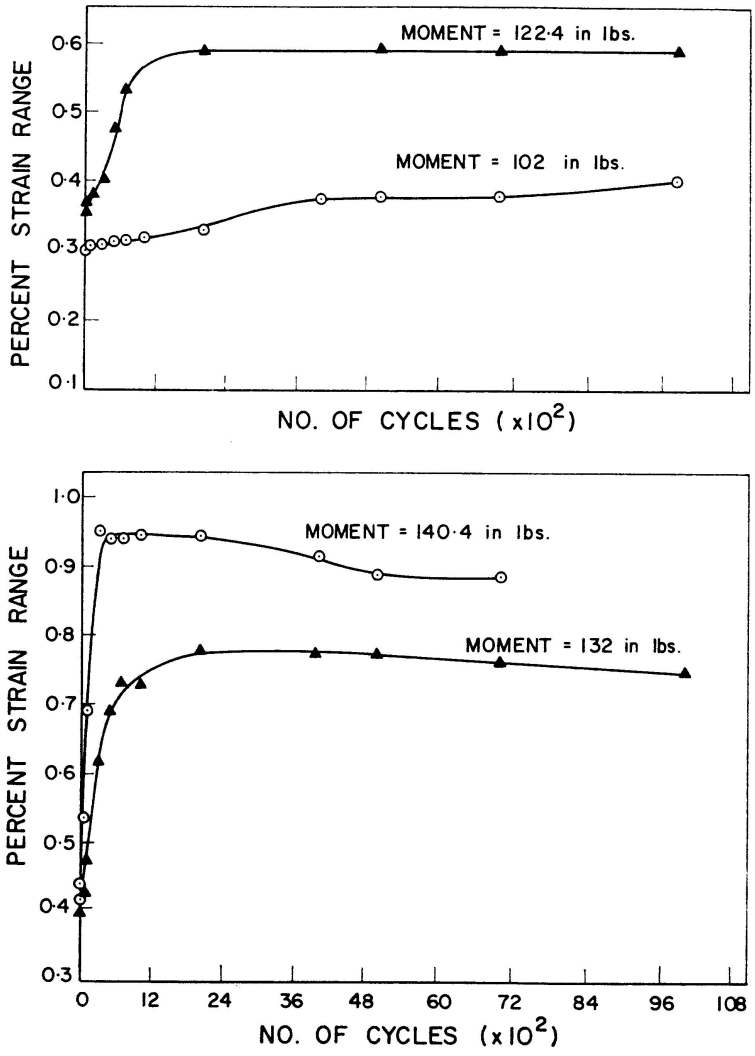
MOMENT = 122·4 in lbs.
MOMENT = 102 in lbs.
PERCENT STRAIN RANGE
0·6
0·5
0·4
0·3
0·2
0·1
NO. OF CYCLES (x10²)
MOMENT = 140·4 in lbs.
MOMENT = 132 in lbs.
PERCENT STRAIN RANGE
1·0
0·9
0·8
0·7
0·6
0·5
0·4
0·3
0
12
24
36
48
60
72
84
96
108
NO. OF CYCLES (x10²)

Fig. 7a.

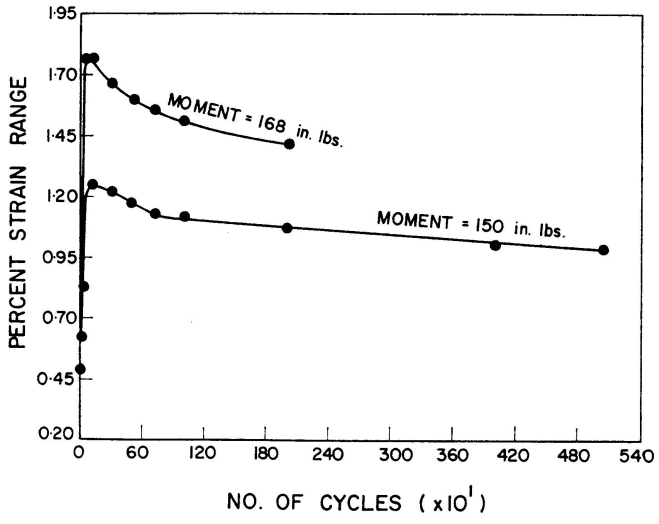
MOMENT = 168 in. lbs.
MOMENT = 150 in. lbs.
PERCENT STRAIN RANGE
1·95
1·70
1·45
1·20
0·95
0·70
0·45
0·20
0
60
120
180
240
300
360
420
480
540
NO. OF CYCLES (x10¹)

Fig. 7b.

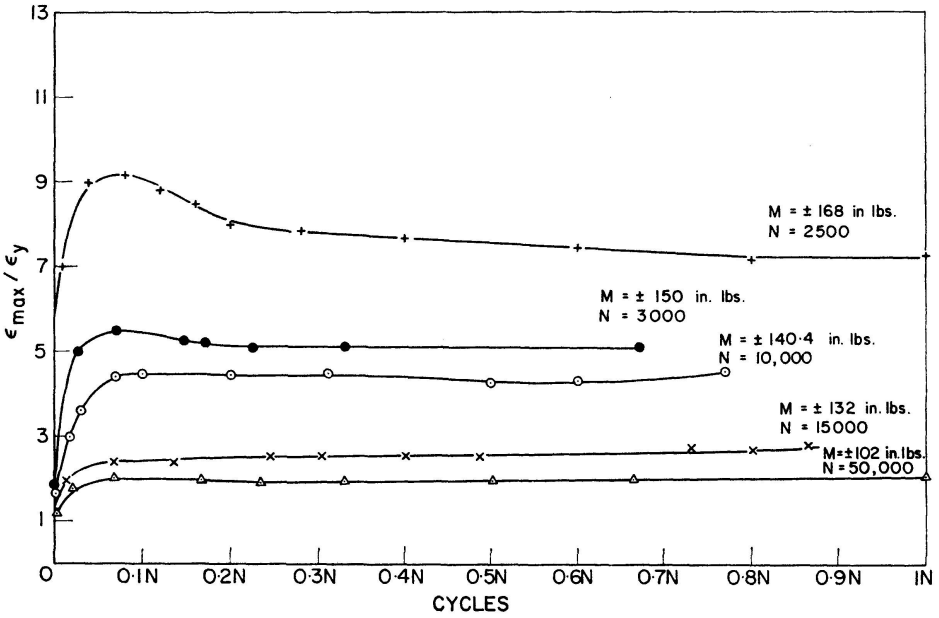

Fig. 7c.

Fig. 7a–c. Cyclic variation of strain range under constant moment.

Strain Control Tests [1]

Values of moment and curvature (or strain) are selected from the curves of Fig. 6 to construct cyclic moment-curvature characteristics. These relationships can be represented mathematically in non-dimensional form:

$$\begin{aligned} k &= m && \text{elastic} \\ k &= 1.0 + \alpha (m-1)^{\beta} && \text{inelastic} \end{aligned} \qquad (1)$$

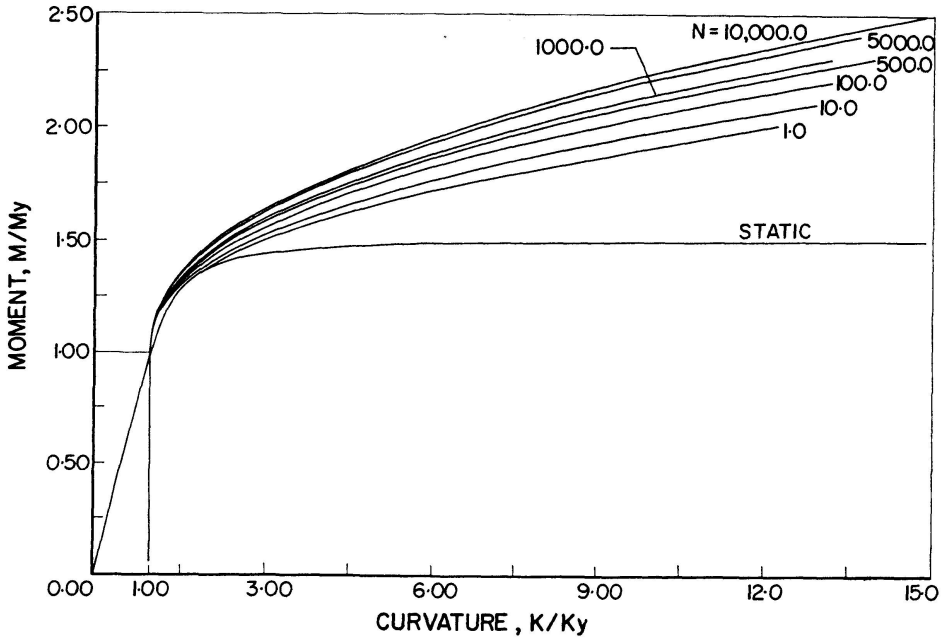

Fig. 8. Cyclic moment curvature characteristics for various cycles: Strain control.

k and m being dimensionless moment and curvature, respectively, and α, β geometric parameters which are functions of cyclic material behaviour. It is to be noted from Fig. 6 that the material softens up to a certain range of strain and subsequently hardens. There will be neither softening nor hardening of the material when it is strain cycled in the elastic range. Hence, it will be appropriate to assume a moment-curvature relationship which is linear up to the yield point and nonlinear beyond (Eq. (1)). The constants α, β for various numbers of cycles are computed by plotting the data from Fig. 6 in log-log form. The cyclic moment-curvature models generated by employing these constants are shown in Fig. 8. These moment-curvature characteristics are employed to predict analytically the cyclic response of structural components under reversed bending.

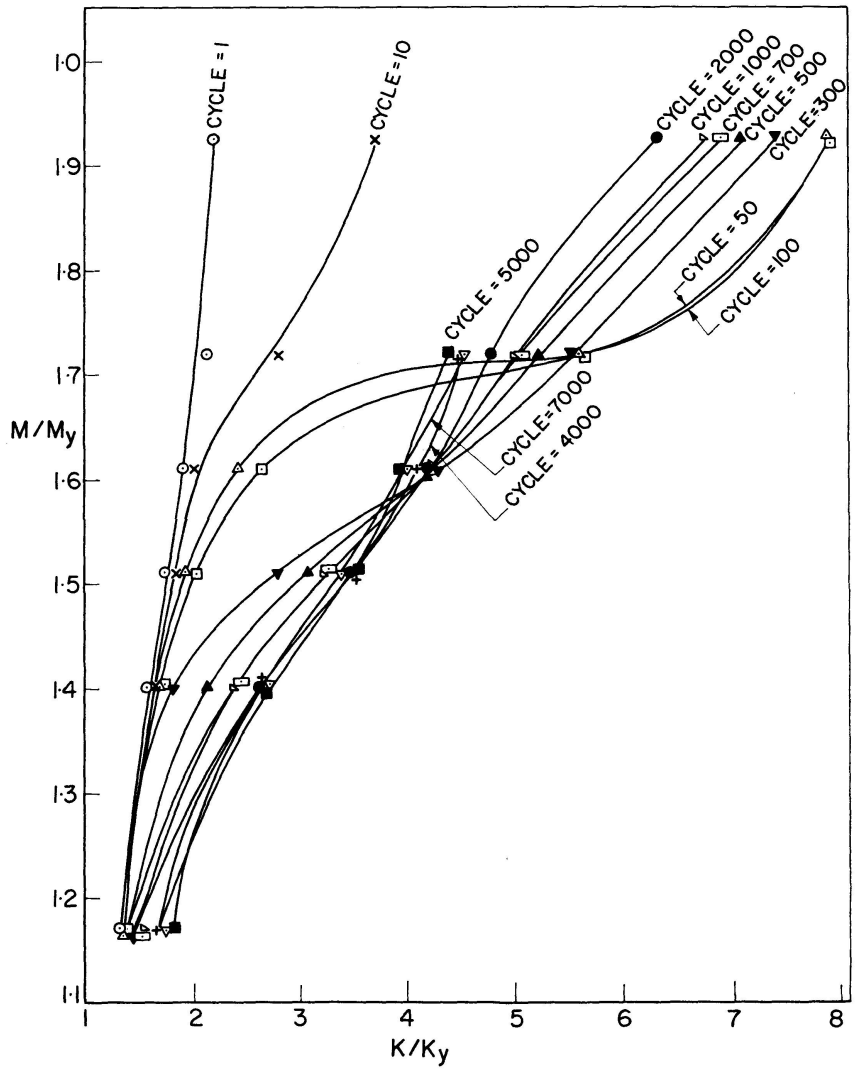

Fig. 9. Cyclic moment-curvature relations for various cycles: Moment control (curvature range vs. moment amplitude).

Moment Control Tests [2]

The data from Fig. 7 a and b is plotted as moment vs. curvature and curves for all cycles are shown on the same graph, Fig. 9. A few comments are evident. Up to about 100 cycles, softening goes on over the entire range and thereafter there seems to be a converging point for all the curves up to about 5,000 cycles. Below the value of the moment at the point of convergence, the material softens while above this value the material hardens. At this value of moment (for cycles between 3,000 and 5,000), the material seems to be independent of cyclic history.

When the moment range is held constant, initially the material strain-softens and then strain hardens. Eventually it settles down to a stable condition. However, unlike the case of strain control tests, the material creeps under constant moment range cycling as in Fig. 5 b. Plots of M/M_y vs. K/K_y for half strain range and for maximum amplitude are shown on the same graph for each cycle (Fig. 10). For the same moment, the difference between the two curves on the abscissa shows the effect of cyclic creep.

For the reasons indicated in the case of strain cycling, the moment-curvature relationship up to the yield moment can be written as

$$k = m.$$

Values of moment and strain ranges selected from the plots in Fig. 7 a–b are plotted on a log-log scale in dimensionless form as in Fig. 11 to develop cyclic

Fig. 10a.

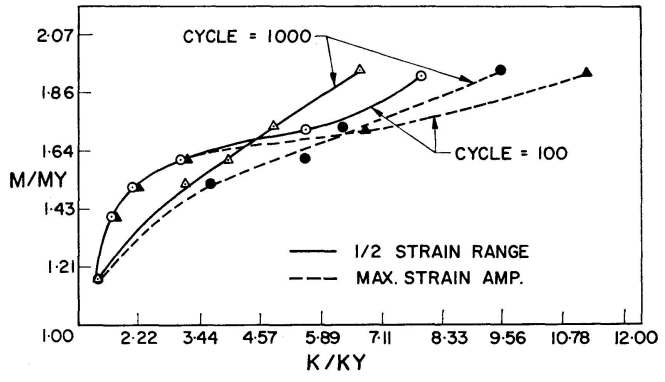

Fig. 10b.

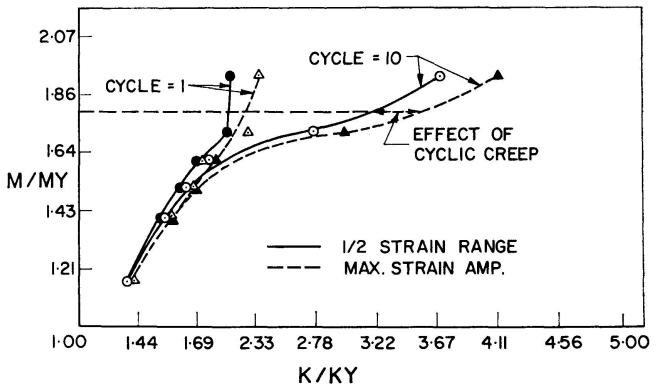

Fig. 10a–b. Cyclic moment-curvature characteristics for various cycles (showing the effect of "cyclic creep"): Moment control.

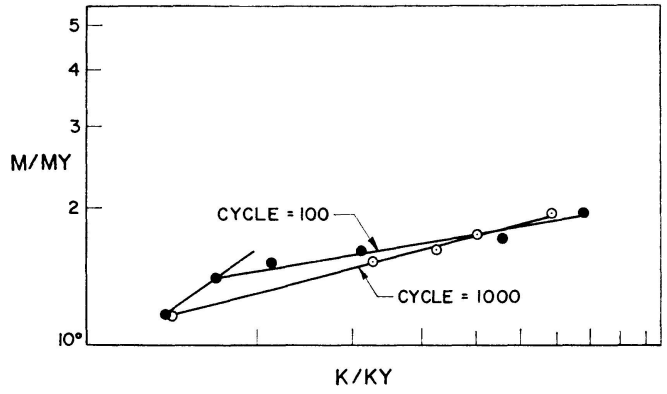

Fig. 11b.

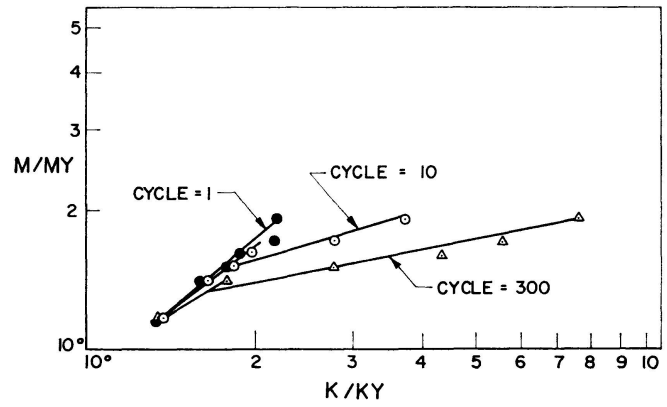

Fig. 11a.

Fig. 11a–b. Moment - curvature characteristics for various cycles: Moment control (curvature-range vs. moment amplitude on a log-log scale).

moment-curvature relationships. It can be seen that for cycles from 10 to 300 the test points fall on two straight lines. The moment-curvature relation might thus be represented beyond the yield point by a power law of the form

$$k_i = \alpha_i m^{\beta_i}, \tag{2}$$

where α_i, β_i have only one value for all cycles except from 10 to 300 and two values for cycles from 10 to 300. For purposes of computer programming it is easy to consider α, β as always having two values each, though these may be identical in some cases.

The relationships representing the cyclic state of a material at any stage as developed above, when applied to find structural response, would yield deflections which are equal to half the deflection range. In order to compute the creep effect the maximum deflection amplitudes are also necessary. An attempt is made to formulate a set of moment-curvature relationships which, when applied to yield response of a structure, would give maximum deflection amplitudes.

The value of α_i in the new relationship will be the same as in Eq. (2), but β_i will be modified to include time, $\beta_i t_i$, reflecting the creep effect. These modified parameters can be calculated from the maximum strain amplitudes calculated earlier in the pure bending tests. The calculations for this are shown

in Appendix A. Consequently, the moment-curvature relation beyond yield can be written more generally as

$$k = \alpha_i m^{\beta_i t_i}, \tag{3}$$

where the value of i has already been discussed.

In the above expression βt has the following value (Appendix A):

$$\beta t = \frac{\log\left(\frac{2\epsilon_{max}}{\Delta\epsilon}\right)}{\log m} + \beta.$$

Here, β is a constant for each cycle and βt will have a value depending upon ϵ_{max} and $\Delta\epsilon$ which, in turn, depend on time and on the moment range applied. βt is thus a function of time and moment range although the variation in βt for each cycle is not much (see Table 1 for few cycles), since, when m increases,

Table 1

Moment	Value of βt for Cycle = 1	Cycle = 2	Cycle = 10,000
102.0 in. lbs	1.1436	3.8386	2.8579
122.4 in. lbs	1.1654	3.6535	2.7823
132.0 in. lbs	1.1319	3.6321	2.8650
140.4 in. lbs	1.1192	3.7350	
150.0 in. lbs	1.1646	3.8780	
168.0 in. lbs	1.1957	4.0644	

$2\epsilon_{max}/\Delta\epsilon$ also increases. For simplicity, the value of βt is considered constant for each cycle. For this purpose, it is seen that the highest value of βt for each gives better results.

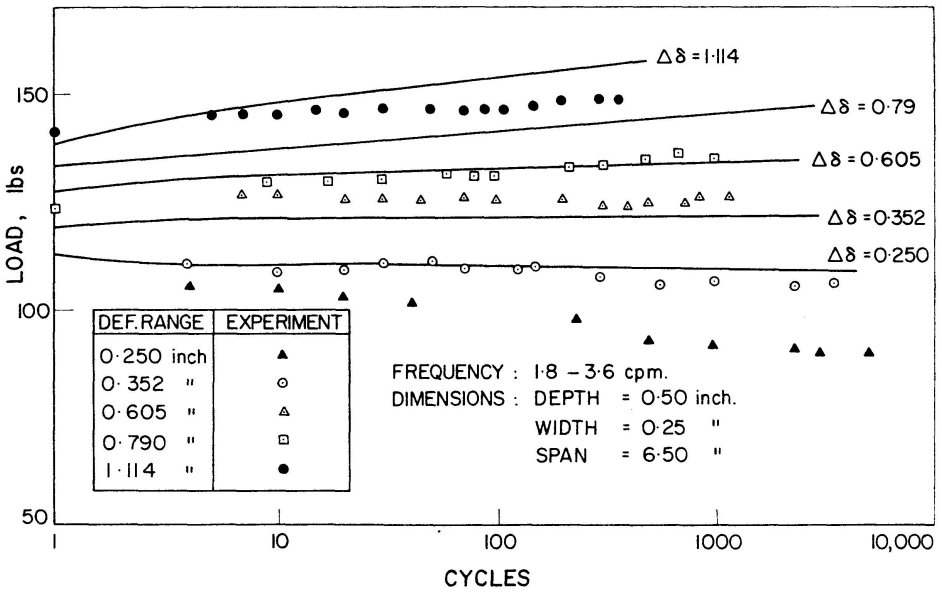

Fig. 12. Cyclic variation of load on cantilever beam under constant deflection range: Theory and experiment.

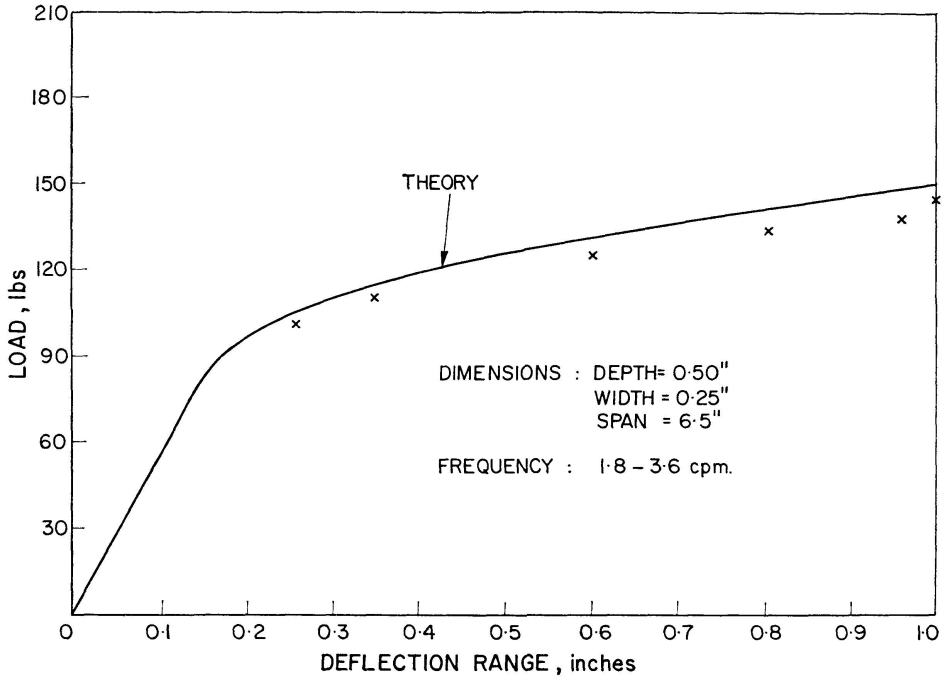

Fig. 13. Load-deflection of cantilever beam under constant deflection range: $N = 50$.

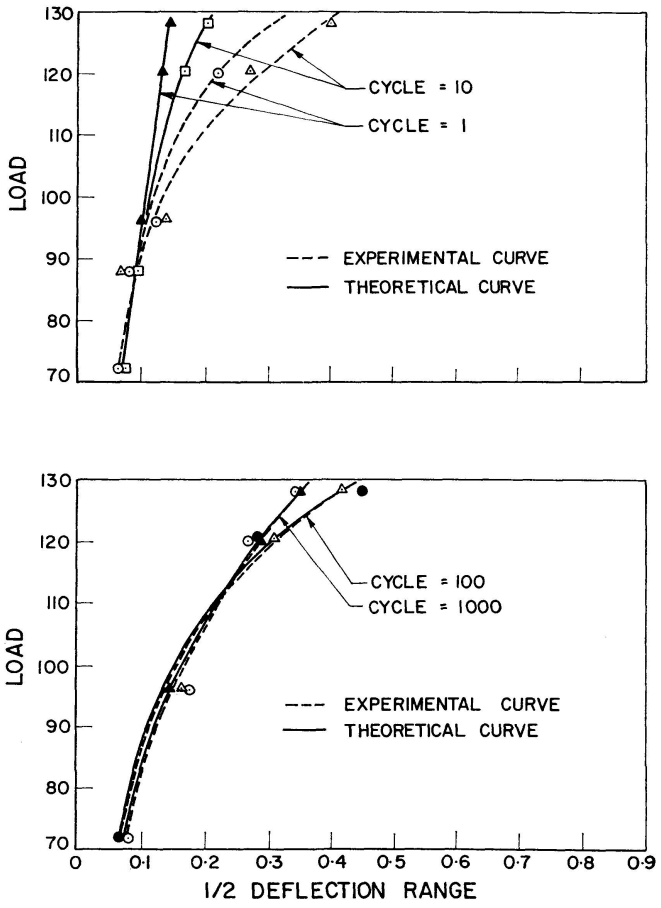

Fig. 14a. Load-deformation behaviour of cantilever beam: Experimental and theoretical results.

Analysis of Structural Components

The moment-curvature relations developed above are applied to predict the cyclic response of structures subjected to repeated loading under ambient conditions of load and deformation control. An approach based on the moment-area technique has been developed and cantilever beams are analyzed theoretically and experimentally. Theoretical investigations are reported in detail elsewhere [4, 5].

Deformation Control

The method developed (in Ref. 4) is applied to predict the variation of cyclic load on cantilever beams subjected to fully reversed deflections. The results are compared with experiments.

Tests are carried out on six cantilever beam specimens. The deflection ranges are so chosen to cover the whole strain range possible, i. e., up to $\pm 2.5\%$. The frequency of the loading varies from 1.8 cpm to 6 cpm, depending upon the deflection range. The computed results are plotted with the experimental

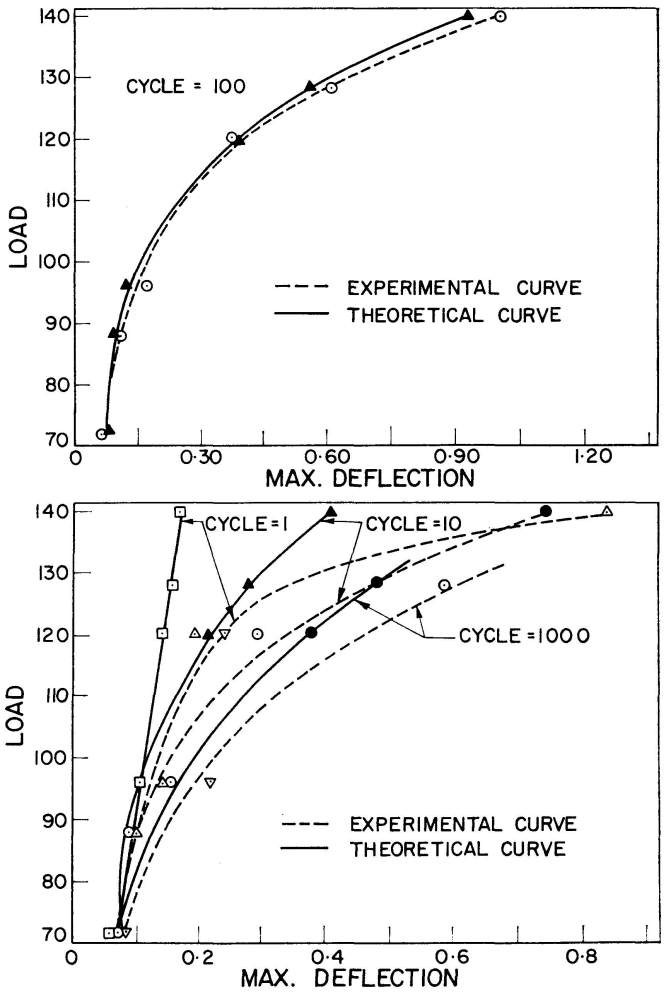

Fig. 14b. Load-deformation behaviour of cantilever beam: Experimental and theoretical results showing the "cyclic creep" effect.

results in Fig. 12. In Fig. 13, the load-deflection curve is plotted for one particular cycle along with the corresponding experimental results.

Load Control

Predictions are made of the variation in cyclic deflection of a cantilever beam subjected to reversed loading under load control conditions. As mentioned earlier, deflections are found both by neglecting and by including creep effects and the results are compared with experiments.

Six cantilever beam specimens were subjected to loads ranging from ± 72 lbs to ± 140 lbs. The test speed varied from 3 cpm to 30 cpm depending upon the amount of load imposed on the beams. It is noted that in the above experiments deflection amplitudes in hogging and sagging are unequal and that a continuous shift of the control axis of the beam takes place in one direction. The theoretical results are plotted and compared with experiments in Figs. 14a and 14b.

Failure of Structural Components

Many investigations have been carried out in the past to examine the failure of metals under low endurance fatigue conditions. These investigations have established the existence of a relationship coupling the value of cyclic life, N_f, and true plastic strain range. In this investigation a failure criterion is established from cyclic straining tests on specimens under pure bending. This failure criterion, in conjunction with "stable" moment-strain curves derived from cyclic pure bending tests, are used to predict the life of structural components under low endurance fatigue.

"Stable" Moment-Strain Range Relationship

As explained earlier, a metal subjected to cyclic loading "shakes" down to a "stable" state (Figs. 6 and 7), which usually extends from 25% to 75% of the life to failure. Moment-strain curves, then, can be established by plotting strain and moment amplitudes pertaining to half life. Fig. 15 shows the stable moment-strain curve for strain and moment control tests. It is to be noted that the material "shakes" down to the same "stable" state, irrespective of the control to which it is subjected. Therefore, a single moment-strain range curve in Fig. 15 is sufficient for further calculations. The experimental points can be represented by a mathematical function of the form

$$k = a_1 (m)^{b_1},$$

where $k = K/K_y$, $m = M/M_y$ and a_1, b_1 are geometrical constants which can be computed from Fig. 15.

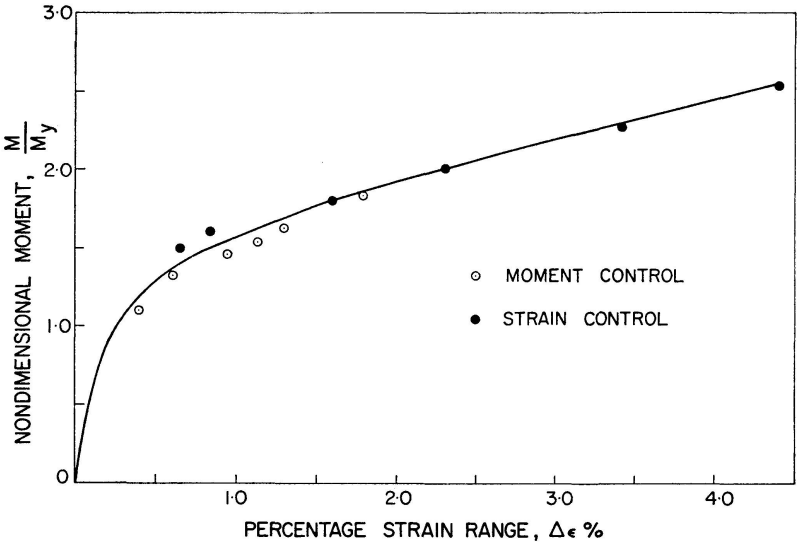

Fig. 15. Stable moment-curvature relationship: Half life values from constant moment range tests.

"Stable" Load-Deformation Characteristic

The "stable" moment-strain range relationship developed above is now applied to predict the "stable" load-deformation relationship for a cantilever beam subjected to load and deformation control. The analytical technique has been explained earlier in this paper.

It can be seen that cantilever beams also "shake-down" to a "stable" state after an initial period of softening or hardening (Figs. 16 and 17). The theo-

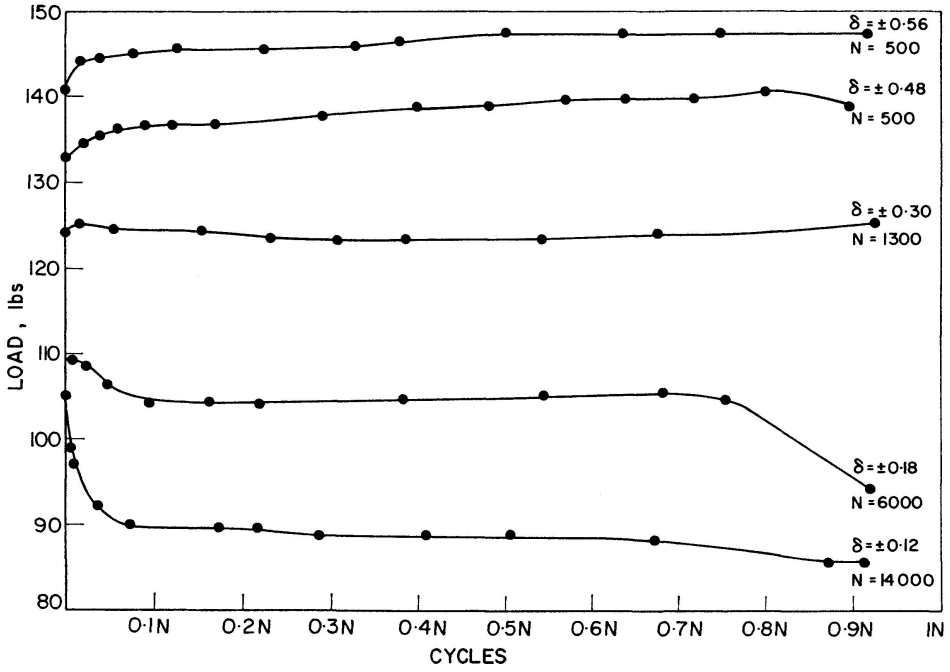

Fig. 16. Cyclic variation of load on cantilever beam (experiment): Constant deflection range.

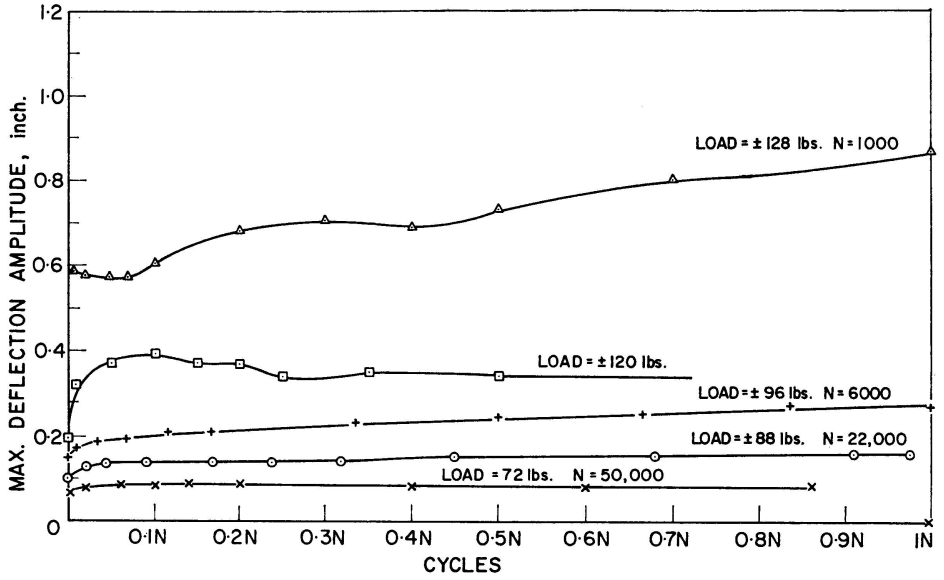

Fig. 17. Cyclic variation of maximum deflection amplitude for cantilever beam under load control.

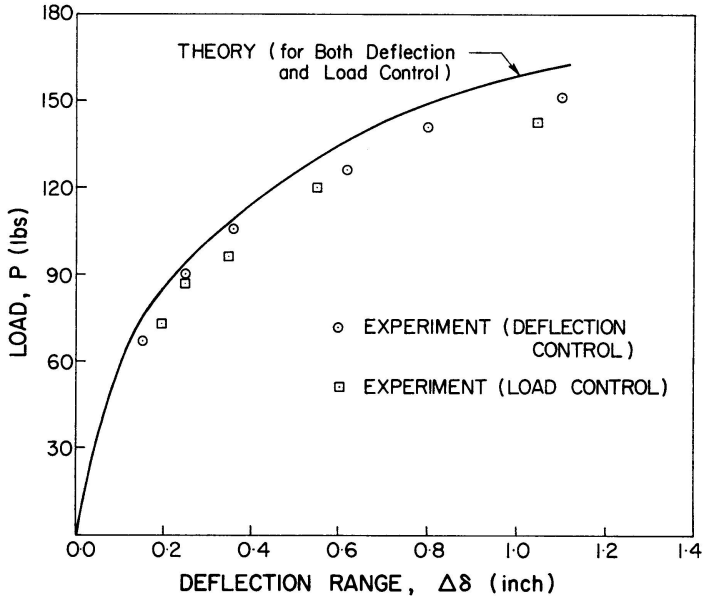

Fig. 18. "Stable" load-deflection curve for cantilever beam: Load and deformation control.

retical predictions are compared with experimental values pertaining to half life state for different beams (Fig. 18). The theory is seen to correlate reasonably well with experiments.

Failure Criterion from Pure-bending Tests

A failure criterion is established, as shown in Fig. 19, from strain as well as moment control tests. A more defined failure criterion than the usual complete fracture of the specimen is necessary since a structural component in an actual situation may be rendered unserviceable due to excessive growth of cracks, refusal of further load, or increased deflection, prior to complete fracture.

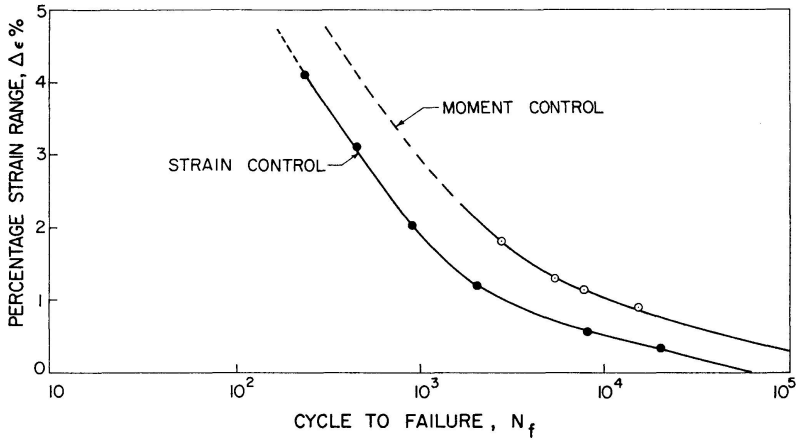

Fig. 19. Failure of beams under pure-bending: Moment and strain control.

Consequently, the failure criterion adopted is that of final reduction in bending moment in the case of strain control tests and increase in strain range when the specimens are under moment control.

Based upon the above failure criteria, the cycles to failure, N_f, for various tests were found from experiments.

Life of Structural Components under Cyclic Loading

The failure criteria developed above can be used in predicting the life of cantilever beams subjected to deformation as well as load control. The procedure adopted is as follows:

1. The "stable" moment-curvature relationship (Fig. 15) developed earlier is applied to predict the "stable" load-deformation characteristic of cantilever beam; theoretical results are compared with experiments (Fig. 18).
2. Values of bending moments (yielding the maximum strain range in the beam) corresponding to a "stable" state are computed (a) from the theoretical load-deformation characteristic in Fig. 18 for deformation-control tests, and (b) from the imposed loads on the beams in the case of load-control tests.
3. The strain ranges corresponding to the "stable" state are then calculated from Fig. 15 and then are employed to predict the life of cantilever beams from Fig. 19.

Figs. 20 and 21 show theoretical and experimental results for cantilever beams under deformation as well as load control. Prediction of lives of beams are made in two ways: one from the results of strain-control tests and the other from the results of moment-control tests.

It can be seen from Figs. 20 and 21 that the failure criterion based upon moment-control tests yields an upper bound while the criterion derived from strain control tests provide a lower bound on test performance.

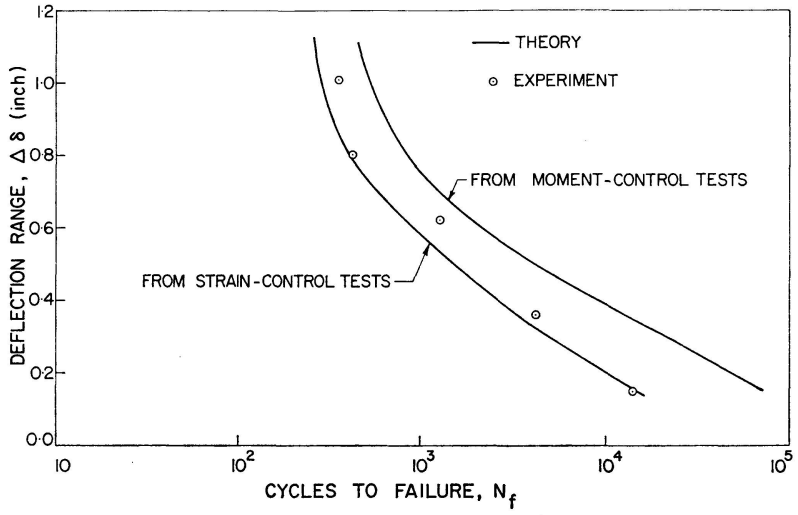

Fig. 20. Failure of cantilever beams under deflection control: Theory and experiment.

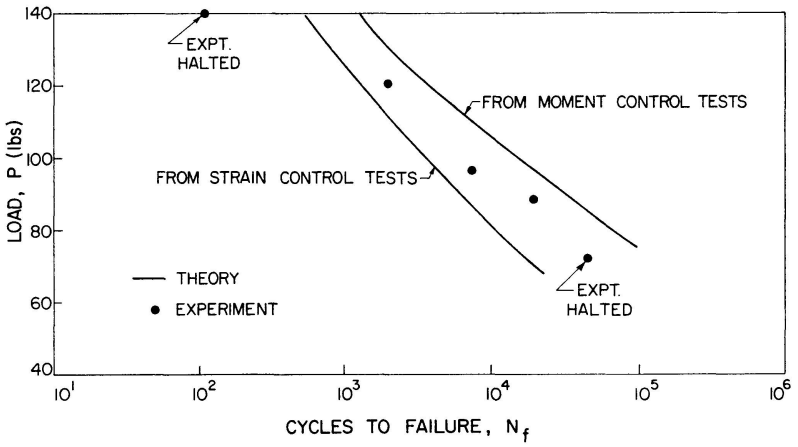

Fig. 21. Failure of cantilever beams under load control: Theory and experiment.

When a beam in service or test is subjected to deflection control, it is neither strain nor moment controlled. In fact, when the deflection range at one point is controlled, the strain range and the moment at every other point changes from cycle to cycle because of the varying strain hardening rates under different strain ranges. However, the behaviour of a beam under preset deflection ranges can be approximated to a strain controlled case without introducing significant error. Hence, the lives of beams predicted from the failure criterion derived from strain control tests are closer to experimental values than the lives predicted from the failure criterion based upon moment control tests (Fig. 20).

In a beam under load control, the moment at every point will remain constant while the strain range will change from cycle to cycle. Therefore, it is logical to expect that the endurance of beams can be very closely predicted by employing the failure criterion derived from moment controlled tests. As indicated earlier, the material creeps under constant moment (load) cycling

introducing mean strain in the beam: the mean strain (or creep) is zero in the case of strain (deflection) cycling. However, it can be seen from Fig. 21 that predictions based upon the criterion derived from moment-controlled tests are non-conservative. The value of mean strain in a beam under pure bending may be more than in a cantilever beam for the same moment-range, thus causing cantilever beams to fail earlier than beams under pure bending.

Discussion and Conclusions

A method is developed for determining the behaviour and life of simple structural components subjected to a constant range of alternating deflection or load. Cyclic moment-curvature models developed from pure bending tests are applied to predict the cyclic behaviour of cantilever beams and the results are compared with experiments.

A "stable" moment-strain range relationship is established by plotting values of moment amplitude and strain range pertaining to half-life of several different beams. It has been established that, irrespective of the type of control imposed on a beam, it shakes down to the same stable state. This moment-strain range characteristic, coupled with a failure criterion developed from pure-bending tests, is employed in predicting the lives of cantilever beams subjected to cyclic alternating load or deflection.

A reasonably good correlation has been found in the prediction of cyclic behaviour of cantilever beams subjected to alternating deflections. However, in the case of beams under alternating loads, the theoretical values of cyclic deflection and experiments correlate well for all but the first 10 cycles. The correlation is not good at high loads. The discrepancy at low life and high loads may be associated with the difference in ranges under which two types of experiments were conducted:

1. to formulate the theory (pure bending tests), and
2. to compare the results (load control tests on cantilever beams).

For pure bending tests under moment control, the maximum moment amplitude applied was $1.92\,M_y$ while for cantilever tests, the maximum moment amplitude attained was $2.154\,M_y$. A glance at Fig. 7 shows that strain range rises abruptly as the moment amplitude increases. One can imagine the strain range to rise to this peak value in the very first cycle at moment amplitudes greater than the largest value applied in the pure bending tests. Discontinuous yielding in mild steel can keep the strain range low at low life and at comparatively lower values of moment amplitude in the case of pure bending tests. As the value of moment amplitude increases the span of low life during which the discontinuous yield phenomena takes place decreases and there will be a limiting value of the moment amplitude when this phenomenon will

disappear at the outset, giving a full value of strain range. This seems to occur in cantilever beam tests with the highest load giving rise to greater deflections at low life and high loads.

It has already been stated that "cyclic creep" occurs in the case of beams subjected to moment (load) control. Whenever ductile materials are subjected to cycles of plastic deformation between load limits, progressive deformation, generally called "cyclic creep", invariably occurs. The presence of cyclic creep during repeated tension can be readily accepted because of the mean stress present. In symmetrical reversed loading, when the mean stress is nominally zero, the presence of cyclic creep is attributed to the tensile mean stress resulting from cyclic deformation of the specimen which causes the true maximum tensile stress to exceed the complementary compressive stress during cycles between constant load limits. If this is accepted as the sole reason for the accumulation of strain, then a small value of tensile mean stress should give rise to cyclic creep in that direction. It has been found by TILLY [6] from fully reversed (push-pull) and repeated tension load tests at room temperatures that, under the action of cyclic loads, the material is less resistant to tensile stress; the tensile stroke was always applied first in Tilly's experiments. If this argument is valid, it remains to explain why cyclic creep occurs in bending tests under load control where half the section is subjected to tensile stress alternately each half cycle and degeneration of stiffness in one direction due to tensile load is compensated by the loss of rigidity in the other direction by an equal and opposite tensile load. It appears that the direction of cyclic creep depends on the nature of the residual stresses which are set up during the first half cycle of reversed loading. It seems quite logical to assume that applied load can be superimposed upon residual stresses and the combined force effect can give rise to a mean stress which is responsible for the occurrence of cyclic creep.

The life predictions based upon failure criteria derived from strain-controlled and moment-controlled tests will yield lower and upper bounds, respectively, to the actual values.

Notations

K	Curvature due to flexure.
K_y	Curvature at yield.
k	Non-dimensional curvature K/K_y.
M	Moment amplitude.
M_y	Moment at yield.
m	Non-dimensional moment M/M_y.
N	Number of cycles.
N_f	Number of cycles to failure.

$\Delta\epsilon$	Strain range for any cycle.
ϵ_{max}	Maximum strain amplitude for any cycle.
ϵ_y	Strain at yield.
$\alpha_1, \alpha_2, \beta_1, \beta_2$	Constants in moment-curvature relationships for half deflection range.
$\alpha_1 t_1, \alpha_2 t_2,$ $\beta_1 t_1, \beta_2 t_2$	Constants in moment-curvature relationships for maximum deflection amplitude.

Acknowledgments

This investigation was carried out in the Department of Civil Engineering of the University of Waterloo, with financial assistance from the National Research Council of Canada, Grant No. A-1582, and the Department of University Affairs, Ontario.

Appendix A. Calculations for Modified Material Parameters to Yield Maximum Deflection Amplitude

$$k = \alpha m^{\beta}, \tag{1}$$

where

$$k = \frac{K}{K_y} \text{ and } m = \frac{M}{M_y}.$$

$$K = \frac{\epsilon}{d},$$

$$K_y = \frac{\epsilon_y}{d},$$

$$\frac{K}{K_y} = \frac{\epsilon}{\epsilon_y} = \frac{2\epsilon}{2\epsilon_y} = \frac{\Delta\epsilon}{2\epsilon_y}.$$

Substituting in (1) we get

$$\frac{\Delta\epsilon}{2\epsilon_y} = \alpha m^{\beta}. \tag{2}$$

Let modified relation be represented by

$$k_{max} = \alpha m^{\beta t},$$

where

$$k_{max} = \frac{K_{max}}{K_y} = \frac{\epsilon_{max}}{\epsilon_y}.$$

Thus

$$\frac{\epsilon_{max}}{\epsilon_y} = \alpha m^{\beta t}. \tag{3}$$

Divide (2) by (3)

$$\frac{\Delta\epsilon}{2\epsilon_y}\frac{\epsilon_y}{\epsilon_{max}} = \frac{m^{\beta}}{m^{\beta t}},$$

or

$$m^{(\beta t-\beta)} = \frac{2\epsilon_{max}}{\Delta\epsilon},$$

or

$$(\beta t-\beta)\log m = \log\left(\frac{2\epsilon_{max}}{\Delta\epsilon}\right).$$

Therefore,

$$\beta t = \frac{\log\left(\frac{2\epsilon_{max}}{\Delta\epsilon}\right)}{\log m} + \beta.$$

References

1. KRISHNASAMY, S. and SHERBOURNE, A. N.: Mild Steel Structures under Reversed Bending. RILEM Symposium on the "Effects of Repeated Loading on Mild Steel Structures", Mexico City, 1966.
2. KRISHNASAMY, S. and SHERBOURNE, A. N.: Response of a "Plastic Hinge" to Low Cycle Alternating Deflections. Experimental Mechanics, Vol. 8, No. 6, 1968, p. 241–248.
3. KRISHNASAMY, S., SHERBOURNE, A. N. and KHURANA, K. K.: Deformation Behaviour of Mild Steel Beams under Alternating Loads. Accepted for publication in Materials and Structures (RILEM).
4. SHERBOURNE, A. N. and KRISHNASAMY, S.: Mild Steel Beams under Cyclic Alternating Deflections. Vol. 30/I of "Publications", Int. Association for Bridge and Structural Eng., 1970.
5. KHURANA, K. K.: Deflection of Beams under Symmetric Alternating Bending Moment. M. Sc. Thesis, University of Waterloo, Waterloo, Ontario, Canada.
6. TILLY, G. P.: Cumulative Strain Behaviour of a Nickel-Chromium Alloy and an 11% Chromium Martensitic Type of Steel. (IME), Applied Mechanics Convention, Vol. 181, Part 31, 1966.

Summary

A method is developed for predicting the life of simple structural components subjected to a constant range of cyclic alternating load or deflection. The method makes use of the fact that, irrespective of the nature of the control imposed, the components shake down to the same "stable" terminal state. The moment-strain range characteristics coupled with a failure criterion, both developed from data on beams under pure bending, is used in estimating structural life. Controlled moment and strain are also seen to bound the test performance, the former from above, the latter from below.

Résumé

On développe une méthode pour estimer la durée de vie d'éléments structuraux simples soumis à des charges cycliques alternatives ou à des déflexions variant entre des limites constantes. La méthode tient compte du fait que, indépendamment de la nature du contrôle imposé, les éléments atteignent à la ruine le même état final "stable". On utilise pour estimer la durée de vie de la structure les caractéristiques moment-déformation liées à un critère de ruine, tous deux étant obtenus à partir d'essais de poutres soumises à la flexion pure. On voit que le moment et la déformation contrôlés influencent l'exécution de l'essai, le premier par le haut, le dernier par le bas.

Zusammenfassung

Es wird eine Methode zur Voraussage der Lebensdauer einfacher baulicher Komponenten entwickelt, die einer konstanten Reihe wechselnder zyklischer Belastungen oder Durchbiegungen ausgesetzt sind. Die Methode bedient sich der Tatsache, dass die Komponenten, unabhängig von der Natur der Kontrolle, sich auf den gleichen «stabilen» Endzustand einspielen. Die Moment/Deformation-Charakteristiken, zusammen mit einem Versagenskriterium, wobei beide aus Daten von Balken unter reiner Biegung entwickelt werden, benützt man um die Lebensdauer eines Bauwerkes zu schätzen. Das kontrollierte Moment und die Deformation werden auch zur Durchführung der Versuche herangezogen, das erstere von oben, das letztere von unten.

Leere Seite
Blank page
Page vide

Moment-Curvature-Time-Relations for Reinforced Concrete Beams

Relations entre moment, flexion et temps sur les poutres en béton armé

Beziehung zwischen Moment, Biegung und Zeit an Stahlbetonbalken

R. F. WARNER
Associate Professor of Civil Engineering, The University of New South Wales

J. H. LAMBERT
Graduate Student, School of Civil Engineering, The University of New South Wales

1. Introduction

Analytic studies have shown that the time-varying behaviour of a reinforced concrete section subjected to sustained bending moment is nonlinear in nature, even when the applied moment is small and the concrete itself is acting as a linear material [6, 8]. Any general method of structural analysis for concrete structures under varying sustained loading must take into account this creep-induced non-linear behaviour, as well as the non-linearities inherent in the instantaneous response to short-term loading [3].

As pointed out by FERRY BORGES [3], the development of accurate techniques of non-linear analysis is of importance, not simply for use in the design of special structures, but also, and perhaps more important, to provide a means of calibrating and evaluating simplified calculation procedures.

In the case of short-term, non-linear response to "instantaneous" loadings, consideration must be given to overall unloading of the structure during an unloading cycle and also to unloading of localized regions during a loading cycle. In order to treat such effects properly, an incremental analysis is required in which a sequence of loading stages is considered.

For the more general case of long-term response to time-varying load history, the non-linear incremental analysis becomes, in effect, a simulation of structural behaviour, whereby the state of the structural system, as represented by stresses and strains in selected sections and by deformations and deflections at selected points, is evaluated for a sequence of load levels and time instants. Simulation of structural behaviour clearly becomes a practical possibility only with the use of a digital computer.

Before the computer simulation of the general time-varying behaviour of a reinforced concrete frame structure can be undertaken, methods must be developed for generating moment-curvature-time relations for flexural members and moment-thrust-curvature-time relations for columns.

In the present paper a method is outlined for computing the curvature history of a reinforced concrete section which is subjected to any prescribed moment history. The method is an extension of a previously reported procedure for computing the biaxial moment-thrust-curvature relations of a column section under short-term loading [9]. The analysis has been generalized to take into account the effects of creep and shrinkage in the concrete. In order to simplify the presentation, the method is here described for the special case of a rectangular section in pure uniaxial bending. However, extension to a cross section of irregular shape under time-varying thrust and skew bending follows directly from the treatment of short-term loading in Ref. [9].

2. General Description of Method

The time-varying moment applied to the cross section is approximated by a finite sequence of moment values $M(1), M(2), .. M(n), .. M(N)$, being taken to act during a sequence of time intervals $\Delta t(1), \Delta t(2), .. \Delta t(n), .. \Delta t(N)$. The time intervals $\Delta t(n)$ are small enough to ensure that the moment increments

$$\Delta M(n) = M(n) - M(n-1) \tag{1}$$

are also small in magnitude. See Fig. 1. If the moment history contains a large instantaneous change in moment, for example as at time zero when the initial loading is applied, it is necessary to use a sequence of moment increments, in order to preserve the incremental nature of the analysis.

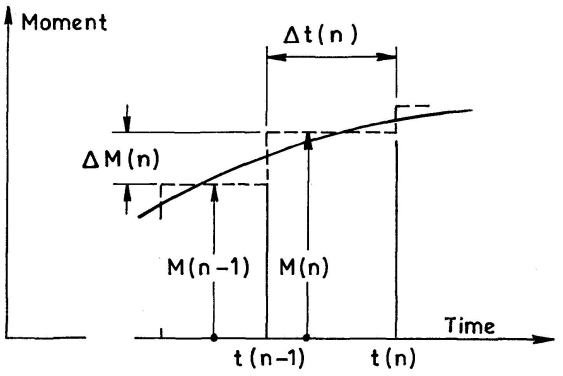

Fig. 1. Discretization of moment history.

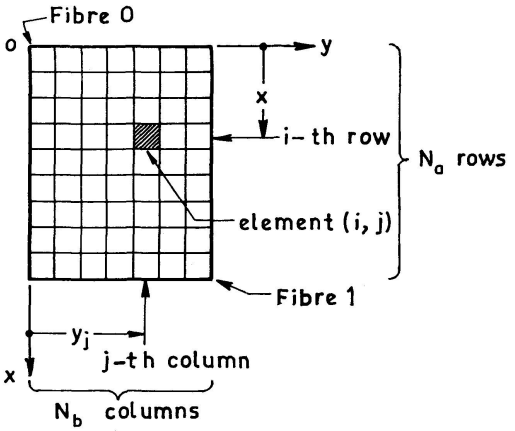

Fig. 2. Partitioning of concrete section.

No restriction is placed on the values $M(n)$. Should a moment be stipulated which is greater than the carrying capacity of the section at any particular time, then failure is recorded and the computation is terminated.

To simplify equilibrium calculations, the section is replaced by a finite number of elemental areas of concrete and steel. The N_s steel elements are actual reinforcing bars in the section or, when more convenient, groups of bars. The procedure of partitioning the concrete section has been described previously [9], and is illustrated in Fig. 2. For the special case of uniaxial bending it is appropriate to take the number of element columns, N_b, as one. However, the two-way partitioning in Fig. 2 allows an immediate extension of the analysis to treat non-rectangular sections and skew bending.

The total strain in a typical concrete element in the i-th row and j-th column is assumed to be composed of an instantaneous, a creep and a shrinkage component. The time-varying stress history of each element is also discretized by assuming that changes in stress level occur only at the time instants $t(n)$ which define the end of the time intervals. The stress $\sigma_{ij}(n)$ acting during time interval $\Delta t(n)$ is thus taken to be constant.

Computations are carried out in cycles; each cycle corresponds to the passage of a time interval. Time interval $\Delta t(n)$ begins at time $t(n-1)$ *after* the moment increment $\Delta M(n)$ has been applied. The state of stress and strain in each concrete and steel element at $t(n-1)$ is known from the previous computation cycle. All concrete elements are allowed to creep and shrink freely during $\Delta t(n)$. Resulting increments in creep and shrinkage strains in all concrete elements are calculated using an appropriate constitutive relation.

As a result of the assumed free straining of the concrete elements, strain incompatibilities develop throughout the section between adjacent concrete elements and also between steel elements and the surrounding concrete. Furthermore, at the end of the time increment, i.e. just before the instant $t(n)$, the moment increment $\Delta M(n+1)$ is applied to the section. The computation cycle is therefore completed by adjusting instantaneous strains and associated stresses in the elemental areas so that, at time $t(n)$,

a) compatibility of deformations over the entire section is re-established, and

b) all equilibrium requirements are fulfilled.

The stresses and strains thus obtained provide the initial conditions required for the next cycle of computations.

This calculation procedure is fairly standard, having been used in creep studies of both metal and concrete structures. The particular method used here resembles the "creep method" proposed by BRESLER [1]. However, a rather general formulation has been attempted, which is potentially applicable to sections of arbitrary shape subjected to arbitrarily varying moment histories ranging from zero up to the section carrying capacity.

3. Stress and Strain in Plain Concrete

A non-dimensionalized stress,

$$S = \frac{\sigma}{\sigma_u} \tag{2}$$

and a normalized strain,

$$E = \frac{\epsilon}{\epsilon_c'} \tag{3}$$

are introduced to represent stresses and strains in the concrete elements. The reference stress σ_u is the strength of the concrete in the member at a specified time, for example at 28 days after casting, and ϵ_c' is the instantaneous strain associated with σ_u. Compressive stresses and strains are taken as positive.

The total concrete strain, composed of instantaneous, creep and shrinkage components, is

$$\epsilon = \epsilon^i + \epsilon^c + \epsilon^s \tag{4a}$$

or in normalized form,

$$E = E^i + E^c + E^s. \tag{4}$$

The following equations are here used to represent the relation between instantaneous strain and stress for monotonicylly increasing strain [9].

$E^i < 0$: $\quad S = 0.$ (5a)

$0 \leqq E^i \leqq 1.0$: $\quad S = \gamma_1 E^i + (3 - 2\gamma_1) E^{i2} + (\gamma_1 - 2) E^{i3}.$ (5b)

$1.0 \leqq E^i \leqq \gamma_2$: $\quad S = 1 - \dfrac{1 - 2E^i + E^{i2}}{1 - 2\gamma_2 + \gamma_2^2}.$ (5c)

$E^i > \gamma_2$: $\quad S = 0.$ (5d)

The parameters γ_1 and γ_2 define the shape of the loading and unloading portions of the curve, respectively. See Fig. 3a. The initial slope, γ_1, is fixed by the initial elastic modulus of concrete E_c,

$$\gamma_1 = \frac{E_c \epsilon_c'}{\sigma_u}. \tag{6}$$

This parameter is also used to define the stress-strain relation for non-monotonic changes in instantaneous strain. The term $\max(E^i)$ is introduced to denote the maximum instantaneous strain which has occurred in the particular concrete element during all previous loading stages and time instants. If the current value E^i is larger than $\max(E^i)$ then Eqs. (5) apply; otherwise, the stress is determined as follows,

$$0 < E^i \leqq \max(E^i): \quad S = \max(S) - \gamma_1 [\max(E^i) - E^i]. \tag{7}$$
$$\geqq 0$$

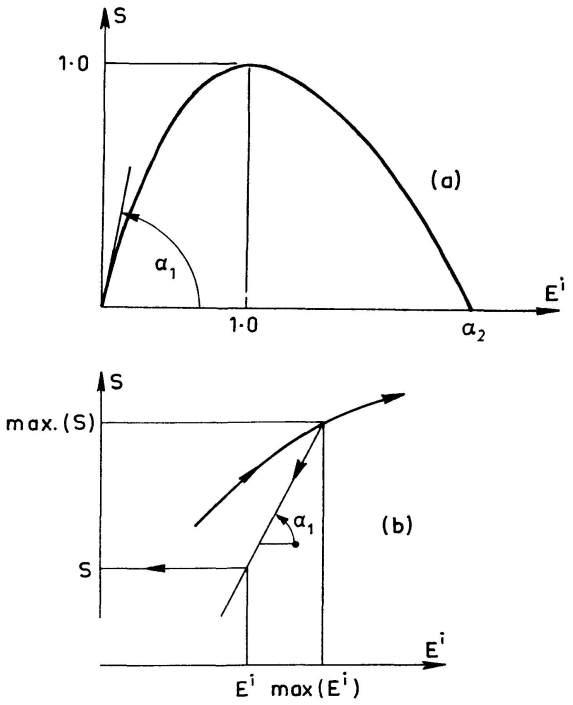

Fig. 3. Relation between stress and instantaneous strain.

Eq. (7) gives non-zero values of stress for $\max(E^i) < \gamma_2$. The term $\max(S)$ is the maximum recorded stress and is related to $\max(E^i)$ by Eqs. (5). See Fig. 3b.

The stress S corresponding to a current strain E^i and a given pre-history of strain is defined jointly by Eqs. (5) and (7), which can be expressed as

$$S = FC\{E^i, \max(E^i)\}. \tag{8a}$$

This computation is carried out by means of an elementary sub-program. The presence of $\max(E^i)$ in Eq. (8a) emphasizes the incremental, step-wise nature of the analysis. For the calculation of stress in the (i,j)th concrete element for the n-th computation cycle, Eq. (8a) can be written more precisely as

$$S_{ij}(n) = FC\{E^i_{ij}(n), \max_{1 \leqq m < n}[E^i_{ij}(m)]\}, \tag{8}$$

where the indicator m, $m < n$, refers to previous cycles.

From Eq. (7) it can be seen that the instantaneous strain is composed of a linear-elastic, recoverable component E^e, and a non-linear, non recoverable plastic component E^p,

$$E^i = E^e + E^p. \tag{9}$$

Considering briefly the stress-strain relation for the reinforcing steel, we note that total steel strain consists of an elastic and a plastic component. The stress in the k-th steel element for the n-th computation cycle can be expressed in a form similar to Eq. (8),

$$S_k(n) = F\,S\{E_k(n), \max_{1 \leqq m < n}[E_k(n)]\}. \tag{10}$$

The yield stress σ_y and the yield strain ϵ_y provide convenient reference values for the definition of non-dimensional stress S_k and normalized strain E_k.

Creep strains in the concrete are accounted for by means of a constitutive relation which takes into account non-linear effects at high stress, as well as the characteristic properties of partial ageing and partial recovery. Details of the particular model of concrete creep here used are given in Ref. [10].

The creep strain at time t, $\epsilon^c(t)$, is assumed to be made up of three components:
$\epsilon^d(t)$ is linear, ageing and non-recoverable; $\epsilon^v(t)$ is linear, non-ageing and recoverable; and $\epsilon^n(t)$ is non-linear. The rate-of-change of creep strain is thus

$$\dot{\epsilon}^c(t) = \dot{\epsilon}^d(t) + \dot{\epsilon}^v(t) + \dot{\epsilon}^n(t). \tag{11}$$

An expression for $\dot{\epsilon}^d(t)$ follows from the Dischinger creep theory (2),

$$\dot{\epsilon}^d(t) = \epsilon^e(t)\,\dot{\phi}^d(t), \tag{12}$$

in which $\epsilon^e(t)$ is the linear-elastic component of the instantaneous strain and $\dot{\phi}^d(t)$ is a creep function, yet to be defined (see Eq. (17)), but which is similar in all major aspects to the Dischinger creep function. It will be noted that $\dot{\epsilon}^d(t)$ is directly related to stress level through $\epsilon^e(t)$.

The linear viscoelastic creep rate can be expressed as (4)

$$\dot{\epsilon}^v(t) = [\epsilon^e(t)\,\phi^v_* - \phi^v(t)]\frac{1}{T_v}, \tag{13}$$

in which ϕ^v_* and T_v are constant material parameters. Depending on the relative magnitudes of the two bracketed quantities in Eq. (13), $\dot{\epsilon}^v(t)$ may be positive (creep) or negative (creep recovery).

Both $\dot{\epsilon}^d(t)$ and $\dot{\epsilon}^v(t)$ are linear with respect to stress. The additional non-linear component is assumed to be non-zero only when the instantaneous stress $\sigma(t)$ exceeds some threshold value σ_c. A creep test conducted at a constant stress σ which is less than σ_c yields a record of experimental values for the total linear component,

$$\sigma \leqq \sigma_c: \qquad \epsilon^c(t) = \epsilon^d(t) + \epsilon^v(t). \tag{14}$$

The creep functions $\phi(t)$ and $\phi^d(t)$ are defined in terms of the experimentally obtained values of $\epsilon^c(t)$ in Eq. (14) as follows,

$$\phi(t) = \frac{\epsilon^c(t)}{\epsilon^e}, \tag{15}$$

$$\phi_* = \phi(\infty) = \frac{\epsilon^c(\infty)}{\epsilon^e}, \tag{16}$$

$$\phi^d(t) = \frac{\epsilon^c(t) - \epsilon^v(t)}{\epsilon^e}, \tag{17}$$

$$\phi^d_* = \phi^d(\infty) = \frac{\epsilon^c(\infty) - \epsilon^v(\infty)}{\epsilon^e}. \tag{18}$$

The parameter ϕ^v_* is defined as

$$\phi^v_* = \frac{\epsilon^v(\infty)}{\epsilon^e}, \tag{19}$$

so that the following relations apply,

$$\phi^d_* = \alpha_d \phi_*, \qquad \alpha_d \leqq 1.0, \tag{20}$$

$$\phi^v_* = \alpha_v \phi_*, \qquad \alpha_v \leqq 1.0, \tag{21}$$

$$\alpha_d + \alpha_v = 1.0. \tag{22}$$

For the creep test at constant stress, the assumed viscoelastic component is

$$\epsilon^v(t) = \epsilon^e \phi^v_* (1 - e^{-t/T_v}). \tag{23}$$

If numerical values can be given to ϕ^v_* and T_v, then the creep function $\phi^d(t)$ can be evaluated from the experimentally determined $\phi(t)$,

$$\phi^d(t) = \phi(t) - \phi^v_* (1 - e^{-t/T_v}). \tag{24}$$

We have yet to consider non-linear creep at stresses in excess of σ_c. It is convenient to relate $\dot{\epsilon}^n(t)$ back to the total linear component by introducing a stress-dependent multiplying factor, $G(\sigma)$,

$$\dot{\epsilon}^n(t) = [\dot{\epsilon}^d(t) + \dot{\epsilon}^v(t)]\, G(\sigma). \tag{25}$$

Setting $H(\sigma) = 1 + G(\sigma)$, we obtain for the total creep rate

$$\dot{\epsilon}^c(t) = [\dot{\epsilon}^d(t) + \dot{\epsilon}^v(t)]\, H(\sigma). \tag{26}$$

The multiplier $G(\sigma)$ is taken to be a power function of stress. A convenient and appropriate non-dimensional expression for $H(\sigma)$ is then

$$\sigma \leqq \sigma_c: \qquad H(\sigma) = 1.0, \tag{27a}$$

$$\sigma_c < \sigma \leqq \sigma_u: \qquad H(\sigma) = 1.0 + \alpha_m \left[\frac{\sigma - \sigma_c}{\sigma_u - \sigma_c}\right]^{\alpha_n}. \tag{27b}$$

The material parameters α_d, α_m, α_n and T_v, together with the creep function $\phi(t)$, have to be evaluated from test data, Suggested values of the parameters are [9],

$$\alpha_d \approx 0.3, \qquad \alpha_v \approx 0.7,$$

$$30 \leqq T_v \leqq 60 \quad \text{(For time } t \text{ measured in days)},$$

$$10 \leqq \alpha_m \leqq 20,$$

$$3 \leqq \alpha_n \leqq 4.$$

A typical creep function $\phi(t)$, obtained from test data (7), is shown in Fig. 4. For convenience the function

$$f(t) = \frac{\phi(t)}{\phi_*} \leqq 1.0 \tag{28}$$

has been plotted.

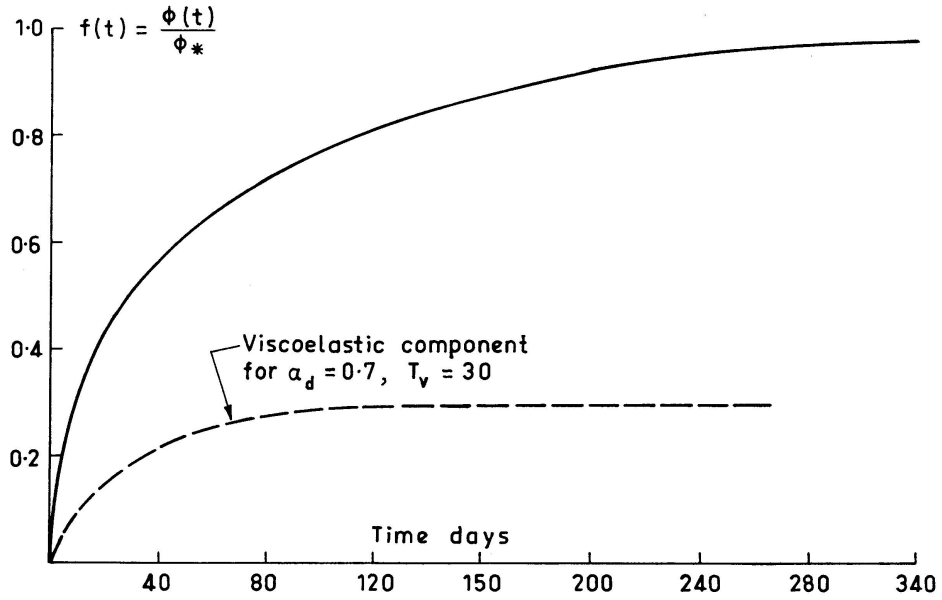

Fig. 4. Creep function used in calculations.

The above creep equations can be expressed in difference form using normalized strains. For the time interval $\Delta t(n)$ the increment in creep strain in the $(i-j)$th concrete element, which is subjected to stress $S_{ij}(n-1)$, is

$$\Delta E^c_{ij}(n) = [\Delta E^d_{ij}(n) + \Delta E^v_{ij}(n)]\, H[S_{ij}(n-1)], \tag{29}$$

where

$$\Delta E^d_{ij}(n) = E^e_{ij}(n-1)\, \Delta \phi^d(n), \tag{30}$$

$$\Delta \phi^d(n) = \phi[t(n)] - \phi[t(n-1)], \tag{31}$$

$$\Delta E^v_{ij}(n) = [E^e_{ij}(n-1)\, \phi^v_* - E^v_{ij}(n-1)] \frac{\Delta t(n)}{T_v}, \tag{32}$$

$$S_{ij}(n-1) \leqq S_c: \qquad H[S_{ij}(n-1)] = 1.0, \tag{33a}$$

$$S_c \leqq S_{ij}(n-1) \leqq 1.0: \qquad H[S_{ij}(n-1)] = 1.0 + \alpha_m \left[\frac{S_{ij}(n-1) - S_c}{1 - S_c}\right]^{\alpha_n}. \tag{33b}$$

Shrinkage strains, assumed to occur independently of stress level, can be expressed as

$$\epsilon^s(t) = \epsilon^s_*\, g(t), \tag{34}$$

in which ϵ^s_* is the end value and $g(t)$ is an experimentally obtained pure-time function which increases monotonically from zero to unity. Eq. (34) is rewritten as

$$\Delta E^s_{ij}(n) = E^s_* \Delta g(n), \tag{35}$$

$$\Delta g(n) \quad = g[t(n)] - g[t(n-1)]. \tag{36}$$

4. Computation Cycle

To simplify the computation cycle, it is convenient to choose the sequence of time intervals $\Delta t(n)$ in such a manner that all increments $\Delta \phi(n)$ in the creep function are of the same magnitude. Thus for a total of N time steps,

$$\Delta \phi(n) = \Delta \phi = \frac{\phi_*}{N}, \tag{37}$$

$$\phi(n) = n \Delta \phi. \tag{38}$$

The appropriate time instants $t(n)$ are obtained from an experimentally obtained creep curve, such as Fig. 4.

The associated values $\Delta \phi^d(n)$ vary in magnitude, but can be obtained from Eq. (24). Corresponding increments in the shrinkage function $g(t)$, i.e. $\Delta g(n)$ in Eq. (36), are obtained from experimental curves. Eqs. (29) and (35) can thus be used to determine the strain increments $\Delta E^c_{ij}(n)$ and $E^s_{ij}(n)$ in each concrete element during time interval $\Delta t(n)$.

At the end of the time interval $\Delta t(n)$ the total creep and shrinkage strains in each element are obtained as

$$E^c_{ij}(n) = E^c_{ij}(n-1) + \Delta E^c_{ij}(n), \tag{39}$$

$$E^s_{ij}(n) = E^s_{ij}(n-1) + \Delta E^s_{ij}(n). \tag{40}$$

It is assumed that total concrete strains at time $t(n)$ are linearly distributed over the section, and also that the strain in each steel element is equal to that in the surrounding concrete. In the case of uniaxial bending, the strain distribution in the section is completely defined by the upper and lower extreme fibre strains $E_0(n)$ and $E_1(n)$. If these values are known or assumed, the strain in the (i,j)th concrete element is given as

$$E_{ij}(n) = E_0(n) - [E_0(n) - E_1(n)]\,\alpha_i, \tag{41}$$

in which α_i defines the depth of the element below the top fibre.

$$\alpha_i = \frac{x_i}{a} = \frac{i+0.5}{N_a}. \tag{42}$$

The instantaneous strain component, obtained by subtracting the creep and shrinkage components, is

$$E^i_{ij}(n) = E_{ij}(n) - E^c_{ij}(n) - E^s_{ij}(n) \tag{43}$$

and the associated stress, $S_{ij}(n)$, is given by Eq. (8).

The total strain in the k-th steel element is also obtained from the extreme fibre strains,

$$E_k(n) = \frac{1}{\eta}\{E_0(n) - [E_0(n) - E_1(n)]\,\alpha_k\} \tag{44}$$

and this allows the stress $S_k(n)$ in this element to be obtained by means of Eq. (10). The depth of the k-th steel element is given by α_k,

$$\alpha_k = \frac{x_k}{a} \tag{45}$$

and η is the ratio of reference strains.

$$\eta = \frac{\epsilon_y}{\epsilon_c'}. \tag{46}$$

With all stresses known, the total force in the section can be obtained by summing the elemental forces acting in all elemental areas. Defining the non-dimensional force term,

$$\bar{P} = \frac{P}{\sigma_u b\, a} \tag{47}$$

one obtains for the resultant force in the section,

$$\bar{P} = \frac{1}{N_s}\sum_i \sum_j S_{ij}(n) + \mu m \frac{1}{N_s}\sum_k S_k(n) - \mu \frac{1}{N_s}\sum_k S_k^c(n). \tag{48}$$

Here, μ is the ratio of steel and concrete areas,

$$\mu = \frac{A_s}{b\, a}, \tag{49}$$

m is the ratio of reference stresses,

$$m = \frac{\sigma_y}{\sigma_u} \tag{50}$$

and N_c is the total number of concrete elements,

$$N_c = N_b N_a. \tag{51}$$

The third summation term in Eq. (48) has been introduced to account for the concrete area which has been replaced by the steel elements. The term $S_k^c(n)$ is the concrete stress at the level of the k-th steel element.

The resultant moment acting in the section is found by taking moments of the elemental forces about the horizontal y axis shown in Fig. 2. With

$$\bar{M} = \frac{M}{\sigma_u b\, a^2}, \tag{52}$$

this gives

$$\bar{M} = \frac{1}{N_c}\sum_i \sum_j S_{ij}(n)\,\alpha_i + \mu m \frac{1}{N_s}\sum_k S_k(n)\,\alpha_k - \mu \frac{1}{N_s}\sum_k S_k^c(n)\,\alpha_k. \tag{53}$$

At any time instant $t(n)$, the correct values of $E_0(n)$ and $E_1(n)$ are such that the following equilibrium requirements are fulfilled:

a) The force P is zero;

b) The moment M is equal to the prescribed moment, $M(n+1)$,

$$M(n+1) = M(n) + \Delta M(n+1). \tag{54}$$

For practical calculation purposes, strain values are accepted if they fulfil the equilibrium requirements to within specified tolerances t_p and t_M, viz

$$|\bar{P}| \leq t_p, \tag{55}$$

$$|\bar{M} - \bar{M}(n+1)| \leq t_M. \tag{56}$$

A nested search technique has been developed, which consists of an outer procedure to find $E_0(n)$ and an inner procedure to find $E_1(n)$. The inner procedure, called SEEKE 1, establishes a value of $E_1(n)$ which, together with any value of $E_0(n)$ prescribed by the other procedure, satisfies Eq. (55). Basically, SEEKE 1 consists of two phases. In the first phase, bounds on E_1 are found, E_1^U and E_1^L, for which the corresponding value of $\bar{P}$ are positive and negative, respectively. These bounds define a search region within which the required value lies. In the second phase, a halving process is used, whereby the mid point of the search region,

$$E_1^M = \tfrac{1}{2}[E_1^U + E_1^L]$$

is tested. If this value satisfies Eq. (55) the search is terminated; otherwise, the search region is halved and the process continues. Figs. 5 and 6 show schematically the two phases of SEEKE 1.

The outer search procedure, SEEKE 0, establishes a value of $E_0(n)$ which fulfills Eq. (56). However, for every trial value of E_0, SEEKE 0 calls on SEEKE 1 to carry out a subsidiary search for an E_1 value so that Eq. (55) is always fulfilled. The structure of SEEKE 0 is quite similar to that of SEEKE 1. Upper and lower bounds are first established, E_0^U and E_0^L, such that the computed $\bar{M}$ is greater than and less than $\bar{M}(n+1)$, respectively. The halving procedure then brings convergence to a set of values which together satisfy Eqs. (55) and (56).

Although the nested search procedure is certainly non optimal, it is extremely simple in structure and has proved to be surprisingly efficient and reliable, not only for the case uniaxial bending but also, in an extended form, for calculations involving biaxial bending and compression.

With the strain distribution determined, it is a simple matter to obtain curvature. A reference curvature is introduced,

$$K_{ref} = \frac{\epsilon_c'}{a}$$

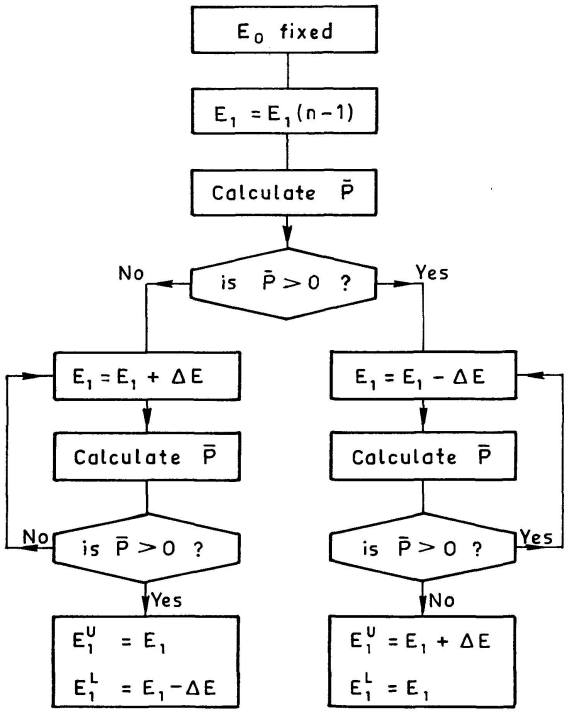

Fig. 5. Seeke 1. Bounds on E_1.

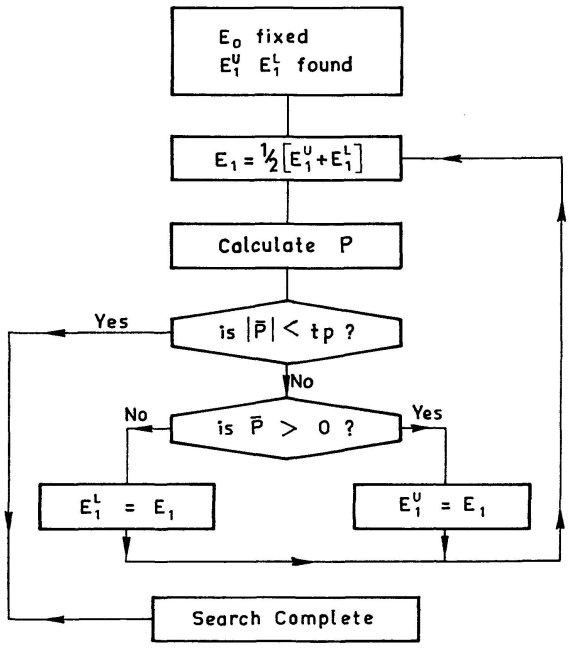

Fig. 6. Seeke 1. Halving procedure.

and the non-dimensional curvature $\bar{K}$ is calculated simply as

$$\bar{K} = \frac{K}{K_{ref}} = E_0(n) - E_1(n).$$

The computation cycle described above is applicable provided the moment increments $\Delta M(n)$ are reasonably small. It remains to take care of instantaneous loadings and unloadings, including the first loading at time zero when the initial conditions are established for the first computational cycle.

When a significant jump in moment occurs, the extreme compressive fibre strain E_0 is incremented repeatedly by a small value ΔE. Thus, for the initial loading, a sequence of strains ΔE, $2\Delta E$, ... is considered. An appropriate value of E_1 is in each case determined, by means of SEEKE 1, such that Eq. (55) is fulfilled, and the corresponding moment $\bar{M}$ is calculated by means of Eq. (53). The strain E_0 is thus incremented until $\bar{M}$ becomes larger than the prescribed value. When this occurs, upper and lower bounds on E_0 have been established and the halving process in SEEKE 0 can be used to fulfill Eq. (56).

In the case of a sudden unloading, a similar calculation procedure is adopted, whereby E_0 is decremented incrementally.

5. Numerical Results

In order to test the adequacy of the computation procedure prior to its use in the analysis of time varying structural behaviour, calculations were made

for a variety of different cross sections, material parameter values and loading histories. The calculations provided a means for checking the reliability of the search procedures and also gave information on the sensitivity of numerical results to variations in the values of the parameters which are used to define the deformation characteristics (including creep and shrinkage) of the concrete.

Results of several typical calculations are presented in Figs. 8 to 15. Except where otherwise noted, calculations were made for the section details given in Fig. 7 and for the parameter values given in Table 1. The curve used for the creep function $\phi(t)$ is that shown in Fig. 4. The calculations were made with an IBM 360/50 installation. Execution time for a complete variable moment history, followed by an incremental loading to failure, was usually in the order of 30 seconds.

A characteristic of the computed results is the slightly non-smooth nature of almost all resulting curves. This can be seen in Fig. 11 for stress variation

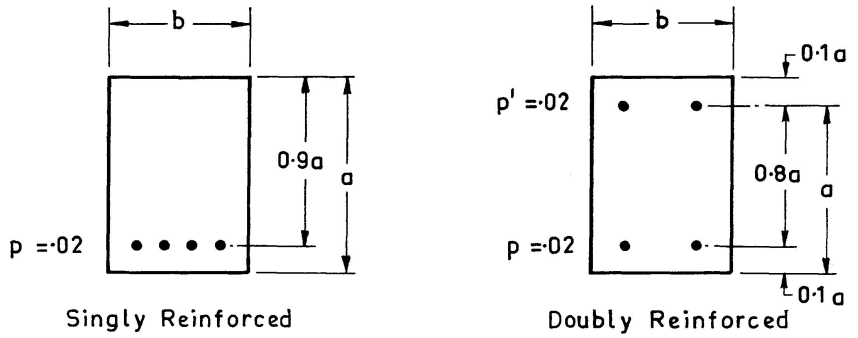

Fig. 7. Cross sections for numerical calculations.

Table 1. Values for Numerical Computations

Stress-strain Relation:	γ_1	= 2.0
	γ_2	= 3.0
Creep Law:	α_d	= 1.0, 0.7, 0.5
	α_m	= 20
	α_n	= 4
	T_v	= 30, 60
	σ_c	= 0.4 σ_u
	ϕ_*	= 3.0
	E^s_*	= 0, 0.25
Section Details:	μ	= 0.02, 0.04
	p	= 0.02
	p^1	= 0, 0.02
Calculation Details:	N_a	= 20
	N_b	= 1
	N_s	= 4
	t_P	= 0.01
	t_M	= 0.01

over the cross-section, in Fig. 10 for variation of stress with time, and in Fig. 9 for time variation of curvature. The non-smoothness stems of course from the finite computation procedure. Smoothing of the results can nevertheless be achieved, at the expense of additional computation time, by using a finer partitioning grid for the section, smaller time intervals, and, most important of all, finer tolerances t_p and t_M.

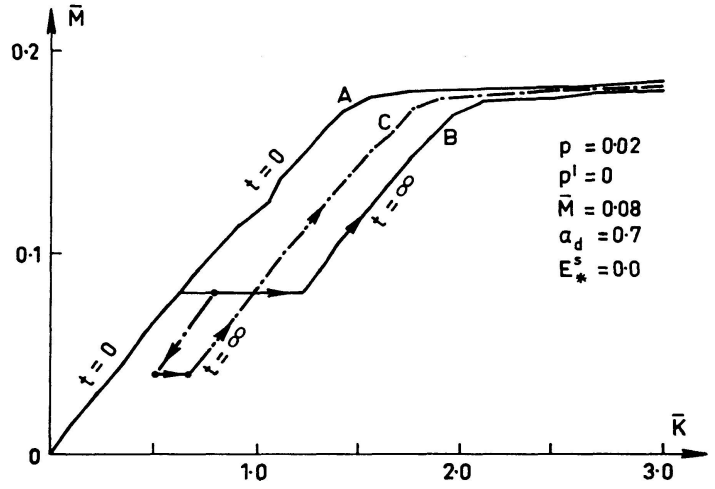

Fig. 8. Curvature histories for three loading cases.

In Fig. 8 curvature histories are shown for three different moment histories applied to a singly reinforced section. Curve A shows the moment-curvature relation for short-term, monotonically increasing loading. Curve B shows moment versus curvature for the case where the moment is raised instantaneously to the value $\overline{M} = 0.08$ (about 40 percent of the ultimate moment) and held there indefinitely, with a final loading to failure at time infinity. In the third case, represented by curve C, the moment is raised instantaneously to $\overline{M} = 0.08$ and held there for 7 days, when it is reduced to $\overline{M} = 0.04$ and held there indefinitely, with a final loading to failure at time infinity. The curves are terminated arbitrarily at a curvature value of $\overline{K} = 3.0$. It is seen that the effet of prior history of loading on moment capacity, and also on the latter portion of the moment-curvature relation, is almost imperceptible.

Fig. 9 shows the increase in curvature with time for a singly reinforced and a doubly reinforced section, each subjected to a moment of $\overline{M} = 0.08$ (about 40 percent of ultimate moment). As is to be expected, the compression reinforcement plays a decisive role in restricting the development of curvature. Fig. 9 also shows that concrete shrinkage plays a significant part in the time-increase in curvature in both the singly reinforced and the doubly reinforced section.

It is significant that the curvature in the doubly reinforced section for non-zero shrinkage reaches a maximum value and then remains constant over the final few time intervals. The reason for this can be seen in Fig. 10, where the attenuation of maximum concrete compressive stress in the section is plotted.

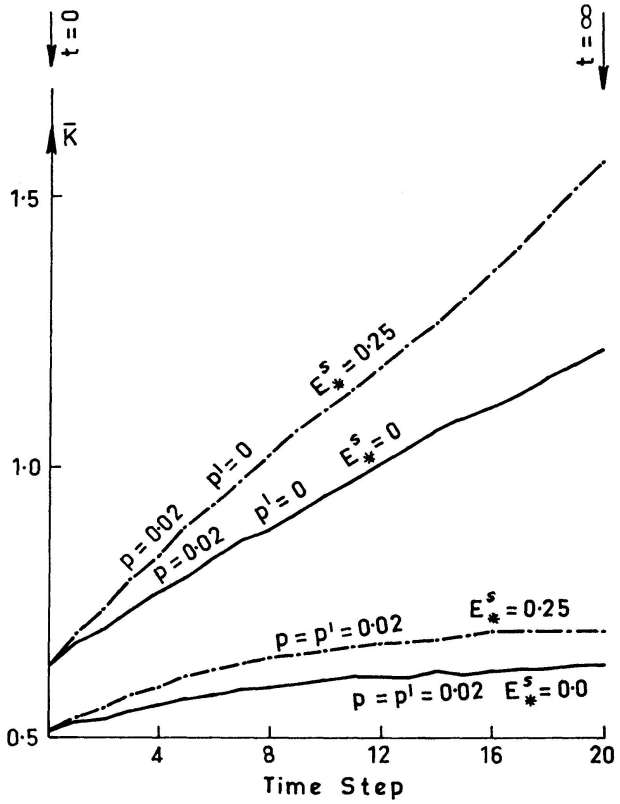

Fig. 9. Curvature histories.

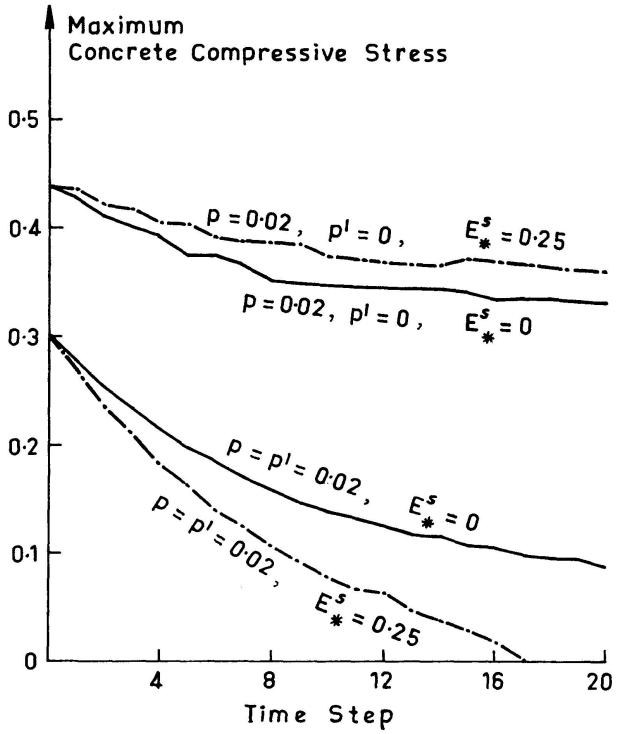

Fig. 10. Attenuation of max. concrete compressive stress.

Due to the restraint provided by the compression reinforcement, coupled with both creep and shrinkage of the concrete, the concrete compressive stresses have completely disappeared and the applied moment is being resisted entirely by a compressive steel force and a tensile steel force. In fact, tensile stresses

would develop in the upper fibres of this section. The development of tensile stress fields in the "compression" zone of doubly reinforced beams has been reported previously [6]. Fig. 10 also shows that the concrete compressive stress cannot disappear completely without the presence of concrete shrinkage.

Although shrinkage strains result in an overall reduction in concrete compressive stress in the doubly reinforced section, they result in slightly higher stresses, relative to the no-shrinkage case, in the singly reinforced section. This is explained by the redistribution of stresses in the section with time, as shown in Fig. 11 for the singly reinforced section and in Fig. 12 for the doubly reinforced section. The neutral axes of stress and strain coincide for times

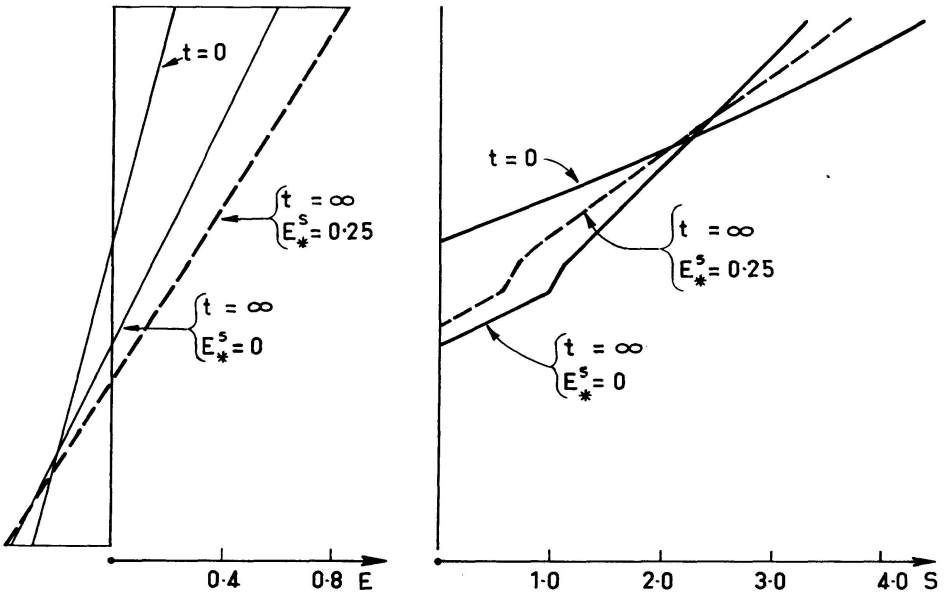

Fig. 11. Stresses and strains in concrete. Singly reinforced section.

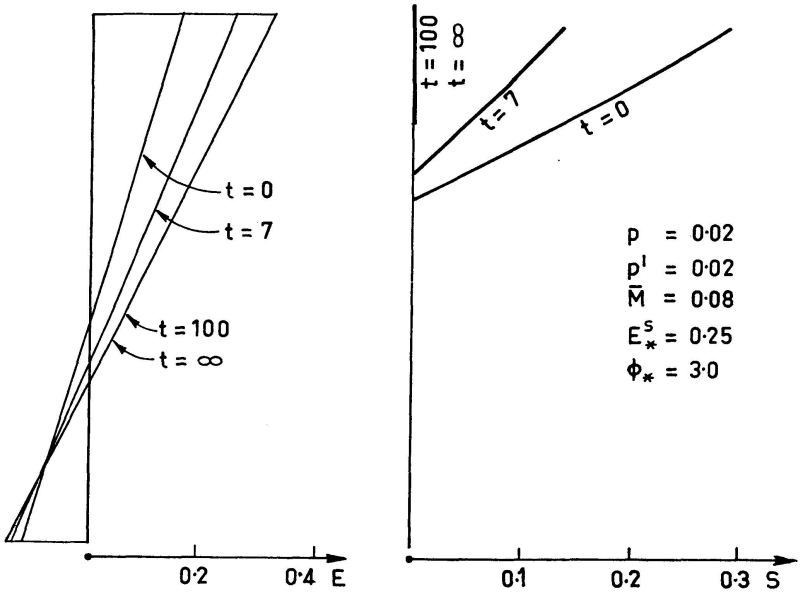

Fig. 12. Stresses and strains in concrete. Doubly reinforced section.

$t > t_0$ only when shrinkage strains are zero. For non-zero shrinkage the stress axis rises above the strain axis, and the effective reduction in the area of the compressive stress block requires in the singly reinforced section some increase in stress over that calculated for zero shrinkage.

Shrinkage strains in the doubly reinforced section also force the neutral axis of stress to rise above that of strain. See Fig. 12. However, the reduction of total concrete compressive stress, due to unloading onto the compression steel, is the over-riding effect here.

A question of prime importance in any analysis of time-varying structural behaviour is the sensitivity of the results to the type of creep law assumed and, further, to the numerical values used for the parameters of the creep law.

It is clear tht ϕ_* and E^s_* are measures of total creep and shrinkage and that they must have an important influence on final deformations in the section. It is also clear that the shape of the creep and shrinkage curves, i. e. $f(t)$ and $g(t)$, will determine, to a large extent, the rate of increase of curvature in the case of constant sustained loading.

The importance of secondary parameters such as α_d, α_m, α_n and T_v is not so obvious. If concrete stress does not change greatly with time, for example as in a singly reinforced section under constant sustained moment, it is reasonable to expect that creep calculations will not depend greatly on α_d and T_v, since these parameters define the ageing and recovery properties of the concrete. Situations most sensitive to variations in these parameters are likely to be those in which large changes occur in the stress level with time.

Fig. 13 shows the attenuation of concrete compressive stress in a doubly reinforced section calculated for values of α_d ranging from 0.5 to 1.0. The value $\alpha_d = 1.0$ corresponds, in the linear range, to Dischinger creep. For the lower value of $\alpha_d = 0.5$, the time constant T_v must be increased, in order to allow some non-recoverable creep to occur during the first few days of loading,

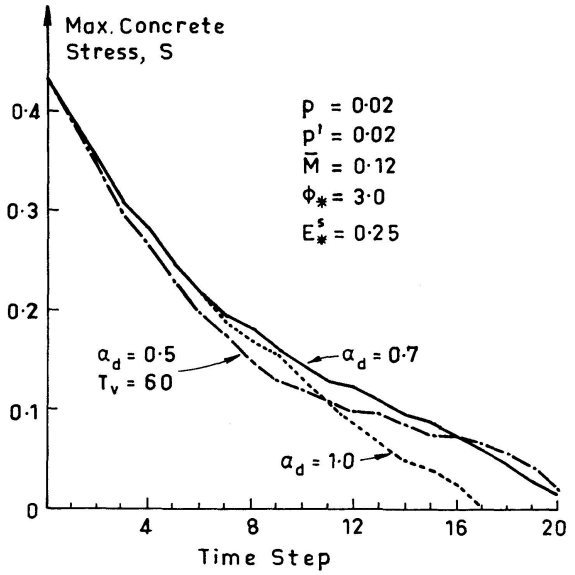

Fig. 13. Effect of parameter α_d-stresses.

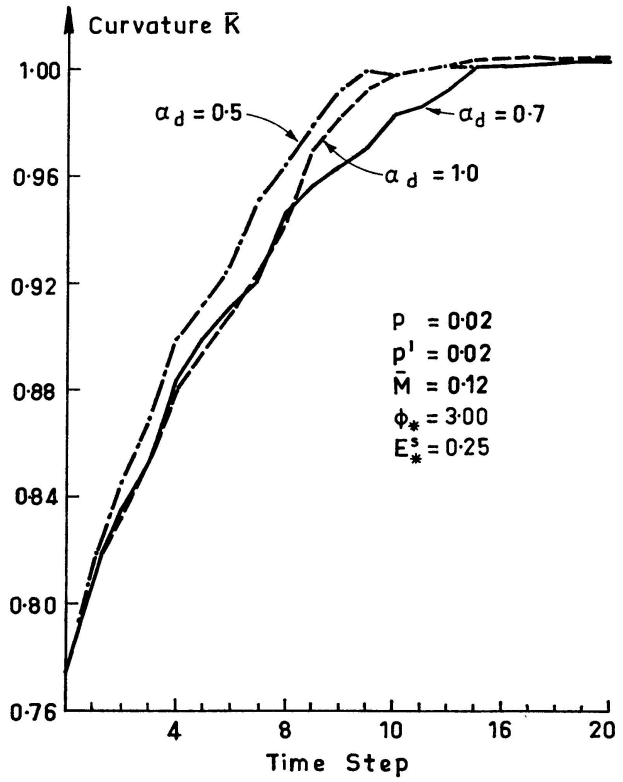

Fig. 14. Effect of parameter α_d-curvature.

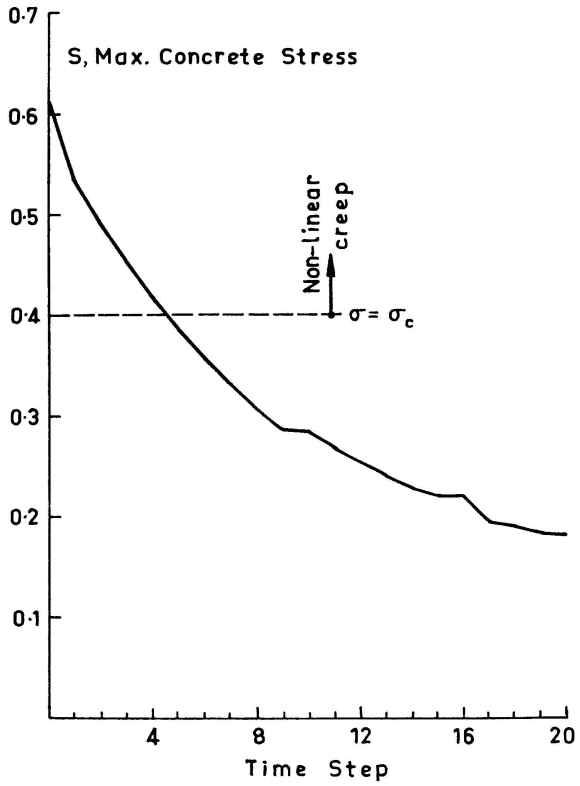

Fig. 15. Non linear creep.

i.e. to ensure that $\epsilon^c(t) > \epsilon^v(t)$. For these calculations T_v was increased from 30 to 60. Creep behaviour shown in Fig. 13 is essentially linear, since the extreme concrete stress exceeds the threshold level of $S_c = 0.4$ only during the first time interval, i.e. during portion of the first day of loading. Results of

the calculations shown in Fig. 13 are encouraging, in that changes in α_d have not resulted in very significant changes in the stress history. Corresponding curvature histories are shown in Fig. 14.

The very strong tendency for concrete to unload onto surrounding steel reinforcement lessens the importance of non-linear creep in the case of pure flexure. In Fig. 15a sustained overload moment of $\bar{M} = 0.18$ (nearly 90 percent of ultimate moment) produced an initial concrete stress of 0.53. This has attenuated to the threshold level of 0.4 in five time intervals, so that, even at high overload, non-linear creep has occurred only during the first week of loading. Non-linear creep increases the rate of transfer of stress from concrete to steel and, to this extent, tends to be self destroying. Non-linear creep may nevertheless become of prime importance in sections of slender columns. Here, increase in curvature with time results in large increases in deflection and in the geometric non-linearities. This can, in turn, bring about creep buckling.

6. Concluding Remarks

The procedure described in this paper can be used to calculate the curvature history of a reinforced concrete section for any prescribed moment history. This allows the time-varying behaviour of a statically determinate member to be analysed for any variable load history [5]. The procedure also provides a basis for the analysis of time-varying behaviour of indeterminate members, and is at present being used for this purpose.

The procedure can be extended without difficulty to apply to members of irregular section subjected to skew bending.

Although one specific constitutive relation for concrete has been used throughout the present study, changes both in the instantaneous stress-strain relation and in the creep law can be made without affecting in any way the calculation procedure. It is only necessary that the creep law be expressed in difference formulation.

Possible variations with time in concrete material properties such as concrete strength and stiffness have not been considered. Although such variations can be accounted for without difficulty, they do not usually have a significant effect on structural behaviour. Indeed, some of the effects included in the present analysis have proved to be of minor importance. This was, of course, not unexpected: a prime motivation in the development of such a complex procedure is to provide a standard of comparison for simplified methods of analysis [11].

7. List of Symbols

a = depth of section
A_s = total area of steel in section
b = width of section
E_c = initial elastic modulus of concrete
$E_{ij}(n)$ = $\frac{\epsilon_{ij}(n)}{\epsilon_c'}$; normalized concrete strain in (i,j)th element at time $t(n)$
$E^c_{ij}(n)$ = creep component of $E_{ij}(n)$
$E^d_{ij}(n)$ = ageing component of $E^c_{ij}(n)$
$E^e_{ij}(n)$ = linear elastic component of $E^i_{ij}(n)$
$E^i_{ij}(n)$ = $E^e_{ij}(n) + E^p_{ij}(n)$; instantaneous component of $E_{ij}(n)$
$E^p_{ij}(n)$ = plastic component of $E^i_{ij}(n)$
$E^v_{ij}(n)$ = viscoelastic component of $E^c_{ij}(n)$
$E^s_{ij}(n)$ = shrinkage component of $E_{ij}(n)$
$E_k(n)$ = $\frac{\epsilon_k(n)}{\epsilon_y}$; normalized strain in k-th steel element at time $t(n)$
$E_0(n)$ = normalized concrete strain in extreme compression fibre
$E_1(n)$ = normalized concrete strain in extreme tension fibre
$f(t)$ = pure time function defining the shape of the creep function
$g(t)$ = pure time function defining the shape of the shrinkage function
$G(\sigma)$ = non-linear, power function of stress
$H(\sigma)$ = $1 + G(\sigma)$; non-linear multiplying factor
K = curvature
K_{ref} = $\frac{\epsilon_c'}{a}$; reference curvature
$\overline{K}$ = $\frac{K}{K_{ref}}$; non dimensionalized curvature
m = $\frac{\sigma_y}{\sigma_u}$
$\max(E^i)$ = maximum value of instantaneous strain occurring in previous loading history
$\max(S)$ = maximum value of S occurring in previous loading history
$\overline{M}$ = $\frac{M}{\sigma_u b a^2}$; non-dimensionalized moment
$M(n)$ = moment prescribed for time increment $\Delta t(n)$
N_a = number of rows of concrete elemental areas
N_b = number of columns of elemental concrete areas
N_c = $N_a N_b$; total number of elemental concrete areas in rectangular section
p = proportion of tension steel
p' = proportion of compression steel
$\overline{P}$ = $\frac{P}{\sigma_u b a}$; resultant longitudinal force acting in section, non-dimensionalized

S = $\frac{\sigma}{\sigma_u}$; non-dimensionalized concrete stress

S_c = $\frac{\sigma_c}{\sigma_u}$; threshold stress level at which creep becomes non-linear

$S_{ij}(n)$ = non dimensional stress in (i,j)th concrete element during time interval $\Delta t(n)$

$S_k(n)$ = non-dimensional stress in k-th steel element during time interval $\Delta t(n)$

$S_k^c(n)$ = equivalent stress (non-dimensional) in concrete at k-th steel element

t_p = tolerance on computed longitudinal force in section

t_M = tolerance on computed moment in section

$t(n)$ = time instant

T_v = time parameter of viscoelastic component of creep

x_i = x component of (i,j)th concrete element

x_k = x component of k-th steel element

α_i = $\frac{x_i}{a}$

α_k = $\frac{x_k}{a}$

$\alpha_d, \alpha_m, \alpha_n, \alpha_v$ = parameters in creep law

γ_1, γ_2 = parameters defining shape of instantaneous stress-strain relation for concrete

$\epsilon(t)$ = $\epsilon^i(t)+\epsilon^c(t)+\epsilon^s(t)$; total strain in concrete at time t

ϵ_c' = instantaneous strain corresponding to σ_u

ϵ_y = steel yield strain

$\epsilon^c(t)$ = $\epsilon^d(t)+\epsilon^v(t)+\epsilon^n(t)$; creep strain

$\epsilon^d(t)$ = ageing component of $\epsilon^c(t)$

$\epsilon^e(t)$ = linear elastic component of $\epsilon^i(t)$

$\epsilon^i(t)$ = $\epsilon^e(t)+\epsilon^p(t)$; instantaneous component of $\epsilon(t)$

$\epsilon^n(t)$ = non-linear component of $\epsilon^c(t)$

$\epsilon^p(t)$ = plastic component of $\epsilon^i(t)$

$\epsilon^s(t)$ = shrinkage component of $\epsilon(t)$

$\epsilon^v(t)$ = viscoelastic component of $\epsilon^c(t)$

η = $\frac{\epsilon_y}{\epsilon_c'}$

μ = $\frac{A_s}{b\,a}$; total steel proportion

$\sigma_{ij}(n)$ = stress in (i,j)th concrete element during time interval $\Delta t(n)$

σ_u = strength of concrete in member

σ_y = steel yield stress

$\phi(t)$ = creep function

ϕ_* = $\phi_*^d+\phi_*^v$; end value of $\phi(t)$

$\phi^d(t)$ = creep function (Dischinger component of $\phi(t)$)

ϕ^d_* = end value of $\phi^d(t)$
ϕ^v_* = concrete creep parameter
ΔE = increment in normalized strain
ΔM = increment in moment
$\Delta t(n)$ = time interval

8. References

1. Bresler, B., and Selna, L.: Analysis of Time-Dependent Behaviour of Reinforced Concrete Structures, Paper No. 5, Symposium on Creep of Concrete, ACI Publication SP-9, 1964.
2. Dischinger, F.: Untersuchungen über die Knicksicherheit, die elastische Verformung und das Kriechen des Betons bei Bogenbrücken, Bauingenieur, Vol. 20, 1939, Vol. 18, 1937.
3. Ferry Borges, J., and Arantes e Oliveira, E. R.: Non-linear Analysis of Reinforced Concrete Structures, Publications, International Association for Bridge and Structural Engineering, Zürich, Vol. 23, 1963.
4. Flügge, W.: Viscoelasticity, Blaisdell, Waltham, Mass. 1967.
5. Lambert, J.: Long Term Deformations in Reinforced Concrete Flexural Members, M. Eng. Sc. Thesis, The University of New South Wales, April, 1972.
6. Leong, T. W., and Warner, R. F.: Creep and Shrinkage in Reinforced Concrete Beams, Journal of the Structural Division, ASCE, Vol. 96, No. ST3, Proc. Paper 7150, March, 1970.
7. Ramu, P., Grenacher, M., Baumann, M., and Thürlimann, B.: Versuche an gelenkig gelagerten Stahlbetonstützen unter Dauerlast, Bericht Nr. 7418-1, Institut für Baustatik, ETH Zürich, May, 1969.
8. Sackman, J. L., and Nickel, R. E.: Creep of a Cracked Reinforced Beam, Journal of the Structural Division, ASCE, Vol. 94, No. ST1, Proc. Paper 5764, Jan., 1968.
9. Warner, R. F.: Biaxial Moment Thrust Curvature Relations, Journal of the Structural Division, ASCE, Vol. 95.
10. Warner, R. F.: Non-Linear Creep in Concrete Columns, Final Report, Madrid Creep Symposium 1970, International Association for Bridge and Structural Engineering.
11. Warner, R. F.: Simplified Model of Creep and Shrinkage Effects in Reinforced Concrete Flexural Members, UNICIV Report No. R-81, The University of New South Wales, February, 1972.

Summary

A method is described for determining the non-linear, time-varying response of a reinforced concrete beam section to any prescribed moment history. The cross section is partitioned into a finite number of elemental areas of steel and concrete, and a non-linear constitutive relation is used to represent the behaviour of each concrete element.

An incremental, step-wise numerical computation procedure allows curvature and stresses and strains to be evaluated for moment histories which may include loading and unloading cycles as well as periods of sustained loading at the service load level and at any overload level up to the carrying capacity of the section.

Résumé

On décrit une méthode pour la détermination de la réaction non-linéaire et dépendant du temps de la section d'une poutre en béton armé à des changements prescrits du moment. La section est divisée en un nombre fini d'éléments en acier et en béton. On se sert d'une relation non-linéaire constitutive pour représenter le comportement de chaque élément en béton.

Une procédure graduelle supplémentaire par ordinateur permet à évaluer flexion, tension et déformation pour le changement du moment, comprenant des cycles de charge et de décharge ainsi que des périodes de charges continues au niveau de service et à n'importe quel niveau de surcharge jusqu'à la capacité de charge de la section.

Zusammenfassung

Es wird eine Methode zur Bestimmung der nichtlinearen, zeitabhängigen Reaktion eines Stahlbetonquerschnitts auf ein vorgeschriebenes veränderliches Moment beschrieben. Der Querschnitt ist in eine finite Anzahl von Elementflächen aus Stahl und Beton unterteilt, und eine nichtlineare konstitutive Beziehung dient zur Darstellung des Verhaltens jedes Betonelements.

Ein inkrementales, stufenweises Computerverfahren gestattet Biegung, Spannung und Deformation für ein veränderliches Moment auszuwerten, welches Belastungs und Entlastungszyklen sowie Perioden dauernder Betriebslast einschliesst, und bei irgendwelchem Überlastniveau bis zur Belastbarkeit des Querschnitts.

Leere Seite
Blank page
Page vide